



**TECHNISCHE  
UNIVERSITÄT  
WIEN**

Vienna University of Technology

# DISSERTATION

## **Synchrotron Micro X-Ray Fluorescence Imaging of Trace Elements in Articular Cartilage and Bone in Health and Disease**

Ausgeführt zum Zwecke der Erlangung des Akademischen Grades eines Doktors  
der technischen Wissenschaften unter der Leitung von

**Ao. Univ-Prof. Dipl.-Ing. Dr. Christina Strelt**

E141

Atominstitut

eingereicht an der Technischen Universität Wien

Fakultät für Physik

von

**Dipl.-Ing. Bernhard Pemmer**

Mat. Nr.: 0026048

Ferdinand Grasser Strasse 352

A-3511 Furth bei Göttweig

Wien, 1. September 2013



## Kurzfassung

Bei der Analyse von entnommenen Gewebeproben lebender Organismen mit hochempfindlichen Messmethoden können Elemente in sehr geringen Mengen ( $< \mu\text{g/g}$ ) nachgewiesen werden. Diese sogenannten Spurenelemente können für den Organismus essentiell, unwichtig oder sogar schädlich sein. Jedoch ist die Rolle, welche die zahlreichen Spurenelemente in unterschiedlichen Geweben z.B. Knochen spielen, kaum bekannt. Eines dieser Spurenelemente ist das toxische Element Blei (Pb). Die Exposition gegenüber Pb wird mit unterschiedlichen chronischen Erkrankungen des Nerven-, Blutbildendensystems, des Skelettes, der Nieren und des Verdauungstraktes assoziiert. Etwa 95 % des Bleis im menschlichen Körper ist im Skelett gespeichert. Andere Spurenelemente, die im Zusammenhang mit dem Stoffwechsel und der Mineralisierung von Knochen wichtig sind, sind Zink (Zn) und Strontium (Sr). Zn ist ein wesentlicher Bestandteil vieler Enzyme und an der Knochenresorption beteiligt. Sr ist seit mehreren Jahren als Wirkstoff zur Behandlung von postmenopausaler Osteoporose (pmpOP) in Form von Strontiumranelat (SrR) zugelassen. Knochen ist ein inhomogener anisotroper organisch-mineralischer Verbundwerkstoff, der sich aus grundlegenden strukturellen Einheiten (BSUs) – z.B. Knochenpakete und Osteone –, getrennt durch die sogenannten Zementlinien, zusammensetzt. Knochen wird ständig umgebaut und Krankheiten wie pmpOP verändern diesen Umbauprozess.

Es war ein Ziel, herauszufinden, ob der veränderte Knochenstoffwechsel in pmpOP die Verteilung und Menge von Zn, Sr und Pb im Knochen beeinflusst. Weiters war von Interesse ob es einen Zusammenhang zwischen der Zn, Sr und Pb Verteilung und der Struktur vom Knochen gibt. Analysiert wurden humane Knochenproben von Patienten mit einem osteoporotischen Schenkelhalsbruch und gesunde Kontrollen mit Synchrotronstrahlungs induzierter Mikro-Röntgenfluoreszenzanalyse (SR  $\mu$ -XRF). Es konnte gezeigt werden, dass die Verteilung und Menge von Zn, Sr und Pb stark mit der Knochenstruktur korreliert ist. Die Zementlinien wiesen eine signifikante Ansammlung von Zn und Pb, im Vergleich zum Benachbarten Knochen auf, und in den BSUs zeigten Sr und Pb einen überproportionalen Anstieg mit dem Ca-Gehalt des Knochens. Durch den veränderten Knochenstoffwechsel bei pmpOP scheint es allerdings nicht zu signifikanten Veränderungen auf der Ebene der Spurenelemente (Verteilung und Menge) zu kommen.

In früheren Studien konnte eine Ansammlung von Zn und Pb in der Grenzschicht zwischen mineralisiertem und nicht mineralisiertem Gelenksknorpel – der sogenannte Tidemark (TM) – entdeckt werden. Da sich der Gelenksknorpel und der Kno-

chen in ihrer chemischen Zusammensetzung grundlegend unterscheiden, könnte spekuliert werden, dass Pb in diesen beiden Geweben unterschiedlich gebunden ist. In Proben von Patienten ohne bekannte Knochenkrankheiten wurden mittels Röntgen Absorptions-Spektrometrie (XAS) der chemische Bindungszustand von Pb untersucht. Es stellte sich heraus, dass Pb sowohl in der TM als auch im Knochen an kohlenstoffhaltigen Kalziumhydroxyapatit gebunden ist. SrR ist seit mehreren Jahren zur Behandlung von pmpOP zugelassen. In verschiedenen Tier- und Humanstudien wurde die frakturhemmende Wirkung bewiesen. Dennoch sind die Auswirkungen der Ernährung, im speziellen der Ca-Gehalt, auf die Sr Aufnahme in den Knochen unklar. Weiters ist die Verteilung des, im trabekulären Knochen eingebauten Sr, nicht gut dokumentiert. Um diese Fragen zu beantworten, wurden Knochenproben eines Tierversuches mit Ratten mit SR  $\mu$ -XRF untersucht. In diesem Tierversuch wurde die Ca Aufnahme (normal und niedrig) und die Verwendung von verschiedenen Sr Wirkstoffen (SrR und  $\text{SrCl}_2$ ) getestet. Es konnte gezeigt werden, dass Sr überwiegend in, während der Behandlung gebildetem, neuem Knochengewebe akkumuliert wird. Die Ca Aufnahme stellte sich als wesentlicher Faktor für die Sr Akkumulation im Knochen heraus. Zu niedrige Ca Aufnahme führte zu deutlich erhöhten Sr Werten im Knochen. Der SrR Wirkstoff hat in allen Fällen zu einer höheren Sr Menge im Knochen geführt als das  $\text{SrCl}_2$ .

Die SR  $\mu$ -XRF Experimente wurden an der ANKA FLUO Beamline (Karlsruhe, Deutschland) mit einem konfokalen Aufbau aus zwei Polykapillaren und einer laterale Auflösung von etwa  $12\text{ }\mu\text{m} \times 12\text{ }\mu\text{m}$  ausgeführt. Die XAS Messungen in der XANES Region, zur Bestimmung der Bindung von Pb in Knochen und TM, wurden an der ANKA SUL-X Beamline (Karlsruhe, Deutschland) gemacht. Die histologischen Eigenschaften der inspizierten Knochenareale wurden mittels quantitativer Rasterelektronenmikroskopie (qBEI) bestimmt.

Da Strahlzeit an Synchrotrons begrenzt, und schwer zu bekommen ist, wurde ein konfokales  $\mu$ -XRF System mit einer Niederleistungsrontgenröhre (50 W) im Labor getestet, um zu sehen, ob es zum Prescreening für künftige SR  $\mu$ -XRF Studien benutzt werden kann. Die Idee ist, die optimalen Messbereiche bereits im Labor auszuwählen, um am Synchrotron möglichst wenig Zeit zu verlieren. Die SR  $\mu$ -XRF Ergebnisse des Rattenterversuches wurden mit Messungen der gleichen Proben im Labor verglichen. Trotz der weniger optimalen Messbedingungen im Labor wurden die gleichen signifikanten Unterschiede für die verschiedenen Behandlungsgruppen gefunden. Das Laborsystem eignet sich offenbar als leicht zugängliches Prescreening-Werkzeug für künftige SR  $\mu$ -XRF Messungen.



## Abstract

Analyzing tissue of living beings using highly sensitive methods, elements in very minute quantities ( $< \mu\text{g/g}$ ) can be found. These so called trace elements can be essential and / or non-essential for the living organism. However, the role of many trace elements in tissues e.g. bone is poorly understood. One of these trace elements is the toxic element lead (Pb). Exposure to it is associated with chronic diseases in the nervous, hematopoietic, skeletal, renal and endocrine system. About 95 % of the total human body burden of Pb are present in the skeleton. Other trace elements important in the context of bone metabolism and mineralization are zinc (Zn) and strontium (Sr). Zn is an essential part of several enzymes involved in bone remodeling and since several years Sr is approved as therapeutic agent for postmenopausal osteoporosis (pmpOP) in the form of Strontium Ranelate (SrR).

Bone tissue is an inhomogeneous anisotropic organic mineral composite material made up of basic structural units (BSUs) –e.g. bone packets and osteons – separated by the so called cement lines. Bone tissue is continuously remodelled and diseases like pmpOP drastically alter this remodelling process.

It was an aim to find out if the altered bone metabolism in pmpOP influences the distribution and the levels of Zn, Sr and Pb in bone. Further it was of interest to see if the microscopic structure of bone (bone packets, osteons, cement lines) is linked to the localization and the levels of these trace elements. Analyzing osteoporotic fractured and non-fractured human bone samples with synchrotron radiation induced micro X-Ray fluorescence analysis (SR  $\mu$ -XRF) it could be shown that the distribution and amounts of Zn, Sr and Pb are strongly correlated with the structural units of bone. The cement lines presented significant accumulations of Zn and Pb compared to adjacent bone, and in the BSUs Sr and Pb were found to have a strong over proportional correlation with the calcium (Ca) content. However, the altered bone metabolism in pmpOP turned out to have not significant influence on the trace element levels or distribution. In previous studies an accumulation of Zn and Pb at the interface between mineralized and non-mineralized articular cartilage – the so called tidemark (TM) – was discovered. As the chemical environment in the articular cartilage is completely different from bone tissue it could be speculated that the chemical binding of Pb different in the TM and in bone. Human joint samples with no known bone disease were examined using X-Ray absorption spectrometry (XAS) to clarify this issue. It turned out that Pb found in the TM and bone is present in the same chemical compound, carbonated calcium hydroxyapatite.

Since several years SrR is an approved therapeutic agent for pmpOP. In various animal and human studies the anti-fracture effect of SrR was documented. However the impact of the nutritional Ca intake - and thus the Ca serum levels - on the Sr uptake into bone was unclear. Additionally, the localisation of the incorporated Sr in trabecular bone was not well documented. In order to address these issues bone samples from a rat animal model were investigated applying SR  $\mu$ -XRF. This animal model was simulation the different nutritional Ca intake (normal and deficient) and the use of different Sr drugs (SrR and SrCl<sub>2</sub>). It could be shown that the Sr is predominantly accumulated in the bone tissue formed during the treatment. The nutritional Ca intake turned out to have a tremendous impact on the Sr incorporation into bone. Deficient Ca intake lead to distinctly elevated Sr levels in bone. The SrR drugs lead to slightly higher Sr incorporation in all cases compared to SrCl<sub>2</sub>.

The SR  $\mu$ -XRF experiments were carried out at the ANKA FLUO beamline (Karlsruhe, Germany) using a confocal setup with two polycapillary half lenses yielding a lateral resolution of about 12  $\mu$ m x 12  $\mu$ m. The XAS analysis in the XANES region, to elucidate the speciation of Pb in bone and TM, were carried out at the ANKA SUL-X beamline (Karlsruhe, Germany) offering a spot size on the sample in the range of 20  $\mu$ m to 200  $\mu$ m. The histological properties and the morphology of the inspected bone areas were determined using quantitative backscattered electron imaging (qBEI).

As beamtime at synchrotron facilities is limited and not easy to obtain a laboratory based confocal  $\mu$ -XRF system, issued with a low power X-Ray tube (50 W) was tested to see if the laboratory  $\mu$ -XRF setup can be used as pre-screening tool for future SR  $\mu$ -XRF studies. The idea was that the most promising areas can already be selected in the laboratory, to gain optimal use of the allocated synchrotron beamtime. Results from the rat animal model obtained with SR  $\mu$ -XRF were compared to measurements of the same samples in the laboratory. Despite the inferior measurement conditions in the laboratory compared to the synchrotron, the same significant differences that were found for the different treatment groups. The idea of using the laboratory system as easy accessible pre-screening tool for synchrotron studies is therefore reasonable.

**A part of the work presented in this thesis -**

**appears in the following refereed publications:**

1. MEIRER, F., PEMMER, B., PEPPONI, G., ZOEGER, N., WOBRAUSCHEK, P., SPRIO, S., TAMPIERI, A., GÖTTLICHER, J., STEININGER, R., MANGOLD, S., ROSCHGER, P., BERZLANOVICH, A., HOFSTÄTTER, J., STRELI, C.: Assessment of chemical species of lead accumulated in tidemarks of human articular cartilage by X-ray absorption near-edge structure analysis. In: *Journal of Synchrotron Radiation* 18 (2011), No. 2, P. 238–244. DOI: <http://dx.doi.org/10.1107/S0909049510052040>
2. PEMMER, B., HOFSTÄTTER, J., MEIRER, F., SMOLEK, S., WOBRAUSCHEK, P., SIMON, R., FUCHS, R. K., ALLEN, M. R., CONDON, K. W., REINWALD, S., PHIPPS, R. J., BURR, D. B., PASCHALIS, E., KLAUSHOFER, K., STRELI, C., ROSCHGER, P.: Increased strontium uptake in trabecular bone of ovariectomized calcium-deficient rats treated with strontium ranelate or strontium chloride. In: *Journal of Synchrotron Radiation* 18 (2011), No. 6, P. 835–841. DOI: <http://dx.doi.org/10.1107/S090904951103038X>
3. SMOLEK, S., PEMMER, B., FÖLSER, M., STRELI, C., WOBRAUSCHEK, P.: Confocal micro-x-ray fluorescence spectrometer for light element analysis. In: *Review of Scientific Instruments* 83 (2012), No. 8, P. 083703–1 – 083703–6. DOI: <http://dx.doi.org/10.1063/1.4744934>
4. PEMMER, B., ROSCHGER, A., WASTL, A., HOFSTÄTTER, J. G., WOBRAUSCHEK, P., SIMON, R., THALER, H. W., ROSCHGER, P., KLAUSHOFER, K., STRELI, C.: Spatial distribution of the trace elements zinc, strontium and lead in human bone tissue. In: *Bone* 52 (2013), No. 1, 184–193. DOI: <http://dx.doi.org/10.1016/j.bone.2013.07.038>. – ISBN 8756–3282

**has been presented at the following conferences and meetings as posters or oral presentations:**

1. MEIRER, F., HOFSTÄTTER, J., SMOLEK, S., PEMMER, B., WOBRAUSCHEK, P., SIMON, R., FUCHS, R. K., ALLEN, M. R., CONDON, K. W., REINWALD, S., MCCLENATHAN, D., KECK, B., PHIPPS, R. J., BURR, D. B., ROSCHGER, P., PASCHALIS, E., KLAUSHOFER, K., STRELI, C.: *Level and spatial distribution of trace elements in bone following strontium treatment in calcium deficient rats*. 2009. – Vortrag: ICXOM 2009, Karlsruhe; 2009-09-17 – 2009-09-20
2. MEIRER, F., PEMMER, B., ZÖGER, N., STRELI, C., GÖTTLICHER, J., STEININGER, R., MANGOLD, S., TAMPIERI, A., SPRIO, S., PEPPONI, G., HOFSTÄTTER, J., ROSCHGER, P., KLAUSHOFER, K.: *Speciation of Pb in the tidemark of human articular Cartilage using XANES at the SUL-X beamline of ANKA*. 2009. – Vortrag: ICXOM 2009, Karlsruhe; 2009-09-17 – 2009-09-20
3. MEIRER, F., ZÖGER, N., PEMMER, B., STRELI, C., GÖTTLICHER, J., STEININGER, R., MANGOLD, S., TAMPIERI, A., SPRIO, S., PEPPONI, G., HOFSTÄTTER, J.,

- ROSCHGER, P., KLAUSHOFER, K.: *Speciation of Pb in the tidemark of human articular Cartilage using micro-XRF-XANES*. 2009. – Vortrag: öpg Jahrestagung 2009 Innsbruck, Innsbruck; 2009-09-02 – 2009-09-04
4. ZÖGER, N., MEIRER, F., PEMMER, B., STRELI, C., GÖTTLICHER, J., STEININGER, R., MANGOLD, S., TAMPIERI, A., SPRIO, S., PEPPONI, G., HOFSTÄTTER, J., ROSCHGER, P., KLAUSHOFER, K.: *Speciation of Pb in the tidemark of human articular Cartilage*. 2009. – Vortrag: 36th ECTS conference, Wien; 2009-05-23 – 2009-05-27
  5. MEIRER, F., HOFSTÄTTER, J., SMOLEK, S., PEMMER, B., WOBRAUSCHEK, P., SIMON, R., FUCHS, R. K., ALLEN, M. R., CONDON, K. W., REINWALD, S., MCCLENATHAN, D., KECK, B., PHIPPS, R. J., BURR, D. B., ROSCHGER, P., PASCHALIS, E., KLAUSHOFER, K.: *Levels and Spatial Distribution of Trace Elements in Bone Following Strontium Treatment in Calcium Deficient Rats*. 2010. – Posterpräsentation: EXRS 2010, Figueira da Foz, Portugal; 2010-06-20 – 2010-06-25
  6. MEIRER, F., HOFSTÄTTER, J., SMOLEK, S., PEMMER, B., WOBRAUSCHEK, P., SIMON, R., FUCHS, R. K., ALLEN, M. R., CONDON, K. W., REINWALD, S., MCCLENATHAN, D., KECK, B., PHIPPS, R. J., BURR, D. B., ROSCHGER, P., PASCHALIS, E., KLAUSHOFER, K., STRELI, C.: *Levels and Spatial Distribution of Trace Elements in Bone Following Strontium Treatment in Calcium Deficient Rats*. 2010. – Vortrag: 59th Annual Denver X-ray Conference, Denver; 2010-08-02 – 2010-08-06
  7. MEIRER, F., PEMMER, B., ZÖGER, N., STRELI, C., GÖTTLICHER, J., STEININGER, R., MANGOLD, S., TAMPIERI, A., SPRIO, S., PEPPONI, G., HOFSTÄTTER, J., ROSCHGER, P., KLAUSHOFER, K.: *Speciation of Pb at the Tidemark of Articular Cartilage and in Trabecular Bone*. 2010. – Posterpräsentation: EXRS 2010, Figueira da Foz, Portugal; 2010-06-20 – 2010-06-25
  8. GÖTTLICHER, J., MEIRER, F., PEMMER, B., ZÖGER, N., STRELI, C., STEININGER, R., MANGOLD, S., TAMPIERI, A., SPIRO, S., PEPPONI, G., HOFSTÄTTER, J., KLAUSHOFER, K.: *Speciation of Pb in Human Trabecular Bone and the Tidemark of Articular Cartilage*. 2010. – Vortrag: 88. Jahrestagung der Deutschen Mineralogischen Gesellschaft, Münster, Deutschland; 2010-09-19 – 2010-09-22
  9. STRELI, C., MEIRER, F., WOBRAUSCHEK, P., ZÖGER, N., SMOLEK, S., PEMMER, B., ROSCHGER, P., HOFSTÄTTER, J., KLAUSHOFER, K., PEPPONI, G., FALKENBERG, G., SIMON, R., GÖTTLICHER, J.: *Ortsaufgelöste Elementverteilung in Knochenproben mit Mikro-Röntgenfluoreszenzspektrometrie*. 2010. – Vortrag: Institutsseminar 2010, Institut für Leichtbau, TU Wien; 2010-01-08
  10. MEIRER, F., HOFSTÄTTER, J., SMOLEK, S., PEMMER, B., WOBRAUSCHEK, P., SIMON, R., FUCHS, R. K., ALLEN, M. R., CONDON, K. W., REINWALD, S., MCCLENATHAN, D., KECK, B., PHIPPS, R. J., BURR, D. B., ROSCHGER, P., PASCHALIS, E., KLAUSHOFER, K., STRELI, C.: *Levels and Spatial Distribution of Trace Elements in Bone Following Strontium Treatment in Calcium Deficient Rats*. 2011. – Posterpräsentation: 7th European Winter School on Neutrons and Synchrotron Radiation, Planneralp, Austria; 2011-03-06 – 2011-03-12

11. MEIRER, F., PEMMER, B., ZOEGER, N., STRELI, C., PEPPONI, G., GÖTTLICHER, J., STEININGER, R., MANGOLD, S., TAMPIERI, A., SPRIO, S., ROSCHGER, P., KLAUSHOFER, K., HOFSTÄTTER, J.: *Speciation of Pb at the Tidemark of Articular Cartilage and in Trabecular Bone*. 2011. – Posterpräsentation: 7th European Winter School on Neutrons and Synchrotron Radiation, Planneralp, Austria; 2011-03-06 – 2011-03-12
12. MEIRER, F., ZOEGER, N., Pemmer, B.and, STRELI, C., GÖTTLICHER, J., STEININGER, R., MANGOLD, S., TAMPIERI, A., SPRIO, S., PEPPONI, G., HOFSTÄTTER, J., ROSCHGER, P., KLAUSHOFER, K.: *Speciation of Pb at the Tidemark of Articular Cartilage and in Trabecular Bone*. 2011. – Posterpräsentation: ANKA Seminar, Karlsruhe, Germany; 2011-10-13 – 2011-10-14
13. PEMMER, B., ROSCHGER, A., WOBRAUSCHEK, P., STRELI, C., HOFSTÄTTER, J., ROSCHGER, P., KLAUSHOFER, K., SIMON, R.: *Trace element distribution in trabecular and cortical bone of fractured femoral necks of postmenopausal osteoporotic women: a synchrotron micro x-ray fluorescence imaging study*. 2011. – Posterpräsentation: Denver X-Ray Conference, Colorado Springs, USA; 2011-08-01 – 2011-08-05
14. PEMMER, B., ZOEGER, N., STRELI, C., PEPPONI, G., MEIRER, F., GÖTTLICHER, J., STEININGER, R., MANGOLD, S., TAMPIERI, A., SPIRO, S., ROSCHGER, P., KLAUSHOFER, K., HOFSTÄTTER, J.: *Speciation of Pb at the Tidemark of Articular Cartilage and in Trabecular Bone*. 2011. – Posterpräsentation: Denver X-Ray Conference, Colorado Springs, USA; 2011-08-01 – 2011-08-05
15. GÖTTLICHER, J., STEININGER, R., GAMALETOS, P., GODELITSAS, A., KERSTEN, M., MAJZLAN, J., MEIRER, F., MERTZIMEKIS, T. J., PEMMER, B., PEPPONI, G., ROSCHGER, P., SCHMIDT, G., STRELI, C., WOBRAUSCHEK, P., ZOEGER, N.: *Environmental Research at the SUL-X Beamline of the Synchrotron Radiation Source ANKA*. 2011. – Vortrag: Frontiers in Environmental Geosciences, Wales, GB; 2011-06-21 – 2011-06-24
16. PEMMER, B., ROSCHGER, A., HOFSTÄTTER, J., WOBRAUSCHEK, P., SIMON, R., ROSCHGER, P., KLAUSHOFER, K., STRELI, C.: *SR  $\mu$ -XRF Imaging of Osteoporotic Bone*. 2011. – eingeladen; Vortrag: ANKA User Meeting 2011, Karlsruhe, Germany; 2011-10-13 – 2011-10-14
17. PEMMER, B., ROSCHGER, A., HOFSTÄTTER, J., WOBRAUSCHEK, P., SIMON, R., ROSCHGER, P., KLAUSHOFER, K., STRELI, C.: *Trace element distribution in trabecular and cortical bone of fractured femoral necks of postmenopausal osteoporotic women: a synchrotron micro x-ray fluorescence imaging study*. 2011. – Posterpräsentation: öGKM Herbsttagung 2011, Vienna, Austria; 2011-10-25
18. PEMMER, B., WOBRAUSCHEK, P., STRELI, C., ROSCHGER, A., ROSCHGER, P., KLAUSHOFER, K., HOFSTÄTTER, J.: *2D and 3D Imaging of Human Tissue*. 2011. – Vortrag: Imaging in Life Sciences 2, Vienna, Austria; 2011-12-07
19. ROSCHGER, A., PEMMER, B., ROSCHGER, P., HOFSTÄTTER, J., SIMON, R., KLAUSHOFER, K., STRELI, C.: *Lokale Verteilung der Spurenelemente Blei, Zink und Strontium im menschlichen Knochen*. 2011. – Vortrag: 3 Ländertagung der öGMP, DGMP und SGSMP - medizinische Physik 2011, Vienna, Austria; 2011-10-01

20. ROSCHGER, P., PEMMER, B., FRATZL, P., KLAUSHOFER, K.: *Strontium-ranelate treatment leads to uptake of strontium in bone.* 2011. – Vortrag: ÖGKM Herbsttagung 2011, Vienna, Austria; 2011-10-25
21. STRELI, C., INGERLE, D., PEMMER, B., WOBRAUSCHEK, P., MEIRER, F., PEPPONI, G.: *Synchrotron radiation induced x-ray spectrometry.* 2011. – Vortrag: Micro-analytical techniques based on nuclear spectrometry for environmental monitoring and material studies, Vienna, Austria; 2011-10-10 – 2011-10-14
22. STRELI, C., PEMMER, B., MEIRER, F., PEPPONI, G., WOBRAUSCHEK, P.: *Synchrotron radiation induced TXRF and micro XRF.* 2011. – Vortrag: Seminar, Mumbai, India; 2011-12-05
23. STRELI, C., WOBRAUSCHEK, P., KREGSAMER, P., PEMMER, B., MEIRER, F., PEPPONI, G., ZOEGER, N., FALKENBERG, G., SIMON, R., GÖTTLICHER, J.: *Synchrotron X-Ray Fluorescence Spectrometry.* 2011. – Vortrag: 7th European Winter School on Neutrons and Synchrotron Radiation, Plannersalm, Austria; 2011-03-06 – 2011-03-12
24. WOBRAUSCHEK, P., MEIRER, F., PEMMER, B., STRELI, C.: *Synchrotron radiation based micro and trace XRF analysis.* 2011. – eingeladen; Vortrag: Seminar on Nondestructive Instrumental Analysis for Forensic investigation, Osaka, Japan; 2011-11-10
25. WOBRAUSCHEK, P., STRELI, C., PEMMER, B.: *Synchrotron radiation based micro and trace XRF analysis.* 2011. – Vortrag: Seminar, Indore, India; 2011-12-07
26. PEMMER, B., ROSCHGER, A., HOFSTÄTTER, J., WOBRAUSCHEK, P., SIMON, R., ROSCHGER, P., KLAUSHOFER, K., STRELI, C.: *Distribution of Trace Elements Zn, Pb and Sr in Bone Packets and Cement Lines of Cortical and Trabecular Human Bone.* 2012. – Posterpräsentation: European Calcified Tissue Society 2012, Stockholm, Sweden; 2012-05-19 – 2012-05-23
27. PEMMER, B., ROSCHGER, A., HOFSTÄTTER, J., WOBRAUSCHEK, P., THALER, H., SIMON, R., ROSCHGER, P., KLAUSHOFER, K., STRELI, C.: *SR  $\mu$ -XRF Imaging of Osteoporotic Bone.* 2012. – Vortrag: EXRS Conference, Vienna, Austria; 2012-06-18 – 2012-06-22
28. PEMMER, B., WOBRAUSCHEK, P., SMOLEK, S., STRELI, C.: *2D and 3D elemental imaging using X-ray sepctrometry.* 2012. – Vortrag: Imaging in Life Sciences Workshop IV, Vienna, Austria; 2012-11-12
29. STRELI, C., PEMMER, B., WOBRAUSCHEK, P.: *2D and 3D elemental imaging of human tissue.* 2012. – Vortrag: Imaging in Life Sciences Workshop III, Vienna, Austria; 2012-06-28

**and has been reported in not refereed scientific contributions:**

1. PEMMER, B., MEIRER, F., STRELI, C., WOBRAUSCHEK, P., ROSCHGER, P., HOFSTÄTTER, J., GÖTTLICHER, J.: Micro XANES spetroscopy in human bone and cartilage / ANKA. 2009. – Annual Report

2. PEMMER, B., HOFSTÄTTER, J., STADLBAUER, F., WOBRAUSCHEK, P., SIMON, R., ROSCHGER, P., KLAUSHOFER, K. , STRELI, C.: Synchrotron Micro X-Ray Fluorescence Imaging of Trace Elements in Articular Cartilage and Bone in osteonecrose / ANKA. 2010. – Annual Report
3. PEMMER, B., PEPPONI, G., MEIRER, F., STRELI, C., WOBRAUSCHEK, P., HOFSTÄTTER, J., ROSCHGER, P., GÖTTLICHER, J. , STEININGER, R.: Speciation of Lead in Articular Cartilage and Subchondral Bone in case of Osteoarthritis / ANKA. 2010. – Annual Report
4. PEMMER, B., ROSCHGER, A., HOFSTÄTTER, J., SIMON, R., ROSCHGER, P., KLAUSHOFER, K., WOBRAUSCHEK, P. , STRELI, C.: Spatial Distribution of Trace Elements in Human Osteoporotic Bone using Synchrotron Micro X-Ray Fluorescence Imaging / ANKA. 2010. – Annual Report
5. PEMMER, B., ROSCHGER, A., HOFSTÄTTER, J., SIMON, R., ROSCHGER, P., KLAUSHOFER, K., WOBRAUSCHEK, P. , STRELI, C.: Trace Element Distribution in Human Osteoporotic Fractured Femoral Necks using Synchrotron Micro X-Ray Fluorescence Imaging / ANKA. 2011. – Annual Report
6. STRELI, C., INGERLE, D., PEMMER, B., WOBRAUSCHEK, P., MEIRER, F. , PEPPONI, G.: Synchrotron radiation induced x-ray spectrometry / IAEA. 2011. – Final report on the second research co-ordination meeting (RCM) of the co-ordinated research project (CRP) on micro-analytical techniques based on nuclear spectrometry for environmental monitoring and material studies





# Acknowledgement

This work would never have been possible without my girlfriend Claudia, my mother Ilse and my sister Teresa, who have supported and encouraged me throughout my studies and the preparation of this thesis.

I would like to express my gratitude to my supervisor Christina Streli for the guidance and the scientific freedom she has endowed me with, since the beginning.

I also have Peter Wobrauschek and Peter Kregsamer to thank for supporting me, sharing their experience with me and for the fruitful debates on the topic and beyond.

Many more are to be thanked for the help in executing the experiments and discussions. They will be mentioned in no particular order:

- Andreas Roschger for support during the beamtimes, with data evaluation, critical review of the publications and sample preparation
- Stehpan Smolek for providing useful software tools, support during the beamtimes and with data evaluation.
- Martin Fölser for his efforts in developing software for PCA and cluster analysis
- Paul Roschger and Jochen Hofstätter (Ludwig Boltzmann Institute of Osteology at the Hanusch Hospital of WGKK and AUVA Trauma Centre Meidling, Vienna, Austria) for discussion of the data and critical review of the publications.
- Rolf Simon, Jörg Göttlicher, Ralph Steininger (Karlsruhe Institute of Technology, Institute for Synchrotron Radiation, Eggenstein, Germany) for their support during the numerous beamtimes.

This work was financially supported by:

- FWF (Austrian Science Fund): P21905-N20
- European Community's Seventh Framework Programme (FP7/2007-2013), grant agreement 226716
- European Community Six Framework Programme: "Structuring the European Research Area" ("Integrating Activity on Synchrotron and Free Electron Laser Science" (IA-SFS) RII3-CT-2004-506008)
- AUVA (Research funds of the Austrian workers compensation board) and the WGKK (Viennese sickness insurance funds)



# Contents

<b>1 Introduction .....</b>	<b>1</b>
<b>2 X-Ray Fluorescence Analysis .....</b>	<b>5</b>
2.1 X-Ray Sources .....	5
2.1.1) Synchrotron Radiation .....	5
2.1.1.1) Origin and Intensity .....	6
2.1.1.2) Time Structure and Spatial Distribution .....	9
2.1.1.3) Polarization .....	10
2.1.1.4) Characterization Parameters .....	11
2.1.1.5) Insertion Devices .....	11
2.1.2) X-Ray Tubes .....	15
2.1.2.1) Properties of X-Ray Tube Spectra .....	16
2.1.2.2) Continuous Spectrum .....	17
2.1.2.3) Characteristic Spectrum .....	17
2.2 Interaction of X-Rays with Matter .....	19
2.2.1) Coherent Scattering .....	20
2.2.2) Incoherent Scattering.....	20
2.2.3) Photo Effect .....	20
2.2.4) Attenuation Coefficient .....	21
2.2.5) Information Depth .....	23
2.3 Energy Dispersive X-Ray Fluorescence Analysis (EDXRF) .....	24
2.3.1) Intensity of the Fluorescence Radiation .....	25
2.3.2) Energy Dispersive Detectors .....	27
2.3.2.1) Si(Li) Detectors .....	27
2.3.2.2) Silicon Drift Detectors (SDD) .....	29
2.3.3) Signal Processing and Detector Artefacts .....	30
2.4 Micro X-Ray Fluorescence Analysis ( $\mu$ -XRF) .....	31
2.4.1) X-Ray Optics .....	32
2.4.1.1) Monochromators .....	32
2.4.1.2) Reflective Optics .....	35
2.4.2) Confocal $\mu$ -XRF .....	37
2.5 X-Ray Absorption Analysis (XAS) .....	39
2.5.1) X-Ray Absorption Near Edge Structure (XANES) .....	39
<b>3 Quantitative Backscattered Electron Imaging (qBEI) .....</b>	<b>43</b>
3.1 Principle of Scanning Electron Microscopy (SEM) .....	43
3.2 Electron - Matter Interaction .....	45
3.2.1) Backscattered Electrons .....	46

3.3 Electron Detectors .....	48
3.3.1) Backscattered Electron Detector - Solid State Detector .....	48
3.3.2) Secondary Electron Detector - Everhart-Thornley Detector .....	49
<b>4 Characteristics of Bone and Important Trace Elements .....</b>	<b>51</b>
4.1 Structure and Architecture of Bone .....	51
4.1.1) Bone Matrix .....	51
4.1.2) Cement Lines .....	52
4.2 Bone Metabolism .....	52
4.2.1) Bone Remodelling .....	52
4.2.2) Osteoporosis .....	53
4.3 Structure of Articular Cartilage .....	54
4.4 Trace Elements in Bone .....	55
4.4.1) Lead (Pb) .....	56
4.4.2) Zinc (Zn) .....	57
4.4.3) Strontium (Sr) .....	57
<b>5 Data Evaluation Methods .....</b>	<b>59</b>
5.1 Spectrum Processing and Map Generation .....	59
5.2 Data Analysis with ImageJ .....	60
5.2.1) Evaluation of the Femoral Neck & Head Samples .....	61
5.2.1.1) Selection of Regions of Interest .....	61
5.2.1.2) Normalization of SR $\mu$ -XRF-Maps .....	62
5.2.1.3) Reliability of $k_j$ -Factor .....	63
5.3 Automated Data Analysis .....	65
5.3.1) Principal Component Analysis - PCA .....	66
5.3.2) K-Means Clustering .....	66
5.3.3) Applying PCA and KMC to $\mu$ -XRF Maps .....	67
5.4 Statistics .....	69
5.4.1 Measure of Central Tendency and Dispersion .....	69
5.4.2) Statistical Tests .....	71
<b>6 Experimental Setup and Sample Preparation .....</b>	<b>73</b>
6.1 Synchrotron Beamlines at ANKA .....	73
6.1.1) SUL-X Beamline .....	73
6.1.2) XAS Beamline .....	75
6.1.3) FLUO Beamline .....	76
6.2 Laboratory $\mu$ -XRF Setup at Atominstitut .....	79
6.3 SEM at LBIO Lab at UKH Meidling .....	80
6.4 Sample Preparation .....	82

<b>7 Stability and Reliability Check of Normalisation to the Ring-Current at ANKA FLUO Beamline .....</b>	<b>85</b>
7.1 Introduction .....	85
7.2 Repetitive Measurements of a AXO Thin Film Reference Sample .....	86
7.2.1) Instrumentation and Measurement Parameters .....	86
7.2.2) Sample .....	86
7.2.3) Data Evaluation .....	87
7.2.4) Results & Discussion .....	88
7.3 Influence on the Quality of $\mu$ -XRF Elemental Maps when Measuring over an Injection .....	91
7.3.1) Instrumentation and Measurement Parameters .....	91
7.3.2) Sample .....	91
7.3.3) Data Evaluation .....	91
7.3.4) Results & Discussion .....	93
7.4 Conclusion .....	95
 <b>8 Trace Element Distribution and Levels in Human and Animal Bone Samples .....</b>	 <b>97</b>
8.1 Speciation of the Lead Accumulated in the Tidemark of Human Articular Cartilage and Subchondral Bone by X-ray Absorption Near Edge Analysis .....	97
8.1.1) Introduction .....	97
8.1.2) Bone Samples .....	98
8.1.3) qBEI Analysis .....	98
8.1.4) Reference Materials .....	99
8.1.4.1) Synthesis of Pb-Substituted HA .....	100
8.1.4.2) Characterization of Pb-Substituted HA .....	100
8.1.5) Setup & Parameters for Pb-L <sub>3</sub> Edge XANES Measurements .....	102
8.1.5.1) Measurements Parameters HASYLAB .....	102
8.1.5.2) Measurements Parameters ANKA SUL-X and XAS .....	103
8.1.5.3) XANES Data Analysis .....	105
8.1.6) Results .....	105
8.1.6.1) Comparison ANKA and HASYLAB Setup .....	105
8.1.6.2) Comparison ANKA SUL-X <-> XAS Beamline .....	106
8.1.6.3) XANES Spectra of Pb in the Tidemark and Subchondral Bone .....	107
8.1.6.4) Comparison of XANES Spectra Tidemark/Bone vs. Reference Spectra .....	107
8.1.7) Discussion .....	109
8.1.8) Conclusion .....	111

8.2 Differential Accumulation of Zinc, Strontium and Lead in Human Bone .....	112
8.2.1) Introduction .....	112
8.2.2) Bone Samples .....	113
8.2.3) qBEI Analysis .....	114
8.2.4) SR $\mu$ -XRF Analysis .....	114
8.2.5) Data Evaluation .....	115
8.2.5.1) Statistical Evaluation .....	115
8.2.6) Results .....	116
8.2.6.1) $\mu$ -XRF Maps of Bone Tissue .....	116
8.2.6.2) Comparison of Trace Element Levels Between Cement Lines and Mineralized Bone Matrix .....	117
8.2.6.3) Dependency of Zn, Pb and Sr Levels on the Mineralization in Mineralized Bone Matrix .....	121
8.2.6.4) Influence of Osteoporotic Fractures on the Trace Element Levels and Distribution .....	121
8.2.7) Discussion .....	122
8.2.7.1) Mineralized Bone Matrix vs. Cement Lines .....	123
8.2.7.2) Trace Element Content vs. Mineralization .....	124
8.2.7.3) General and Medical Implications .....	126
8.2.7.4) Limitations .....	127
8.2.8) Conclusion .....	128
8.3 Sr Incorporation into Bone During Osteoporosis Treatment with Sr Drugs .....	129
8.3.1) Increased Strontium Uptake in Trabecular Bone of Ovariectomized Calcium Deficient Rats Treated with Strontium Ranelate or Strontium Chloride .....	130
8.3.1.1) Samples .....	130
8.3.1.2) qBEI Analysis .....	131
8.3.1.3) SR $\mu$ -XRF Analysis .....	131
8.3.1.4) Data Evaluation .....	131
8.3.1.5) Results .....	133
8.3.1.6) Discussion .....	136
8.3.1.7) Limitations .....	137
8.3.1.8) Conclusions .....	138
8.3.2) Human Biopsy Samples of Strontium Ranelate Treated Patients .....	139
8.3.2.1) Samples .....	139
8.3.2.2) qBEI Analysis .....	140
8.3.2.3) SR $\mu$ -XRF Analysis .....	140

8.3.2.4) Data Evaluation .....	140
8.3.2.5) Results .....	141
8.3.2.6) Discussion & Conclusions .....	144
<b>9 Comparison of SR <math>\mu</math>-XRF with ATI Lab Setup Measurements .....</b>	<b>147</b>
9.1 Introduction .....	147
9.2 Samples .....	147
9.3 SR $\mu$ -XRF Analysis .....	148
9.4 Lab $\mu$ -XRF Analysis .....	148
9.5 Data Evaluation .....	148
9.6 Results & Discussion .....	149
9.7 Conclusion .....	151
<b>10 Concluding Remarks .....</b>	<b>153</b>
<b>Bibliography .....</b>	<b>157</b>





# Chapter 1

## Introduction

When tissue of living organisms is analysed by highly sensitive analytical methods, specific chemical elements in very minute quantities ( $< \mu\text{g/g}$ ) can be found. These so called trace elements can be essential and / or non-essential for the living organism. [1]. However, the role of many trace elements in tissues e.g. bone is poorly understood [2]. One of these trace elements is the toxic element lead (Pb). Exposure to it is associated with chronic diseases in the nervous, hematopoietic, skeletal, renal and endocrine system [3, 4]. About 95% of the total human body burden are present in the skeleton [5]. Other trace elements important in the context of bone metabolism and mineralization are zinc (Zn) and strontium (Sr). Zn is an essential part of several enzymes involved in bone remodelling [6-9] and since several years Sr is approved as therapeutic agent for postmenopausal osteoporosis (pmpOP) in the form of Strontium Ranelate (SrR) [10].

Many studies were dealing with the bulk content of trace elements in bone (e.g. Pb [11, 12]) or just differentiated between cortical and trabecular bone material [13-18], neglecting it's microscopic substructure. Bone is neither homogeneous nor isotropic, it is an organic mineral composite material made up of basic structural units (BSUs) -e.g. bone packets and osteons - which are separated by the so called cement lines [19, 20]. The tissue is continuously remodelled. Diseases like pmpOP drastically alter this remodelling process. In cases pmpOP the resorption rate of bone is increased caused by an elevated bone turnover, increasing the number of young, low mineralized, BSUs [21].

It was unknown if the altered bone metabolism in pmpOP influences the distribution and the levels of Zn, Sr and Pb in bone. Further it was of interest to see if the microscopic structure of bone (e. g. BSUs, cement lines) is linked to the localization and the levels of the trace elements: Is the different chemical composition of the cement line, compared to the mineralized bone matrix, of importance for the accumulation of trace elements? Does the degree of mineralization influence the amount of incorporated Zn, Sr or Pb? Bone samples

## Introduction

from human patients suffering an osteoporotic femoral neck fracture and age-matched non-osteoporotic controls were used to elucidate these questions.

The treatment of pmpOP involves different drugs among them Strontium Ranelate (SrR). Since several years SrR is an approved therapeutic agent for pmpOP. In various animal and human studies the anti-fracture effect of SrR was documented. However the impact of the nutritional calcium (Ca) intake - and thus the Ca serum levels - on the Sr uptake into bone was unclear. Additionally, the localisation of the incorporated Sr in trabecular bone was not well documented. In order to address these issues bone samples from a rat animal model [22] were investigated. This animal model was simulation the different nutritional Ca intake (normal and deficient) and the use of different Sr drugs (SrR and SrCl<sub>2</sub>).

In previous studies [23-25] dealing with the trace element distribution in the osteochondral region of human bone an accumulation of the toxic trace element Pb at the interface between mineralized and non-mineralized articular cartilage - the so called tidemark (TM) - is described. Articular cartilage has a completely different chemical composition compared to subchondral bone[26]. In articular cartilage high amounts of sulphur, with a maximum near the TM are present [27]. Thus it can be speculated that the Pb found in the TM is bonded differently than in bone. Different joint samples from humans with no known degenerative bone disease were examined to clarify this issue.

Within the present work different analytic methods were combined to address the questions that arose in the context of trace element distribution, levels and chemical species with respect to the structure of bone and degenerative bone diseases:

- Synchrotron radiation induced micro X-Ray fluorescence analysis (SR  $\mu$ -XRF)
- X-Ray absorption spectrometry (XAS)
- Quantitative backscattered electron imaging (qBEI)

The unique properties of synchrotron radiation (SR) - linear polarization in orbital plane, high flux, low beam divergence - allow the analysis of trace elements like Zn, Sr or Pb in very low concentrations ( $\mu\text{g/g}$  range) at a high spatial resolution ( $\sim 15\mu\text{m}$ ) [28]. A confocal  $\mu$ -XRF setup at a synchrotron beamline was considered the proper analytical tool to reveal the distribution and levels of Zn, Sr and Pb in human and animal bone samples, as this method yielded good results in previous studies dealing with the trace element distribution

in human joint samples [23, 25, 29]. The data obtained with SR  $\mu$ -XRF should be finally correlated with the histological and morphological information obtained by qBEI to be able to put them into a proper biological / medical context.

X-Ray absorption spectrometry (XAS) is an established method to determine the chemical composition by comparing the X-Ray absorption near edge structure (XANES) spectra of the sample to the XANES spectra of wellknown reference materials. It had to be tested if the microscopic variant of XAS was suitable for the planed analysis of Pb in the TM and subchondral bone region. Therefore several bone like standards (synthetic calcium hydorxyapatite) with low Pb content were prepared.

Beamtime at synchrotron facilities is limited and not easy to obtain. Thus a laboratory based confocal  $\mu$ -XRF system, issued with a low power X-Ray tube (50 W) was tested. Results from the rat animal model obtained with SR-XRF were compared to the measurements in the lab. This way it was planed to see if the laboratory  $\mu$ -XRF setup can be used as pre-screening tool for future SR  $\mu$ -XRF studies. The idea is that the most promising areas can already be selected in the laboratory, to gain optimal use of the allocated beamtime.

All studies involving human bone samples were in accordance and approved by the local ethics committee (Institutional Ethical Review Board of the Medical University of Vienna) and the rat animal study was approved by Indiana University's Institutional Animal Care and Use Committee.



## Chapter 2

# X-Ray Fluorescence Analysis

X-Ray fluorescence analysis (XRF) is a well established analytical method in many research areas and industrial applications to determine the elemental composition of an unknown sample. It is a non-destructive technique needing no or just simple sample preparation. Elements in the range from aluminium (Al,  $Z=13$ ) to uranium (U,  $Z=92$ ) can be analyzed rather easy, while special conditions - vacuum, detector and tube with thin window, optimal excitation - are required to measure elements in the low  $Z$  range down to carbon (C,  $Z=6$ ). The basis of this analytical method was founded by the discovery of the X-Rays by W. C. Röntgen in the end of the 19th century, when carrying out experiments with a Hittorf-Crookes tube studying cathode rays.

### 2.1 X-Ray Sources

Today three different variants of X-Ray sources are commonly used in X-Ray analytical applications:

- X-Ray Tubes
- Synchrotron radiation
- radio isotopes

These sources differ from each other with respect to the spectral distribution of the emitted radiation and the number of available photons (brilliance of the radiation source). The X-Ray sources used within the frame of this work - X-Ray tube and synchrotron radiation - are described in the following.

#### 2.1.1) Synchrotron Radiation

The radiation emitted by a charged particle moving with relativistic velocities on a curved path is called "synchrotron radiation". It is named that way due to the fact that it was first observed in a General Electric 70 MeV synchrotron in 1947 by Elder and colleagues [30].

The outstanding properties of synchrotron radiation make it an ideal radiation source for many spectrometry methods:

- High Intensity
- Polarization
- Natural collimation (in the direction the particle moves)
- Wide spectral range (from infrared to hard X-Rays)
- Well defined time structure (pulse length down to 100 ps)
- Small source size (size and spread of the electron bunches)

It has to be mentioned that all of these properties are fully calculable. Within this work only a short overview on the origin and the properties of synchrotron radiation should be given in the following. The detailed calculations and more explanations can be found in the work of Schwinger [31] and in several books dealing with this topic [30, 32-37].

### 2.1.1.1) Origin and Intensity

According to classical electrodynamics accelerated charged particles emit electromagnetic radiation, for example moving electrons in an antenna creating a Hertzian dipole field which looks like a slightly flattened torus (similar to Fig. 2.1.1b).

The same radiation pattern is emitted if a charged particle (e.g. electron) with non-relativistic speed is accelerated perpendicular to its moving direction, as it happens in a magnetic field, forcing the particle on a curved trajectory. The power irradiated of such a particle is

$$\frac{d^2 P}{d\Omega} = \frac{e^2}{(4 \cdot \pi)^2 \cdot \epsilon_0 \cdot c_0} \cdot |\beta|^2 \cdot \sin^2(\theta)$$

$\theta$  is representing the angle between the vector to observer and the direction of the acceleration.  $e$  is the electron charge,  $\epsilon_0$  the vacuum permittivity,  $\beta=v/c_0$  with  $v$  the speed of the particle ( $v \ll c_0$ ) and  $c_0$  the speed of light in vacuum. In Fig. 2.1.1 an illustration of the (a) coordinate system of the moving particle and (b) the corresponding 3D distribution of the emitted radiation is shown.

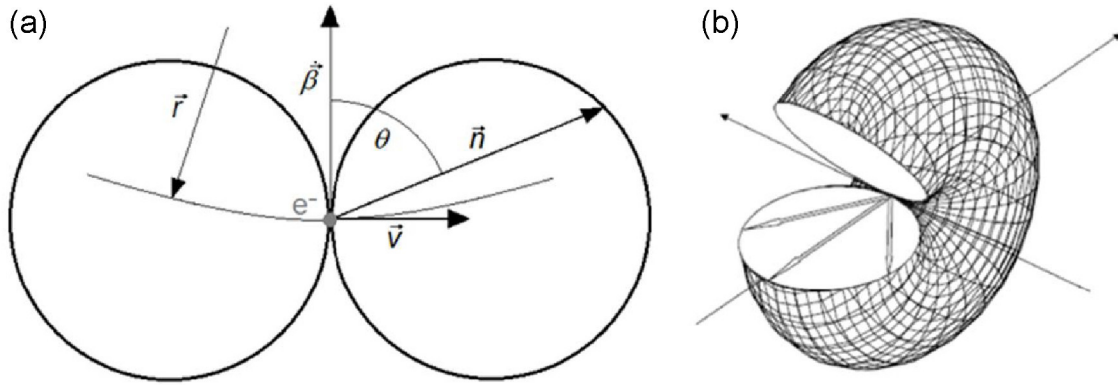


**Figure 2.1.1: Radiation Pattern of a non-relativistic moving particle (a) Coordinate system [38] and (b) spatial distribution [35].**

The total emitted power is obtained by integrating over the full solid angle and yields

$$P = \frac{e^2}{6 \cdot \pi \cdot \epsilon_0 \cdot c_0} \cdot |\beta|^2$$

known as Larmor formula.

When the velocity of the electron becomes relativistic ( $v \sim c_0$ ) the Lorentz transformation has to be used to obtain the emitted power. If the movement of the electron is always perpendicular to the acceleration (as in a synchrotron) and an approximation for small angles is applied the emitted power per unit solid angle is

$$\frac{d^2 P}{d\Omega} = \frac{e^2}{(4 \cdot \pi)^2 \cdot \epsilon_0 \cdot c_0} \cdot \frac{8 \cdot \gamma^6 \cdot |\beta|^2}{(1 + \gamma^2 \cdot \theta^2)^3} \cdot \left[ 1 - \frac{4 \cdot \gamma^2 \cdot \theta^2 \cdot \cos^2(\varphi)}{(1 + \gamma^2 \cdot \theta^2)^2} \right]$$

with  $\theta$  representing the angle between the observer and the moving direction of the particle and

$$\gamma = \frac{1}{\sqrt{1 - \beta^2}}.$$

The emission pattern of the radiation changed from the form of a Hertzian dipole field to a "cigar" like distribution pointing in tangential direction (Fig. 2.1.2) perpendicular to the acceleration of the electrons, within the orbital plane of the synchrotron.

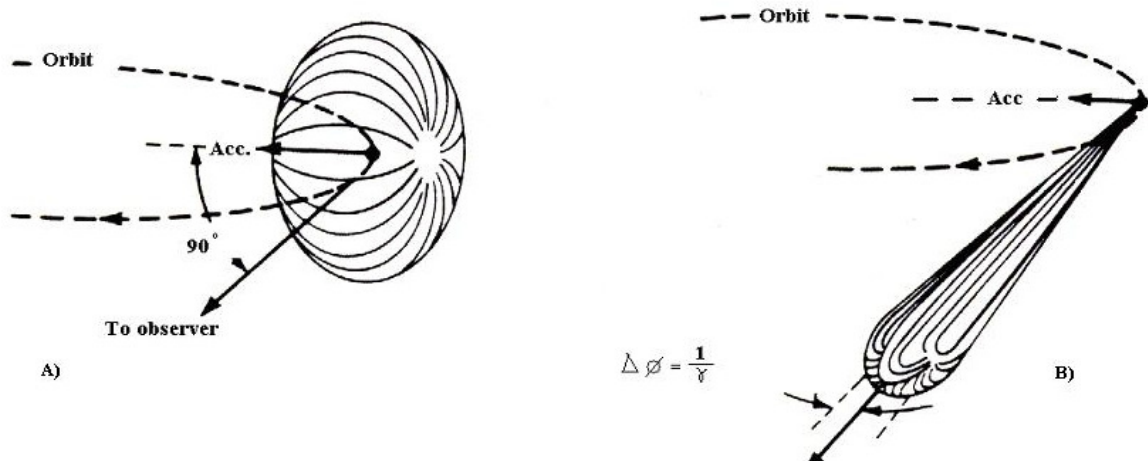


**Figure 2.1.2: Radiation pattern of a electron moving (a) with non-relativistic speed and (b) with relativistic speed [39].**

The characteristic opening angle of this "cigar" is defined as the root of mean square of the angel  $\theta$ .

$$\langle \theta \rangle^2 = \frac{1}{\gamma^2}$$

with  $\gamma \gg 1$ .

For an electron with an energy of 1 GeV the natural collimation of the beam is about 0,5 mrad. This value is only valid for the vertical spread. As this cone is emitted at every point along the circular trajectory of the electron the spread in the orbital plane is much larger.

Integrating over the whole solid angle gives the total power that is emitted from an electron moving with relativistic speed when passing through a bending magnet.

$$P = \frac{e^4 \cdot \beta^2}{6 \cdot \pi \cdot \epsilon_0 \cdot E_0^4 \cdot c_0} \cdot E^2 \cdot B^2$$

$E_0$  is the rest mass of the electron and  $E = \gamma \cdot E_0$  the energy of the electron and  $B$  the magnetic field of the bending magnet.

Comparing the emitted power of electrons and protons accelerated under the same conditions (particle energy  $E$  and  $B$  field remain unchanged) it turns out that electrons are about  $10^{13}$  more efficient in creating synchrotron radiation.



### 2.1.1.2) Time Structure and Spectral Distribution

At the position of the observer only a short electromagnetic pulse with a length  $\Delta t$ , produced by the relativistic moving electron is seen. This is due to the small opening angle of the radiation cone. As illustrated in Fig. 2.1.3 an observer can see the synchrotron radiation when the electron enters the field of view at point A and stops seeing the radiation when the electron passes point B.

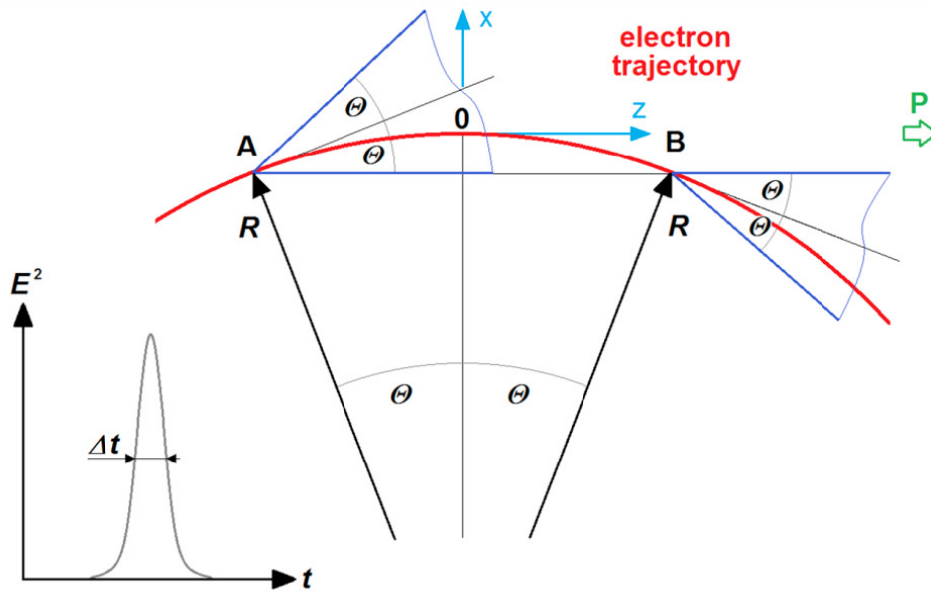


**Figure 2.1.3: Time Structure of Synchrotron Radiation - illustration of origin [38].**

The length of this interval is given as the difference between the time of flight of the photon and the electron. The radius of the orbit is  $R$ .

$$\Delta t = t_B - t_A = \frac{2 \cdot R \cdot \theta}{\beta \cdot c_0} - \frac{2 \cdot R \cdot \sin(\theta)}{c_0}$$

Expanding the sinus in into a row and approximating  $\theta \sim 1/\gamma$  and  $\gamma \cdot \beta \sim \gamma - 1/2 \cdot \gamma^{-3}$

$$\Delta t = \frac{2 \cdot R}{c_0} \cdot \left( \frac{1}{\gamma \cdot \beta} - \frac{1}{\gamma} + \frac{1}{6 \cdot \gamma^3} \right) \approx \frac{4 \cdot R}{3 \cdot c_0 \cdot \gamma^3}$$

Performing a Fourier transformation the typical frequency  $\omega_t$  is obtained which is used to define the critical frequency  $\omega_c$ .

$$\omega_c = \frac{\omega_t}{\pi} = \frac{3}{2} \cdot \gamma^3 \cdot \omega_0$$

The angular frequency of the moving electron is given as  $\omega_0 = c_0/R$ .

The spectrum of the synchrotron radiation is divided by the critical frequency  $\omega_c$  into two parts of the same power. Further it can be seen from this equation that an electron moving with relativistic speed is emitting a broad radiation spectrum [38].

Schwinger [31] was the first to calculate the frequency spectrum of the synchrotron radiation. From these calculations it can be deduced that:

- For large angles  $\theta$  the radiation is negligible
- The intensity maximum is in the orbital plane (forward collimation)

## 2.1.1.3) Polarization

The degree linear polarization  $P_l$  can be obtained from the following formula

$$P_l = \frac{I_p - I_N}{I_p + I_N} = \frac{K_{2/3}^2(\xi) - \frac{\gamma^2 \cdot \theta^2}{1 + \gamma^2 \cdot \theta^2} \cdot K_{1/3}^2(\xi)}{K_{2/3}^2(\xi) + \frac{\gamma^2 \cdot \theta^2}{1 + \gamma^2 \cdot \theta^2} \cdot K_{1/3}^2(\xi)}; \quad \xi = \frac{\omega \cdot R}{3 \cdot c_0 \cdot \gamma^3} \cdot (1 + \gamma^2 \cdot \theta^2)^{3/2}$$

$I_p$  is the intensity polarized parallel and  $I_N$  the intensity polarized perpendicular to the orbital plane.  $K_{1/3}(\xi)$  and  $K_{2/3}(\xi)$  are the modified Bessel functions and  $\phi$  is the angle between the observer and the orbital plane.

It can be easily seen that for  $\theta=0$   $P_l=1$  as  $I_N$  is vanishing. Thus the synchrotron radiation in the orbital plane is totally linear polarized (see also Fig. 2.1.4).

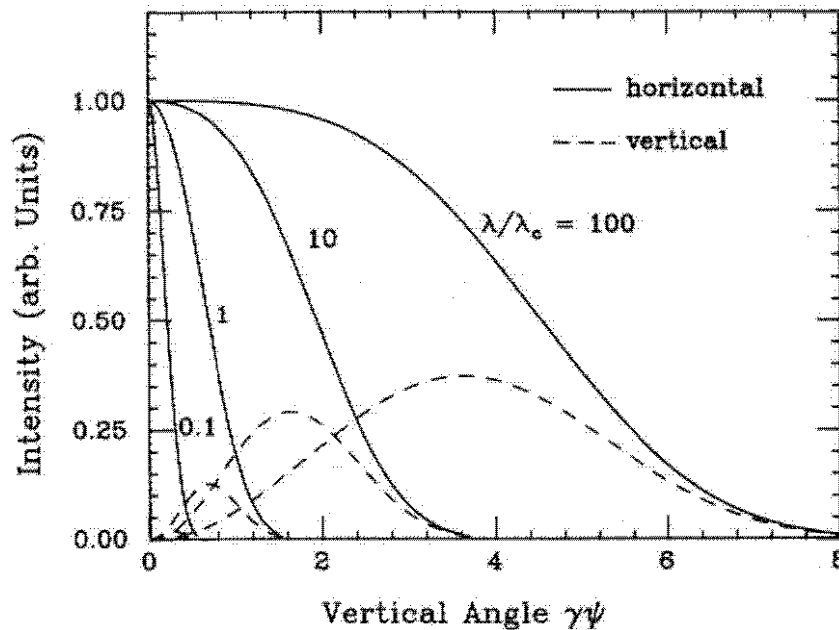


**Figure 2.1.4: Angle dependence of horizontal and vertical polarization of synchrotron radiation; vertical angle  $\psi$  [40].**

#### 2.1.1.4) Characterization Parameters

The synchrotron radiation sources are characterized by the

$$\text{Total Flux} = \frac{\text{Photons}}{\text{s}}$$

$$\text{Spectral Flux} = \frac{\text{Total Flux}}{0,1\% \text{ Energy Bandwidth}} = \frac{\frac{\text{Photons}}{\text{s}}}{0,1\% \cdot \frac{\Delta E}{E}}$$

$$\text{Brightness} = \frac{\text{Spectral Flux}}{\text{Beam Bivergence}} = \frac{\frac{\text{Photons}}{\text{s}}}{\text{mrad}^2 \cdot 0,1\% \cdot \frac{\Delta E}{E}}$$

$$\text{Brilliance} = \frac{\text{Brightness}}{\text{Source size}} = \frac{\frac{\text{Photons}}{\text{s}}}{\text{mm}^2 \cdot \text{mrad}^2 \cdot 0,1\% \cdot \frac{\Delta E}{E}}$$

#### 2.1.1.5) Insertion Devices

A synchrotron radiation source consist of an electron gun, a linear accelerator (LINAC), a small booster ring (the actual synchrotron) and a large storage ring with the beamlines and experiments. An illustration of such a synchrotron facility is shown in Fig. 2.1.5.

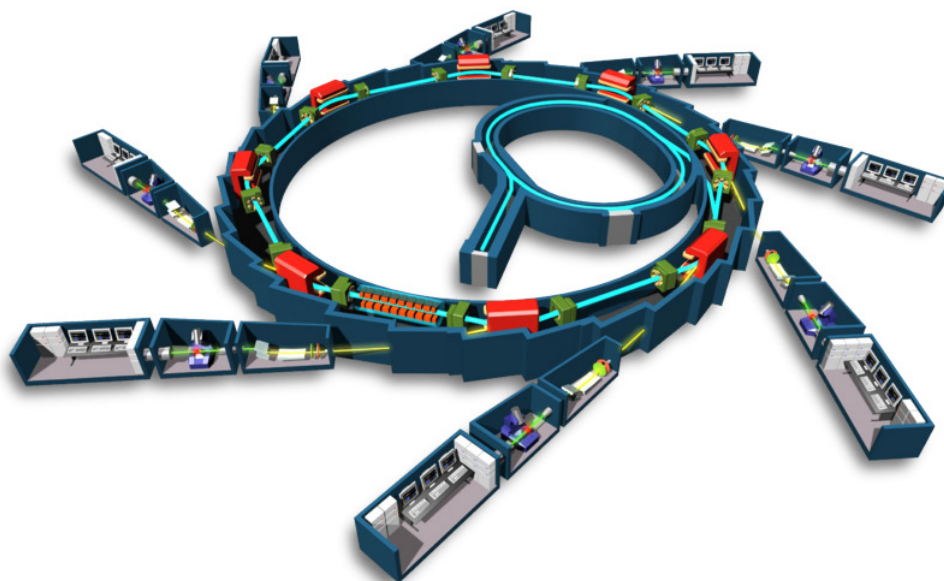


**Figure 2.1.5: Schematic of a synchrotron. [41].**

The free electrons are produced in the electron gun by heating tungsten to temperatures in the range of 1000°C. The electrons are accelerated within the electron gun to about 100 keV (~55% of  $c_0$ ). In the next step they are accelerated to round 100 MeV by a LINAC or microtron (99,9987% of  $c_0$ ). Then the electrons are accumulated in the booster ring, until the desired number of electrons (i.e. the ring current) is reached. After being accelerated in the booster synchrotron to several GeV, the electrons are transferred into the storage ring (1 GeV ~ 99,9999869% of  $c_0$ ). There the electron bunches are circulating for a longer period of time. At the synchrotron ANKA (Karlsruhe, Germany) for example the electrons are accelerated to 2,5 GeV with an initial ring current of 150 to 180 mA and storage times between 9 and 11 hours.

To keep the electrons in the storage ring and to keep the energy constant several devices are necessary:

**Bending magnets:** The magnetic dipole field of these electro magnets forces the electrons on a circular trajectory. Simultaneously synchrotron radiation for various experiments is produced (red boxes in Fig. 2.1.5)

**Quadrupole and sextupole magnets:** These are magnetic lenses to focus the electron bunches and stabilize the beam (slim green boxes in Fig. 2.1.5)

**Radio frequency (RF) cavities:** These are installed at strait sections of the storage rings and are required to replace the energy that the beam loses through the synchrotron radiation.

Besides these devices modern 2nd and 3rd generation storage rings are equipped with so called insertion devices. These insertion devices -wiggler, undulator, wave length shifter - are used to produce synchrotron radiation with different properties than the radiation from the bending magnets.

**Multipole Wigglers:** A wiggler is a periodic structure of magnetic dipoles with alternating field directions (see Fig. 2.1.6). The fields of all dipoles have the same strength. The electrons passing through the magnetic structure are forced on a sinusoidal path. Each dipole is the source of a short synchrotron radiation burst. If these short pulses are superimposed this leads to an N-fold increase of the intensity, if the wiggler has N+2 poles. The dipoles at both ends ensure a continuous transition of the electrons between the wiggler and the beam trajectory in the storage ring.

The wiggler is characterized by the deflection parameter  $K$

$$K = \frac{e \cdot B_0 \cdot \lambda_0}{2 \cdot \pi \cdot m \cdot c_0} = 0,934 \cdot B_0[T] \cdot \lambda_0[cm]$$

$B_0$  is the magnetic field and  $\lambda_0$  the magnetic period of the dipoles.

For a wiggler  $K$  is much larger than 1 ( $K \gg 1$ ), and the radiation pulses are incoherently superimposed.

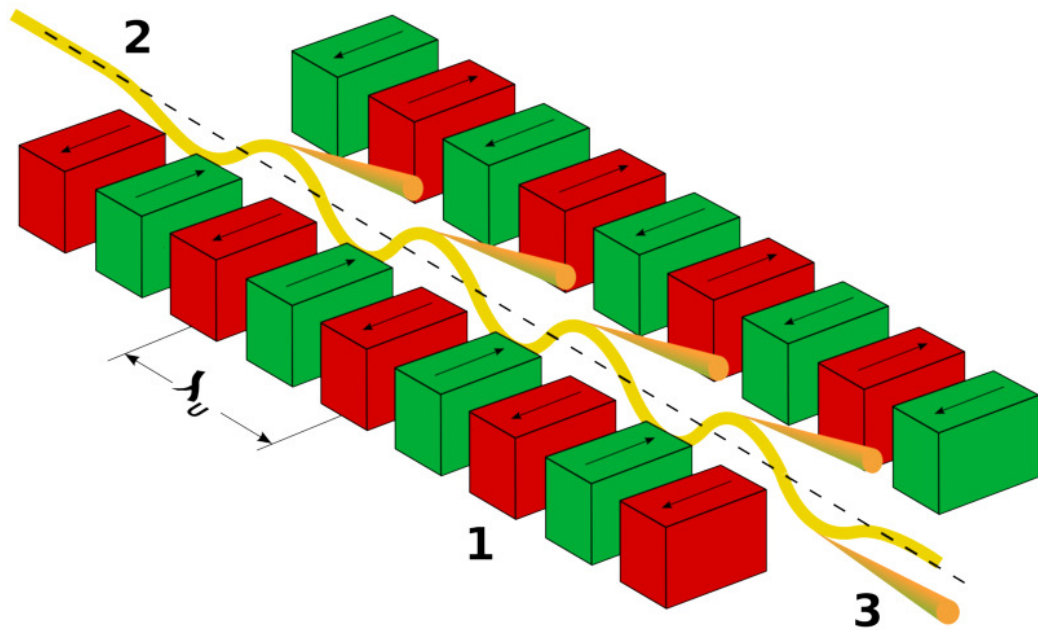


**Figure 2.1.6: Schematic of a Wiggler / Undulator. (1) dipole magnets, (2) electron beam, (3) synchrotron radiation [42].**

**Undulators:** Undulators have a similar structure than the wigglers. They are differentiated by the  $K$  value which is less or equal to 1 for the undulators ( $K \leq 1$ ). The magnetic field is smaller than in wigglers and thus the deflection angle is less than the opening of the cone of the synchrotron radiation. Hence the electromagnetic waves of the subsequent emission points (one at each pole) are coherently interfering, resulting in a spectrum presenting sharp peaks with discrete wave length  $\lambda$ .  $\theta$  is the angle of observation point and the  $z$ -axis. The intensity increase of an undulator is  $N^2$ .

$$\lambda = \frac{\lambda_0}{2 \cdot j \cdot \gamma^2} \cdot \left( 1 + \frac{1}{2} \cdot K^2 + \gamma^2 \cdot \theta^2 \right); \quad j = 1, 2, 3, 4, 5$$

In Fig. 2.1.7 a comparison of the properties of the bending magnet, the wiggler and the undulator synchrotron radiation is shown.

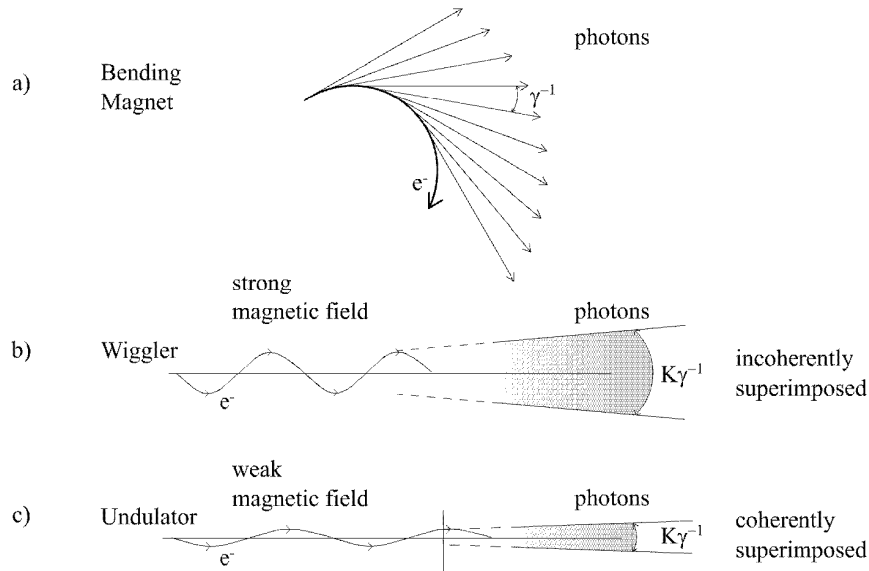


**Figure 2.1.7: Comparison of radiation produced by (a) bending magnets, (b) wigglers and (c) undulators [43].**

Fig. 2.1.8 gives an overview of the brilliance of different X-Ray radiation sources.

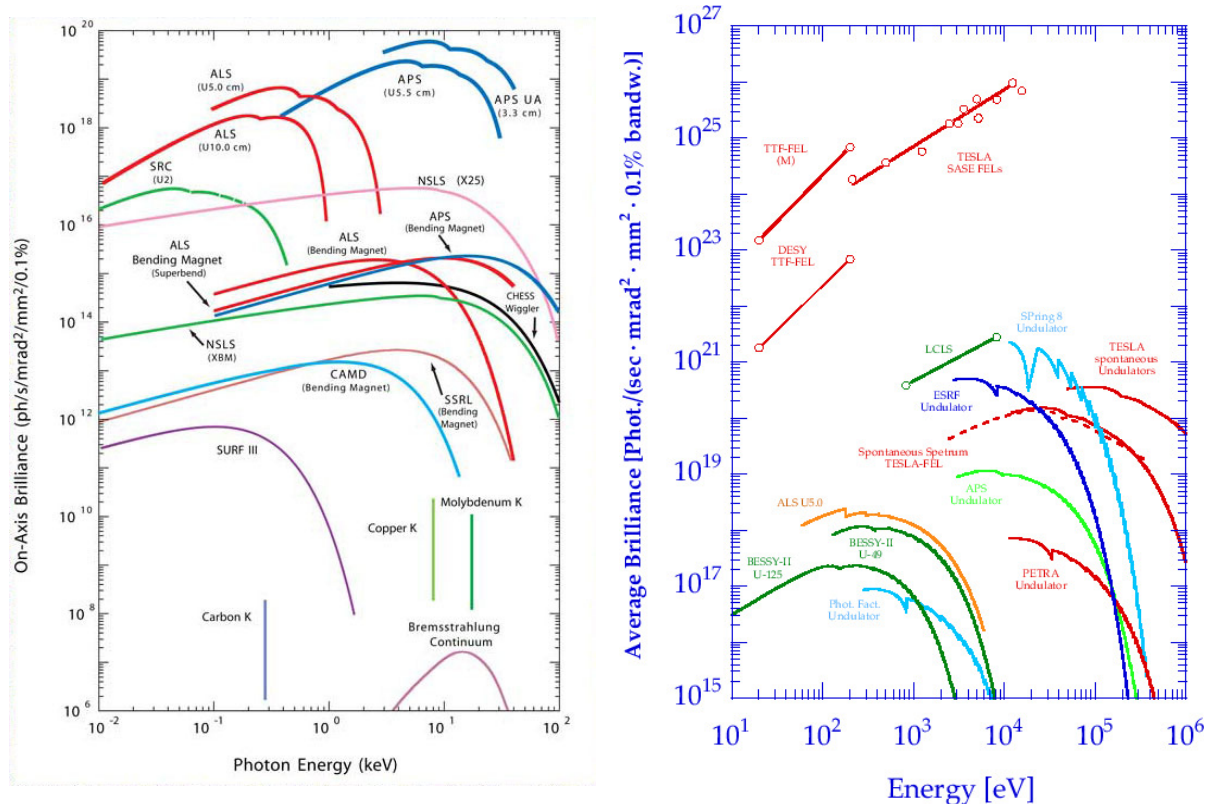


**Figure 2.1.8: Brilliance of different X-Ray radiation sources (a) including X-Ray tubes [44] and (b) free electron lasers (FELs) [45].**

### 2.1.2) X-Ray Tubes

The concept that is still applied in modern X-Ray tubes was suggested by W.D. Coolidge [46] in 1913.

The X-Ray tube basically consists of a highly evacuated glass cylinder in which an anode and a cathode are placed opposing each other. In the cathode a tungsten filament is used to create free electrons, which are focused by means of a Wehnelt cylinder. A high DC voltage applied between the cathode and anode accelerates the electrons towards the anode. The electrons impinging on the anode interact with the material producing continuous radiation (bremsstrahlung) and characteristic radiation. To minimize the attenuation of the produced X-Rays the exit windows of tubes are usually manufactured of 100-300µm thick beryllium (Be).

The high DC voltage between cathode and anode is in the keV range and the anode usually on ground potential. The energy of the electrons  $E_{kin}$  is determined by the accelerating voltage  $U$  and the charge of the electron:

$$E_{kin} = e \cdot U$$

The efficiency  $\eta$  of an X-Ray tube is very small. It is given by the ratio of the produced radiation power ( $P_{rad}$ ) and the used electrical power ( $P_{el}$ ).

$$\eta = \frac{P_{rad}}{P_{el}} \approx \frac{C \cdot i \cdot U^2 \cdot Z}{i \cdot U} = C \cdot U \cdot Z$$

For  $U$  in V and  $i$  in A the experimentally determined constant  $C \approx 1,4 \cdot 10^{-9} \text{ 1/V}$ . Thus for a tube operating at  $U=50\text{kV}$  and a molybdenum (Mo,  $Z=42$ ) anode the efficiency  $\eta \approx 0,3\%$ .

Hence the main portion of the input energy is converted to heat. Therefore the anode has to be sufficiently cooled. In high power tubes which operate in the kW range a water cooling system is required. In low power tubes operating in the range of about 20-100 W an internal oil cooling cycle with external forced air cooling is sufficient. In Fig. 2.1.9 the schematic of a high tube is shown.

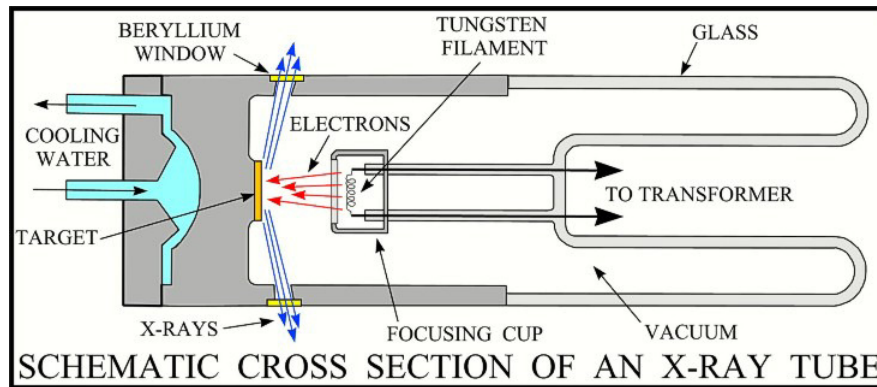


**Figure 2.1.9: Schematic of a water cooled X-Ray diffraction tube [47].**

## 2.1.2.1) Properties of X-Ray Tube Spectra

The description of the intensity  $I$  of the radiation per unit energy  $E$ , frequency  $\nu$  or wavelength  $\lambda$  is called a spectrum.  $E$ ,  $\nu$  and  $\lambda$  are linked in the following way:

$$E = h \cdot \nu = \left( \frac{h \cdot c_0}{\lambda} \right); \quad c_0 = \nu \cdot \lambda$$

Thus different ways to display a spectrum provided similar information.

A typical X-Ray tube spectrum is shown in Fig. 2.1.10. It shows the continuous radiation with a broad maximum and the relatively sharp peaks of the characteristic radiation. The two different interaction processes of the electrons with the anode material leading to such a spectrum will be discussed in the following.

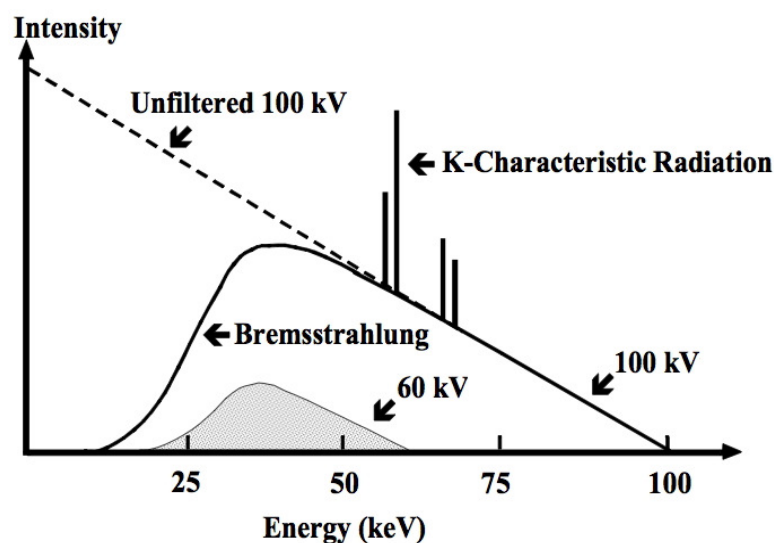


**Figure 2.1.10: Spectrum of a X-Ray tube. Continuous radiation superimposed with characteristic radiation [48].**



### 2.1.2.2) Continuous Spectrum

The continuous part of the X-Ray spectrum is produced when high energy charged particles (e.g. electrons) are decelerated in mater. When the charged particles are impinging on the anode material inelastic scattering occurs in the Coulomb field of the nuclei. As already mentioned in the context of the production of synchrotron radiation, accelerated / decelerated charged particles emit electromagnetic radiation. The energy of this radiation is depending on the strength of the scattering, and can not be greater than the primary energy of the impinging charged particles. As there are no discrete energy levels the produced radiation has a continuous spectrum. The energy of the photons ( $E_{ph}$ ) is determined by the kinetic energy of the electrons before ( $E_{kin}$ ) and after ( $E'_{kin}$ ) a scattering process

$$E_{ph} = E_{kin} - E'_{kin} = h \cdot \nu$$

The maximum of the photon energy is reached when an incoming electron is completely stopped in the first scattering process:

$$E_{ph_{max}} = E_{kin} = e \cdot U = h \cdot \nu_{max}$$

U is the tube voltage, h the Planck's constant and  $\nu$  the frequency of the emitted radiation. Hence the maximum energy of the continuous spectrum is determined by the applied tube voltage.

### 2.1.2.3) Characteristic Spectrum

The discrete characteristic spectrum consists of line families, which are superimposed with the continuous spectrum. The properties of these line families result from the quantum structure of the atoms, which is in this case sufficiently described with the Bohr model. If a bound electron of one of the inner shells (e.g. K- or L-shell) is hit by a particle (e.g. electron, photon) with sufficient energy it can be kicked out of its shell into the continuum. The energy of the incoming particle has to be higher than the ionization energy of the hit electron. The vacancy in the inner shell is then filled with an electron from an outer shell (see Fig. 2.1.11). Not all electron transitions between the shells are allowed.

## X-Ray Fluorescence Analysis

The refilling process follows the selection rules for dipole radiation:

$$\Delta n \neq 0, \quad \Delta l = \pm 1, \quad \Delta j = 0, \pm 1$$

$n \dots$  principal quantum number;  $n=1,2,3, \dots$  (describing the shells K, L, M,  $\dots$ )

$l \dots$  azimuthal quantum number;  $l=0,1,2,3, \dots, n-1$

$j \dots$  total angular momentum quantum number;  $j=l \pm 1/2$

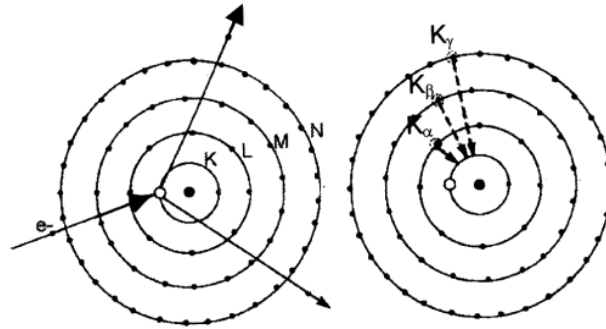


**Figure 2.1.11: Interaction of an incident electron with an inner shell electron, ionizing the atom. Refilling of the hole [49].**

The difference of the binding energies of the outer ( $E_i$ ) and the inner ( $E_f$ ) shell is emitted in form of a photon with the energy  $E_{ph}$

$$E_{ph} = E_i - E_f \text{ with } E_i > E_f.$$

Filling a vacancy in the inner shells is a cascade process. For example a vacancy in the K-shell is filled with an electron from the L-shell, the emerging hole in the L-shell is filled with an electron from the M-shell. In Fig 2.1.12 a schematic of the possible transitions is shown. Thus ionizing the K-shell of an atom a whole line family is created, which is characteristic for each element.

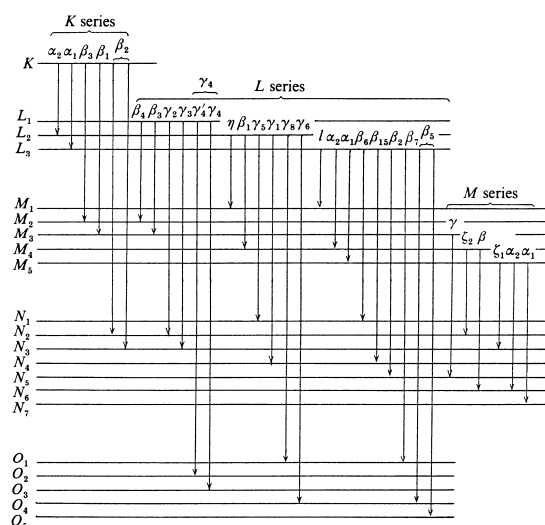


**Figure 2.1.12: X-Ray lines and corresponding energy levels [50].**

A competitive process to the emission of characteristic photons is the Auger effect. The difference in the binding energies is transferred to a bound electron, which is subsequently ejected out of the atom. This electron is called Auger electron and is emitted with a characteristic energy. The probability of the Auger effect is getting smaller with increasing atomic numbers.

The so called fluorescence yield  $\omega$  is describing the probability of creating a characteristic photon and it is defined as:

$$\omega_x = \frac{I_x}{n_x}$$

where  $I_x$  is the intensity of the emitted radiation and  $n_x$  is the number of primary vacancies in shell  $X = K, L, M, \dots$ . In Fig 2.1.13 the fluorescence yields of the K-, L- and M-shell are shown.

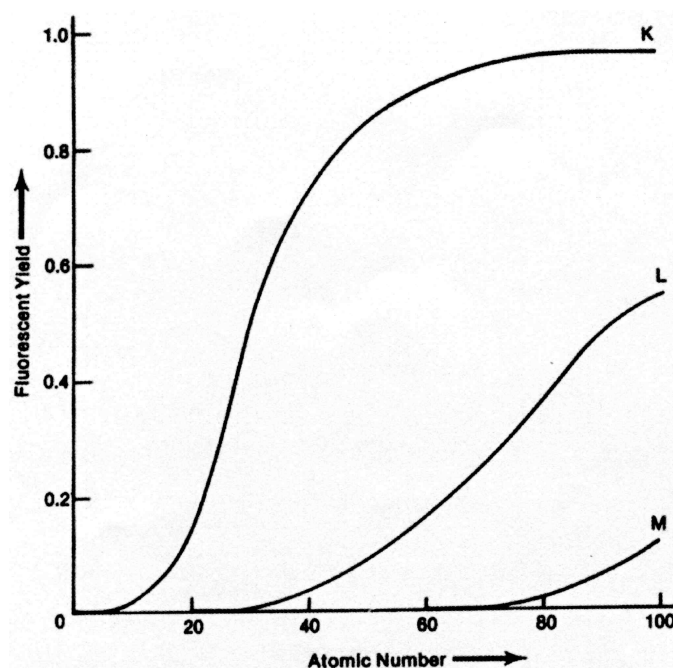


Figure 2.1.13: Fluorescence yields of the K-, L- and M-shell [51].

## 2.2 Interaction of X-Rays with Matter

X-Rays passing through matter interact with it through different processes, depending on the energy of the impinging photons: coherent and incoherent scattering, photo effect, pair production<sup>1</sup>

<sup>1</sup> The pair production is omitted as the energy range used in the work is far to low for this process.

### 2.2.1) Coherent Scattering

Coherent scattering, also called elastic or Rayleigh scattering, the incoming photons are interacting with the bound electrons, without ionizing or exciting the atoms. The direction of the photons is changed but the energy is unaffected.

The atomic form factor is required for correcting for the influence of all bound electrons of an atom on the scattering process. It is the integral over the electron density of an atom.

### 2.2.2) Incoherent Scattering

Contrary to the coherent scattering, incoming photons lose energy in the incoherent (also called inelastic or Compton-) scattering process. The photon interacts with the outer loosely bound (quasi free) electrons of an atom. In this process a part of the momentum and the energy of the incoming photon are transferred to the electron. When the transferred energy is large enough, the loosely bound electron is leaving the atom as so called Compton electron. The photon changes its energy and momentum (i. e. direction). The incoherent scattering function is correcting for the fact that the electrons are not free but loosely bound and that the atom is ionized after the scattering process.

### 2.2.3) Photo Effect

First observed and described by A. Einstein in 1905 photons of sufficient energy  $E_{ph}$  are able to excite electrons to higher shells, if vacant, or ionize the atom. The electron ejected out of the atom is called photo electron. In Fig. 2.2.1 a schematic of the photo effect is shown.

The refilling process of the vacancies produced by the impinging photons is the same as for vacancies produced by electrons, which is described in Chap. 2.1.2.3. Again, the radiation emitted is characteristic for the element.

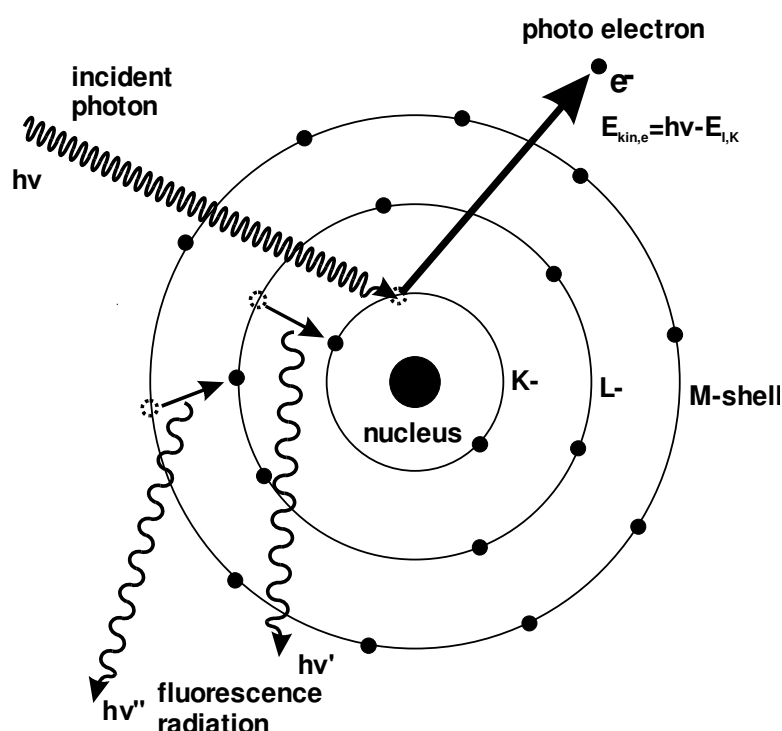


Figure 2.2.1: Illustration of photo-effect [52].

#### 2.2.4) Attenuation Coefficient

X-Rays passing through the matter are attenuated due to the above described interactions - photon effect, coherent and incoherent scattering. In Fig. 2.2.2 the contributions of these effects in lead (Pb) are shown. The total attenuation is indicated by the solid line.

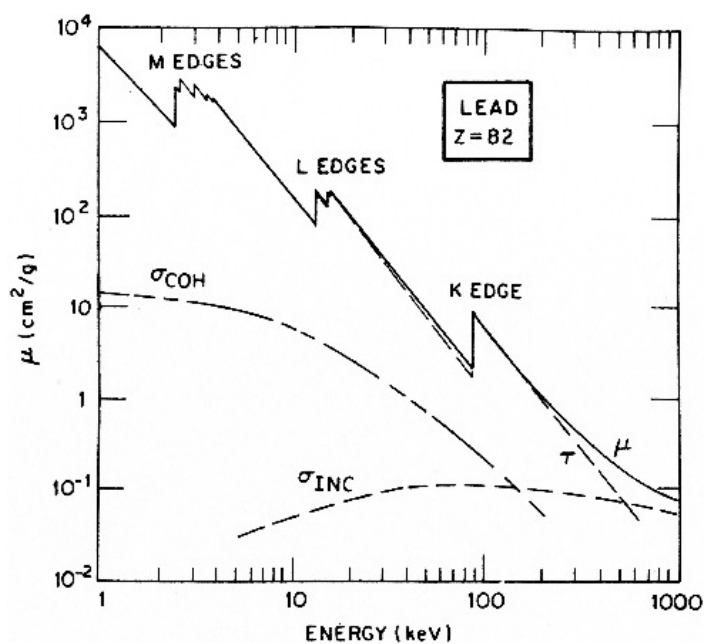


Figure 2.2.2: Linear absorption coefficient (solid line) of lead (Pb) [53].

The attenuation is described using the linear absorption coefficient  $\mu$  or the equivalent mass absorption coefficient  $\mu_m = \mu/\rho$ , where  $\rho$  is the density of the material. The attenuation is depending on the energy (E) of the incoming photons and the atomic number (Z) of the absorbing material. Both absorption coefficients are composed of the contributions of the photoelectric  $\tau$ , the coherent  $\sigma_{\text{coh}}$  and the incoherent  $\sigma_{\text{inc}}$  (mass) absorption coefficients.

$$\mu(E, Z) = \tau(E, Z) + \sigma_{\text{inc}}(E, Z) + \sigma_{\text{coh}}(E, Z), \quad \mu_m = \tau(E, Z)/\rho + \sigma_{\text{inc}}(E, Z)/\rho + \sigma_{\text{coh}}(E, Z)/\rho$$

In the energy range relevant for the analysis described in this work (2-20 keV) the photoelectric absorption (photo effect see Chap 2.2.3) is dominant. When the energy of the incoming photons is dropping below the binding energy of the electrons of a specific shell, the electrons of this shell cannot be ejected any more. This results in the characteristic absorption edges of the (mass) attenuation coefficients (Fig. 2.2.2).

The decrease in X-Ray intensity when passing through matter is described with the Beer-Lambert law [54, 55]:

$$I(x) = I_0 \cdot e^{-\mu(Z,E) \cdot x} = I_0 \cdot e^{-\frac{\mu(Z,E)}{\rho} \cdot \rho \cdot x} = I_0 \cdot e^{-\mu_m(Z,E) \cdot \frac{m}{A}}$$

with

$I_0$  . . . intensity before passing through the matter

$I(x)$  . . . intensity after passing through the matter

$\mu(E, Z)$  . . . linear attenuation coefficient [1/cm]

$\mu_m(E, Z)$  . . . mass attenuation coefficient [cm<sup>2</sup>/g]

$x$  . . . thickness of the absorber [cm]

$\rho$  . . . density of the absorber [g/cm<sup>3</sup>]

$A$  . . . area of the absorber [cm<sup>2</sup>]

$m$  . . . mass of the absorber [g]

In case the absorbing material is not a single element but a composition of many elements the attenuation coefficient is composed according to the weight fractions of the respective elements.

### 2.2.5) Information Depth

The attenuation of X-Rays in matter limits the depth inside a sample from which fluorescence radiation can be detected. This depth is called information depth. It is determined by the attenuation of the primary radiation when penetrating the sample and the attenuation of the fluorescence radiation when it is passing through the matrix on the way out of the sample. Due to the energy dependency of the attenuation, the attenuation of the fluorescence radiation, with an energy always smaller than the energy of the primary radiation, is dominating the information depth.

The information depth  $d_{\text{inf}}$  is the depth where the fluorescence intensity is decreased on the way out of the sample to  $1/e$  (about 37%) of its original value. This definition is not considering the attenuation of the primary radiation [56].

A principal problem is emerging especially in spatially resolved XRF due to the strong energy dependence of the information depth - illustrated in Fig 2.2.3.

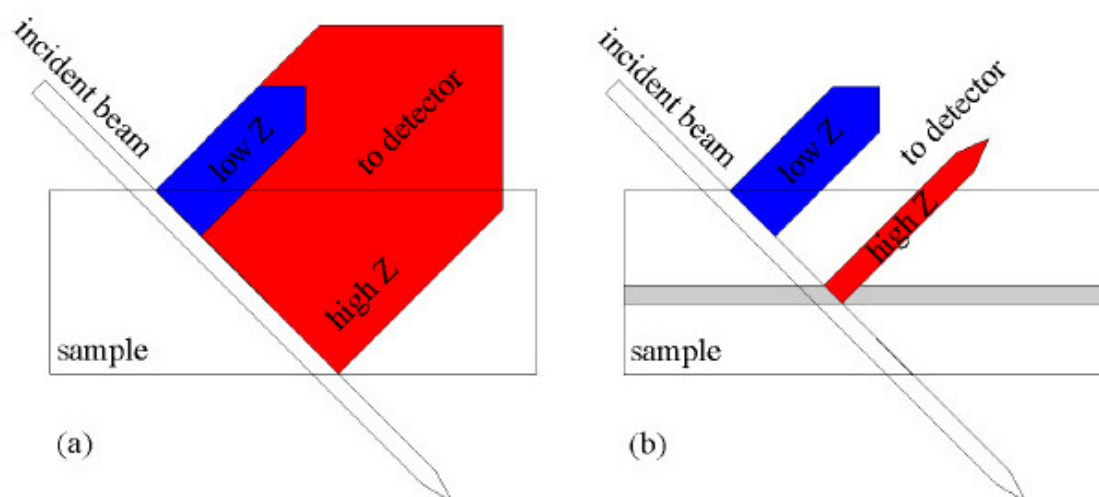


**Figure 2.2.3: Information depth in a (a) homogeneous and (b) inhomogeneous sample for low and high Z elements [43].**

The detected fluorescence radiation from low Z elements originates only from the top layer of the sample. The fluorescence radiation from high Z elements can reach the detector from much deeper layers inside the sample. Measuring inhomogeneous samples like illustrated in Fig. 2.2.3b the qualitative interpretation of the obtained results is problematic and quantification is impossible. This problem is elaborated in the PhD thesis of N. Zöger [43] in more detail.

To minimize the above described effects in micro XRF the detection volume is limited to the top layer of the sample (see also Fig 2.4.8). This can be done using a confocal micro XRF setup as described in Chap. 2.4.2.

Though the influence of information depth is reduced in this measurement geometry a quantitative analysis is still problematic as the spot size of the focusing optics is depending on the photon energy (energy dependency of the total reflection of photons) and thus the measurement volume is different for each element.

### 2.3 Energy Dispersive X-Ray Fluorescence Analysis (EDXRF)

Energy dispersive X-Ray fluorescence analysis (EDXRF) is a flexible, powerful and non-destructive analytical method to determine the elemental composition of an unknown sample. In EDXRF the energy of the fluorescence radiation emitted from a sample irradiated with X-Rays (see photo-effect and characteristic radiation) is measured with a semi conductor detector. This is based on the fact that the signal at the detector output is direct proportional to the energy of the photon absorbed in the detector. The most common detector types are lithium drifted silicon detectors (Si(Li)-detectors) and since several years silicon-drift-detectors (SDDs). The big advantage of EDXRF is on the one hand that all energies are measured simultaneously, especially in multi element samples like bone, and that no complicated setups with goniometers and analyzer crystals, like in wavelength dispersive XRF, are necessary.

The characteristic fluorescence lines can be used to qualitatively identify the elemental composition of unknown sample as the energies of these lines are characteristic for each element. The correlation between the energy  $E$  of the characteristic radiation and the atomic number  $Z$  was described by H. Moseley in 1914 [57, 58]

$$E = k \cdot (Z - \sigma)^2$$

$k$  . . . constant, depending on the regarded line

$\sigma$  . . . screening constant depending on the atomic number and the regarded line

With help of the intensity of each characteristic fluorescence line it is possible to quantitatively determine the amount of each element present in the sample. However this is not straight forward, as several factors, among then the homogeneity of the sample and absorptions processes of the fluorescence radiation and secondary excitation within the



sample, have to be taken into account. The correlation of the concentration of an analyte in the sample and the fluorescence intensity is shown in the next section. It has to be mentioned right away that a reliable and quantitative analysis of bone using confocal  $\mu$ -XRF is not achievable at the moment.

### 2.3.1) Intensity of the Fluorescence Radiation

In Fig. 2.3.1 an illustration of a typical XRF geometry is shown. The radiation with an energy interval  $[E, E+dE]$  impinges on the sample with an angle  $\Phi_1$  and the angle between detector axis and sample is  $\Phi_2$ . The primary radiation is passing through the sample to the depth  $x$  where it is interacting with the material producing characteristic photons in the finite layer  $dx$ . It is assumed that the sample is homogeneous.

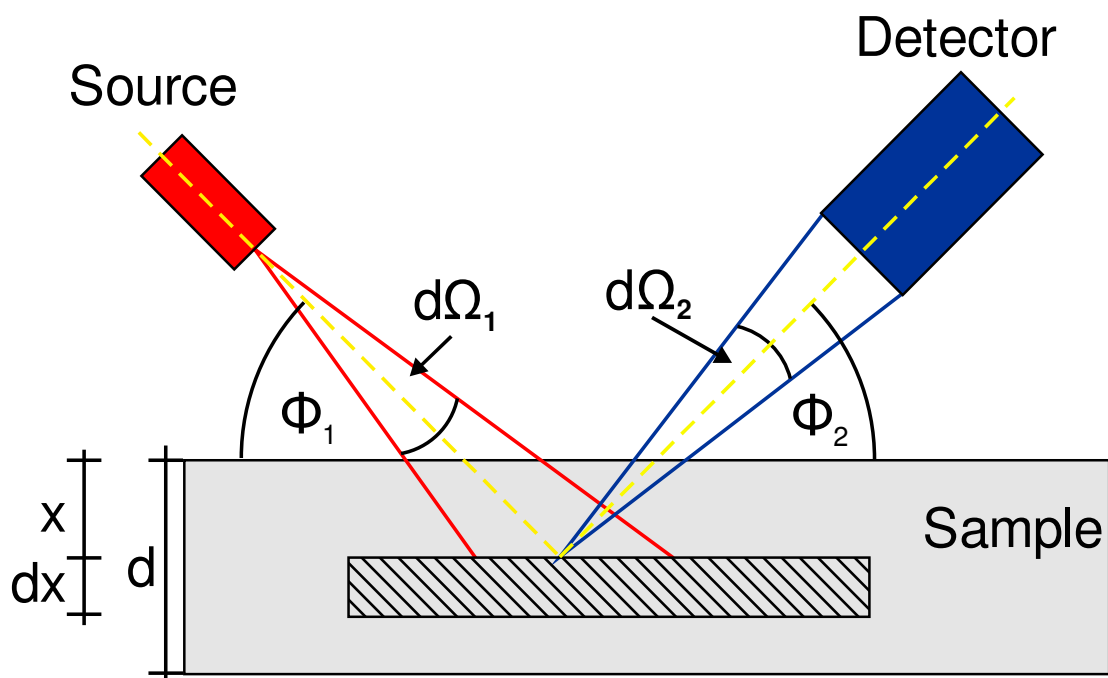


**Figure 2.3.1: Schematic illustration of the EDXRF geometry [52].**

Considering all factors describing the correlation between the concentration  $c_i$  of an element  $i$  and the fluorescence intensity emitted by a transition from shell  $j$  to shell  $n$ , one obtains the following formula for the intensity:

$$I(E_{i,j,n}) = \int_{E_{i,abs}}^{E_{max}} \int_0^d I_0(E) \cdot \underbrace{e^{\frac{\mu_i(E) \cdot x}{\sin(\Phi_1)}}}_1 \cdot c_i \cdot \underbrace{\tau_i(E) \cdot \frac{1}{\sin(\Phi_1)}}_2 \cdot \underbrace{\left(1 - \frac{1}{r_{i,n}}\right)}_3 \cdot \underbrace{\omega_{i,n}}_4 \cdot \underbrace{p_{i,j,n}}_5 \cdot \underbrace{V_i}_6 \cdot$$

$$\underbrace{e^{\frac{\mu_i(E_{i,j,n}) \cdot x}{\sin(\Phi_2)}}}_7 \cdot \underbrace{f(E_{i,j,n}) \cdot \varepsilon(E_{i,j,n})}_8 \cdot \frac{1}{4 \cdot \pi} \cdot d\Omega_1 \cdot d\Omega_2 \cdot dx \cdot dE$$

whereas:

$c_i$  . . . concentration of the analyte (element i)

$I_0(E)$  . . . intensity of primary photons emitted by the source into the solid angle  $d\Omega_1$

$d\Omega_2$  . . . solid angle of the detector

$d$  . . . overall sample thickness

$E_{i,abs}$  . . . Energy of absorption edge of element i

$\mu(E)$  . . . linear absorption coefficient of the sample

$\tau_i(E)$  . . . linear photoelectric cross section of element i

$r_{i,n}$  . . . jump ratio of the absorption edge of shell n

$\omega_{i,n}$  . . . fluorescence yield of shell n

$p_{i,j,n}$  . . . probability of transition from shell j to n

$E_{i,j,n}$  . . . energy of the emitted radiation

$f(E_{i,j,n})$  . . . absorption between sample surface and detector (=1 from vacuum)

$\varepsilon(E_{i,j,n})$  . . . detector efficiency

$V_i$  . . . factor for secondary excitation within the sample

The parts of the formula marked by the underneath brackets account for:

1. Attenuation of the incident radiation
2. Photo electric interaction of the primary radiation with the atoms of element i
3. Refilling of the shell n
4. Fluorescence yield (probability for a X-Ray emission)
5. Probability of the emission of the considered X-Ray line (transition from shell j to n)
6. Factor accounting for secondary excitation
7. Attenuation of characteristic radiation
8. Detector efficiency for the considered X-Ray line

Under the assumption of a homogeneous sample the integral over the sample thickness can be calculated and the terms describing the absorption can be grouped to  $A(d, E, E_{i,j,n})$ . All fundamental parameters, terms just depending on basic physical properties can be grouped to  $Q_i(E)$  and all factors concerning the measurement geometry can be grouped to a geometry factor  $G(E_{i,j,n})$ .

For the integration over the energy the spectral distribution of the excitation source has to be known. In case of monochromatic excitation with the energy  $E_0$  the integration is not necessary and the intensity formula can be rewritten as:

$$I(E_{i,j,n}) = G(E_{i,j,n}) \cdot I_0(E_0) \cdot Q_i(E) \cdot A(d, E, E_{i,j,n}) \cdot V_i \cdot \epsilon(E_{i,j,n}) \cdot c_i$$

The monochromatization of the exciting energy is most commonly accomplished by using a single crystal or multilayer monochromator (see Chap. 2.4.1.1).

### 2.3.2) Energy Dispersive Detectors

As stated before measuring the fluorescence radiation is done by converting the energy of the photons into an electrical signal proportional to the absorbed energy. In the following two detector types that were used within the frame of this work are described, the Si(Li) detector and the silicon-drift-detector.

#### 2.3.2.1) Si(Li) Detectors

The lithium drifted silicon detector consists of a PIN-structure, where the intrinsic (I) region is sensitive to the incoming radiation. The used silicon crystal is about 3-5 mm thick and the cross section range from about 30 mm<sup>2</sup> to 80mm<sup>2</sup>. The electrical contacts of the p- and n-doped silicon are usually a 20 nm thick gold layer. On the p-doped side a negative DC high voltage (500-1000 V) is applied (reverse biased). The radiation enters the detector - see Fig. 2.3.2 - from the p-doped side.

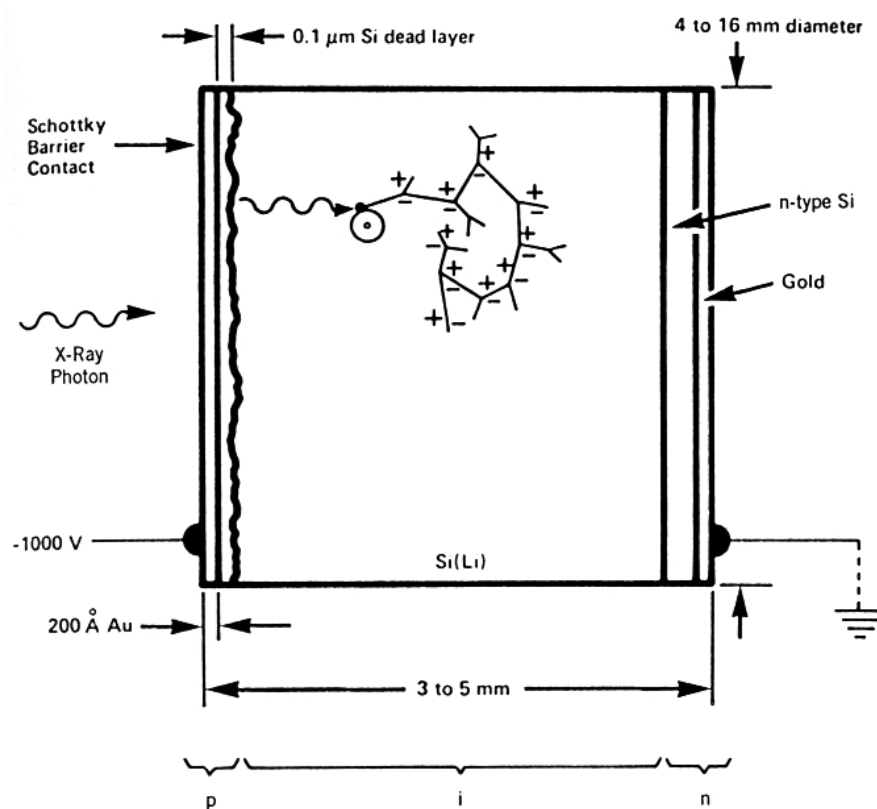


**Figure 2.3.2: Schematic of a Si(Li) detector [53].**

To reach the sensitive intrinsic volume the photons have to pass through the gold contact layer and a “dead layer” consisting of p-doped silicon. This “dead layer and the gold layer limit the detection on low energy photons, as they are absorbed before reaching the intrinsic region.

If a photon is absorbed in the intrinsic region  $n$  electron-hole-pairs are produced. Their number is proportional to the photon energy  $E_{ph}$ .

$$n = \frac{E_{ph}}{\varepsilon}$$

Herby  $\varepsilon$  is the energy needed to create such a electron-hole-pair. For silicon at a temperature of 77 K this is  $\varepsilon \approx 3,7$  eV.

To keep the noise of the pre-amp and the leakage current as small as possible the detector crystal and the pre-amp are cooled to about 77 K using liquid nitrogen (LN2).

Further the detector is operated in high vacuum. The detector window usually is made of thin beryllium (7-25  $\mu\text{m}$ ). To be able to detect the radiation emitted from low  $Z$  elements ultra thin polymer windows are used.

### 2.3.2.2) Silicon Drift Detectors (SDD)

The silicon-drift-detectors (SDDs) use a PSN-diode structure and the principle of sideward depletion [59]. These detectors are characterized by their relatively small dimensions (not LN2 cooling required) and the rather easy handling.

These detectors are made out of silicon wafers and thus their thickness is about 300  $\mu\text{m}$ . The n- doped silicon is covered on one side completely with a p-doped layer and on the other side with rings of p-doped material. In the centre of these rings the collecting anode is placed. A schematic is shown in Fig. 2.3.3

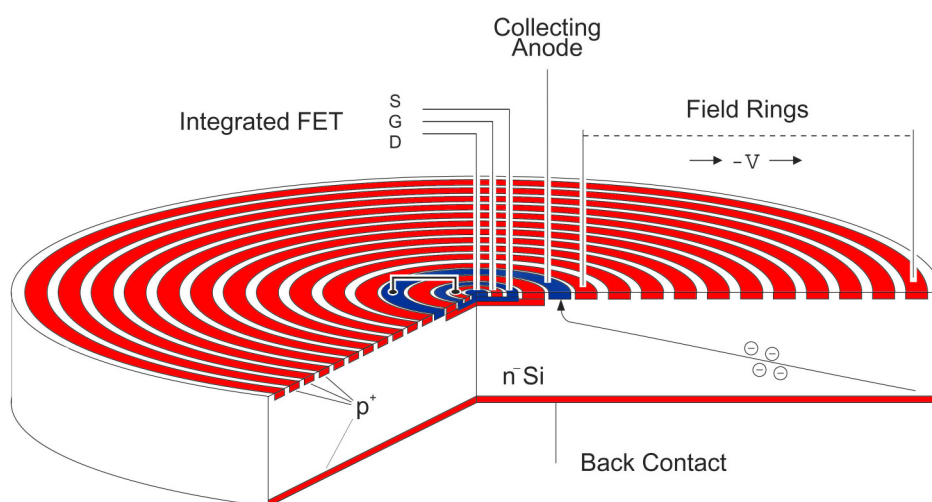


**Figure 2.3.3: Principle of the silicon-drift-detector (SDD) (adopted from [60]).**

The p-doped rings are used to create an electric field guiding the electrons, created in the sensitive area, to the anode. A potential divider chain contacted to the p-doped rings is defining the gradient of the drift field. The lowest voltage, at the collecting anode, is about 0-5 V. The maximum voltage at the outer ring is in the range of 100 V. (see Fig 2.3.4)

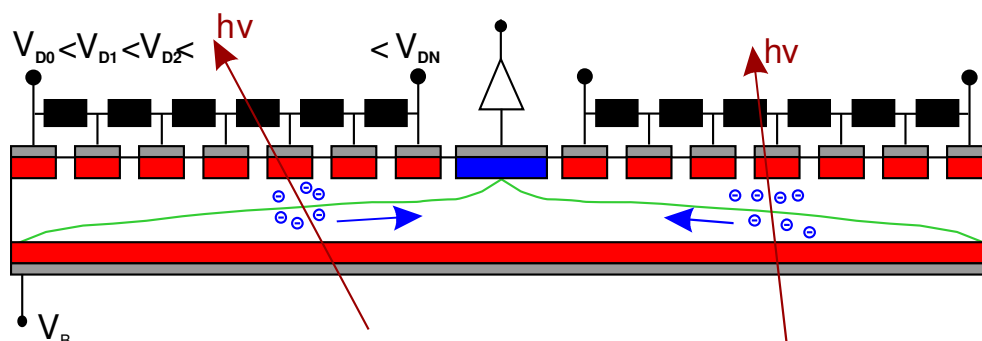


**Figure 2.3.4: Cross section of SDD with potential divider chain and [52]**

The photons enter the sensitive area through the homogeneous p-doped side of the detector. According the applied drift field the electrons move to the anode in the middle of the back

side and the holes to the front side. The anode of the SDD is much smaller than the one of a Si(Li). Thus the input capacity of the pre-amp is very small and hence the noise. The direct integration of the pre-amp on the detector crystal - in the centre of the anode (see Fig. 2.3.3) the noise can be further reduced.

Due to the low voltage and the construction of the pre-amp it is not required to cool this detector type with LN<sub>2</sub>. Peltier elements cooling the detector to about -15 °C are sufficient. Another advantage of the SDD is that it can handle much larger input count rates, up to 10<sup>6</sup> photons/s, than a Si(Li). As the SDDs have a very thin active volume they cannot be used to detect photons with energies larger than 20 keV. The detector efficiency rapidly drops at higher energies.

### 2.3.3) Signal Processing and Detector Artefacts

The signal processing electronics convert the charges collected at the anode (detector output) to a spectrum. A typical signal processing chain is shown in the illustration in Fig. 2.3.5.

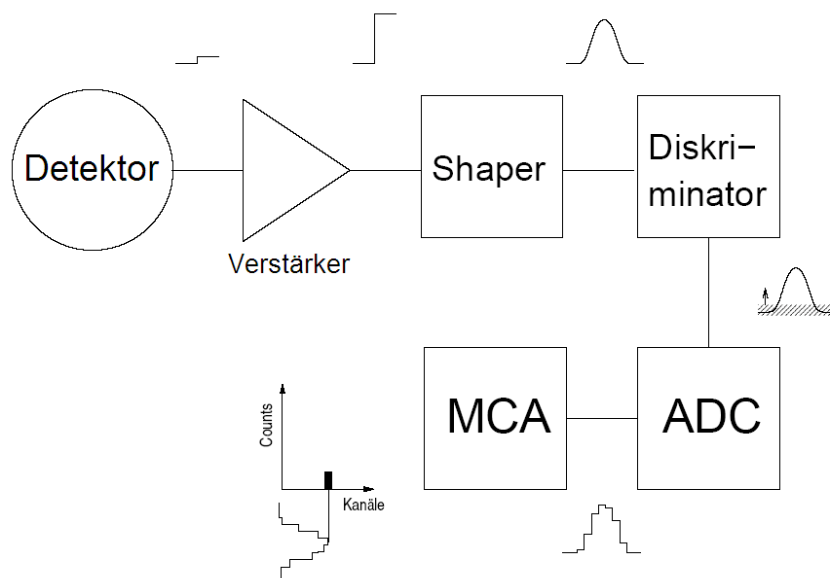


**Figure 2.3.5: Schematic of the signal processing chain [60].**

The pre-amplifier generates a voltage signal from the charge collected at the anode which is immediately amplified. The main amplifier, not necessarily build into the detector, further amplifies the signal. In combination with the main amplifier a pulse-shaper, a pileup-

rejecter and a discriminator treat the incoming signal, so that the multi channels analyzer is finally able to create a spectrum that can be displayed and evaluated with a computer.

Detector artefacts are peaks that are directly created within the detector and cannot be correlated with absorbed photons. They have to be taken into account when evaluating a spectrum, to avoid wrong interpretations of peaks found in the spectrum.

**Sum Peaks:** At high count rates it is possible that two photons enter the detector within a very short time interval, so that they cannot be separated or rejected by the electronic filters. These two signals are counted as one signal at the energy equal to the sum of the energies of the two incoming photons

**Escape Peaks:** If photons entering the intrinsic region are able to ionize the inner shells of the atoms of the detector material (e.g. Si). The characteristic photons that are created in that way are usually absorbed within the detector. However at the boarder of the intrinsic volume it is possible that such an characteristic photon (1,74 keV for Si) can leave the detection volume. Thus the signal detected is 1,74 keV smaller than the energy of the incoming photon, resulting in an artificial peak in the spectrum, shifted to lower energies.

It is possible that these two detector artefacts occur simultaneously, leading to an escape peak of a sum peak. Two photos enter the detector at the same time and during the absorption process one Si-K $\alpha$  photon escapes from the detection volume. This can be observed when the count rate of one X-Ray line is very high (e.g. Ca-K $\alpha$ ).

## 2.4 Micro X-Ray fluorescence Analysis ( $\mu$ -XRF)

Micro X-Ray fluorescence Analysis ( $\mu$ -XRF) is the microscopic variant of the bulk EDXRF technique. The sample is irradiated with X-Rays and the emitted characteristic photons are detected with an energy dispersive detector. Typically the angles between sample and source and detector are 45°. The angle source to detector is 90°. A CCD camera is used to check which point is actually measured

This method is used to determine the elemental composition only of a very small well defined area on the sample, by limiting the beam size of the exciting X-Rays. This can be done on selected single points on the sample or by scanning the sample with this small beam to obtain the spatial distribution of the elements present in the sample (see Fig: 2.4.1).

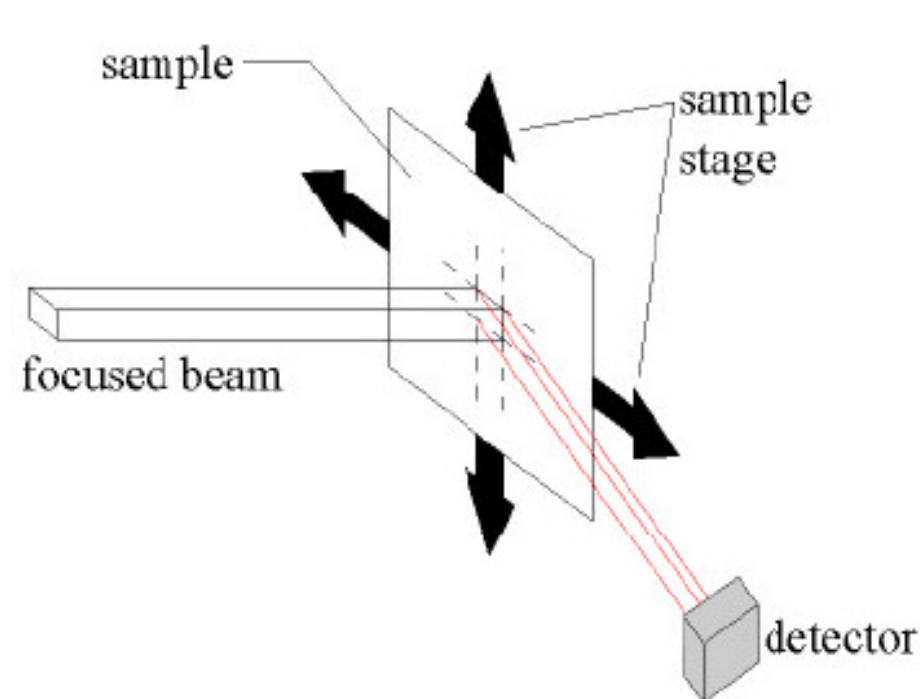


**Figure 2.4.1: Schematic of a  $\mu$ -XRF setup [43].**

To limit the primary beam size several approaches are possible - pinholes, monocapillaries, polycapillaries, refractive lenses, mirrors. These components are often called X-Ray optics. In the following a short description of the X-Ray optics used within the frame of this work is given. Details on X-Ray optics can be found in various books and articles e.g. [61]. A list of different X-Ray optics including their parameters, properties, advantages and drawbacks can be found at [62].

### 2.4.1) X-Ray Optics

#### 2.4.1.1) Monochromators

Using monochromatic excitation energies has the advantage to reduce the spectral background of the obtained data. There are several ways to get monochromatic radiation out of a polychromatic spectrum, e.g. crystals, artificial multi layer structures, absorption filters, cut-off reflectors. Here only the crystal and multilayer monochromators shall be presented briefly, as they were used.



**Single Crystal Monochromator:** The simplest monochromator is a crystal. The radiation impinging on the crystal is reflected according to Bragg's law (Fig. 2.4.2).

$$n \cdot \lambda = 2 \cdot d \cdot \sin(\theta)$$

with  $n$  the order of the Bragg reflex,  $\theta$  the incident angle and  $d$  the lattice spacing.

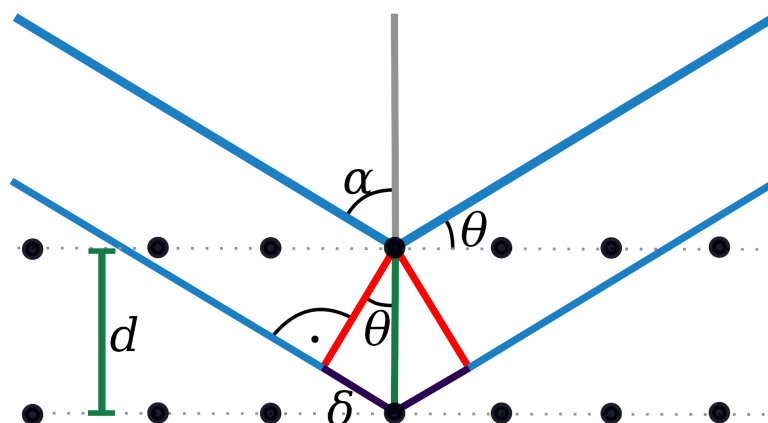


**Figure 2.4.2: Bragg reflex on single crystal [63].**

The energy is selected by tilting the multilayer, the incident angle changes, thus a different energy is fulfilling Bragg's law.

The crystal monochromators offer a very narrow energy bandwidth in the range of  $\Delta E/E = 10^{-4}$ . A typical application where crystal monochromators are needed is the X-Ray Absorption Analysis (XAS).

In synchrotrons setups double crystal monochromators (DCMs) in fixed-exit-geometry are used. In Fig. 2.4.3 a schematic of fixed-exit geometry for two different angles is shown. Both crystal surfaces are kept parallel to each other. If the first crystal is rotated in point A to change the energy, the second crystal is rotated by the same angle and translated along the x-axis, so the beam reflected from the first crystal is hitting the second crystal again in B. Thus the distance  $d$  between the incoming and the monochromatized beam and its position in space are fixed for all energies.

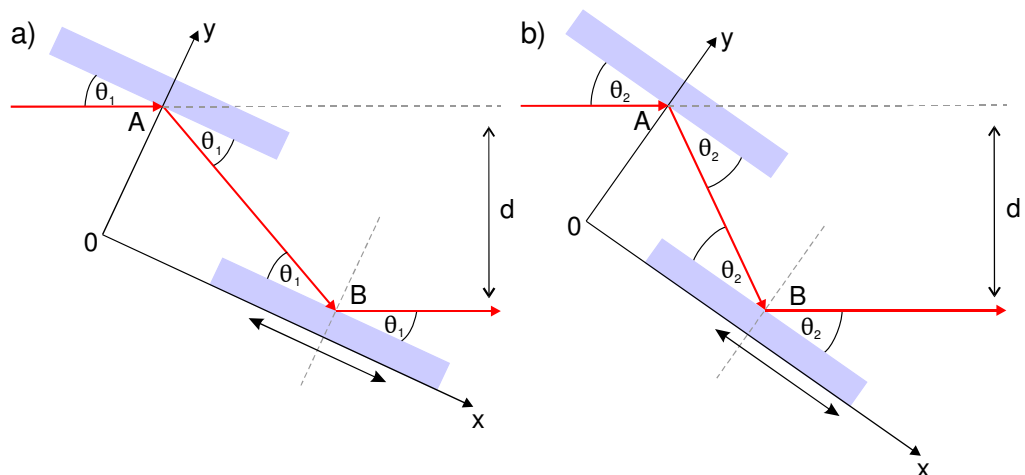


**Figure 2.4.3: Double crystal monochromator in fixed exit geometry for two different incident angles  $\theta_1$  and  $\theta_2$  corresponding to two different energies  $E_1$  and  $E_2$ .**

**Multilayer Monochromator:** Multilayer as periodic layer structures whereas on layer of a low Z element is followed by a layer of a high Z element (see Fig. 2.4.4), e.g. W/Si, Mo/Si, Ni/C.

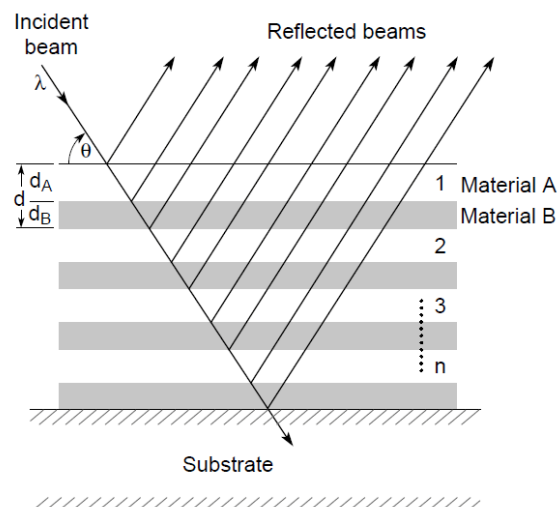


**Figure 2.4.4: Schematic of a multilayer monochromator [64].**

The thickness of these layerpairs  $d_m$  is usually constant.

$$d_m = d_A + d_B$$

with  $d_A$  and  $d_B$  corresponding to the thickness of the low Z and high Z layer respectively.

X-Rays are always reflected on the transition surface from the low absorbing material to the high absorbing material, as the real part of the refraction index for

X-Rays is much smaller than one. The monochromatic radiation is created through coherent interference of the beams reflected at different layers according to

Bragg's law

$$n \cdot \lambda = 2 \cdot d_m \cdot \sin(\theta)$$

with  $n$  the order of the Bragg reflex,  $\theta$  the incident angle and  $d_m$ , as defined above, the thickness of a low  $Z$  high  $Z$  pair. The energy is selected by tilting the multilayer, the incident angle changes and thus a different energy is fulfilling Bragg's law.

Besides the simple multilayers with constant thickness of the layers, multilayers with gradually changing thicknesses  $d_A$ ,  $d_B$  and  $d_m$  parallel to the surface (laterally graded multilayer) can be used. Using these so called graded multilayers spectrometers with a fixed angle between source and detector can be achieved. The energy is selected by translation of the graded multilayer. Thus  $d_m$  is changed in the Bragg equation while  $\theta$  remains fixed.

The bandwidth  $\Delta E/E$  of a multilayer is about  $10^{-2}$  and thus two orders of magnitude larger than the bandwidth of a Si crystal. Multilayers are typically used in TXRF (Total reflection XRF), EDXRF or  $\mu$ -XRF applications.

In synchrotrons setups double multilayer monochromators in a fixed-exit-geometry are used, which is done the same as for crystal monochromators (see above).

#### 2.4.1.2) Reflective Optics

Reflective optics are based on the principle of total reflection of X-Rays (for details on total reflection of X-Rays see e.g. [40, 65]). The total reflection of X-Rays occurs if the radiation impinges on a smooth surface under a very small angle. The angle has to be smaller than critical angle  $\theta_c$  of total reflection.

$$\theta_c = \sqrt{2 \cdot \delta}$$

$\delta$  is the real part of the complex refraction index  $n$ .

$$n = 1 - \delta - i \cdot \beta$$

$\beta$  is representing the absorption of the refracted beam and can be neglected as it is very small compared to  $\delta$  in case of reflection.

**Kirkpatrick-Baez (KB) Mirrors [62, 66]:** They consist of two subsequent perpendicular orientated elliptically bend cylinder mirrors (Fig. 2.4.5). The horizontal mirror is doing the vertical focusing and the subsequent vertical mirror the horizontal focusing. A circular source has an elliptical shape after the focusing process. Depending on the source size focal spots sizes below 1  $\mu\text{m}$  can be obtained. KB-optics are typical focusing systems used at synchrotron beamlines.

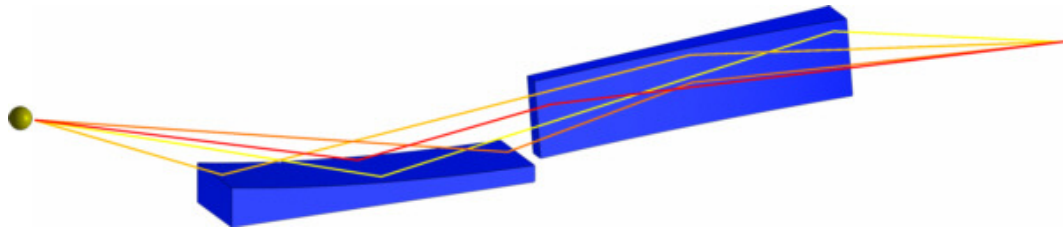


**Figure 2.4.5: Schematic of an Kirkpatrick-Baez Mirror system [62].**

**Polycapillary Lenses [62, 67]:** They consist of a large number of glass capillaries (depending on the purpose from some 1000 up to several millions). Each of these capillaries can be seen a monicapillary. When X-Rays enter such a mono glass capillary with an incident angle smaller than the critical angle for total reflection  $\theta_c$ , they are reflected on the wall of the capillary and hardly lose any intensity. Compared to a non reflecting collimating device an intensity gain is obtained. The gain factor  $I_g$  is

$$I_g = \frac{\Delta\Omega_{eff}}{\Delta\Omega}$$

$\Delta\Omega_{eff}$  is the effective solid angle as it is seen from the X-Ray source, with respect to the critical angle  $\theta_c$ .  $\Delta\Omega$  is the solid angel obtained for the non reflecting collimator, with respect to its length (Fig. 2.4.6).

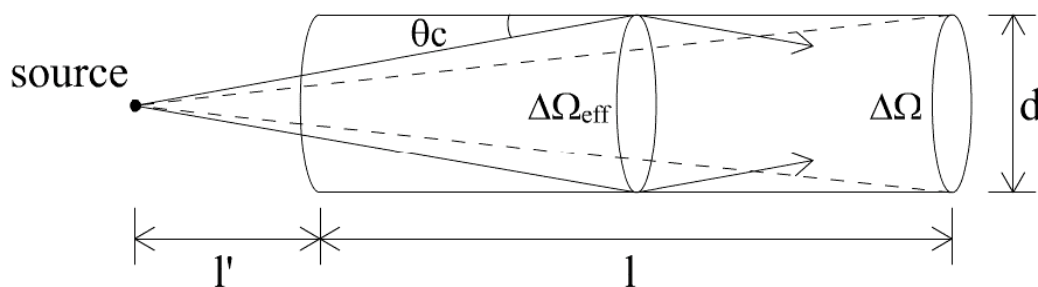


**Figure 2.4.6: Schematic how the intensity gain factor  $I_g$  is obtained [43].**

In polycapillaries these mono glass capillaries are aiming at one point, enabling to capture X-Rays from a large solid angle and focus them on a small spot (point-to-point focusing optics - full lens). At synchrotron beamlines usually polycapillary half lenses are used due to the small angular divergence of the primary beam. The most common types of polycapillaries are displayed in Fig. 2.4.7

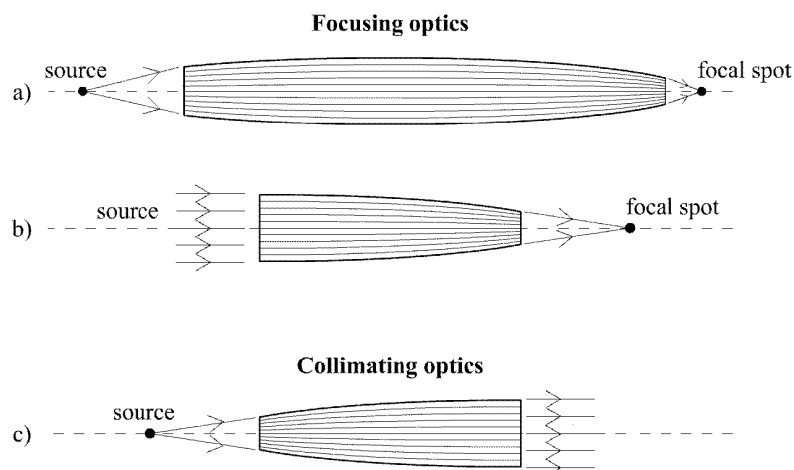


**Figure 2.4.7: Schematic of polycapillary optics (a) full lens, (b) half lens and (c) collimating optics [43].**

The number of single capillaries that can be put together in one polycapillary is limiting the efficiency of the polycapillary. The big advantage is that they are easy to handle and they can be used at synchrotron beamlines as well as in the laboratory. However it has to be kept in mind that the energy dependency of the critical angle is influencing the focusing properties of the polycapillary. This is especially relevant when using polycapillaries in combination with polychromatic radiation, e.g. when using a polycapillary lens in front of the detector to limit the detection volume.

#### 2.4.2) Confocal $\mu$ -XRF

Confocal  $\mu$ -XRF [68] is today an established analytical tool that is used since several years in the lab [69] and at synchrotron beamlines [70-73]. The confocal geometry in  $\mu$ -XRF is used to overcome the problem of the different information depth (also see Chap 2.2.5) of different elements. Further more the confocal setup can be used to obtain full 3D representations of the elemental distribution, without the necessity of complicated

reconstruction algorithms as required for fluorescence tomography (for a more details explanation see [43]).

An illustration of a typical confocal setup at a synchrotron is shown in Fig. 2.4.8. To optimize the results monochromatic radiation is used (e.g. W/Si multilayer). The primary radiation is focused with a half lens. Between the detector and the sample usually also a half lens is used, so the distance between the end of the lens and the detection volume is not so critical, especially in vacuum.

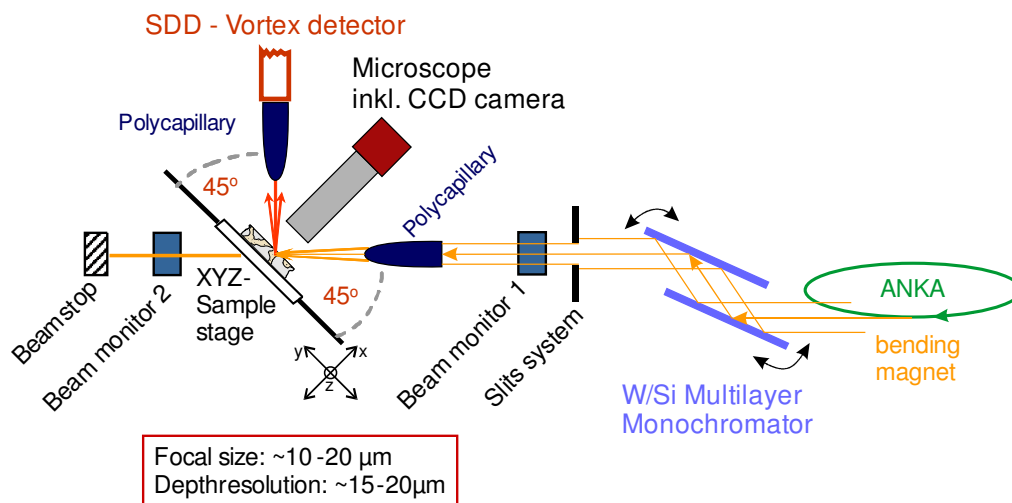


**Figure 2.4.8: Schema of a confocal setup.**

At synchrotron setups typically the focal spots of two half lenses are overlapped defining the measurement voxel (see Fig. 2.4.9).

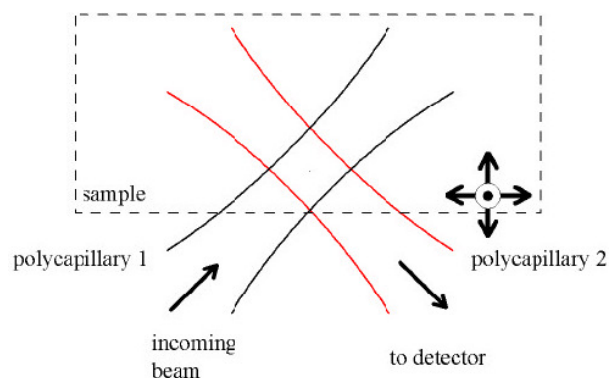


**Figure 2.4.9: Schema of measurement volume [43].**

This voxel is moved point per point over the area of interest just below the sample surface. The size of the detection volume (depth resolution) depends on the energy of the characteristic radiation - i.e. larger for Ca-K $\alpha$  than for Pb-L $\alpha$  or Sr-K $\alpha$  [74].

## 2.5 X-Ray Absorption Analysis (XAS)

As shown in section 2.2.4 the attenuation of X-Rays is described with the linear absorption coefficient  $\mu(E, Z)$ , where  $E$  is the energy of the incoming photon. In the energy range where the photo electric absorption is dominating the absorption coefficient shows abrupt changes at energies corresponding to the binding energy of the inner shell electrons. These jumps in the absorption coefficient are called absorption edges. However these edges are not smooth as it is shown in typical illustrations of the absorption coefficient (see Fig. 2.2.2 in Chap. 2.2.4). They present a very fine sub structure, which was first observed in the 1920s. In this section just a short introduction in the field of X-Ray absorption spectrometry (XAS) is given. More details and elaborated explanations can be found in literature e. g [75-79].

### 2.5.1) X-Ray Absorption Near Edge Structure (XANES)

Let us first consider the absorption of X-Rays by a single atom. If the energy of the incoming radiation is equal to the binding energy ( $E_0$ ) of an inner shell electron the attenuation coefficient shows the edge jump as can be seen in Fig. 2.5.1.

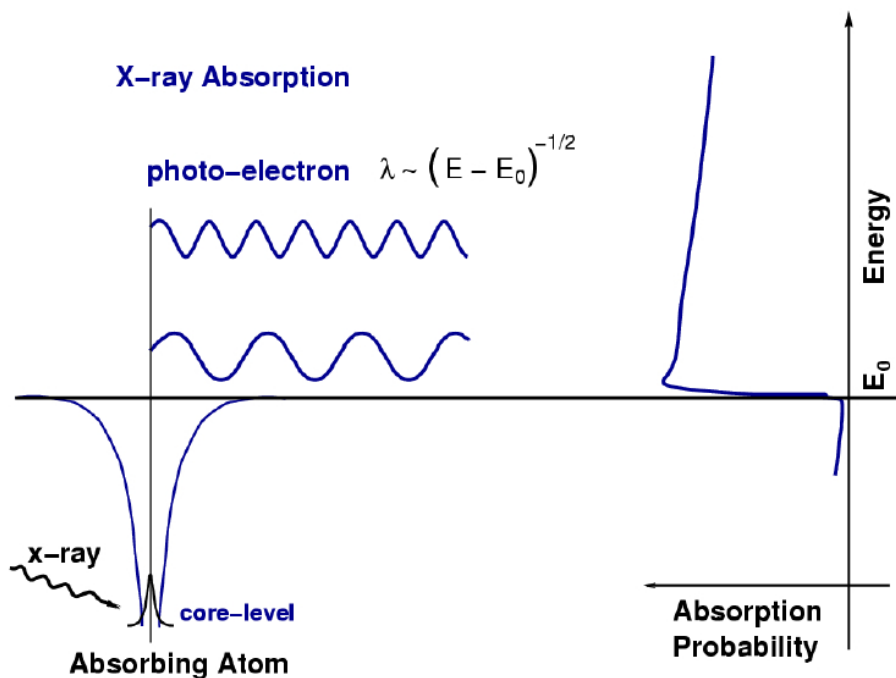


**Figure 2.5.1: Photoelectric absorption on a single atom [77].**

In this process a photo-electron is created. The kinetic energy of the photo electron ( $E_{kin}$ ) is rising with the energy of the incoming X-Rays ( $E_{ph}$ ).

$$E_{kin} = E_{ph} - E_0$$

According to De-Broglie each particle can be assigned a corresponding wave length  $\lambda$ , and the photo electron can be described as wave leaving the atom  $\lambda_{el}$ .

$$\lambda_{el} \propto \sqrt{E_{ph} - E_0}$$

If the atom is not isolated the edge of the absorption coefficient presents oscillations at energies just before and above the edge jump. These oscillations are called X-Ray absorption fine structure (XAFS). The photo-electron created in one atom by absorbing X-Rays can be scattered on the neighbouring atom back to its origin interfering with the photo-electron wave function of the absorbing atom. Hence the absorption coefficient of the atom is changed. An illustration of this process is shown in see Fig. 2.5.2.

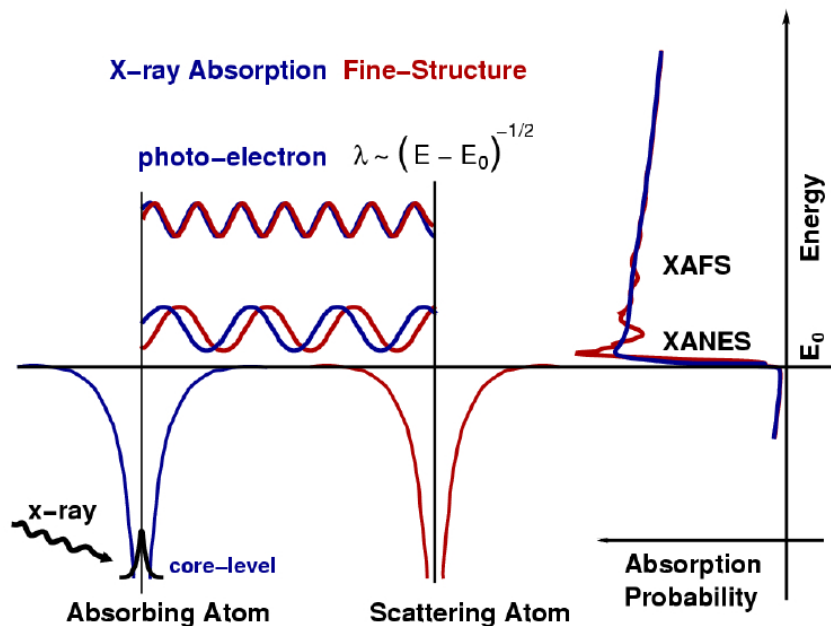


**Figure 2.5.2: Photoelectric absorption one a system consisting of two atoms [77].**

In these oscillations of the absorption coefficient are characteristic for each material and contain information on the oxidation state and the local atomic coordination.

The XAFS can be divided into two regions, the so called

**XANES (X-Ray Absorption Near Edge Structure)** region, which is ranging from about 50-100 eV before the edge to some 10 eV above the edge, and the

**EXAFS (Extended X-Ray absorption Fine Structure)** region reaching from where the XANES region ends to some 100 eV above the absorption edge.



In the XANES region multiple scattering processes with low kinetic energies are dominant while in the EXAFS region the backscattering from the neighbouring atom is prevalent. The XANES region contains information about the oxidation state and the local atomic structure. Changes in the oxidation state of an atom also influence the binding energy of the inner shell electrons. A positive oxidation state - one or more missing outer electrons - leads to an overall positive charge of the atom. Thus the binding energy of the inner shell electrons increases, resulting in a shift and structure change of the absorption edges. Besides the oxidation state the coordination of the atoms is relevant. Different complexes of one element with the same oxidation state result in completely different XANES spectra. In Fig. 2.5.3 the XANES spectra for different iron (Fe) complexes are shown as an example.

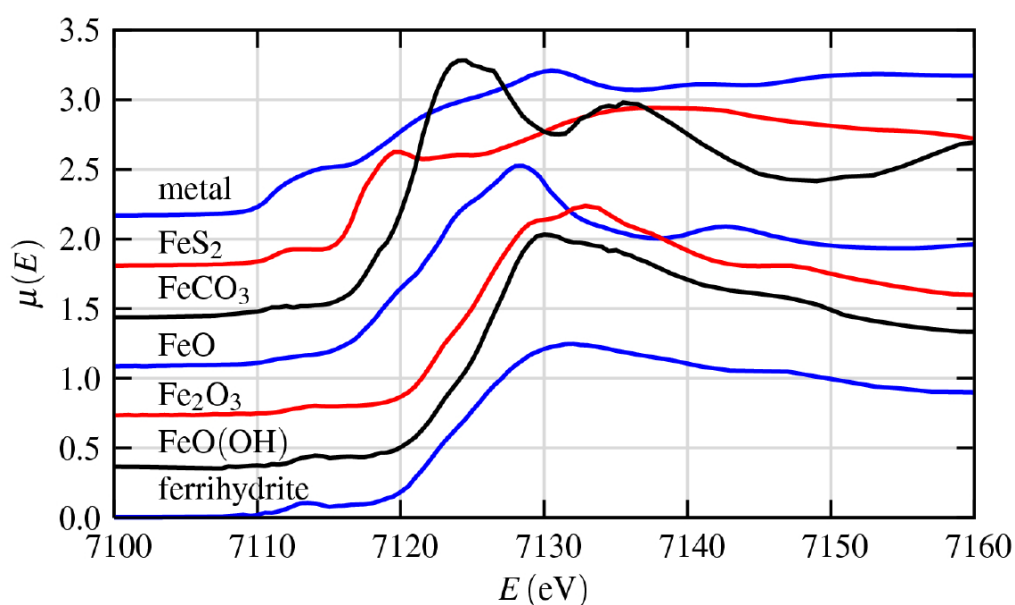


**Figure 2.5.3: K-edge XANES spectra for iron and iron oxides [77].**

These unique structures of the XANES spectra can be used to identify the chemical binding of a desired element. This is achieved by comparing the XANES spectra of the unknown sample with the XANES spectra of well known reference materials. Thus it is a finger print method.



## Chapter 3

# Quantitative Backscattered Electron Imaging (qBEI)

Quantitative Backscattered Electron imaging (qBEI) is a validated technique to visualize and quantify the calcium concentration distribution in bone and mineralized cartilage based on the backscattering of electrons from the sample surface using a scanning electron microscope (SEM).

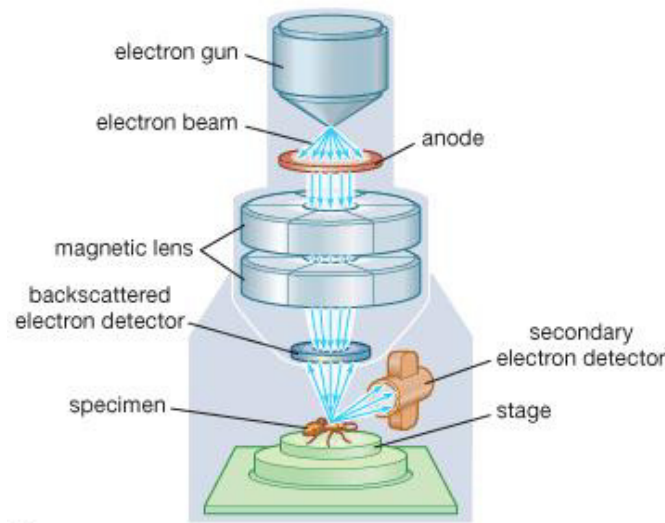
In the following a brief overview on the principle of SEM should be given. An elaborated and more details description can be found in the diploma thesis of A. Roschger 2011 [80] and in the respective literature e.g. Goldstein et al. 1992 [56]. Data and fundamentals were obtained from these sources

### 3.1 Principle of Scanning Electron Microscopy (SEM)

In a SEM a focused beam of electrons is used to scan the sample point per point. In contrast to X-Rays, electrons can be easily focused with electrostatic and magnetostatic fields, as they are charged particles. In modern SEMs spot sizes in the nano metre range can be reached. Motorized sample stages (x-y-z motor systems) enable a stepwise analysis of the area of interest. A schematic illustration of a SEM is given in Fig. 3.1.1.

The resolution of a SEM is influenced by the following parameters [80]:

- the beam diameter
- the size of the interaction volume of beam and sample
- the step size between adjacent voxels
- the quality of the detector signal
- the beam damage on the sample
- the stability of the instrumental setup



© 2008 Encyclopædia Britannica, Inc.

**Figure 3.1.1: Scanning electron microscope (SEM) - Schematic illustrating electron path, sample and detector positions [81].**

The measurements are usually carried out under vacuum condition to avoid signal distortions due to interaction of the electrons with the air molecules.

Like for all other analytical techniques using electrons, sample preparation is a very important factor to obtain good results. Due to the low penetration depth of electrons in matter the method is extremely surface sensitive and not sufficiently polished sample surfaces can distort the obtained results (see Fig. 3.1.2).

Insulating materials have to be coated with a conducting layer - usually carbon or gold- to prevent sample charging during the measurement procedure.

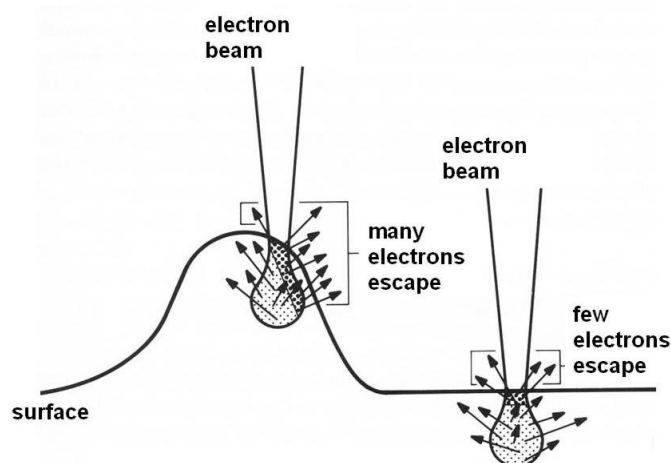


**Figure 3.1.2: Edge-effect in SEM imaging on a not sufficiently polished sample surface: more electrons can leave the sample at edges leading to an increase in detected signal at this position [82].**

### 3.2 Electron - Matter Interaction

There are two type of electron - matter interaction:

1. *Elastic scattering of the primary electrons:*

As in elastic scattering of X-Rays, the energy of the incoming electron remains unchanged, but the direction is changed. Depending on the trajectory in the sample surface, some of the primary electrons are able to escape. The number of escaping electrons is correlated with the average atomic weight of the sample. These electrons are the so called *backscattered electrons (BEs)*.

2. *Inelastic scattering of the primary electrons:*

When interacting with the specimen certain processes lead to an energy loss of the primary electrons: the generation of secondary electrons (SEs), Auger electrons, emission of bremsstrahlung as well as generation of characteristic X-Rays and low energy cathodoluminescence radiation (CL). Furthermore energy from the electrons can be transferred to the sample due to lattice vibrations (Phonons) and electron oscillations (Plasmons). A short description can be found in [83].

The most important of the above stated interactions of the primary electrons (PEs) electrons with a sample are illustrated in Fig. 3.2.1.

The region just below the surface is called interaction volume. This is the volume where the energy of the PE is absorbed and it strongly depends on the mean atomic weight of the sample and the energy of the PE, if the sample has a homogeneous structure.

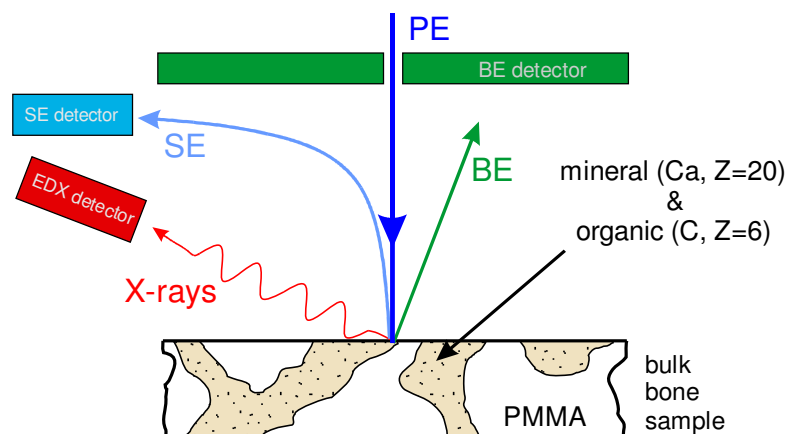


**Figure 3.2.1: Interactions of the primary electrons (PE) - energy range usually 10 to 30 keV - in a SEM with a bulk sample. In this case the bulk is bone embedded in PMMA. Backscattered electron (BE) and secondary electrons (SE) with the respective detectors and X-Rays detected with an energy dispersive detector (EDX-detector - usually Si(Li) or SDD) are illustrated.**

### 3.2.1) Backscattered Electrons

When electrons hit a sample perpendicularly to the surface, most of the primary electrons are only penetrating the first few nanometres of the sample. Some of these electrons sustain elastic collisions and can escape from the sample, the primary electrons are backscattered. Usually several elastic collisions with small scatter angles add up in the backscatter process. The ratio of the number of backscattered electrons ( $n_{BE}$ ) and primary electrons ( $n_{PE}$ ) is the backscatter coefficient  $\eta$ . It is describing the efficiency of the method. It is obvious that as a measure of the number of primary and backscattered electrons the respective currents ( $i_{PE}$  and  $i_{BE}$ ) can be taken.

$$\eta = \frac{n_{BE}}{n_{PE}} = \frac{i_{BE}}{i_{PE}}$$

**Formula 3.1:** Backscatter coefficient  $\eta$ .

$n_{PE}$  = number of primary electrons

$n_{BE}$  = number of backscattered electrons

$i_{PE}$  = current of primary electrons

$i_{BE}$  = current of backscattered electrons

As said before the backscattering process, and thus  $\eta$ , is depending on the sample properties like

- composition (average atomic weight)
- crystallinity
- internal magnetic structure
- surface topography (surface roughness)

and experimental parameters

- energy of primary electrons
- tilt of the sample

The correlation between average atomic weight and BE signal, as shown in Fig. 3.2.2 for different beam energies, can be utilized to measure the Ca content in bone samples.

In case of low atomic numbers ( $Z \leq 20$ ) the correlation between  $Z$  and  $\eta$  is almost linear.

Further it has to be note that the slope for  $Z \leq 20$  is relatively steep, hence the method is very sensitive with respect to changes in the atomic weight in the region. Thus the calibration of the setup for the analysis of materials with an average atomic number  $Z_{av} < 20$  is simple.

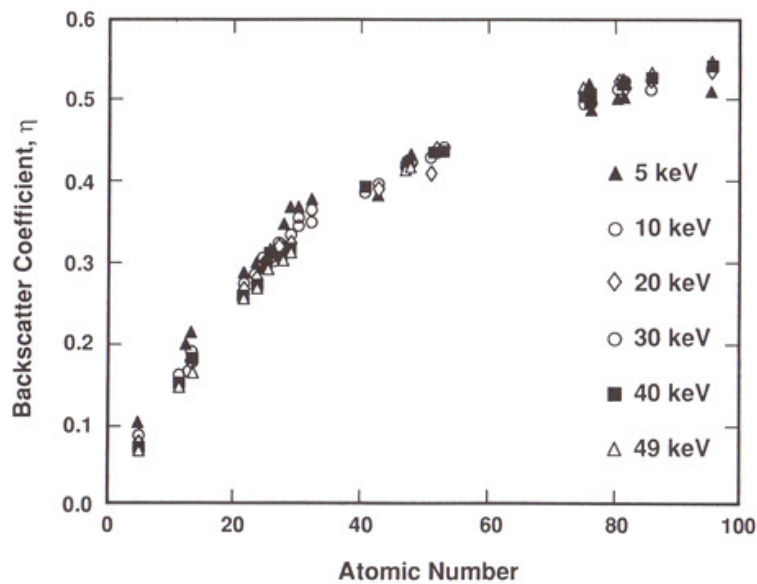


**Figure 3.2.2: Backscatter coefficient  $\eta$  as function of the atomic number for different energies of the primary electron ranging from 5 to 49 keV [56].**

For the constituents of bone and mineralized cartilage, the organic collagen matrix ( $Z_{av} \approx 6$ ) and the carbonated calcium hydroxyapatite (CCaHA) crystals ( $Z_{av} \approx 13,86$ ), a perfect linearization is possible and the contrast with respect to atomic numbers is optimal.

If the sample is a homogeneous mixture of several constituents, a linear combination of the backscatter coefficients of the present elements based on weight fractions / concentrations of the components is appropriate:

$$\eta_{av} = \sum_{i=1}^n \eta_i \cdot c_i$$

**Formula 3.2:** Average backscatter coefficient for a sample made up of several constituents.

$\eta_{av}$  = average backscatter coefficient

$\eta_i$  = backscatter coefficient of element  $i$

$c_i$  = concentration of element  $i$

$i$  = index of elements

$n$  = number of different elements present in the sample

The energy of the primary electron beam is hardly influencing the number of backscattered electrons. The variation of  $\eta$  is smaller than 10% for a fixed atomic number (see Fig. 3.2.2). Thus, regarding the electron yield, the selection of an appropriate energy for the primary electrons is not critical for obtaining consistent results, but plays a major role in terms of information depth.

### 3.3 Electron Detectors

Several electron detector systems are available. The choice is depending on the operation mode of the electron microscope. The most common SEM setups offer a combination of different detector systems. A typical arrangement for SEMs is the combination on a BE-detector (e.g. solid state detector), a SE-detector (e.g. Everhart-Thornley detector) and an energy dispersive X-Ray detector (Si(li) /SDD).

#### 3.3.1) Backscattered Electron Detector - Solid State Detector

The solid state detector is a typical detector for BEs, but it is also able to register SEs and X-Rays, which contribute in a small amount to the detected signal. The solid state detector is working similar as the previously describe X-Ray detectors (Chap.2.3). It is a semiconductor material in which the impinging electrons create electron-hole pairs. In case of a Si-based detector a BE can produce more than 3000 electron-hole pairs, assuming that for one electron hole pair 3,6 eV are necessary. The electrical conduction is provided by a thin Al layer. As the measured current is proportional to the energy of the incoming electrons the contribution of the SEs to the signal is very small. As the number of X-Rays reaching the detector is small, the contribution of the X-Rays to the measured current is negligible. The solid state detectors build as thin plates (a few mm thick) and can thus be used to cover a large solid angle. The position of the backscatter solid state detector is illustrated in Fig. 3.1.1 and 3.2.1

A schematic of the operating principle of the solid state detector is shown in Fig. 3.3.1.

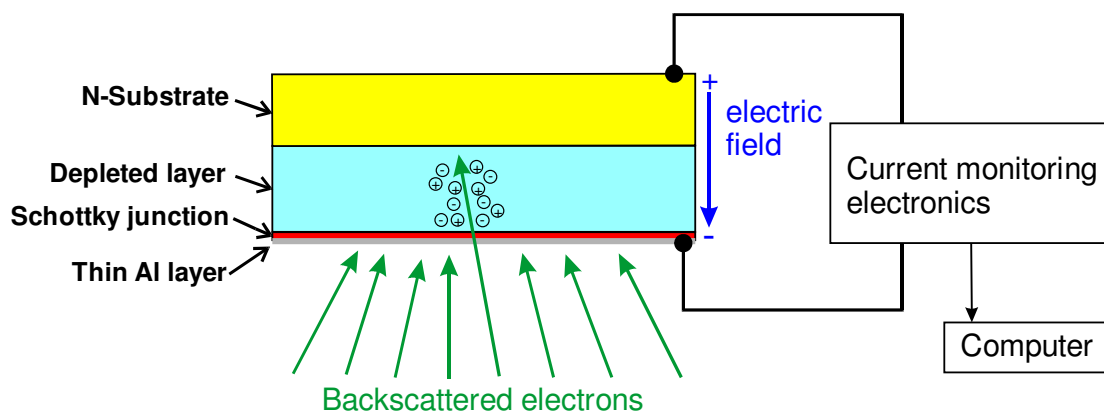


**Figure 3.3.1: Principle of a solid state detector.**



### 3.3.2) Secondary Electron Detector - Everhart-Thornley detector

Everhart-Thornley (E-T) detector is a Faraday-cage in combination with a scintillator and a photomultiplier (Fig. 3.3.2) and it is a combined BE and SE detector. The scintillator is converting incoming electrons to photons, which are transported by a fibre optic to a photocathode. There the photons are converted back to electrons due to the photo electric effect. The signal gets then amplified in the electron multiplier stage.

To create photons in the scintillator energies of more than 10 keV are required. Thus additional acceleration of the electrons to the detector is necessary. To collect the SEs from the sample the potential of the faraday-cage is held at +200 V (positive bias mode). Almost all SEs emerging from the sample can be collected, depending on the surface structure. BEs of typically 20 keV or more are not influence by the 200 V potential of the faraday-cage. However some BEs reach the faraday-cage directly causing a low, but distinct signal. The E-T can be used as pure BE detector if it is run in negative bias mode (-50 V), so that all incoming SEs are reflected and only the high energy BEs can reach the scintillator.

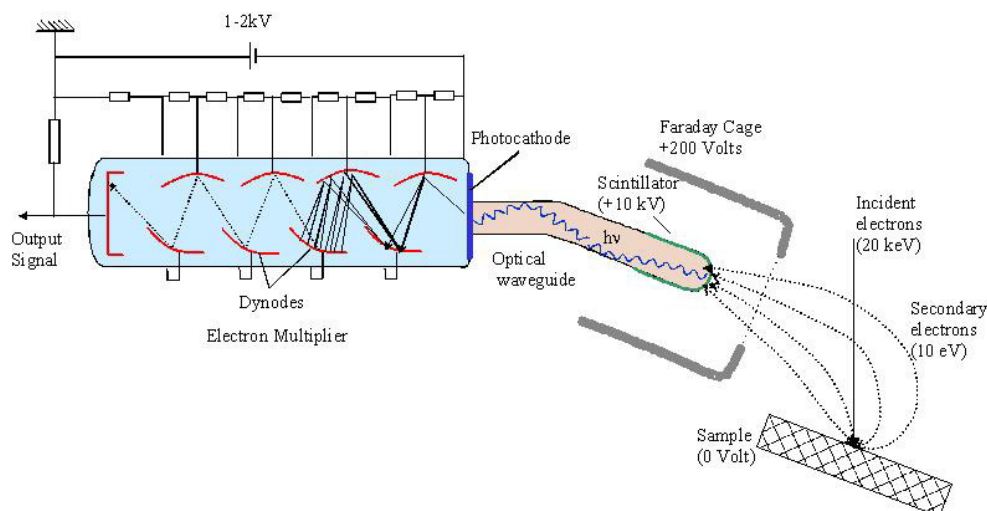


**Figure 3.3.2: Principle of a Everhart-Thornley (E-T) detector used for detecting the secondary electrons - operated in positive bias mode [84].**



## Chapter 4

# Characteristics of Bone and Important Trace Elements

### 4.1 Structure and Architecture of Bone

#### 4.1.1) Bone Matrix

Neither subchondral, cortical nor trabecular bone is homogeneous or isotropic, au contraire is has a complex hierarchical structure. Bones like femoral heads and necks are made up of a compact hard outer shell (cortical bone) and a spongy inner structure (trabecular or cancellous bone) [19] (Fig 4.1.1a). Both the cortical and trabecular bone are assembled of individual osteons (Fig 4.1.1b) and bone packets (Fig 4.1.1a) respectively- often called basic structural units (BSUs). They exhibit a lamellar substructure [85]. The basic material of these bone lamellae is an organic-mineral composite. It consists of cross-linked collagen type I fibrils with several hundred nanometers diameter, in which nanocrystallite particles of (partially carbonated) calcium hydroxyapatite crystal ( $\text{Ca}_5(\text{PO}_4)_3\text{OH}$ ) platelets are embedded (Fig 4.1.1d), giving bone its unique mechanical properties [19, 85].

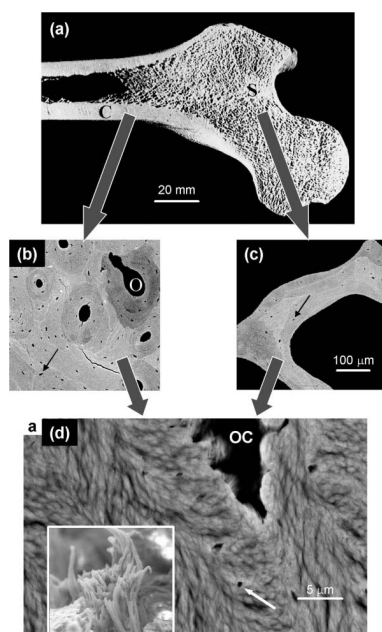


**Figure 4.1.1: Cross-section of a femoral head (a) showing cortical (C) and trabecular (S) bone, with the respective qBEI images (b & c). In (d) the fibril structure next to an osteocyte lacuna is displayed [19].**

### 4.1.2) Cement Lines

Besides bone packets and osteons the so-called cement lines or reversal lines are another structural unit of bone, directly linked with the remodelling process. Rather a cement surface than a line, it's separating osteons or bone packets originating from different remodelling cycles [20]. The cement lines are formed during the bone remodelling after the resorption activities of the osteoclasts have stopped. The material of the cement line, mainly noncollagenous proteins like osteopontin and osteocalcin, is deposited on the reversal surface without transverse collagen fibrils [20, 86] before the osteoblasts start forming new bone. The thickness of these lines is about 1  $\mu\text{m}$  to 5  $\mu\text{m}$  [87]. It has been shown in various studies that the cement lines play an important role in fracture processes and energy absorption by limiting crack propagation through deflecting the cracks in direction of the cement line and absorbing the fracture energy this way [86, 88]. It was controversially discussed in literature over years, whether the cement lines are higher or lower mineralized than the surrounding bone matrix with favouring the hypothesis of higher mineralization of cement lines [20, 89-92]. For example in Fig 8.2.1b numerous parallel cement lines, which show a distinct higher mineralization than the surrounding bone matrix, can be easily identified.

## **4.2 Bone Metabolism**

### 4.2.1) Bone Remodelling

As other biological tissue bone is subjected to continuous remodelling. Osteoclasts resorb the bone matrix, macrophages clean the resorption pit and thereafter osteoblasts form new collagen matrix, which is mineralized after a short lag time [19, 93, 94]. The bone remodelling cycle consists of five steps [95]:

1. Resting Phase
2. Activation
3. Resorption
4. Reversal
5. Formation

In Fig 4.2.1 an illustration of the bone remodelling cycle including the involved cells is shown.

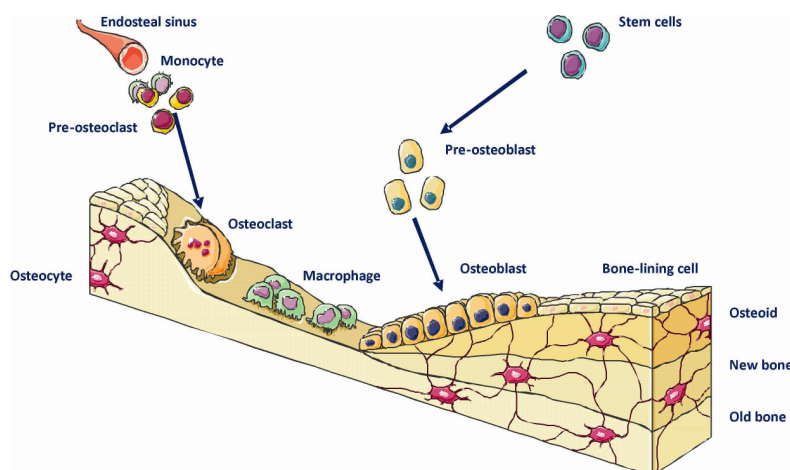


**Figure 4.2.1: Schematic illustration of the bone remodelling cycle [96].**

The mineralization is a two-phase process: within days up to 70% of full mineralization capacity is mineralized and the mineralization of the remaining 30% lasts for several years [19, 97]. In this secondary mineralization phase the Ca concentration goes into saturation at about 26 wt%Ca [85]. The remodelling rate is depending on the type of bone tissue, trabecular bone is renewed with 10-50% per year and cortical bone with 2-5% per year [98]. As a consequence of the remodelling kinetics, the degree of mineralization of bone packets and osteons reflects their age [19]. And there are always BSUs of different age existing parallel.

## 4.2.2) Osteoporosis

Osteoporosis is characterized by a low bone mass and a micro architectural deterioration of bone tissue, with a consequent increase in bone fragility and susceptibility to fracture. The bone remodelling cycle is out of balance in the disease. Changes in the bone remodelling cycle lead to altered bone mineral density (BMD), which is routinely measured for diagnostic purposes. Additionally, the bone mineral density distribution (BMDD) is affected, causing characteristic BMDD patterns depending on the type of the remodelling dysfunction. qBEI offers the possibility to determine the BMDD. In Fig 4.2.2 BMDD histograms are shown. Classical postmenopausal osteoporosis (pmpOP) - line C (dark green) - causes a shift to the left in the diagram. This means that the number of young BSUs is increased [21].

Osteoporosis affects already more than 75 million people in Europe, Japan and the United States. The general prevalence of osteoporosis rises from 5% among women aged 50 years

to 50% at 85 years of age; among men, the comparable figures are 2.4% and 20% [99]. As the population continues to age, the effects of osteoporosis will become increasingly prevalent [100].

Many risk factors have been found which are associated with osteoporotic fracture, including low peak bone mass, hormonal factors, the use of certain drugs (e.g. glucocorticoids), cigarette smoking, low physical activity, low intake of calcium and vitamin D, race, small body size, and a personal or a family history of fracture [101].

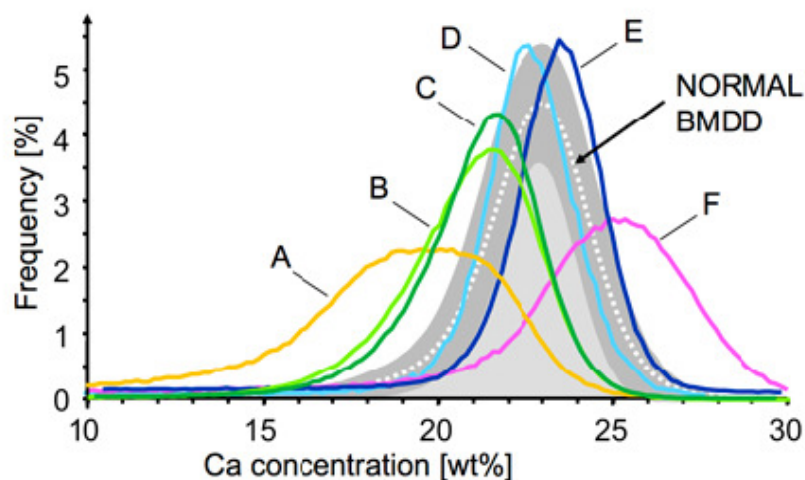


**Figure 4.2.2: Bone mineral density distribution (BMDD) histograms of different bone diseases including postmenopausal osteoporosis (pmpOP) [80]:**

**A: osteomalacia**

**B: idiopathic osteoporosis**

**C: postmenopausal osteoporosis (pmpOP)**

**D: pmpOP treated with bisphosphonates**

**E: osteogenesis imperfecta**

**F: pmpOP treated with NaF**

However it is likely that many environmental factors are still unknown. Khalil et al have recently shown in a prospective cohort study in 533 women an association with blood Pb levels and fractures and lower total hip bone mineral density (BMD) [102]. Elevated blood lead levels may have a direct causative role in the pathogenesis of osteoporosis [4, 103-105].

### 4.3 Structure of Articular Cartilage

The osteochondral unit has a highly complex structure, which is designed to ensure a frictionless movement in articulating joints and to transfer loads from articular cartilage to underlying bone tissue. It is basically composed of articular cartilage, mineralized cartilage

and subchondral bone [106]. The zone of mineralized cartilage is about 100 µm thick and provides the tight bonding of articular cartilage to subchondral bone.

In Fig. 4.3.1 the composition of the osteochondral region is shown. The subchondral bone and the mineralized cartilage are separated by a cement line, similar to the osteons in cortical bone. The mineralized cartilage is separated from the non mineralized cartilage by the so called tidemark (TM) [26].

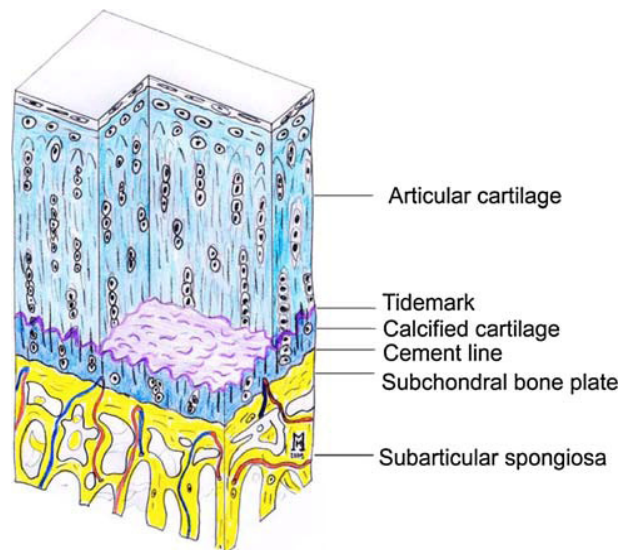


**Figure 4.3.1: Drawing of the region of articular cartilage and subchondral bone [26].**

The extracellular matrix of articular cartilage mostly consists of water, collagen type-II and proteoglycans. The proteoglycans are not homogeneously distributed within the articular cartilage and contain a lot of sulphur (S) in the form of sulphate. The sulphur content has its maximum next to the tidemark, still within the non mineralized cartilage [27]. The organic matrix in calcified cartilage is impregnated with hydroxyapatite (HA) ( $\text{Ca}_{10}(\text{PO}_4)_6(\text{OH})_2$ ) particles, which makes the stiffness of calcified cartilage comparable to that of bone tissue [107]. However, calcified cartilage has no lamellar structure and the Ca content is slightly increased compared to cortical bone - resulting in lighter grey shades in qBEI images (Fig. 8.1.1).

## 4.4 Trace Elements in Bone

The term "trace element" refers to chemical elements which occur in nature in minute quantities or are required by organisms in very low amounts.

The trace elements can be classified into elements essential, possible essential and nonessential for life [1].

The nonessential trace elements also include the toxic elements such as the heavy metals, which are known to be a threat to human health, even in very low amounts.

### 4.4.1) Lead (Pb)

One of the main threats to human health deriving from exposure to heavy metals is linked to lead (Pb) [3]. A vast number of degenerative diseases like cognitive decrements, chronic diseases of the hematopoietic, renal and endocrine system and the development of cardiovascular diseases can be associated to Pb exposure [3, 108]. Even metabolic processes in bone are adversely affected by Pb. Further Pb has been stated as potential risk factor for osteoporosis [109] and the development of osteoarthritic changes due to long term exposure [110]. Moreover negative influences on bone healing mechanisms [111] and potential contributions to osteopenia [112, 113] have reported.

Pb is interfering with the  $\text{Ca}^{+2}$  signaling pathways in cells by blocking calcium binding sites with  $\text{Pb}^{+2}$  ions [4]. The bone synthesizing cells, the osteoblasts, have been reported to be impaired by the toxicity of Pb [114]. Besides that, it has been shown that Pb has a higher affinity to osteocalin than Ca which increases the amount of Pb bond to the bone matrix even at low Pb levels [115]. It is well known that  $\text{Pb}^{+2}$  is able to replace  $\text{Ca}^{+2}$  by cation exchanges in hydroxyapatite minerals [116]. Consequently its comprehensible that for non occupational exposed humans approximately 95% of the total body Pb burden is present in the skeleton, with higher values for men than for women [5]. The approximate half life of Pb in the skeleton is assumed to be up to 20 years [117, 118] depending on the speed of the remodelling kinetics of trabecular and cortical bone with an average overall remodelling rate of 4-14% per year [98]. Thus the bone Pb reflects long term exposure, even to low Pb concentrations.

Exposure to Pb in industrialized countries derived from a variety of sources: leaded gasoline, workplace exposures and leaded water pipes [3]. Thus adults have already accumulated a significant amount of Pb in their skeleton [119, 120]. However the number of sources has been reduced drastically, e.g. selling leaded gasoline is forbidden in the European Union (EU) since 2000 (directive 98/70/EC) [121].



### 4.4.2) Zinc (Zn)

Contrary to Pb and other heavy metals zinc (Zn) is a very important essential trace element in biological processes and a reduced or lacking intake may cause metabolic dysfunctions or lead to chronic diseases, as for all other essential trace elements. It is part of the reactive centre of over 2000 enzymes (Zn metalloenzymes), including DNA and RNA polymerase and is considered to be important for growth [7, 9]. Zn has been reported to have stimulating effects on bone formation and mineralization by increasing osteoblast activity and adversely affecting osteoclast formation [6-8]. Studies on the Zn levels in bone suggest that most of it is present in the mineral phase [122, 123] and that it is concomitantly incorporated with Ca during the mineralization [124].

However over supplementation with Zn may be linked with adverse effects on Ca metabolism and bone formation, impair immunological response or negative interference with other essential trace elements like iron (Fe) or copper (Cu) [125].

### 4.4.3) Strontium (Sr)

Little attention has been paid to strontium (Sr) concerning human biology and pathology as Sr was considered unimportant except the radioactive isotopes, first of all  $^{90}\text{Sr}$ . This changed when Sr turned out to be a possible drug in osteoporosis treatment to reduce the fracture incidence [10]. The dietary amount of Sr can vary widely without occurrence of symptoms of intoxication and it is not under homeostatic control so the blood and serum levels are not kept constant [126]. There are reports, that high Sr levels favour the formation of insoluble Sr phosphates resulting in phosphorus deficiency symptoms [127]. However no pronounced toxicity of Sr is known [126].

As Ca, Sr is part of the 2nd group of the periodic system and is therefore chemical similar to Ca. Animal studies suggest, that Sr can substitute Ca in almost any physiological process [126]. For example the protein binding affinity of Sr is similar to the one of Ca [128]. However, Ca can pass through biological membranes more easily than Sr leading to a natural differentiation of Ca and Sr. For example a poor Sr uptake in the gastro intestinal tract or reduced placental transfer.

Sr has a high affinity to bone. A study showed that administered radioactive  $^{85}\text{Sr}$  almost exclusively deposited in bone, by  $\text{Ca}^{+2}$  substitutions or incorporation during bone formation [126].



## Chapter 5

### Data Evaluation Methods

#### 5.1 Spectrum Processing and Map Generation

The acquired spectra, an example is shown in Fig 5.1.1, were treated in batch mode with the "microxrf2" software package (B. Vekemans, XMI, Universiteit Gent, Gent, Belgium) installed at the beamline, as one map may consist of up to 10706 single spectra.

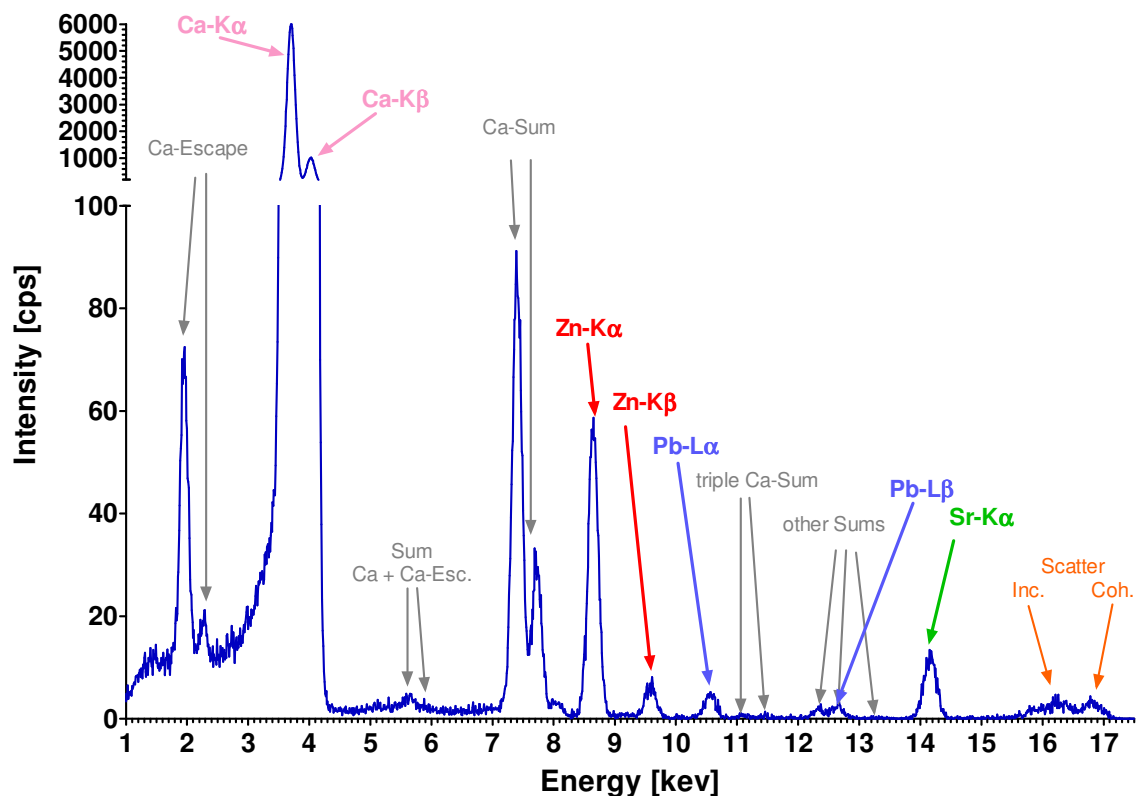


**Figure 5.1.1:** Example spectrum at a cement line position of sample FNX3-A1 (OTH69 scan 106, spectrum 0506; Chap. 8.2) in linear scale with peaks labelled. Normalized to counts per second; Acquisition parameters:  $t=10$  sec, Ring current  $I_{R-C}=137,47$  mA; The peaks labelled in grey denote detector artefacts.

Peak fitting and deconvolution as well a subtraction of the spectral background was done with AXIL for Linux [129] integrated in the "microxrf2" software package.

The elements present in the sample were identified from the sum spectrum of a whole map. Based on this, fit models for AXIL were created and applied to all spectra obtained for one sample group (rat vertebrae, femoral necks & heads, human biopsy samples).

Custom written software<sup>2</sup> was further applied to the "i2txt"-map-files produced by microxrf2 to normalize the net intensity data to counts per second (cps) and 100 mA ring current (R-C). All element intensity maps were saved as "text-images". For each pixel the normalized net intensity value is arranged in a two dimensional matrix, in a standard ASCII file. Tabulators were used as delimiters. To illustrate the element distributions the "text-images" were converted to 8-bit colour coded images. Contrary to "text-images" 8-bit coded images suffer a loss of information, as only 255 colour or grey levels are available. Thus for detailed evaluation with ImageJ the "text-images" were used.

### 5.2 Data Analysis with ImageJ

Part of the data evaluation was performed with the 2D image processing software ImageJ (v1.44b, Wayne Rasband, National Institutes of Health, USA, <http://rsb.info.nih.gov/ij>) [130, 131]. This software is published under public domain and available for Windows, Mac OS, Mac OS X and Linux.

In Fig. 5.2.1 an example how an ImageJ workspace could look like is shown.

ImageJ handles several image file formats including tiff, jpg, "text-images" and some RAW formats, and can display them in various colour scales to enhance the visibility of features in the image. Standard image manipulation like resizing or rotating are possible as well as the evaluation of selected Regions of interest (ROIs). Selections can either be done with line-drawing and area (polygon, freehand, rectangular ...) selection or threshold tools. Using a "ROI Manager" multiple ROIs per image can be handled and saved. The saved ROIs can be applied to any image of the same size. These ROIs can be used to calculate area and pixel value statistics. A very useful option is the image stack, opening up the possibility to group several images of the same size, e.g. the maps of different elements of one scan and the corresponding qBEI. The statistical evaluation, using the prior defined ROIs, can be done for all maps of a scan at once. The "measured" ROI data can be saved in Excel readable ASCII-format.

---

<sup>2</sup> "ANKA-i2txt" and "MatrixMapJob" developed and written by Stephan Smolek, Atominstitut TU Wien 2008.

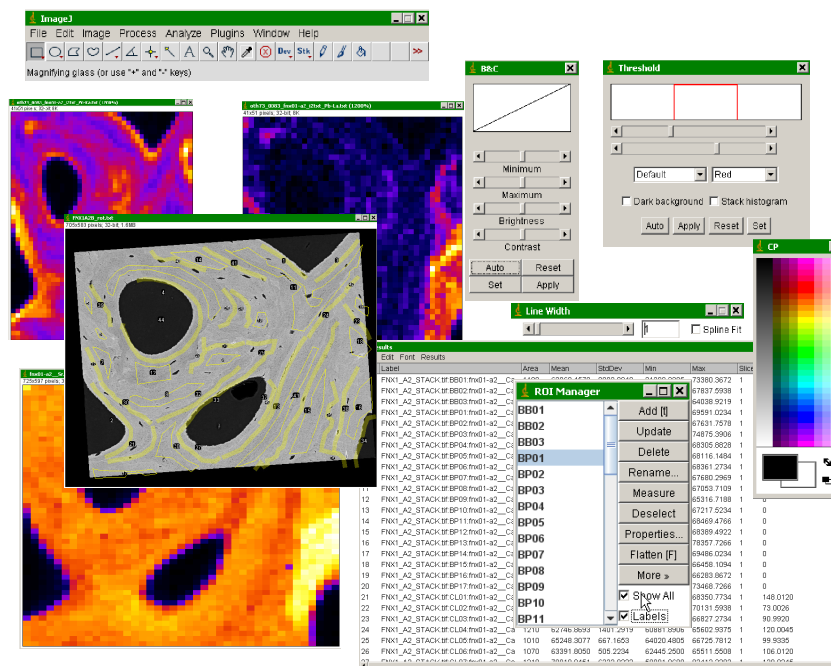


**Figure 5.2.1: Workspace of ImageJ. Showing the main toolbar, Tool-windows like "ROI Manager" and "Results", qBEI image with highlighted ROIs and element images of a bone sample.**

### 5.2.1 Evaluation of the Femoral Neck & Head Samples

It is not possible to exactly match qBEI images and corresponding SR  $\mu$ -XRF element maps as the lateral resolutions are different, in the range of  $1 \mu\text{m}^3$  and  $10 \mu\text{m}^3$  respectively. Thus a procedure using ImageJ was developed to establish a correlation, which was part of the master thesis of A. Roschger 2011 [80]. Details about the samples and the Results are presented in Chap. 8.2.

#### 5.2.1.1) Selection of Regions of Interest

First the qBEI images have been aligned with the corresponding SR  $\mu$ -XRF maps. This was done according to the sharp edges of the bone borders and the positions of haversian channels. Due to the different lateral resolutions corrections were necessary to establish the correlation. The X-Ray images have been scaled to the size of the qBEI images and slight deviations in the orientation due to the sample mounting processes in the two different setups (electron microscope and synchrotron beamline) have been corrected by rotating the qBEI image. It was checked, that this procedure does not cause any errors when evaluating the grey-levels of the qBEI as long as only a single rotation is performed.

Secondly, the ROIs representing the bone matrix and cement lines were marked in the qBEI images. Due to the alignment of the images, the ROIs drawn in the qBEI could be directly transferred to the elemental maps (Fig. 5.2.2).

Features such as osteocyte lacunae or cracks were excluded to minimize errors in obtaining the average absolute Ca content (wt %) for each bone matrix ROI from the qBEI images.

The cement lines were labelled by 10  $\mu\text{m}$  thick lines at the interface of the BSUs (Fig 5.2.2).

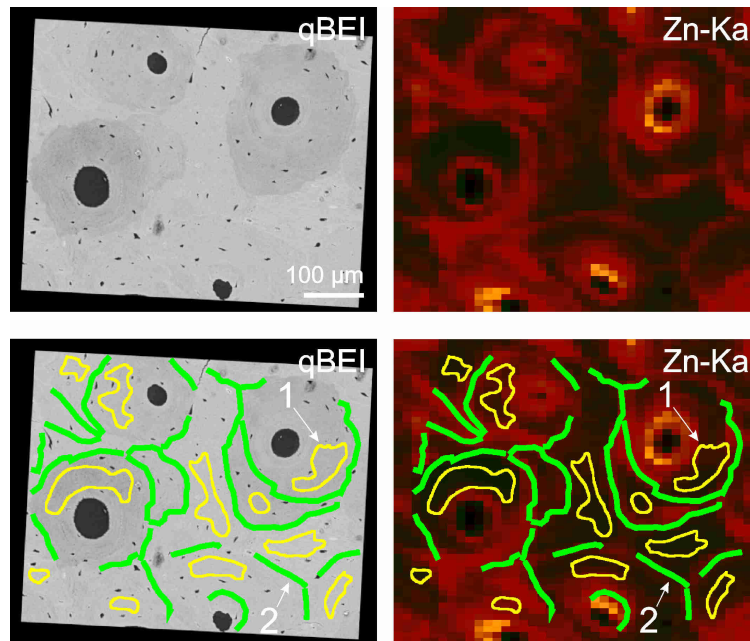


**Figure 5.2.2: Procedure of defining regions of interest (ROIs) (FNX4-A1, OTH69 scan 120) [132]:**

**I) Selection of a qBEI image e.g. of osteonal bone region (top-left) together with the corresponding SR  $\mu$ -XRF map of Zn-K $\alpha$  (top-right).**

**II) Identification of homogenous bone matrix, cement lines in the qBEI image and outlining them (bottom left): (1) bone matrix ROIs (yellow outlined areas) and (2) cement lines (green lines, 10  $\mu\text{m}$  thick).**

**III) Transfer of the ROIs marked in the qBEI image to the SR- $\mu$ XRF map (bottom-right).**

#### 5.2.1.2) Normalization of SR $\mu$ -XRF-Maps

Additionally to the general normalization of the XRF count rates to the synchrotron-ring current of 100 mA the XRF intensities of Pb, Zn, Sr were further corrected for variations in XRF intensities caused by slight changes in the measurement setup between different maps, samples and synchrotron sessions, so that the Pb, Zn, Sr XRF-intensities between all the maps can be directly compared and treated as measures of elemental content. For this purpose an average normalization factor  $k_j$  (see formula 5.2.1) was evaluated for each map  $j$

(j...index of the maps), expressing the mean ratio between Ca as measured by qBEI (wt%Ca) and Ca as measured by SR  $\mu$ -XRF (cpsCa).

$$k_j = \frac{1}{n} \sum_{i=1}^n \frac{wt\%Ca_{ij}}{cpsCa_{ij}}$$

**Formula 5.2.1:** Calculation of the mean normalization factor  $k$  between qBEI and Ca-K $\alpha$  fluorescence count rates.

$i$  = index of the bone matrix ROIs,

$j$  = index of the  $\mu$ -XRF maps,

$n$  = total number of marked bone matrix ROIs in map  $j$ ,

$ROI_{ij}$  = bone matrix ROI  $i$  of map  $j$ ,

$k_j$  = mean normalization factor of the SR  $\mu$ -XRF map  $j$ ,

$wt\%Ca_{ij}$  = averaged Ca concentration of bone matrix  $ROI_{ij}$  measured by qBEI,

$cpsCa_{ij}$  = mean Ca-K $\alpha$  fluorescence count rate in bone matrix  $ROI_{ij}$ ;

Thus, the multiplication of the SR  $\mu$ -XRF cps values of Pb, Zn, Sr from the individual maps with the corresponding factor  $k_j$  (see Formula 5.2.2) leads to a correction / normalization of all the maps based on the relation between the absolute Ca values as obtained by qBEI method and the fluorescence intensities.

$$cpsX_{ij, norm} = k_j \cdot cpsX_{ij}$$

**Formula 5.2.2:** Calculation of the normalized  $\mu$ -XRF count rates for each marked bone matrix ROI.

$i$  = index of the bone matrix ROIs,

$j$  = index of the  $\mu$ -XRF maps,

$n$  = total number of marked bone matrix ROIs in map  $j$ ,

$ROI_{ij}$  = bone matrix ROI  $i$  of map  $j$ ,

$X$  = element Ca, Zn, Sr or Pb

$k_j$  = mean normalization factor of the SR  $\mu$ -XRF map  $j$ ,

$cpsX_{ij}$  = mean fluorescence intensity of element  $X$  in bone matrix  $ROI_{ij}$

$cpsX_{ij, norm}$  = normalized  $\mu$ -XRF count rate of element  $X$  in bone matrix  $ROI_{ij}$ ;

### 5.2.1.3) Reliability of $k_j$ -Factor

The reliability of the normalisation of the X-Ray intensities using the  $k_j$ -factor can be verified based on the normalization of the Ca-K $\alpha$  intensities of each bone matrix ROI ( $cpsCa_{ij, norm} = k_j \cdot cpsCa_{ij}$ ). Due to the construction of the  $k$ -factor the normalized Ca fluorescence count rates ( $cpsCa_{ij, norm}$ ) should have a positive linear correlation with the real (qBEI obtained) Ca content (Fig 5.2.3). Deviations from the perfect correlation most likely

indicates an inhomogeneous Ca distribution just below the surface and hence an altered fluorescence signal.

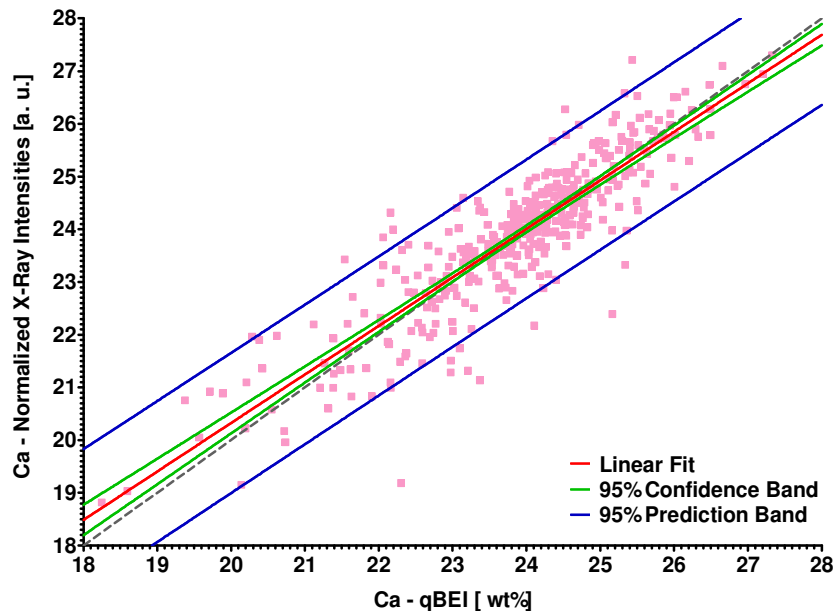


**Figure 5.2.3:** Normalized Ca XRF intensity values (formulas 5.2.1 & 5.2.2) plotted versus qBEI obtained absolute Ca content (wt%) of all bone matrix ROIs – one point per bone matrix ROI. In ideal case the points fit the grey dotted line. The red line is the linear fit of all data points, along with the 95% confidence band (green line) and the 95% prediction band (blue line).

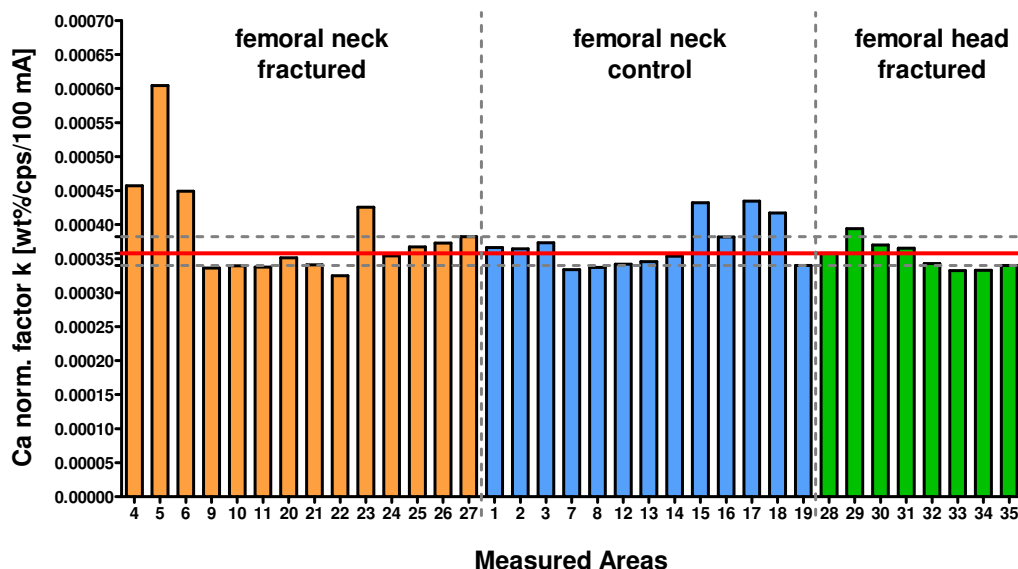


**Figure 5.2.4:** Mean normalization factors  $k$  between qBEI obtained Ca wt% and SR  $\mu$ -XRF Ca-K $\alpha$  intensities, calculated with Formula 5.2.1, for all measured maps grouped according to the sub sample sets. Further the median (red solid line) and the interquartil range (dark grey dotted line) are shown.



Further in an ideal case all k-factors should be equal (Fig. 5.2.4). Deviations are most likely the result of change in the Ca content just below the surface or a not perfectly determined plane of measurement. A larger k-factor indicates a reduced Ca content and a smaller k-factor a larger Ca content determined by SR  $\mu$ -XRF in the depth as expected by the surface qBEI data. This is caused by the big difference of the size of the detection volumes of the two methods ( $\mu$ -XRF:  $\sim 10 \times 10 \times 10 \mu\text{m}^3$ ; qBEI:  $\sim 1 \times 1 \times 1 \mu\text{m}^3$ ). Despite the observed deviations from the perfect case, the normalized Ca-K $\alpha$  intensities and the k-values indicate that the described normalization procedure leads to reasonable data.

### 5.3 Automated Data Analysis

When dealing with large data sets an (semi-)automated method to analyse the data can help saving time and reducing the risk that the results are biased by the evaluating scientist.

In case of the analysis of SR  $\mu$ -XRF data, particularly if dealing with trace elements, a good signal to noise ratio (SNR) is of interest. The SNR can be drastically improved by summing the data of pixel of similar regions. It is usually possible to segment a picture into a limited number of areas containing pixel showing a similar pattern on properties.

This can be achieved using multivariate image processing algorithms for

- a) eliminating redundancies
- b) distinguishing the significant information from random noise
- c) splitting the information into mutually orthogonal, non correlated, components.

For this purpose either

- 1) Clustering algorithms like K-Mean Clustering (KMC) or
- 2) a combination of Principal Component Analysis PCA followed by KMC

can be applied.

PCA is a useful statistical technique that has found application in fields such as face recognition and image compression, and is a common technique for finding patterns in data of high dimension.

All clustering methods employ a means of calculating the degree of similarity (distance in property space) between two of the objects to be clustered. In the case of  $\mu$ -XRF, the objects are pixels (index i) and their properties (index j) are either the net X-Ray intensities derived

from the spectrum of pixel  $i$  or the score values of that pixel on the equivalent principle component (PC) axes.

### 5.3.1) Principal Component Analysis - PCA

Principal Component Analysis (PCA) is a well known statistical technique of multivariate data analysis. It is a way of identifying patterns in data, and expressing the data in such a way as to highlight their similarities and differences. Since patterns in data can be hard to find in data of high dimension, PCA is a powerful tool for analysing data [133].

The central principal of this method is dimension reduction of a data set consisting of a large number of correlated variables, while preserving as much variation as possible existing in the data set by selecting the dimensions with the largest variations. This is achieved by a transformation to a new set of uncorrelated, orthogonal variables, the principal components (PCs), which are sorted in a way that the first few PCs obtain most of the variation present in all original variables [134]. In this lower dimensional data set coherent pattern can be detected more clearly. Such automated multivariate analysis is used in various areas, e.g. image processing [135]. PCA is commonly used in combination with K-means clustering, which is applied in the lower dimensional subspace generated by PCA [136].

A good explanation of the principals of PCA with simple examples, including the mathematical background, can be found in "A tutorial on Principal Components Analysis" by L. I. Smith 2002 [133].

### 5.3.2) K-Means Clustering

Cluster analysis [137-139] is an established statistical method to gain knowledge by subdividing multivariate data into disjoint groups (clusters), so that objects within the same cluster are similar with respect to certain properties. K-Means clustering (KMC) [140-142] is a widely-used and efficient clustering algorithm, which uses centeroids to represent clusters by optimizing the squared error function [135] and it assumes the number of clusters to be known a priori and equal to  $K$ . KMC is commonly used in cases where image segmentation is needed with the pixel intensity or colour as variable for clustering [143]. It could be shown that PCA dimension reduction is particularly beneficial for K-means clustering [135].

### 5.3.3) Applying PCA and KMC to $\mu$ -XRF Maps

Custom made software, developed and written by Stephan Smolek (Atominstitut TU Wien 2008), was used to analyse the  $\mu$ -XRF maps of rat bone sample set applying the above describe methods (see Chap 8.3.1). The human biopsy samples from a study focused on the Sr incorporation into bone were evaluated with a custom made PCA-KMC software developed and written by Martin Fölser (Atominstitut TU Wien 2008) [144].

The pre-treatment using PCA is not indispensable but allows for more rapid processing of the data set by eliminating noise and reducing dimensionality prior to the clustering (e.g. if more than two pixel properties, here X-Ray intensities of specific elements, are investigated). The clustering algorithm could also be applied to the X-Ray maps directly; however, in this case only images should be used showing high contrasts (low noise) which are appropriately scaled to each other. The approach using PCA to pre-process the data before KMC takes care of the noise removal and scaling problem.

In case of analysis Ca-K $\alpha$  and Sr-K $\alpha$  map-pairs, a number of four clusters proved to be sufficient for proper KMC results, as more than four clusters led to empty clusters in the result. PCA and KMC were performed for all samples. The classification of the clusters C1, C2, C3, C4 was done by considering their Sr count fraction values ( $\text{Sr}/(\text{Sr}+\text{Ca})$ ). C1 contains the lowest, and C4 the highest  $\text{Sr}/(\text{Sr}+\text{Ca})$  values. The result of such a clustering approach (after PCA pre-treatment) is displayed in Fig 5.3.1.

More details about PCA and KMC and their application to the analysis of  $\mu$ -XRF image sets can be found in "Automated Segmentation of Image Sets I-XRF" by B. Vekemans 1997 [145].

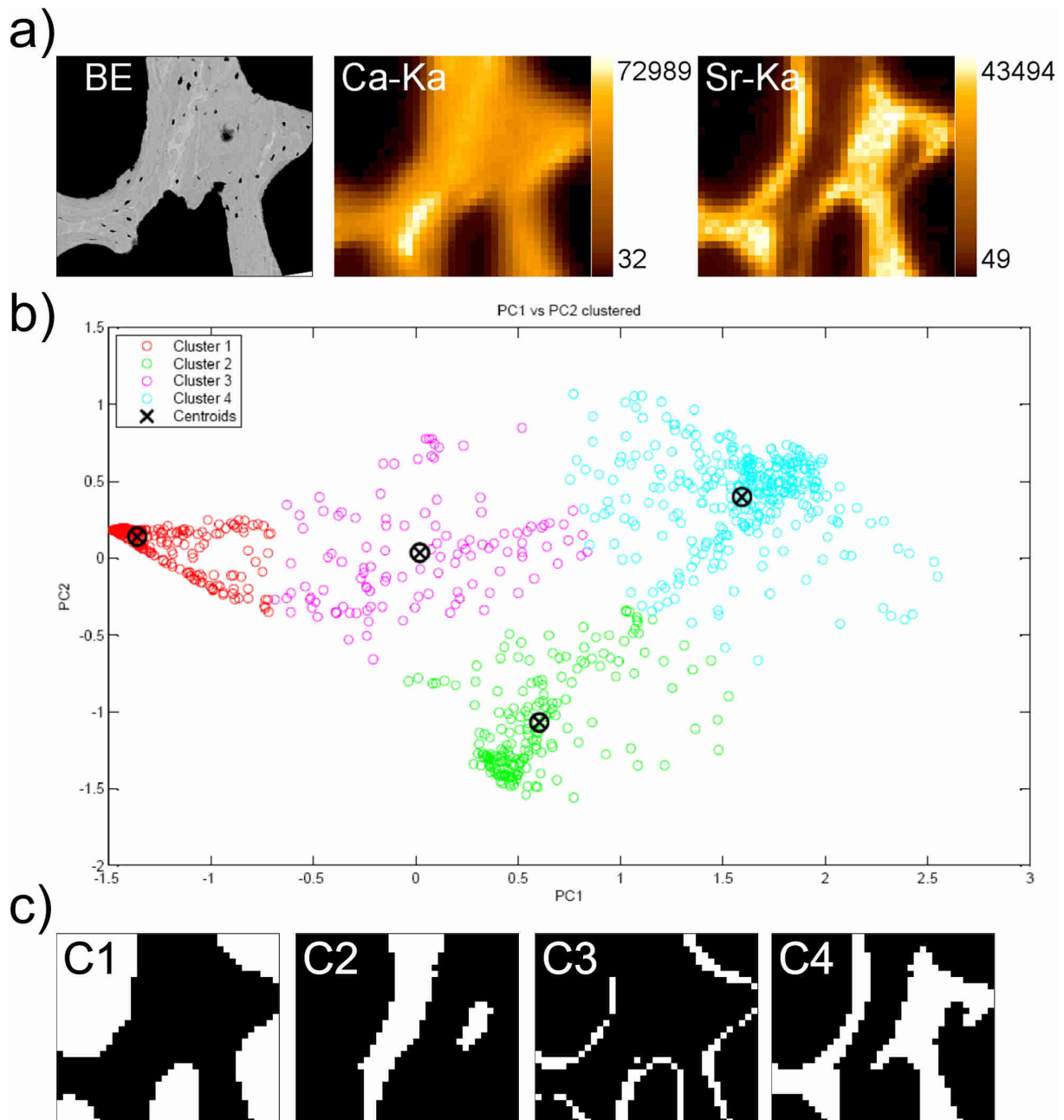


**Figure 5.3.1: Example of a PCA+KMC analysis: The scan was done on a rat bone sample with high dose SrR treatment at deficient Ca diet (P02; OTH51 scan 112; Chap. 8.3.1) [146].**

- a) qBEI and corresponding SR  $\mu$ -XRF maps of Ca and Sr.
- b) Score Plot of the Principal components PC1 and PC2 showing the different cluster centroids (cross) and the points belonging to each cluster in separate colours.
- c) Binary Cluster maps where all pixels corresponding to a certain cluster are displayed in white.

## 5.4 Statistics

Evaluating data from measurements and studies always involve the use of statistical methods, such as significance tests or correlation calculations, and parameters describing the data set, such as mean, median, standard deviation or interquartile range.

In the following a short description of the later used statistical methods and terms should be given. For more details, mathematical definitions and examples one of the many handbooks of statistics or statistic tutorials in the web can be used [147-152].

### 5.4.1 Measure of Central Tendency and Dispersion

A *measure of central tendency* is a central value or a typical value for a probability distribution [153], i.e. where on the numerical scale is the centre of the distribution placed.

In every day use it is often called an *average* or sometimes just the *centre* of the distribution. Typical (but not all) measures of central tendency are

- arithmetic mean
- median
- mode

The dispersion is used to describe how stretched or squeezed a distribution is, i.e. the variance within a data set. Typical (but not all) measures of dispersion are:

- standard deviation
- interquartile range (IQR)
- range
- mean difference

The choice of the *measure of central tendency* and dispersion is depending on the distribution of the data set.

If the data is distributed Gaussian like, arithmetic mean and standard deviation are appropriate descriptions.

In case of skew of distributed data, i.e. Poisson distributed, or if the data is likely to contain remarkable outliers, using the median and the (interquartile) range is the best way of describing the data set. The median is important in robust statistics, as it is the most resistant statistic. Statistics with high breakdown points are sometimes called resistant statistics. The median has a break down point of 50%, which means, that as long as not more than 50% the

data are rogue outliers, the median will not lead to arbitrary low/large result [148, 150, 151]. The effect of large outliers is shown in an example in Fig. 5.4.1.

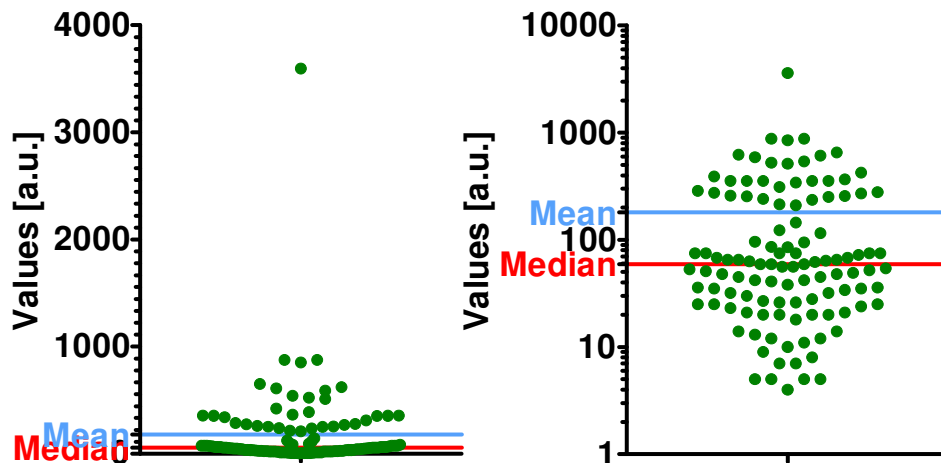


Figure 5.4.1: Influence of outliers on the central tendency - Mean, median, geometric mean.

"Definitions" of the used measures of central tendency and dispersion:

- **Arithmetic mean ( $\mu$ ):** usually simply called *mean*, the sum of all measured values divided by the total number of data points in the data set.

$$\mu = \frac{1}{N} \cdot \sum_{i=1}^N x_i$$

- **Standard deviation ( $\sigma$ ):** The square root of the mean of the squared differences of the values from their mean value.

$$\sigma = \sqrt{\frac{1}{N} \cdot \sum_{i=1}^N (x_i - \mu)^2}$$

- **Lower quartile (Q1):** sometimes denoted as 0,25- percentile; 25% of the data are below and 75% above this value
- **Median:** sometimes denoted as 0,5-percentile; divides the data set in half. 50% of the data are below and 50% are above.
- **Upper Quartile (Q3):** sometimes denoted as 0,75-percentile; 75% of the data are below and 25% above this value
- **Interquartile range (IQR):** difference between upper and lower quartile  $IQR = Q3 - Q1$ . The IQR contains 50% of the data. (see Fig. 5.4.2)
- **Range:** The range of a data set is defined by the smallest and the biggest values present in the data set. range:= [min; max].

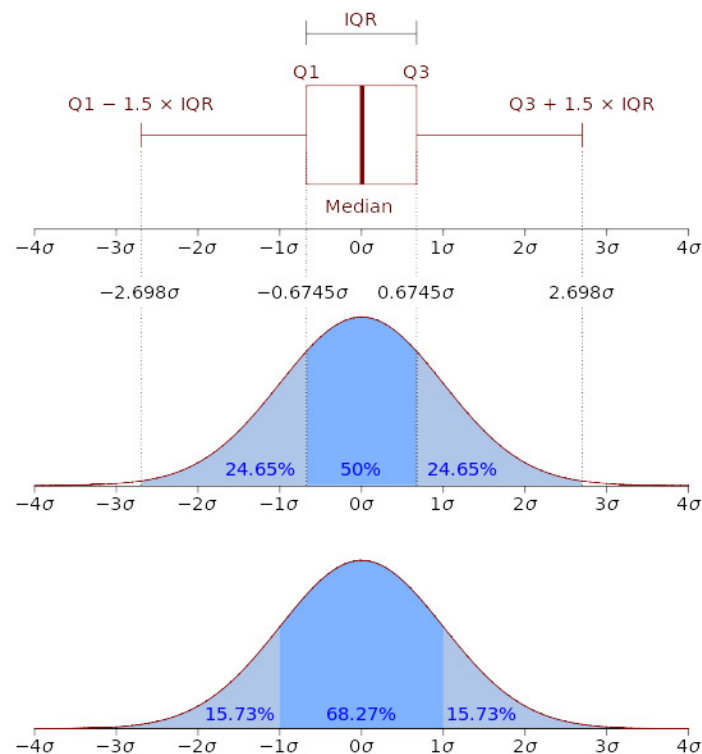


**Figure 5.4.2: Boxplot (with quartiles and an interquartile range) and a probability density function of a normal  $N(0, 1\sigma^2)$  population.**

**Q1:** first quartile, lower quartile or 0,25-percentile

**Q2:** second quartile, median or 0,5-percentile

**Q3:** third quartile, upper quartile or 0,75-percentile

**IQR:** Interquartile range ( $Q3 - Q1$ ) [154]

#### 5.4.2) Statistical Tests

Statistical tests are necessary to test if measured data fulfils a certain hypothesis, the so called "Null Hypothesis  $H_0$ ", with respect to a before selected certainty, the significance level  $p$ .

Common cut off values for  $p$  are 5% or 1%. If the  $p$ -value, calculated from the measured data, is smaller than the cut off value then the  $H_0$  can be accepted.

The names of the statistical tests are not unambiguous. One statistical test can be found under different names. E.g. the Mann-Whitney test is also named: Mann–Whitney U test, Mann–Whitney–Wilcoxon or Wilcoxon rank-sum test). In this thesis the names and descriptions, as used by the statistical data evaluation software using GraphPad Prism (v4.0c, GraphPad Software Inc., La Jolla, USA), will be taken [147].

- **t-test:** The two-sample t-test can be used to check if the means of two (not paired) measured data sets are different, belong to two different distributions, or if they are a measure of the same "theoretical" distribution  $N(\mu_0, \sigma_0^2)$ .

The one-sample t-test compares the mean  $\mu$  of a measured sample data set against a theoretical mean  $\mu_0$ ,  $H_0: \mu = \mu_0$ ;

Limitation: This test can only be used in case of Gaussian distributed data.

- **Mann-Whitney test:** The idea of the Mann-Whitney test is basically the same as for the t-test. However it's a more general, nonparametric, test and can be applied to any data set. Gaussian distribution is not required.

In the present case the test was used to compare the measured X-Ray intensity data of two different bone regions, i.e. check if they are different (two sample test).

- **Wilcoxon signed rank test:** This test is used to compare the median ( $m_S$ ) of one measured sample data set to a theoretical median ( $m_T$ ), thus  $H_0: m_S = m_T$ . The data set must consist of more than five values. It is assumed that the distribution of the data is symmetrical with respect to the median. A Gaussian distribution is not required.

It was used to test if the intensity ratios between two bone tissue type were different from a theoretical equal distribution.

**Non-parametric Spearman test:** This is a test for the strength of the (monochromatic) correlation of a paired set of values. The correlation coefficient  $r_S$  is a measure of the quality of the correlation. Due to the construction of the test  $r_S \in [-1, 1]$ .  $r_S = 1$  means perfect positive correlation and  $r_S = 0$  means the data is not monochromatic or uncorrelated. As the values of  $r_S$  get smaller the correlation becomes weaker.

This test does not require a Gaussian distributed data set. It is a nonparametric test. However it does not work with not monochromatic correlations.

This test came in handy when possible correlations between element levels and mineralization in bone matrix should have been tested.



## Chapter 6

# Experimental Setup and Sample Preparation

### 6.1 Synchrotron Beamlines at ANKA

The synchrotron radiation facility ANKA at the Karlsruhe Institute of Technology (KIT: Karlsruhe, Germany) operates since the end of the year 2000. It is a 2,5 GeV second generation storage ring with a radius of curvature of 5,559 m. The maximal design ring current (R-C) is 200 mA. Practically between 150 mA and 180 mA are reached. The R-C is decaying with time as ANKA has no "To-Up-Mode" and electrons are lost from the beam due to collisions with rest gas atoms and the walls. To inject electrons in the storage ring the beam has to be dumped and then an injection of electron can start.

Currently there are 16 beamlines at the site - some are still under construction [155].

#### 6.1.1) SUL-X Beamline[156]

The SUL-X ("Synchrotron Umwelt-Labor") synchrotron beamline at ANKA is designed to combine different hard X-Ray spectrometric methods, diffraction, absorption and fluorescence spectrometry with microfocus capabilities. This offers the possibility to obtain a detailed characterization of environmentally relevant materials.

The X-Ray source of SUL-X is 27 pole Wiggler operating at  $K=8,5$  (wiggler gap 16 mm). The primary energy can be adjusted with a double crystal monochromator (DCM) in fixed exit geometry. The available crystals and the respective theoretical energy resolutions ( $\Delta E/E$ ) are: Si(111)  $2 \cdot 10^{-4}$ ; Si(311)  $1 \cdot 10^{-4}$ ; YB<sub>66</sub>(004)  $5 \cdot 10^{-4}$ . An additional mirror pair allows the use of white light. Thus an energy range from 2,3 keV to 19 keV (S K-edge, U L<sub>3</sub>-edge) is possible.

Before and after the DMC a crystal mirror is placed to optimize the beam quality: A toroidal mirror is focusing horizontally and collimating vertically (Mirror 1) before and a cylindrical mirror with three coatings acting as a low energy band path with vertical focusing

characteristics is placed after the DCM (see Fig 6.1.1). The setup is equipped with a D-Mostab (Struck, Hamburg, Germany) to suppress the higher harmonics.

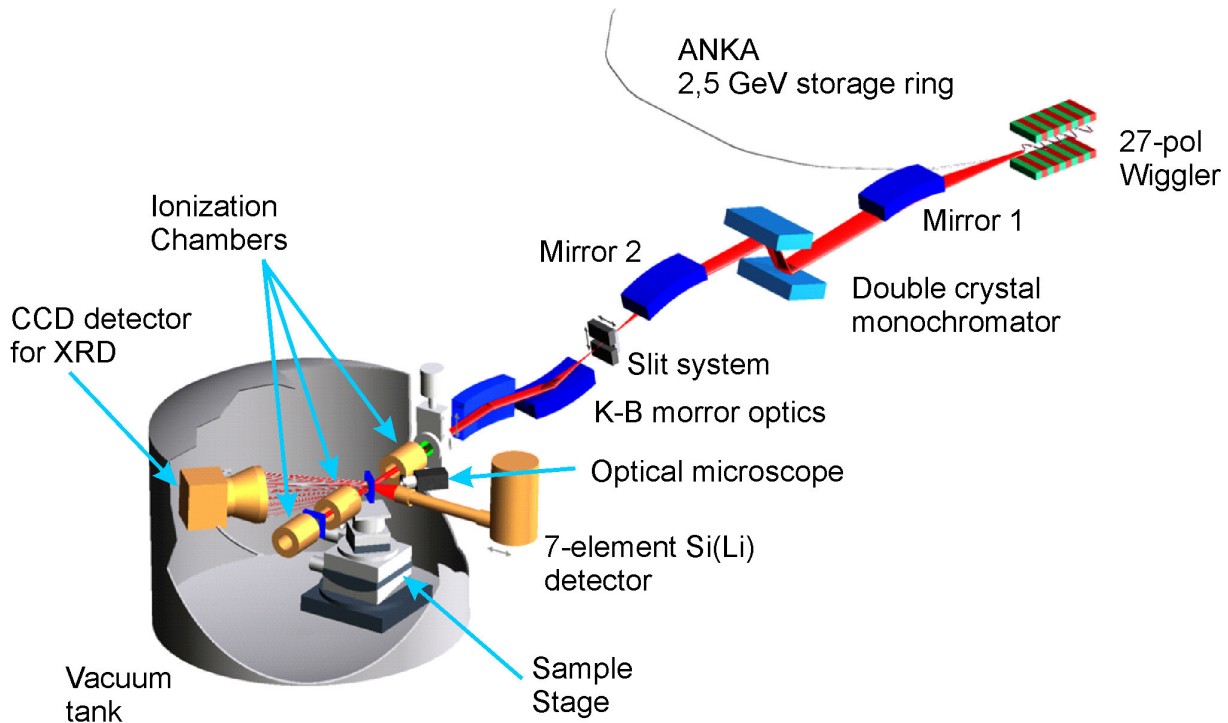


**Figure 6.1.1: Schematic illustration of the main SUL-X beamline components and the path of the primary radiation (adopted from [156]).**

A slit system allows defining a "new" source spot with variable size. The final focusing, of the new source spot, can be done with a Kirkpatrick Baez (K-B) mirror system. Hence beamsizes from about 1 mm (hor.) x 1 mm (vert.) down to 30  $\mu\text{m}$  x 25  $\mu\text{m}$  at the sample position are possible. At a beamsize of 0,2 mm x 0,1 mm (FWHM) at the sample the photonflux [ph/s/100 mA R-C] is about  $4 \cdot 10^{10}$  (@5keV),  $3 \cdot 10^{10}$  (@10keV) and  $3 \cdot 10^{10}$  (@20keV).

The fluorescence radiation is collected with a 7 element Si(Li) solid state detector (Gresham Scientific Instruments Ltd., now SGX Sensortech (MA) Ltd, Wooburn Green, UK) (Fig. 6.1.2) and a digital signal processing system (DXP: XIA LLC., Hayward, USA). In case of high fluorescence intensities the detectorarray is covered with Al layers in variable thickness.



**Figure 6.1.2: Snout of the 7-element Li(Li) [156].**

For absorption measurements in transmission mode and beam normalization three ionization chambers (IC-Plus: FMB Oxford Ltd., Oxford, UK) are available.

Diffraction experiments can be carried out with a charged coupled device (CCD) detector mounted on a  $2\theta$  arm.

The sample stage allows all movements necessary for a diffractometer, with  $\theta$ ,  $\varphi$  circle and  $\chi$  cradle ( $10^\circ$ ), including a xyz-stage.

All detection and sample positioning components are mounted within a huge vacuum tank (Fig. 6.1.3). Thus the samples can be measured under controlled environmental conditions, high vacuum (down to  $\sim 10^{-5}$  mbar) or gas atmosphere ( $N_2$ , Ar,)

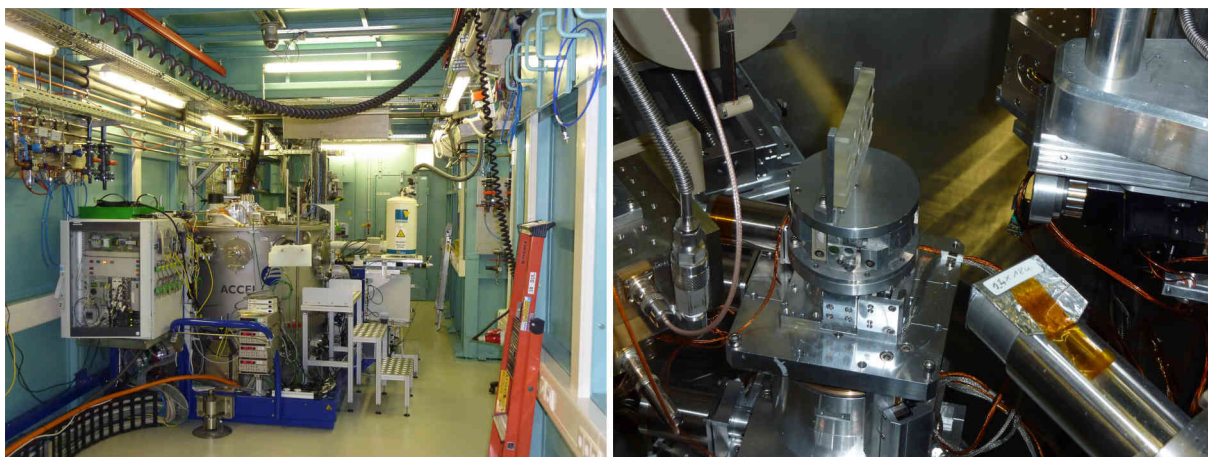


**Figure 6.1.3: SUL-X hutch with vacuum tank (left) and sample stage with detector, optical microscope, entering slit for primary beam, and a set of pellet samples (right).**

### 6.1.2) XAS Beamline [157]

The XAS (X-Ray Absorption Spectrometry) synchrotron beamline at ANKA is dedicated to XAS measurements either in transmission or fluorescence mode.

## Experimental Setup and Sample Preparation

The X-Ray source of the ANKA XAS beamline is a 1,5 T bending magnet with a critical energy  $E_c=6$  keV. The fixed exit DCM of the XAS beamline can be either used with Si(111) or a Si (311) crystal pair. The energy resolution ( $\Delta E/E$ ) is  $2 \cdot 10^{-4}$  and  $1 \cdot 10^{-4}$  respectively. To suppress the higher harmonics a D-Mostab (Struck, Hamburg, Germany) and panar Zerodur mirror are used. The XAS offers an energy range from 2,4 keV to 27 keV (S K-edge, Cd K-edge, U L-edge,).

A beamsize, adjusted with a slit system, from about 20 mm (hor.) x 2 mm (vert.) down to  $1 \mu\text{m} \times 1 \mu\text{m}$  at the sample position is possible. At a beamsize of typically 8 mm x 1 mm at the sample the photonflux [ph/s/mm<sup>2</sup>] at 9 keV using the Si (111) and 140 mA R-C is about  $1.0 \cdot 10^{10}$  (@9keV)

The fluorescence radiation is collected with a 5 element Ge solid state detector (Canberra Industries Inc., Meriden, USA) combined with the digital signal processing system (DXP: XIA LLC., Hayward, USA). For absorption measurements in transmission mode and beam normalization three ionization chambers (IC-Spec: FMB Oxford Ltd., Oxford, UK) are available. A schematic of the beamline is shown in Fig. 6.1.4.

To avoid beamdamage a closed cycle He cryostat (Oxford Instruments plc, Abingdon, UK) is available to keep the samples at a constant temperature (15 K to 320 K in 0,1 K steps).

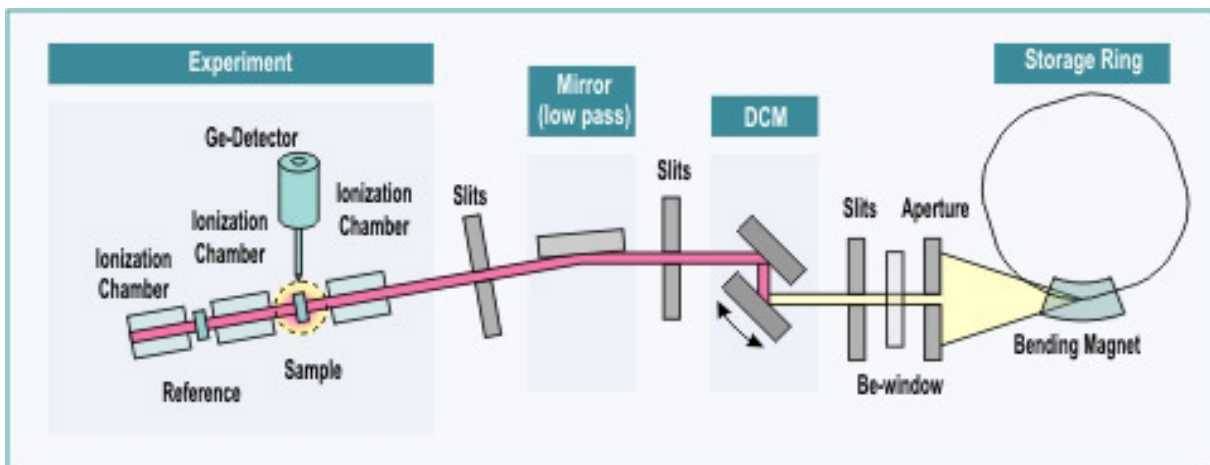


**Figure 6.1.4: Schematic illustration of the main XAS beamline components and the path of the primary radiation [157].**

### 6.1.3) FLUO Beamline [158]

The FLUO (FLUOrescence) synchrotron beamline at ANKA is dedicated to hard X-Ray fluorescence spectrometry in total reflection (TXRF) or microanalysis ( $\mu$ -XRF) mode.

The X-Ray source of the ANKA FLUO beamline is a 1,5 T bending magnet with a critical energy  $E_c=6$  keV. The primary energy can be adjusted with a double multilayer monochromator (DMM) in fixed exit geometry. The available W/Si multilayers has a 2,7 nm period and the respective theoretical energy resolutions ( $\Delta E/E$ ) is:  $2 \cdot 10^{-2}$ . Also the use of white light is possible. The energy range is reaching from 1,5 keV to 33 keV. The primary beam can be adjusted with a slit system and for further focusing the user can choose between a polycapillary half lens (XOS X-Ray Optical Systems Inc., East Greenbush, USA)[67], a compound refractive lens (CRL) or a Fresnel zone plate. The fluorescence radiation can be focused with a second - matched pair - polycapillary half lens from XOS, or a simple collimator. Depending on the focusing optics beamsizes from about 5 mm (hor.) x 2 mm (vert.) down to  $2 \mu\text{m} \times 1 \mu\text{m}$  at the sample position are possible. The beamsizes can be characterised by means of  $4 \mu\text{m}$  thick Au micro structures. The flux at the sample position using the polycapillary half lens is about  $1 \cdot 10^{11}$  ph/s at 17 keV primary energy and a spot of about  $12 \mu\text{m} \times 12 \mu\text{m}$ , and  $2 \cdot 10^9$  ph/s at 17 keV and a spot of  $5 \mu\text{m} \times 2 \mu\text{m}$  using the CRL.

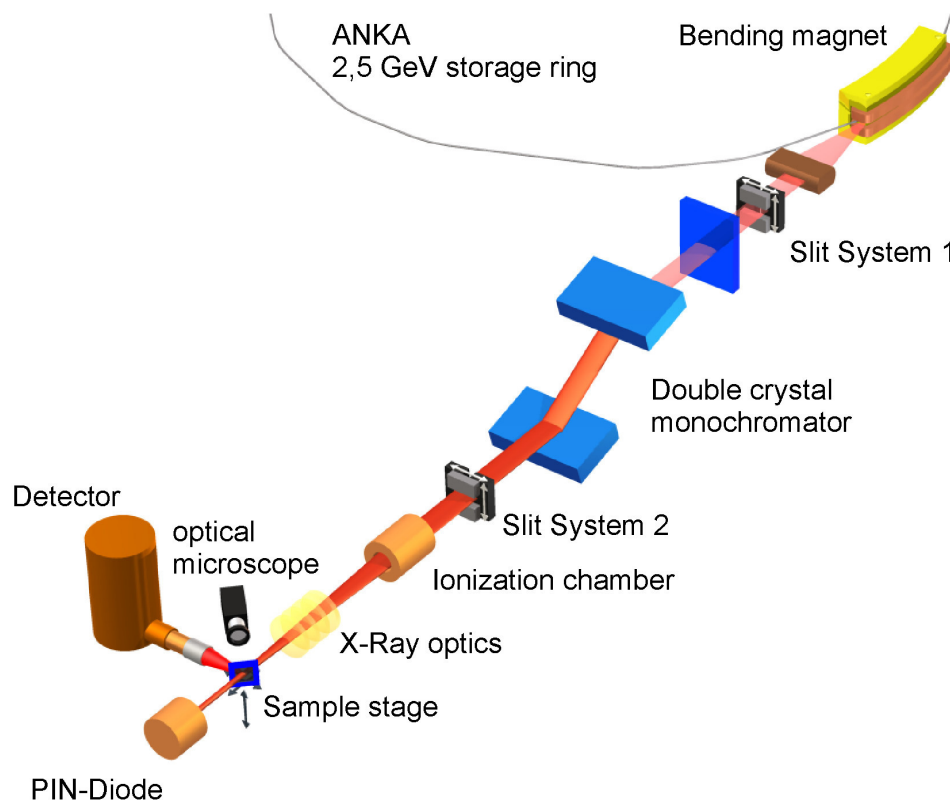


**Figure 6.1.5: Schematic illustration of the main FLUO beamline components and the path of the primary radiation (adopted from [159]).**



## Experimental Setup and Sample Preparation

The measurement position on the sample is controlled with an optical microscope, with a very shallow depth of field (DOF), just a few microns.

The main detector is a 50 mm<sup>2</sup> silicon drift detector (SDD) (Vortex: Radiant Detector Technologies Inc., now Hitachi High-Technologies Science America Inc., Northridge, USA) connected to a digital signal processor (DXP Saturn: XIA LLC., Hayward, USA). Further a Si(Li)-energy dispersive detector (Oxford Instruments plc, Abingdon, UK) and a HPGe-High Purity Germanium detector (Princeton Gamma-Tech Instruments (PGT), now Thermo Fisher Scientific Messtechnik GmbH, Erlangen, Germany) are available.

To monitor the primary beam an ionization chamber (OXFORD) before the X-Ray optics (see Fig. 6.1.5) and additional PIN-Diodes are available.

At the moment there is no equipment to measure in vacuum installed at the FLUO beamline. But a samplechanger for 8 samples is in operation.

In Fig. 6.1.6 photos of the confocal setup, that was used for the measurements presented in Chap. 8, is shown as an example.

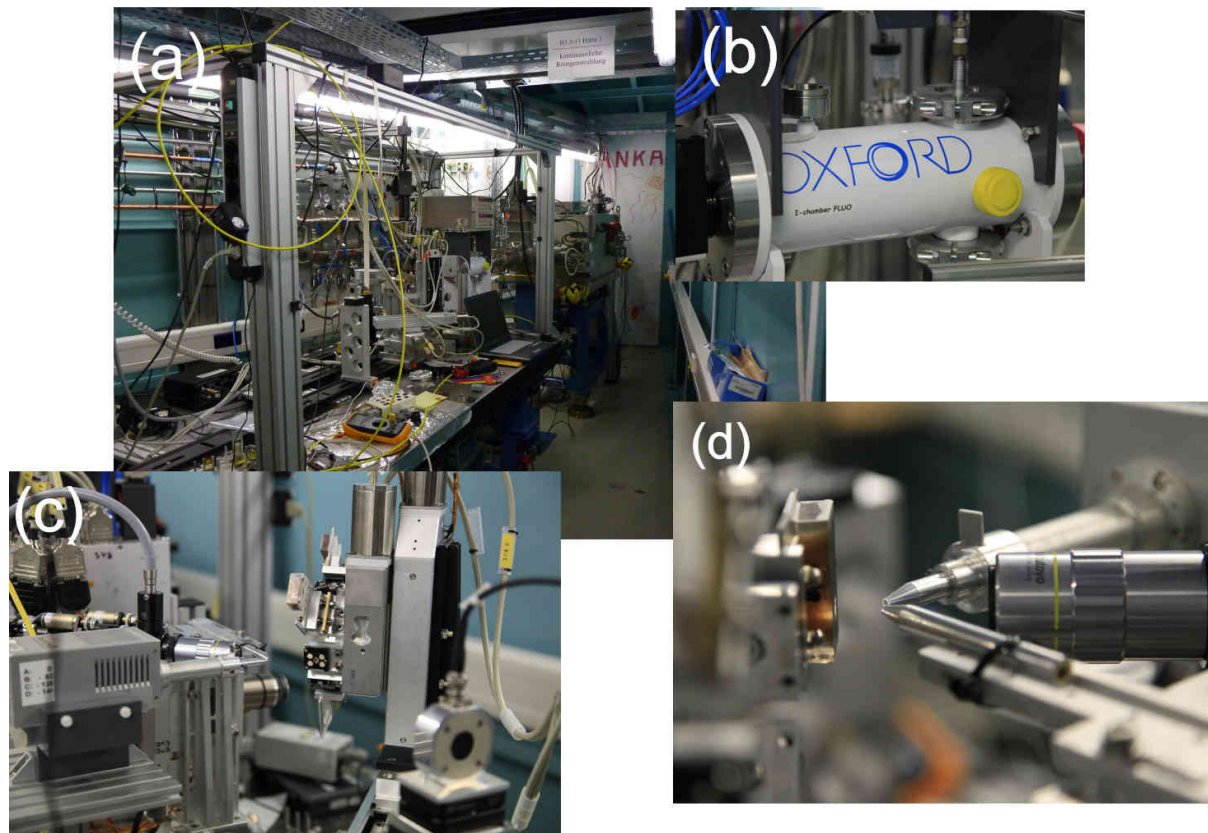


**Figure 6.1.6: The FLUO beamline at ANKA. (a) overview, (b) primary beam monitoring ionchamber, (c) samplechanger and confocal setup, (d) close view of the polycapillaries, optical microscope and a sample.**

## 6.2 Laboratory $\mu$ -XRF Setup at Atominstitut

The confocal  $\mu$ -XRF setup in the laboratory at Atominstitut uses an air cool low power 50 W (50 kV and 1 mA) X-Ray tube (Apogee: Oxford Instruments plc, Abingdon, UK) with a Mo anode. It features a 125  $\mu\text{m}$  thin Be window, allowing the use of the Mo-L lines additional to the Mo-K lines. A small spot of 35  $\mu\text{m}$  on the anode is ideal in combination with a focusing polycapillary. The two polycapillary X-Ray optics (XOS X-Ray Optical Systems Inc., East Greenbush, USA)[67], a full lens in front of the X-Ray tube and a half-lens in front of the detector, are a matched pair (see Fig 6.2.1a). They are both placed on a xyz-motorstage (each on a 2x ANPx101, 1x ANPz101: attocube systems AG, München, Germany). The nominal focus size of the primary capillary for Mo-K $\alpha$  is about 30  $\mu\text{m}$ . The actual resolution was tested with a cross made out of a 10  $\mu\text{m}$  Cu wire (Fig. 6.2.2) revealing a lateral beam size of about 50 x 50  $\mu\text{m}^2$  and a depth resolution of 50  $\mu\text{m}$ .

An optional primary beam filter (e.g. 100  $\mu\text{m}$  Al) can be placed between X-Ray tube and the primary polycapillary.

The samples are mounted on a motorized xyz stage (3x M112.12S: Physik Instrumente (PI) GmbH & Co. KG, Karlsruhe/Palmbach, Germany) with 25 mm travel distance in each direction and a step resolution of less than 1  $\mu\text{m}$ .

The measurement position on the sample is controlled with an optical microscope (M Plan APO: Mitutoyo Corporation, Kawasaki, Japan) combined with a CCD camera (Marlin: Allied Vision Technologies GmbH, Stadtroda, Germany).

The fluorescence radiation is detected with an 30 mm<sup>2</sup> Si(Li) (Gresham Scientific Instruments Ltd., now SGX Sensortech (MA) Ltd, Wooburn Green, UK) equipped with an ultra thin AP1.4 300 nm polymer window. An analogue pulsprocessor (TX 1255, Tracor Northern ) in combination with an MCA (MCA8000A: Amptek Inc., Bedford, USA) is used for signal processing.

The polycapillaries and the samplestage are placed in a cylindrical vacuum chamber (see Fig 6.2.1b).

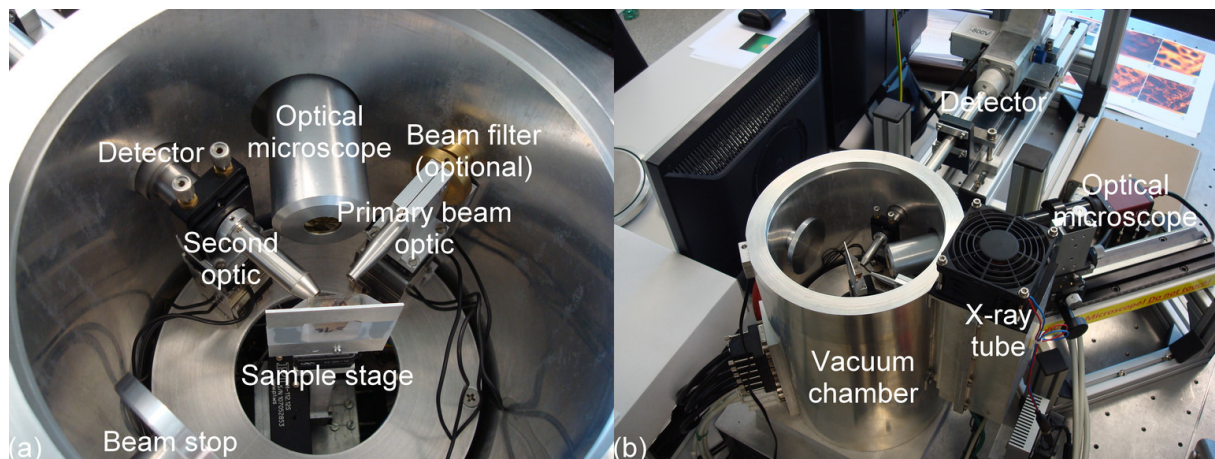


**Figure 6.2.1: Confocal  $\mu$ -XRF setup at the Atominstitut: (a) Components inside the vacuum chamber, (b) Vacuum chamber and outside components [74].**

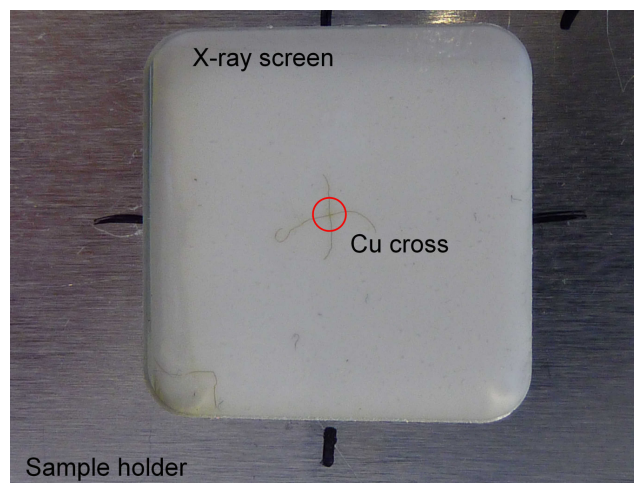


**Figure 6.2.2: Self made Cu cross to determine the beamsize [74].**

### 6.3 SEM at LBIO Lab at UKH Meidling

For the qBEI, the BE data of the solid state detector of a SEM (DSM 962: Carl Zeiss AG, Oberkochen, Germany) were evaluated. The filament current of 3,4 A was heating a hairpin cathode (details see [80] Chap. 3.4) made of tungsten (W). An electron acceleration voltage of 20 kV was chosen and the probe current (current of the PEs) was maintained at 110 pA. The working distance (objective lens - sample) was 15 mm. The vacuum in the measurement chamber was kept below  $10^{-7}$  mbar. In addition this SEM offers the possibility of SE analysis with an E-T detector and EDX measurements (Fig. 6.3.1).

The magnification of the SEM was adjusted according to the needs of the respective study. Detailed measurements were made at 200-fold magnification leading to a lateral pixelsize of  $0,88 \times 0,88 \mu\text{m}^2$ , overviews with a 12-fold magnification.



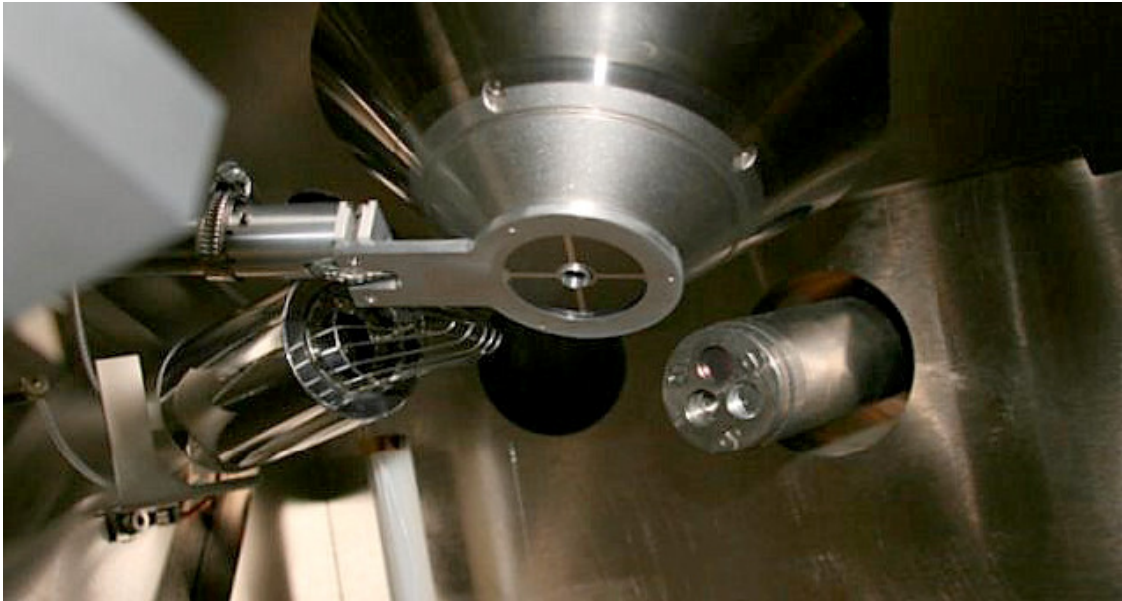


**Figure 6.3.1: Measurement vacuum chamber of the SEM (DSM 962) at the LBIO lab in UKH Meidling. A solid state detector is mounted around the primary beam entrance (centre), a E-T detector is placed on the left side (faraday-cage visible) and an X-Ray detector on the right side (detector snout and Be window are visible) [80].**

The intensity of the BE from the sample surface is proportional to the average atomic number of the target material (Chap. 3.3.1), producing a material contrast. This is essential for the quantitative analysis. The backscatter signal of bone tissue, composed of an organic phase (average atomic number  $Z_{av} \approx 6$ ) and a mineral phase - CCaHA (average atomic number  $Z_{av} \approx 13,86$ ) is dominated by the Ca (atomic number  $Z=20$ ) weight fraction. qBEI can determine the local mineral content in bone with a information depth of  $\sim 1 \mu\text{m}$  [56]. The calibration of the setup for the quantification of Ca content in bone was done with pure C ( $Z=6$ ) and Al ( $Z=13$ ). The grey values of the pixels in the qBEI images can range from 0 to 254 (8-bit), corresponding to the measured BE intensity. One grey level step in the analysis of bone samples corresponds, with this calibration, to a change of the Ca content of 0,17wt% Ca.

In qBEI images areas with bright gray levels reflect well-mineralized matrix with high Ca content, whereas areas with dark gray levels indicate low mineral density.

Younger bone packets /osteons have a characteristic lower mineral content (darker qBEI grey level) than older more mature bone packets /osteons. An example of a cortical bone section can be seen in Fig. 6.3.2.

More details on this method can be found elsewhere [21, 85, 160]

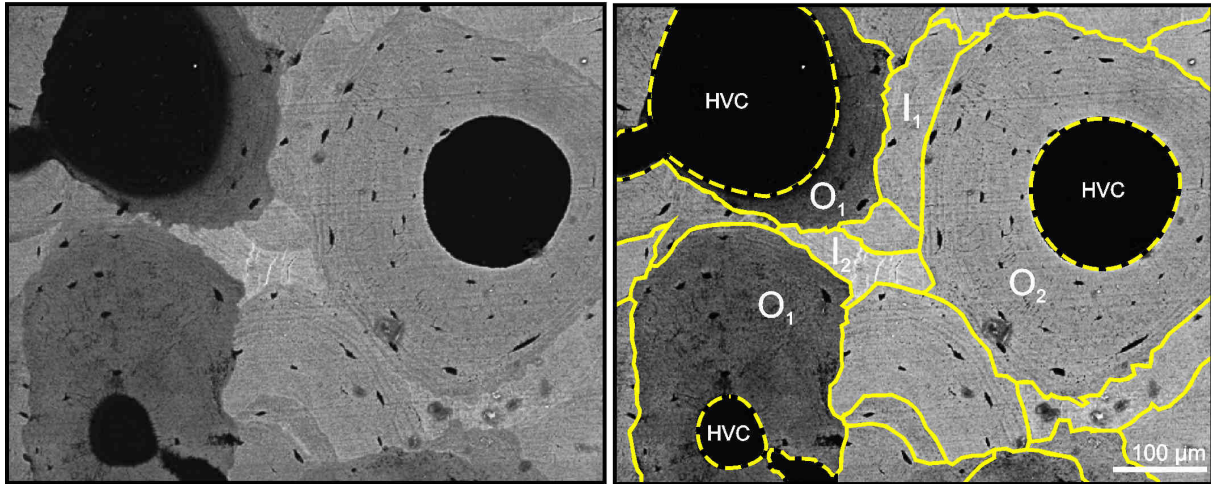


**Figure 6.3.2: Backscattered electron image of a human femoral neck (sample FNX8-A1; OTH69 scan 73; Chap. 8.2) showing osteoids, newly formed weak mineralized ( $O_1$ ) and higher mineralized ( $O_2$ ) in the cortical bone region. Further interstitial bone of various degrees of mineralization can be identified:  $I_1$ : low,  $I_2$ : high**  
The yellow solid lines mark the borders between bone osteoids /interstitial bone, the cement lines. The dotted yellow lines represent the boarder between osteoid and haversian channels. The small black longish holes within the osteoids /interstitial bone are osteocyte lacunae.

## 6.4 Sample Preparation

The bone sample - rat vertebrae (Chap. 8.3.1.1), femoral necks and head (Chap. 8.2.2), patellae (Chap. 8.1.2) - were fixed in 70% ethanol, dehydrated through a graded series of ethanol, and embedded undecalcified in polymethylmethacrylate (PMMA) [21]. The PMMA blocks containing the bone samples were cut using a low speed diamond saw (IsoMet: Buehler - ITW Test & Measurement Group, Lake Bluff, USA). Fig 6.4.1 shows an image of a prepared sample block. All sample section surfaces were ground by sand paper and subsequently polished using a diamond suspension (3 and 1 micron grain size) on a precision polishing device (PM5: Logitech Ltd., Glasgow, UK), except five of the femoral head samples, these were treated with a diamond fraises (SP2600: Leica Microsystems GmbH, Wetzlar, Germany). Fig. 6.4.2 shows microscope images of a polished sample and one treated with the fraises.

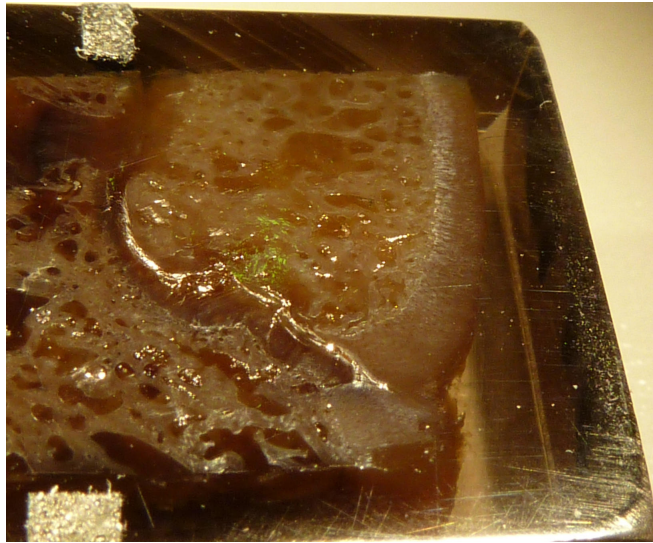


**Figure 6.4.1: Bone sample of the osteochondral region embedded in PMMA and carbon coated (CYX6; BIO5; Chap. 8.2).**

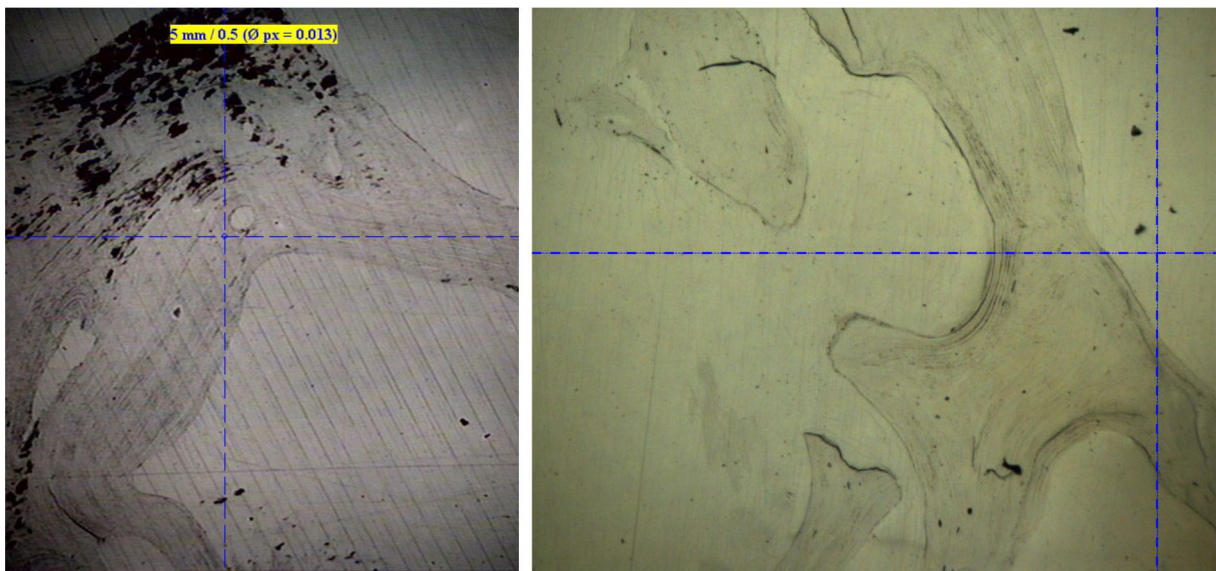


**Figure 6.4.2: Microscope images of a bone sample polished the conventional way (right; FNX6B-A1; OTH73 scan 113; Chap. 8.2) and treated with the diamond fraises (left; CYX6-E; BIO5 scan 60; Chap. 8.2). The pictures were taken in the SR  $\mu$ -XRF setup - the centre of the blue cross denotes the beam position.**

Finally the polished sample surface was carbon coated (SEM Carbon Coater: Agar Scientific Elektron Technology UK Ltd, Stansted, UK) for BE measurements. Due to the ultra low thickness (some 10 nm) and the low atomic weight of the carbon layer, it does not influence the  $\mu$ -XRF measurements.

The PMMA blocks were mounted on a specimen holder with a sticky carbon tape for qBEI analysis and with double sided sticky tape on the sample holder at the FLUO beamline.



Contaminations with Fe were inevitable since the use of steel tools in the sample preparation process is necessary. Typically the steel contaminations were found in holes and cracks in the PMMA and could be identified through the coincidence of high Cr, Ni and Fe intensities (see Fig. 6.4.3). With help of these markers the contaminated areas could be easily excluded in the further data evaluation process.

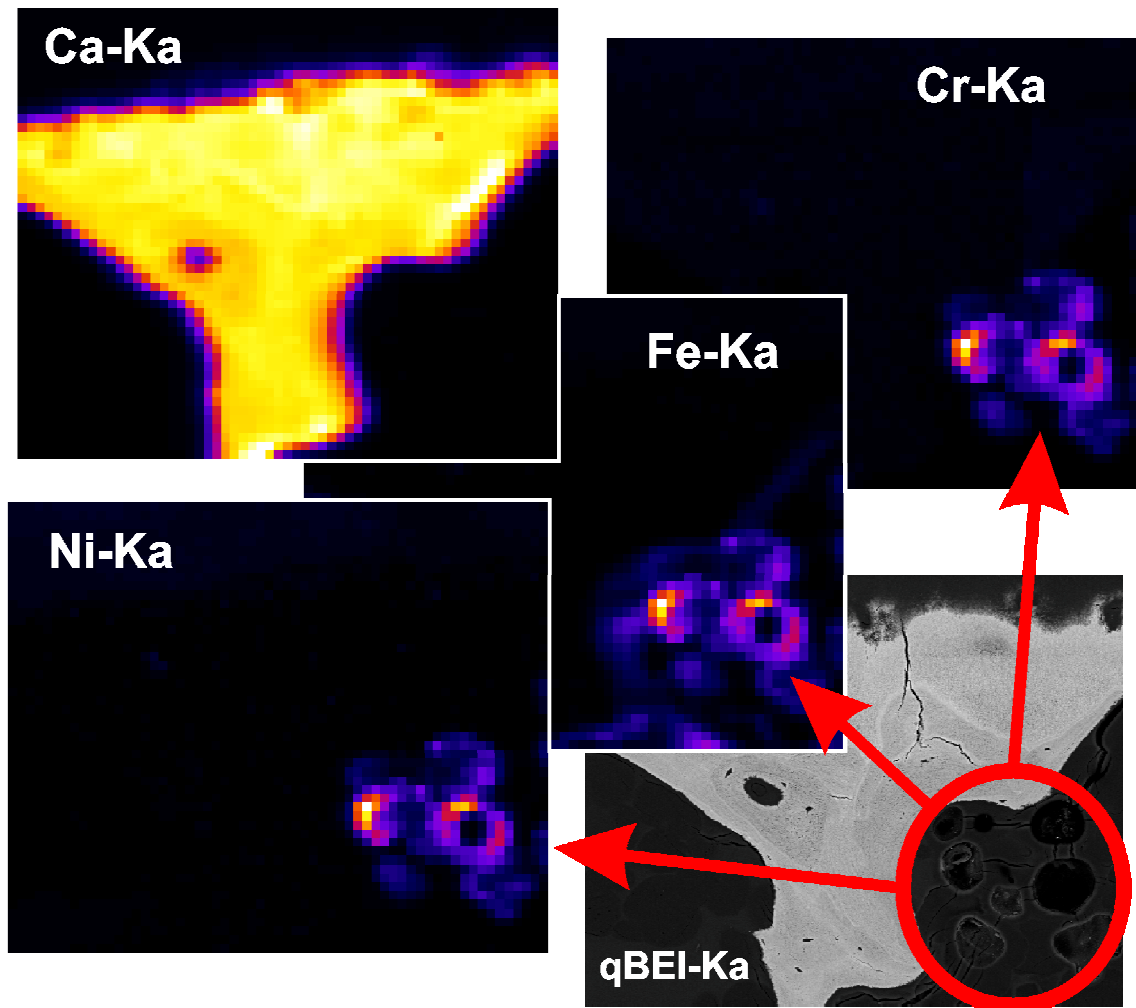


**Figure 6.4.3: Illustration of steel contaminations found in holes in the PMMA next to the bone (Sample CYX10-B, BIO5 scan 120).**

The red circle is highlighting these holes in the PMMA in the qBEI image (bottom right).

## Chapter 7

# Stability and Reliability Check of Normalisation to the Ring-Current at ANKA FLUO Beamline

### 7.1 Introduction

As described in Chap. 6.1 the ring current of the ANKA storage ring decays with a constant rate due to collisions of the beam electrons with remaining gas molecules. Hence a correction of the recorded  $\mu$ -XRF data is obligate. This can be either done by normalization of the recorded fluorescence radiation to the ring current or the signal of the ion chamber placed in the primary beam (see Fig. 6.1.5 Chap. 6.1.3).

Within the last  $\mu$ -XRF projects the obtained elemental  $\mu$ -XRF maps have been normalized to the ring current of the synchrotron. However it has not been tested if this normalization yields reasonable results.

The other goal was to test the "auto shutter" feature of the FLUO beamline (see Chap. 6.1.3), which offers the possibility of measuring  $\mu$ -XRF maps over injections, which was not possible before. Using this feature would allow to make a more efficient use of the scheduled beamtime. Since the discontinuous change of the ring current at some point(s) within a map the reliability of the normalization is required. Further the beam needs to be stable after the shutter has opened.

Normally there are tiny fluctuations of the orbit of the electrons bunches in the storage ring directly after the injection has finished. The operation crew of the synchrotron usually sends the "open" command for the "auto shutter" after the fluctuations faded away. However the possibility remains that the shutter is opened too early and this may affect the quality of the  $\mu$ -XRF map currently measured.

The check of the reliability of the normalization of the fluorescence intensities to the ring current and the stability check when measuring over an injection were done in two steps. On the one hand the normalization was tested with repetitive measurements of a standard reference material (AXO RF4 thin film standard) over a long period during normal user

operation - between two injections. On the other hand two real samples (human bone samples), which had been measured over an injection were evaluated with respect to normalization and stability of the setup. This was achieved by comparing the Ca-K $\alpha$  and the scatter intensities of comparable bone areas before and after the injection.

The  $\mu$ -XRF maps of human bone samples used for the following discussion on the reliability of measurements over an injection were part of a comprehensive study on the distribution of trace elements in human bone, presented in Chap. 8.2.

## 7.2 Repetitive Measurements of a AXO Thin Film Reference Sample

### 7.2.1) Instrumentation and Measurement Parameters

The stability measurement was performed with the same setup that was used for the analysis of the femoral neck bone samples (see Chap. 8.2).

A confocal SR  $\mu$ -XRF setup at the micro focus end-station at the FLUO beamline was used (see Chap. 6.1.1). The lateral beamsize was 17  $\mu$ m x 12  $\mu$ m (horizontal x vertical) and a depth resolution 19  $\mu$ m at 9.71 keV (Au-La). The excitation energy was set to 17 keV.

A "*timescan*" at one position of the RF4 standard was performed for about  $t=4,6$  h, covering almost the period between two injections. The counting time for each spectrum was set to 1 s, which was sufficient for the elements present on the sample. In total  $n=16785$  spectra were recorded. Besides the spectrum data many other parameters of the setup, including the ring current and the values of the primary ionization chamber, are logged.

### 7.2.2) Sample

The RF4, a thin film standard reference sample from AXO (AXO DRESDEN GmbH, Dresden, Germany), which is available at the FLUO beamline was used. The elements and the corresponding nominal concentrations<sup>3</sup> present on the reference standard are listed in Tab. 7.2.1. In Fig 7.2.1 the first spectrum (green) and the sum of the first 21 spectra (red) are shown.

---

<sup>3</sup> An official certificate was not available. Only a list showing the quantitative results from a round robin with different methods, with the final "official" values highlighted, was available.

**Table 7.2.1: Elements and nominal concentrations<sup>3</sup> of AXO RF4 thin film standard reference material available at ANKA FLUO beam line.**

Element	<sup>20</sup> Ca	<sup>26</sup> Fe	<sup>29</sup> Cu	<sup>42</sup> Mo	<sup>46</sup> Pd	<sup>57</sup> La	<sup>82</sup> Pb
Concentration [ng/mm <sup>2</sup> ]	19,31 ±1,10	5,04 ±0,87	2,84 ±0,35	1,32 ±0,40	1,00 ±0,00	11,01 ±0,62	7,61 ±0,96

### AXO RF4 Thin Film Standard

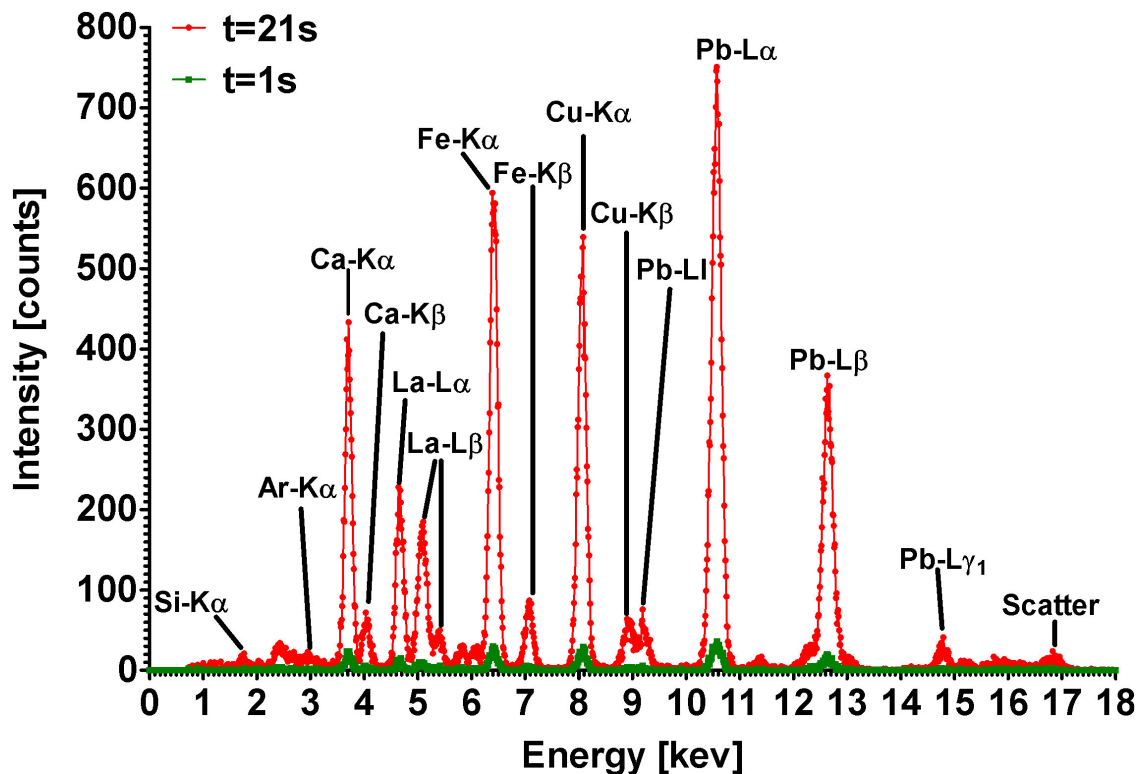


**Figure 7.2.1: AXO RF4 thin film reference sample measured at ANKA FLUO beamline with confocal setup. Two spectra, the first one (acquisition time  $t=1$  s) (green line) and the sum of the first 21 spectra (total acquisition time  $t=21$  s) (red line) are shown (OTH69 scan 148).**

#### 7.2.3) Data Evaluation

Due to the very small spectral background the Pb-L $\alpha$  line (10,55 keV), the biggest fluorescence line in the spectrum (see Fig. 7.2.1), was evaluated using a ROI (10,20 - 10,80 keV). This was considered sufficient, to check the stability of the beamline and the normalization to the ring current or the ionization chamber values. The normalization was performed by dividing each intensity value with the corresponding ring current or ion chamber value. The data evaluation and normalization calculations were done with Microsoft Excel 2003 and statistical analysis - e.g. calculating regression functions - was performed with GraphPad Prism (v4.0c, GraphPad Software Inc., La Jolla, USA).

#### 7.2.4) Results & Discussion

The ring current (Fig. 7.2.2b) as well as the ion chamber signal (Fig. 7.2.3a) are decreasing exponentially, as it was expected. Since the fluorescence intensity is direct proportional to the ring current (Fig. 7.2.4) the fluorescence intensity was also decreasing exponentially (Fig. 7.2.2a). About 99% of the Pb-L $\alpha$  intensity values deviate less than 10% from the fitted exponential function. This variation is due to the statistical effects during the detection process.

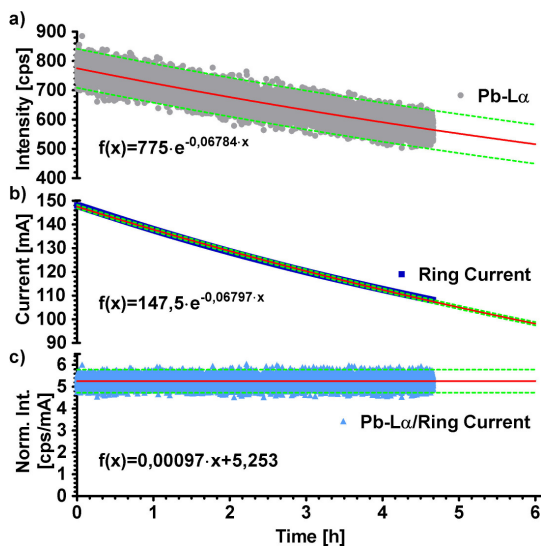


**Figure 7.2.2: Ring current normalization: Time dependency of the count rates and ring current at the ANKA FLOU beamline for 16785 repetitive measurements (t=1 s) at the same position on the AXO RF4 thin film reference sample.**

a) ROI fluorescence data for Pb-L $\alpha$ , b) Ring current of synchrotron ANKA, c) Pb-L $\alpha$  fluorescence intensity normalized to the ring current. For all graphs the exponential / linear regressions (solid red line) and 95% prediction bands (dotted green line) of the data are shown.

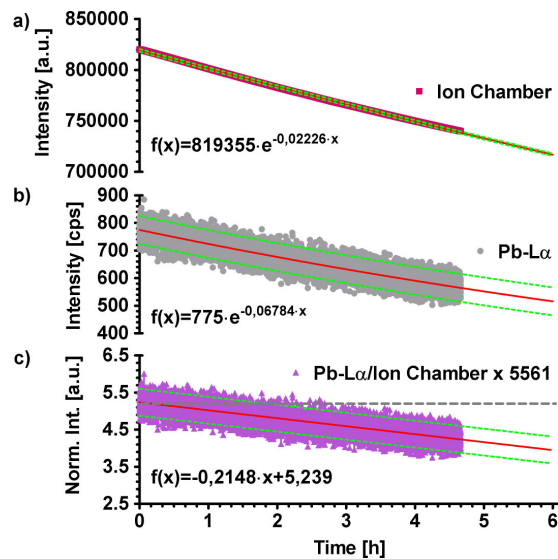


**Figure 7.2.3: Ion chamber normalization: Time dependency of the count rates and ring current at the ANKA FLOU beamline for 16785 repetitive measurements (t=1 s) at the same position on the AXO RF4 thin film reference sample.**

a) ROI fluorescence data for Pb-L $\alpha$ , b) Signal of primary ion chamber of the FLUO beamline, c) Pb-L $\alpha$  fluorescence intensity normalized to the ion chamber signal and multiplied by 5561 with a slope is significantly different from zero (dotted grey line).

For all graphs the exponential / linear regressions (solid red line) and 95% prediction bands (dotted green line) of the data are shown.



In an ideal situation the rate of decay would be the same for the ring current, the ion chamber signal and the fluorescence intensity. This would lead to a horizontal regression line of the normalized data. However, when taking a look at the fluorescence data normalized to the ring current (Fig 7.2.2c) and the ion chamber signal (Fig. 7.2.3c) one can easily see that the ring current normalization is in very good agreement the assumption, the normalization to the ion chamber signal on the other hand is quite poor.

The calculated difference between the decay constants of the fluorescence intensity and the ring current is  $\Delta\lambda_{R-C} = 1,3 \cdot 10^{-4}$  and  $\Delta\lambda_{I-C} = -0,046$  for the ion chamber signal, respectively. Thus normalization to the ion chamber signal will not be further considered as additional correction functions would be necessary to obtain a good normalization.

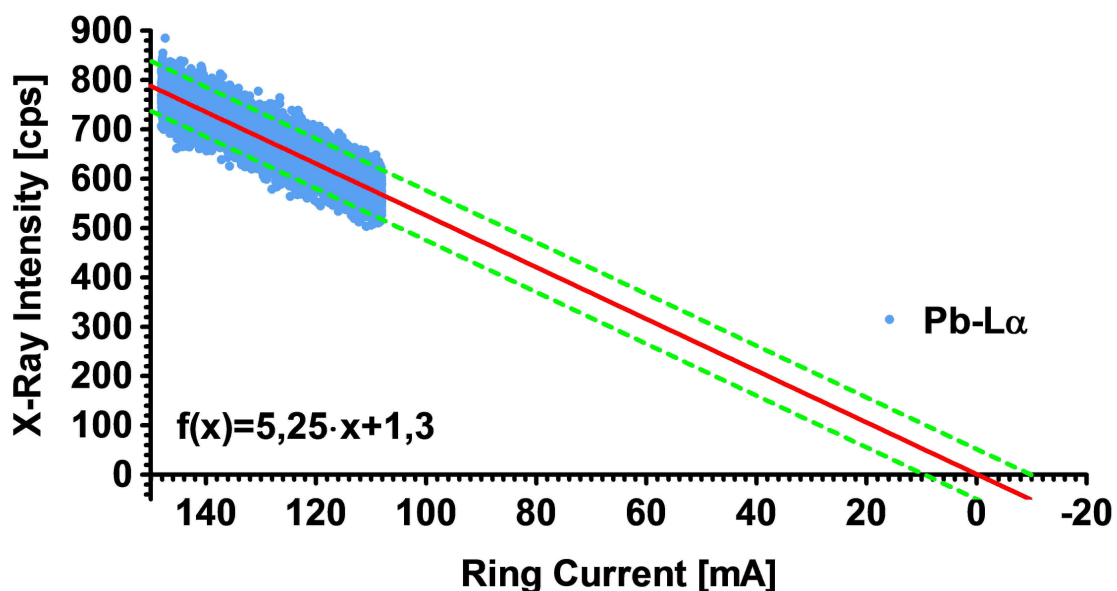


**Figure 7.2.4: Correlation of ring current and fluorescence intensities. The linear regression (solid red line) and 95% prediction band (dotted green line) of the data extrapolated to the intercept with the abscissa.**

The parameters of the exponential function  $f_{\text{norm}}(t)$  fitted to the ring current normalized intensity values are in perfect agreement with the parameters of the exponential function  $f_{\text{norm}}^*(t)$  calculated from the fitted functions of the ring current  $f_{R-C}(t)$  and the uncorrected fluorescence intensity values  $f_{\text{Pb-La}}(t)$ .

$$f_{\text{norm}}^*(t) = f_{\text{Pb-La}}(t) / f_{R-C}(t)$$

Tab. 7.2.2 shows the values of the parameters for the fitted and calculated exponential functions.

**Table 7.2.2: Fit results of the exponential functions approximating the ring current, the uncorrected fluorescence and ring current normalized fluorescence intensities.**

$f(t)=N_0 \cdot e^{\lambda \cdot t}$	coeff. $N_0$	decay constant $\lambda_{RC}$	Corr. Coef. $R^2$	Note
ring current $f_{RC}(t)$	147.5	-0,06797	0,9994	fitted
fluorescence $f_{Pb-La}(t)$	755	-0,06784	0,8462	fitted
fluorescence norm. $f_{norm}(t)$	5,253	$1,841 \cdot 10^{-4}$	$4,042 \cdot 10^{-5}$	fitted <sup>4</sup>
calculated norm. $f_{norm}^*(t)$	5,119	$1,3 \cdot 10^{-4}$	N. A.	$f_{Pb-La}(t)/f_{RC}(t)$

As the normalized intensities were expected to be constant and the decay constant of the normalized data is in the range of  $10^{-4}$ , a linear fit was tested in addition to the exponential fit. The absolute differences between the two fit types were negligible ( $<10^{-5}$ ). Thus a linear fit gives a sufficient description of the normalized data set.

The difference of the ring current and fluorescence intensity decay constants is a little larger than zero, so the normalized fluorescence intensity values will be slightly increasing with time. To see if this could have a significant influence on our measurements extrapolation calculations were performed.

The deviations of the normalized fluorescence intensities from a perfect constant correlation between the beginning and end of the measurement are shown in Tab. 7.2.3. Due to the counting statistics the ring current normalized fluorescence intensity values vary about +/- 14 % around the fitted linear function. So the relative variation due to the counting statistics is about 60 times bigger (assuming a 12h measurement), then the one introduced by the slightly "imperfect" normalization.

**Table 7.2.3: Deviation of mean fluorescence intensity normalized to the ring current between start and end of the long-time measurement. Including extrapolation to longer measuring times.**

time [h]	absolute deviation [cps/mA]	relative deviation [%]	Note
4,6	0,004	+0,08	actual measurement
6	0,006	+0,11	linear extrapolation
12	0,012	+0,23	linear extrapolation
24	0,023	+0,44	linear extrapolation

<sup>4</sup> This correlation is bad, as the error due to the counting statistics is relatively big compared to the normalized fluorescence intensity.

### **7.3 Influence on the Quality of $\mu$ -XRF Elemental Maps when Measuring over an Injection**

#### 7.3.1) Instrumentation and Measurement Parameters

The setup used for these measurements was the same as described in Chap. 8.2.4).

The measuring time was set individually for each map (7 - 20 sec./pixel) depending on the lead intensities obtained from a line scan across the mapping areas. Area scans on the sample surface in the range of 600 x 400  $\mu\text{m}^2$  up to 600 x 600  $\mu\text{m}^2$  were performed.

#### 7.3.2) Sample

One undecalcified human femoral neck section, embedded in PMMA, which were prepared as five-millimetre-thick sections, cut in transversal plane had been used. For this evaluation two areas of samples FNX4, one in the trabecular part of bone (area A3; OTH69 scan 120) and one in the cortical bone (area A1; OTH69 scan 122). Both maps were recorded over an injection. Details on the sample can be found in Chap. 8.2

#### 7.3.3) Data Evaluation

The treatment of the acquired spectra and the generation of the  $\mu$ -XRF maps are described in Chap. 5.1. The free image analysis software *ImageJ* (Ver. 1.46d; Wayne Rasband, National Institutes of Health, USA, <http://rsb.info.nih.gov/ij>) was applied to compare the Ca-K  $\alpha$  and scatter intensities (coherent & incoherent) before and after the injection. These intensities were evaluated without a correction and with normalization to the ring current of the ANKA storage ring or the signal of the primary ion chamber of the FLUO beamline. For reasons of better comparison, the values, obtained from the correction to the ion chamber, were multiplied by  $10^7$ .

qBEI images were used to correlate the measured elemental distribution to the mineralization of the bone matrix.

For sample FNX4-A3 (OTH69 scan 122) two regions of interest have been defined (see Fig. 7.3.5):

1. Trabecular bone before injection: This is the brighter part in the scatter maps, the left part of the bone area.
2. Trabecular bone after injection: This is the bit darker part in the scatter maps, the right part of the bone area.

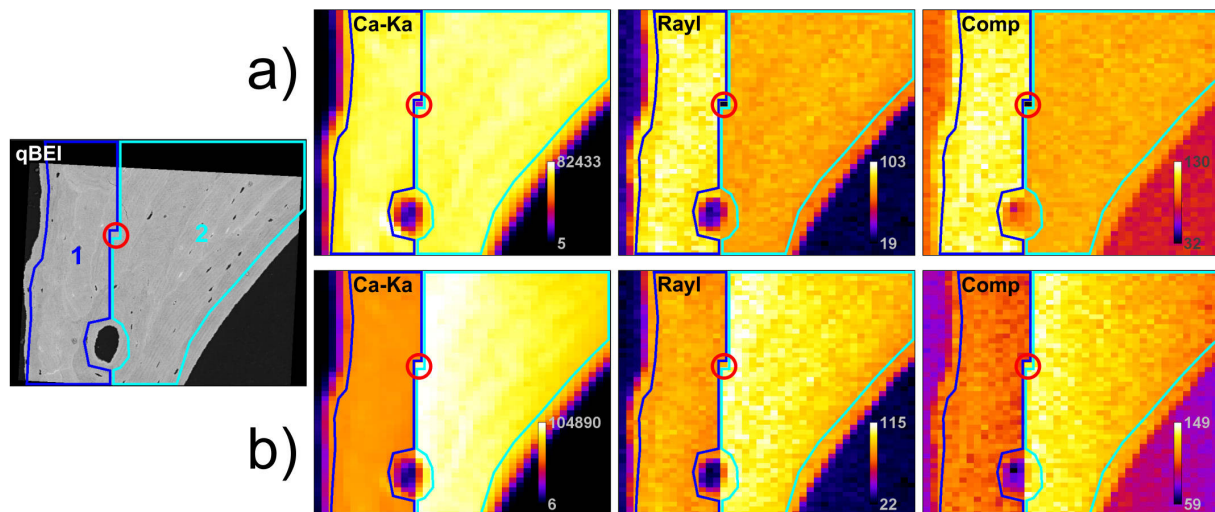


**Figure 7.3.5: Human bone sample FNX4-A3 (OTH69 scan 122); qBEI image and  $\mu$ -XRF maps of Ca-Ka, coherent (Rayl) and incoherent (Comp) scatter normalized to a) ring current and b) ion chamber signal including the ImageJ ROIs for evaluation of count rates before (1; dark blue) and after (2; light blue) the injection. Red circle: first pixel after injection. Resolution:  $15\mu\text{m} \times 10\mu\text{m}$ ; Acquisition time per pixel: 14s;**

For sample FNX4-A1 (OTH69 scan 120) four regions of interest have been defined (see Fig. 7.3.6):

1. Cortical bone at the beginning of the measurement, leaving out young mineralized bone matrix around the haversian channel
2. Cortical bone before the injection, leaving out young mineralized bone matrix around the haversian channel
3. Outliers: 7 points that were measured directly after the injection (rather bright pixels in the scatter maps, darker in the calcium map)
4. Cortical bone after the injection, leaving out young mineralized bone matrix around the haversian channel

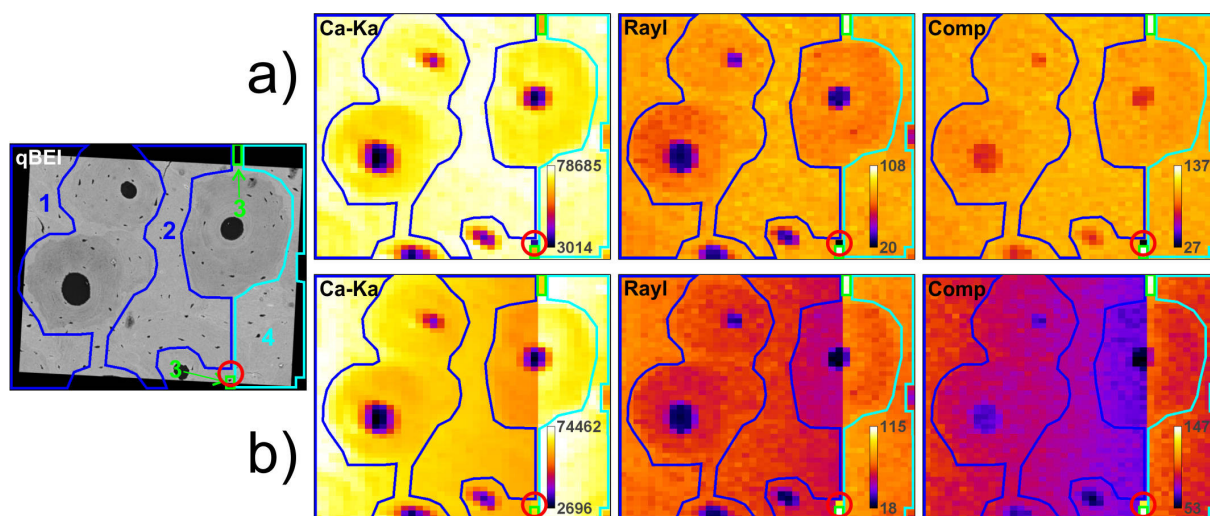


**Figure 7.3.6: Human bone sample FNX4-A1 (OTH69 scan 120); qBEI image and  $\mu$ -XRF maps of Ca-K $\alpha$ , coherent (Rayl) and incoherent (Comp) scatter normalized to a) ring current and b) ion chamber signal including the ImageJ ROIs for evaluation of count rates before (1 & 2; dark blue) and after (4; light blue) the injection. Red circle: first pixel after injection. ROI 3 (green line) marks the 7 pixels directly after the injection, showing some intensity problems (darker in Ca-K $\alpha$  map and brighter in both scatter maps). Resolution: 15 $\mu$ m x 10 $\mu$ m; Acquisition time per pixel: 20s;**

### 7.3.4) Results & Discussion

The evaluation of two  $\mu$ -XRF maps recorded over an injection was done to show that the obtained normalized data yields reasonable results, and measuring over an injection is not influencing the data adversely.

In Fig. 7.3.5 & 7.3.6 the two evaluated areas are shown. Comparing the Ca-K $\alpha$  intensity maps, either normalized to the ring current or the ion chamber signal, it could be clearly seen, that the ring current normalization is perfectly suitable. No differences in the Ca-K  $\alpha$  intensities can be seen before and after the injection for both areas. This is confirmed by the evaluation using the ImageJ set ROIs. There is hardly any variation from the median (horizontal dotted line) for the ring current normalized Ca-K $\alpha$  intensities for all ROIs (see Fig. 7.3.7a). Normalizing to the ion chamber does not suitably correct for the intensity changes due to the decay of the ring current and leads to large intensity differences before and after the injection.

The pixel recorded directly after the injection always had intensity less or equal to the intensity of the neighbouring pixels, though there are no changes in the mineralization of the bone matrix, which was obtained from the qBEI data. This is due to the procedure that is used to enable measuring over an injection. The software checks if the detected intensity is

above a defined threshold. If not, the spectrum is discarded. This is done until sufficient intensity is detected. As the shutter command and the data acquisition software are not linked it is likely that the shutter is opening during an acquisition interval and not at the beginning or end. Thus the recorded intensity corresponded just to an unknown fraction of the set counting time. The corresponding pixels in the two maps in Fig. 7.3.5 & 7.3.6 are marked with a red circle, and were dismissed in the data evaluation of all maps measured over an injection.

The deviation for both scatter intensities for both areas is about 5%, which is acceptable. However, for ROI 1 of map FNX4-A3 (see Fig. 7.3.7b & c) the deviation in the scatter intensities is ~11%. This difference can also be seen in the  $\mu$ -XRF maps (Fig. 7.3.5). No other map of this, the previous and the following beam times have shown comparable abnormalities.

Since the normalization of the Ca-K  $\alpha$  intensities works perfect, this may be due to some causes which are yet unclear.

Map FNX4-A1 (Fig. 7.3.6) shows 7 noticeable points, just after the injection (the significant brighter area in the scatter maps), marked as ROI3 (green). These points seem to be outliers, due to a problem with the orbit of the electrons in the storage ring after the injection. A problem with the AXIL fit could be excluded. A comparison of the uncorrected spectra from the points in ROI 3 with other, "normal", spectra shows, that the Sr-K  $\alpha$  and the scatter peaks are bigger and for the other peaks it is the other way round: e.g. Ca-K  $\alpha$  is larger inside this area than outside.

In later beam times at ANKA FLUO this effect occurred even in the middle between two injections, as a result of an instable electron beam in the storage ring. During this beam times several unscheduled beam dumps occurred due to failures of components of the high voltage RF system of the storage ring

The problem with lost pixel after the injection could be solved by adaption of the procedure used to hold the measurement. Either through synchronisation of the shutter with the data collection software, which would be the most proper solution, or just by discarding one or two additional spectra after the shutter had opened.

The problems due to instabilities of the electron beam in the storage ring can not be solved that easily. Even the ion chamber in the primary beam is not always detecting the fluctuations that lead to strange stripes - like in Fig. 7.3.6 - in the  $\mu$ -XRF maps.

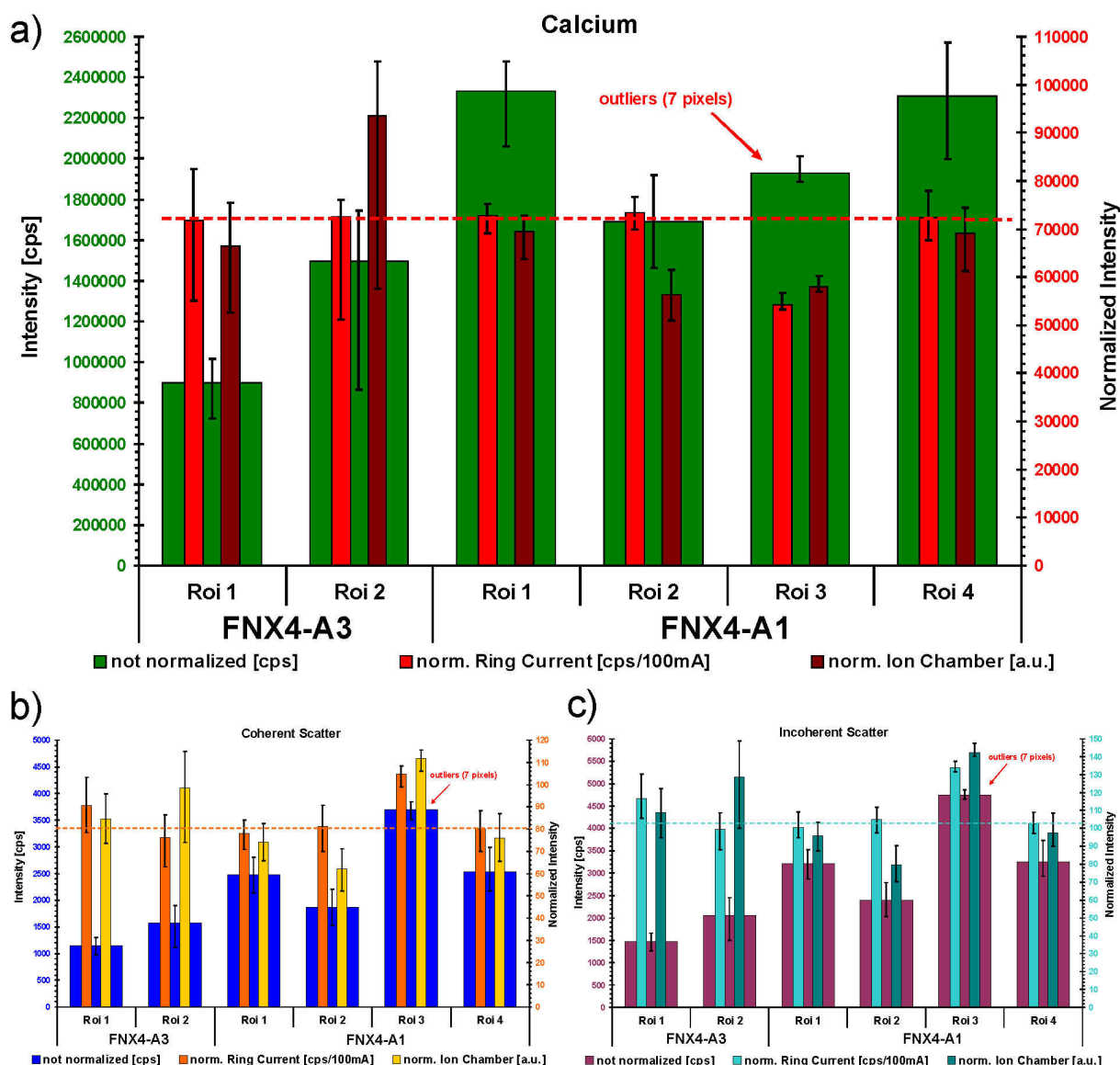


**Figure 7.3.7: Influence of the injection on intensity of the a) Ca-Ka line, b) the coherent and c) the incoherent scatter peak for the samples FNX4-A3 (before: ROI 1; after ROI2) and FNX4-A1 (before: ROI 1 & 2; after ROI 4).**

The y-axis on the left side shows the scale for the uncorrected intensities. On the right y-axis the scale for both normalized intensities is shown.

The dotted horizontal line represents the median of the intensities normalized to the ring current (ignoring the 7 outlier pixels of FNX4-A1 ROI 3).

## 7.4 Conclusion

The ring current normalized fluorescence intensities were only slightly deviating from a horizontal linear correlation. The relative error due to the normalization during a 12 h measurement was about 60 times smaller than the error resulting from the counting

statistics. So it can be concluded, that the normalization of the measured fluorescence intensities to the ring current is satisfactory. Results obtained at different times, normalized to the ring current, can therefore be compared without introducing a significant additional (systematic) error.

The normalization of the Ca-K  $\alpha$  fluorescence intensity to ring current measured before and after the injection was perfect. The normalization to the ion chamber did not lead to adequate results, which is in agreement with the results of the long time experiment with the AXO RF4 thin film reference sample.

Measuring  $\mu$ -XRF maps over an injection is clearly possible. However, it has to be kept in mind that with the current implementation of the "auto shutter" at the FLUO beamline the first pixel after the injection, when the shutter is opening, has to be dismissed in the evaluation process.

A fluctuation of the orbital plane of the electron bunches in the storage ring after or between the injection may also occur and negatively influence the measurement of several pixels, leading to strange stripes in the maps, which have to be excluded during the data evaluation.



## Chapter 8

# Trace Element Distribution and Levels in Human and Animal Bone Samples

### 8.1 Speciation of the Lead Accumulated in the Tidemark of Human Articular Cartilage and Subchondral Bone by X-Ray Absorption Near Edge Analysis [161]

#### 8.1.1) Introduction

As described in Chap. 4.4 lead is a toxic element for the human body and is predominantly accumulated in the bone. Bone is a composite material predominantly made up of collagen type I fibrils in combination carbonated calcium hydroxyapatite (CCaHA) nanocrystallites [19].

In previous and recent studies analyzing the lateral distribution of Pb in the osteochondral region human joints [23] an accumulation of Pb the so called tidemark (TM), the border between mineralized and non mineralized articular cartilage, was discovered. Pb levels in the TM were up to 62-fold increased compared to subchondral and trabecular bone [23, 24, 29]. The TM is a metabolically active region and advancing from the mineralized to the non mineralized cartilage [162]. As already described in Chap 4.3 the sulphur present in articular cartilage has a maximum near the TM. Pb, a chalcogenic element, may form –SH groups there.

It is known, that  $\text{Ca}^{2+}$  ions in calcium hydroxyapatite (CaHA) crystals can be replaced by divalent metal ions, e.g. lead, cadmium copper or zinc, right at the mineralization process or through substitution in the mineralized crystal [116, 163-168]. Therefore, the incorporation of Pb into CaHA in the calcified cartilage region seems most probable, though the high S content next to the TM would allow other Pb compounds.

The aim of this study was to analyze the chemical binding of Pb in subchondral bone and the TM with Micro X-Ray Absorption Spectroscopy ( $\mu$ -XAS) using the  $L_3$ -edge of Pb

(13,035 keV) by comparing XANES spectra recorded at the TM and in bone with the one obtained from reference materials. In addition the capability of the HASYLAB beamline L (DESY, Hamburg, Germany) and the SUL-X beamline at ANKA (Karlsruhe Institute of Technology, Germany) for  $\mu$ -XANES measurements should be tested by comparison with the dedicated XAS beamline at ANKA.

### 8.1.2) Bone Samples

Two human patella samples that were used in a previous study [24, 29] and one additional sample from a femoral head were analyzed (see Tab. 8.1.1). All samples were obtained from randomly selected forensic autopsies. The patients died of an acute illness and had no history of any metabolic bone disease. To the best of our knowledge, none of the patients was exposed to higher Pb concentrations than the natural levels in their living areas. Only samples having no macroscopic signs of osteoarthritis were chosen.

The samples were cut perpendicular to the articular surface from the central region of patella / femoral head (sagittal plane) and prepared as 200  $\mu$ m thick sections as described in Chap. 6.4.

**Table 8.1.1: List of the analyzed bone samples and the labels of the respective measurement points.**

Sample ID	Tissue type	Tidemark	Trabecular Bone
k3807	human patella	k3807_Pos1 k3807_Pos2 k3807_Pos3	not measured
G3776	human patella	G3776_TM1 G3776_TM2	G3776_TBR1 G3776_TBR2 G3776_TBR3
A3753	human femoral head	A3753_TM1	A3753_TBR1

### 8.1.3) qBEI Analysis

Prior to the SR  $\mu$ -XRF of Zöger et.al [24] and current XANES measurements qBEI was performed in a digital SEM, as described in detail in (Chap. 6.3). The areas of interest i.e. the TM and subchondral bone were selected from the qBEIs (e.g. Fig 8.1.1) with respect to bone histomorphology.

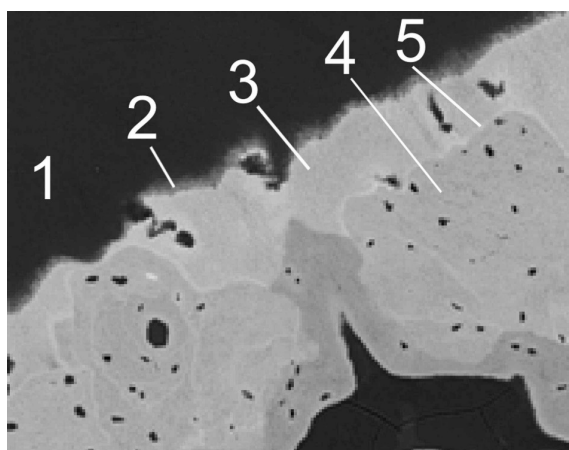


**Figure 8.1.1: qBEI of sample G3776: (1) non mineralized cartilage, (2) tidemark (TM), (3) mineralized cartilage, (4) subchondral bone (4) and (5) cement lines [161].**

#### 8.1.4) Reference Materials

A total of 14 Pb compounds and synthetic Pb substituted CaHAs, listed in Tab. 8.1.2, were analyzed, as they were considered to be possible compounds present in bone or the TM. As all standard Pb compounds were available as powders, they were mixed with polyethylen (Uvasol, Merck) or cellulose, milled to ensure homogeneity, and finally pressed to pellets. For out of the five HA powder standards were pressed with no additive, and one, the Pb-HA 303  $\mu\text{g/g}$  Pb, was mixed with 23wt% cellulose.

**Table 8.1.2: List of measured reference materials**

Reference Materials		
Chemical Formula	Names	Supplier (if knowen)
$\text{PbCO}_3$	lead carbonate	Merck
$\text{PbSO}_4$	lead(II) sulphate	Fluka Chemie AG
$\text{PbO}$	lead(II) oxide	Fluka Chemie AG
$\text{PbS}$	lead(II) sulfide	Alfa Aesar
$\text{PbCl}_2$	lead(II) chloride	Fluka Chemie AG
$\text{Pb}(\text{NO}_3)_2$	lead(II) nitrate	n.a.
$\text{PbO}_2$	lead(IV) oxide	Fluka Chemie AG
$\text{Pb}(\text{OH})_2$	lead(II) hydroxide	n.a.
$2 \text{ PbCO}_3 * \text{ Pb}(\text{OH})_2$	white lead	Fluka Chemie AG
PbHA_1 (400 $\mu\text{g/g}$ Pb)	Pb doted CaHA	synth. by S. Sprio & A. Tampieri
PbHA_2 (700 $\mu\text{g/g}$ Pb)	Pb doted CaHA	synth. by S. Sprio & A. Tampieri
PbHA_3 (1200 $\mu\text{g/g}$ Pb)	Pb doted CaHA	synth. by S. Sprio & A. Tampieri
Pb-HA (303 $\mu\text{g/g}$ Pb)	Pb doted CaHA	synth. by S. Sprio & A. Tampieri
Pb-CHA (335 $\mu\text{g/g}$ Pb)	Pb doted CCHA	synth. by S. Sprio & A. Tampieri

### 8.1.4.1) Synthesis of Pb-Substituted HA

The synthesis of Pb-substituted HA powders (carried out by the collaborators S. Sprio and A. Tampieri) was done by neutralization of a calcium hydroxide suspension ( $\text{Ca}(\text{OH})_2$ , 95% pure) with a orthophosphoric acid solution ( $\text{H}_3\text{PO}_4$ , 85% pure). Lead nitrate ( $\text{Pb}(\text{NO}_3)_2$ , 99.5% pure) was added in the basic suspension and in different amounts, so to have starting Pb/Ca molar ratios of 0.1, 0.5, 1, and 0.05 mol%, according with the general formula  $\text{Ca}_{10-x}\text{Pb}_x(\text{PO}_4)_6(\text{OH})_2$ . All HA powders contain some carbonate due to spontaneous carbonation of the reaction with  $\text{CO}_2$  dissolved in water. One reference with Pb/Ca 0.05 mol% was additionally carbonated; all reactants are provided by Sigma-Aldrich (St. Louis, USA).

The Pb-HA powders were synthesized in a pyrex flask at ambient temperature (22-23 °C) by using 0.38 mol of  $\text{Ca}(\text{OH})_2$  suspended in 0.7 l of  $\text{H}_2\text{O}$ : the acid solution was dropped in the stirring basic suspension and, after, the powders were ripened in the mother liquor for 24 hours, then washed in 2 liters of distilled water and centrifuged for three times, prior drying at 40 °C in ventilated oven and sieving at 150  $\mu\text{m}$ .

### 8.1.4.2) Characterization of Pb-Substituted HA<sup>5</sup>

The phase composition of the as obtained HA powders was determined by X-Ray diffraction (XRD) with Cu-K $\alpha$  radiation (Miniflex: Rigaku, Tokyo, Japan); the chemical composition of the powders, namely the content of calcium, phosphorous and lead, was evaluated by inductively coupled plasma-optical emission spectrometry (ICP-OES) (Liberty 200: Varian, Clayton South, Australia) and energy dispersive spectroscopy (EDS) (INCA 300: Oxford Instruments plc, Abingdon, UK) with a scanning electron microscopy system (SEM) (Stereoscan 360: Leica, Cambridge, UK).

Five different HA powders were obtained and analysed: PbHA\_1, PbHA\_2 PbHA\_3, Pb-HA and Pb-CHA characterized by a starting molar Pb/Ca ratio of 0.1, 0.5, 1, and 0.05 mol% respectively.

Fig. 8.1.2 shows the X-Ray diffractograms of the first three obtained powders: The only crystalline phase detected is hydroxyapatite of very low crystallinity indicated by the broadening of the diffraction peaks.

---

<sup>5</sup> These analyses were carried out by the collaborators S. Sprio and A. Tampieri.

The inductively coupled plasma mass spectrometry (ICP-MS) analysis, whose results are reported in Tab. 8.1.3, shows that Pb is entered in all the investigated powders; anyway, only a fraction of the introduced lead content was found in the final powders, and the remaining part was eliminated through the process of powder washing.

The stoichiometric coefficient was also evaluated, according with the general equation of a HA powder, where lead substitutes calcium:  $\text{Ca}_{10-x}\text{Pb}_x(\text{PO}_4)_6(\text{OH})_2$ .

**Table 8.1.3: Chemical analysis of Pb-substituted HA powders.**

	<b>Expected molar Pb/Ca</b>	<b>Actual molar Pb/Ca</b>	<b>Pb content [<math>\mu\text{g/g}</math>]</b>
<b>PbHA_1</b>	0.001	0.0004	400
<b>PbHA_2</b>	0.005	0.0035	700
<b>PbHA_3</b>	0.01	0.0077	1200
<b>Pb-HA</b>	0.0005	0.0002	303
<b>Pb-CHA</b>	0.0005	0.0002	335

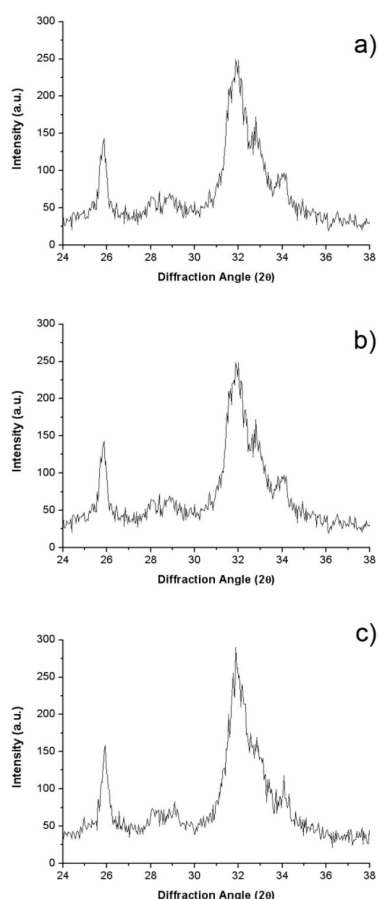


**Figure 8.1.2: X-Ray diffractograms of Pb-HA powders: a): PbHA\_1; b): PbHA\_2; c): PbHA\_3 showing the (002) reflexes (at about  $25,87^\circ 2\theta$ ) and the (211), (112) and (300) reflexes (between about  $31^\circ$  and  $33^\circ 2\theta$ ) which are not angular resolved because of the peak broadening due to small crystallite sizes.**

### 8.1.5) Setup & Parameters for Pb-L<sub>3</sub> Edge XANES Measurements

The XANES analysis is based on the variation of the primary X-Ray energy in a region of some hundred eV across the absorption edge of a specific element present in the sample (here Pb L<sub>3</sub>-edge) and the detection of the change in the absorption /fluorescence intensity. An analysis of the XANES features enables to determine the chemical state and the environment of the element of interest. It is a fingerprint method, comparing the spectra recorded for the unknown samples with spectra gained from reference compounds, expected to be present in the sample. In this case: in the TM and subchondral bone of human bone samples. Further details on this method were described in Chap 2.5.

It is known from literature [169] that bulk XAS can be extended to  $\mu$ -XANES with lateral resolutions in the micrometer range. Thus the local chemical speciation at selected sample ROIs (e.g. tidemark and subchondral bone) can be analyzed. Recording a complete map of the chemical binding is not feasible. The Pb concentrations of about 5 [12] to 10 $\mu$ g/g, [170] would causing tremendous measuring times. Hence XANES was done only at carefully selected points.

#### 8.1.5.1) Measurements Parameters HASYLAB

First test experiments analyzing a PbHA reference material and the patella sample k3807 have been carried out at the micro focus end station at HASYLAB beamline L using  $\mu$ -XANES spectroscopy in fluorescence mode with a spot size of the primary beam of about 15  $\mu$ m (hor.) x 15  $\mu$ m (vert.).

The continuous X-Ray spectrum from the 1,2 Tesla bending magnet has been monochromatized with a Si(111) double crystal monochromator. The focusing of the primary beam was accomplished by means of a polycapillary half lens (XOS X-Ray Optical Systems Inc., East Greenbush, USA)[67]. The fluorescence radiation was detected with a 50mm<sup>2</sup> Silicon Drift Detector (SDD) (Vortex: Radiant Detector Technologies Inc., now Hitachi High-Technologies Science America Inc., Northridge, USA). The incident X-Ray intensity was monitored with an ionization chamber. All acquired data were dead time corrected and normalized to the incident X-Ray intensity.

X-Ray absorption spectra have been recorded by tuning the excitation energy in varying steps across the L<sub>3</sub> absorption edge of Pb (13035 eV) while measuring the Pb-L <sub>$\alpha$</sub>  fluorescence intensity. The energy was calibrated by measuring the absorption of a Pb foil at the L<sub>3</sub> edge in transmission mode. The first inflection point (i.e. the first maximum of the

derivative spectrum) of the Pb metal foil scan was set to 13035 eV (Pb-L<sub>3</sub> edge). The calibration was found to be unaffected during all scans.

To determine the position of the tidemark, which was then used as the position for the  $\mu$ -XANES measurements,  $\mu$ -XRF line scans across the border between non-calcified and calcified cartilage have been performed (similar to the scan shown in Fig. 8.1.3).

The micro focused beam matched the width of the tidemark very well, i.e. the measurements are specific to the region of interest. The total flux in the focused beam is some  $10^9$  photons/s. In addition, Pb-L $\alpha$  radiation originating from the polycapillary tip needs to be shielded efficiently by a suitable detector collimator which limits the solid angle of detection.

The conditions did not allow the acquisition of spectra with satisfying statistics for these samples (see Chap 8.1.6.1). Hence, further measurements were carried out elsewhere.

### 8.1.5.2) Measurements Parameters ANKA SUL-X and XAS

Pb L3-edge XANES spectra of the bone samples and references listed in Tab. 8.1.1 and Tab. 8.1.2 respectively were recorded at the SUL-X beamline at ANKA (detailed description: Chap. 6.1.1). The synthetic Pb-HA samples were also measured at the ANKA-XAS beamline (detailed description: Chap. 6.1.2).

For the measurements at the tidemark the primary beam of the SUL-X was focused to about 100  $\mu$ m (hor.) x 20  $\mu$ m (vert.) and to 200  $\mu$ m (hor) x 50  $\mu$ m for data acquisition in the trabecular bone. The energy was monochromatized using the Si (111). Data were dead time corrected, summed up for all seven channels and divided by the input intensity measured with the first ionization chamber.

To identify the exact location of the TM a line scan from the non-mineralized to the mineralized cartilage - right across the TM - was done. Evaluating the evaluating the Pb-L $\alpha$  fluorescence intensity the position of the TM could be found due to the maximum of the Pb intensity (see [23, 24, 29]). The Pb-L $\alpha$  intensity progression and the corresponding optical microscope images are shown in Fig. 8.1.3. The marker TM01 shows where the XANES scans were performed.

The pellets of all Pb-compounds and synthetic Pb doped hydroxyapatite were measured in transmission mode (except the synthetic HAs), as the fluorescence intensity could be

affected due to self absorption. The synthetic Pb doped HAs and the bone samples were analyzed in fluorescence mode, as the concentrations of Pb were below 1 wt %. The energy ROI was adjusted to the Pb  $L_{\alpha}$  fluorescence line.

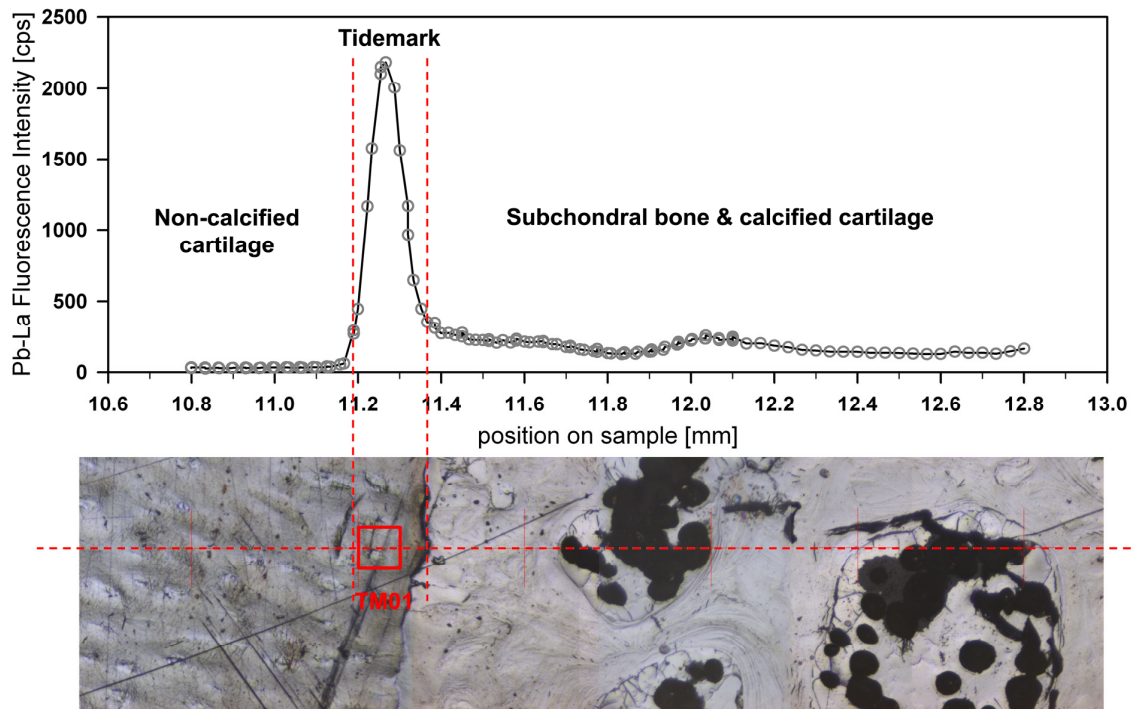


**Figure 8.1.3: Line scan across the TM of the bone sample G3776: Pb- $L_{\alpha}$  intensity (top), corresponding optical microscope images (bottom); (spot size 150  $\mu\text{m}$  x 100  $\mu\text{m}$ ) [161].**

Up to nine, but a minimum of three scans were collected for both, sample and the reference substance. Acquisition times of 3 s or 5 s per energy step up to 20 eV or 75 eV above  $E_0$  (the Pb- $L_3$ -edge) and then at each k step with increasing time according to  $\text{time} \cdot k^{0.5}$  were used. Energy calibration was performed and monitored with a Pb foil at the  $L_3$ -edge in transmission and was found to be unaffected during the scans.

The synthetic Pb-HA samples were also measured at the ANKA-XAS beamline to compare the data quality of both beamlines for spectra from samples with low Pb concentrations. The beamsizes on the sample was about 7 mm (hor.) x 1 mm (vert.). The energy was monochromatized with the Si(111) and the energy calibration was monitored with a Pb-foil - no significant change could be detected. At least two spectra for each reference sample were taken with a measuring time of 3 to 4 seconds before and up to 20 eV above the edge. Beyond 20 eV above the edge the measured energy points were chosen equidistance to k and the acquisition times were increased with a factor of  $k^{0.5}$ .



### 8.1.5.3) XANES Data Analysis

The absorption spectra were recorded summing all fluorescence emission counts within the Pb-L $\alpha$  ROI. The resulting XANES spectra were analyzed with ATHENA, included in the IFEFFIT package for XAS analysis [171-173]. Each scan was normalized to an edge jump of unity and its energy scale was corrected with respect to the Pb-L $_3$  edge of the simultaneously recorded Pb metal foil. Repetitive scans have been merged together to improve the signal to noise ratio.

### 8.1.6) Results

#### 8.1.6.1) Comparison ANKA and HASYLAB Setup

The two  $\mu$ -XANES setups in line for determination of the species of Pb in the tidemark and bone were tested using both, synthetic Pb hydroxiapatite material and a human patella sample (k3807). A comparison of the absorption spectra recorded for the PbHA reference materials (Fig. 8.1.4) and the patella sample (Fig. 8.1.5) obtained for the setups at Hasylab and ANKA revealed that the spectra of both samples show high consistency.

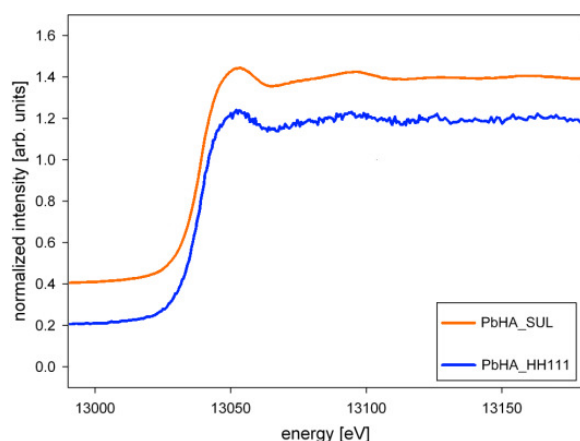


**Figure 8.1.4: XANES of the PbHA reference sample recorded with four different setups: at HASYLAB beamline L using the Si(111), at ANKA SUL-X beamline. The spectra are displaced vertically for clarity.**

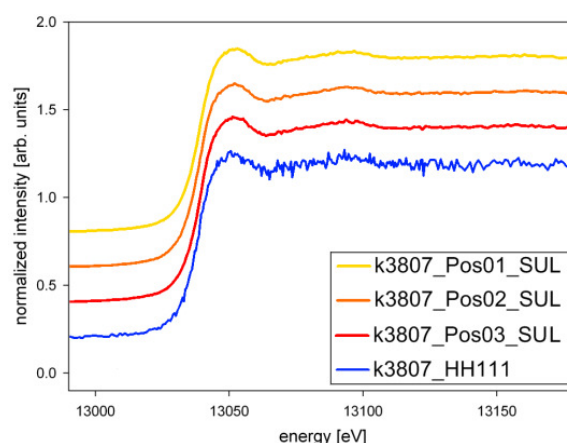


**Figure 8.1.5: Micro-XANES spectra measured at the tindemark of patella sample k3807. The data was obtained with the Si(111) setup at HASYLAB beamline L and at the ANKA SUL-X beamline. At SUL-X spectra have been recorded at 3 different positions at the tidemark of the patella sample. The distance between the measuring points was 500  $\mu$ m.**

As a consequence it was concluded that a comparability (or reproducibility) of data from the different setups is legitimate. The XANES spectra measured at the SUL-X with multi element Si(Li) detector showed signal to noise ratios, which were significantly better than the ones obtained at the Hasylab setup. It should also be noted that the HASYLAB L

beamline uses a microfocus setup with a polycapillary and a focus of  $15 \times 15 \mu\text{m}^2$  at a bending magnet as source, which results in less flux density (in the order of some  $10^9$  ph/s on the sample) than at SUL-X and hence yields, in combination with the a  $50 \text{ mm}^2$  single element SDD, in a lower signal to noise ratio at similar measuring times. Therefore, all other XANES measurements of the bone samples were performed at the SUL-X exclusively because it enables a microfocus capability with good signal to noise ratio due to its wiggler source.

### 8.1.6.2) Comparison ANKA SUL-X <-> XAS Beamline

In Fig. 8.1.6 the XANES data of the PbHA\_1, the PbHA\_2 and the PbHA\_3 reference material, measured at the ANKA SUL-X and XAS beamlines, are shown. The results of both setups were identical. The beam size at sample position at the ANKA XAS was about 7 mm (hor.) x 1 mm (vert.) and at ANKA SUL-X about  $200 \mu\text{m}$  (hor.) x  $150 \mu\text{m}$  (vert.). The a photon flux on the sample, normalized to at  $100 \mu\text{m}^2$  and at 13 keV, for the SUL-X was about  $1 \cdot 10^{11}$  ph/s and for XAS about  $7,5 \cdot 10^8$  ph/s. Thus the total photon flux at the sample was only marginally larger at the SUL-X beamline compared to the ANKA XAS beamline -  $3 \cdot 10^{11}$  ph/s and  $4 \cdot 10^{10}$  ph/s respectively - explaining the similar quality of the spectra. The experiments proved the competitive capability of the SUL-X  $\mu$ XANES setup in comparison to a beamline dedicated to bulk XAS spectroscopy and assured the quality of the results obtained on the real samples.

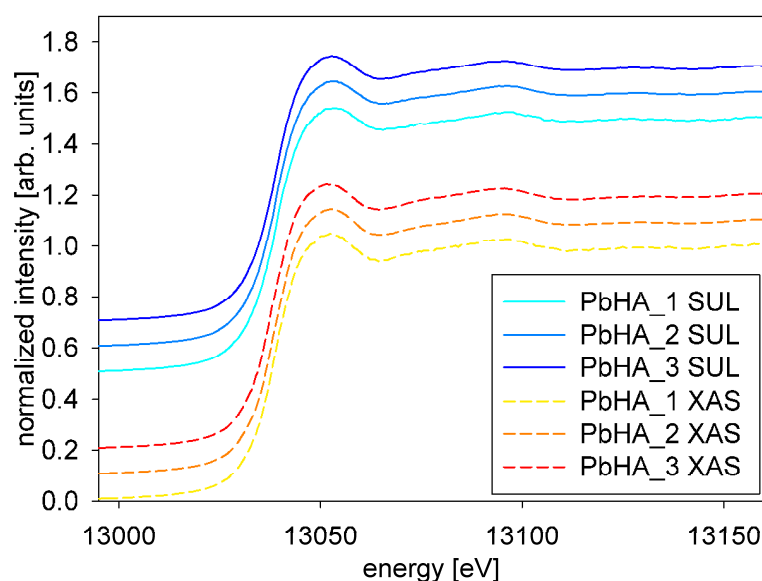


**Figure 8.1.6: Comparison of the XANES spectra recorded for the PbHA reference compounds with different concentrations of Pb measured at the SUL-X and XAS beamline [161].**

#### 8.1.6.3) XANES Spectra of Pb in the Tidemark and Subchondral Bone

At the TM of sample k3807 the XANES data recorded at three positions 500  $\mu\text{m}$  apart show no differences in their features (see Fig. 8.1.5). Similar results were recorded for different positions at the TM of the patella sample G3776 and femoral head sample A3753 (Fig. 8.1.7).

The spectra recorded at tidemark and trabecular bone positions were identical. Hence, all spectra from all samples could be merged for a better signal to noise ratio. This was helpful in the comparison with spectra of reference materials.

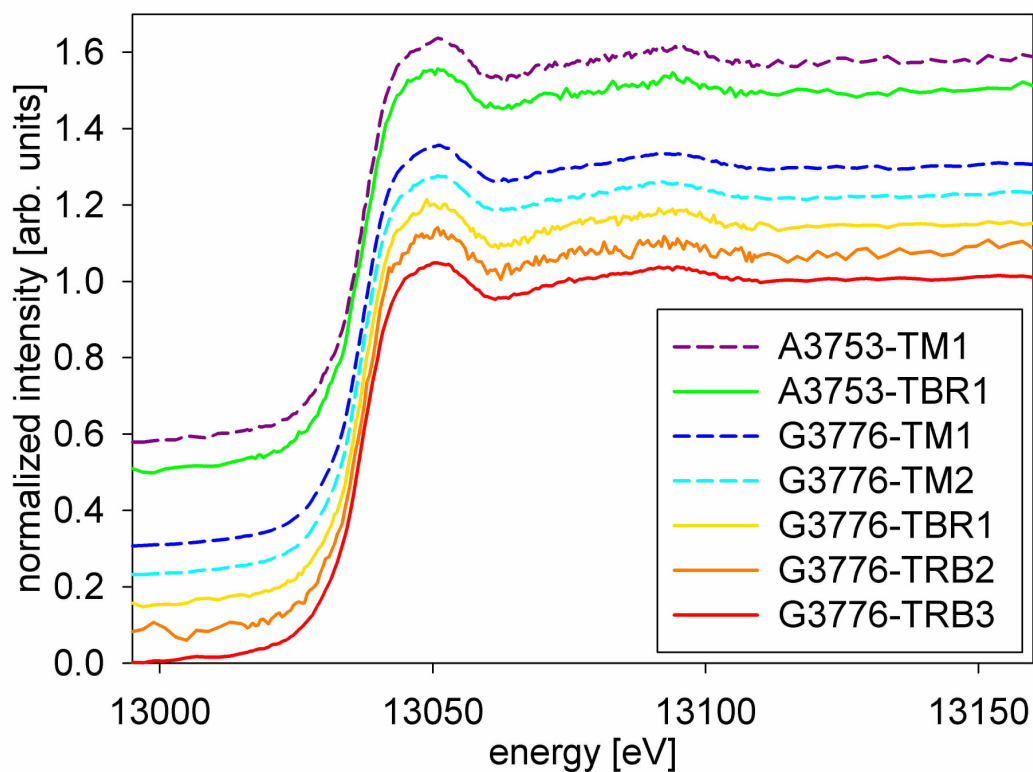


**Figure 8.1.7: Comparison of XANES spectra of tidemark (TM) and trabecular bone (TBR) positions: A3753 femoral head, G3776 patella. The spectra are displaced vertically for clarity.**

#### 8.1.6.4) Comparison of XANES Spectra Tidemark/Bone vs. Reference Spectra

In Fig. 8.1.8 a comparison of all measured Pb compounds, including the PbHA<sub>1</sub>, with the merged bone XANES data is shown. Five of the reference substances, Pb(OH)<sub>2</sub>, PbCO<sub>3</sub>\*Pb(OH)<sub>2</sub>, PbS, PbHA and PbCHA, show similarities with the bone. They are displayed separately in Fig. 8.1.9 for better clarity.

The Pb-CHA standard XANES spectra were most similar to the bone XANES spectra. In Fig. 8.1.10 these two spectra are presented along with their difference. The residual sum of squares (RSS) of the difference is about 0,01, proofing the excellent match.

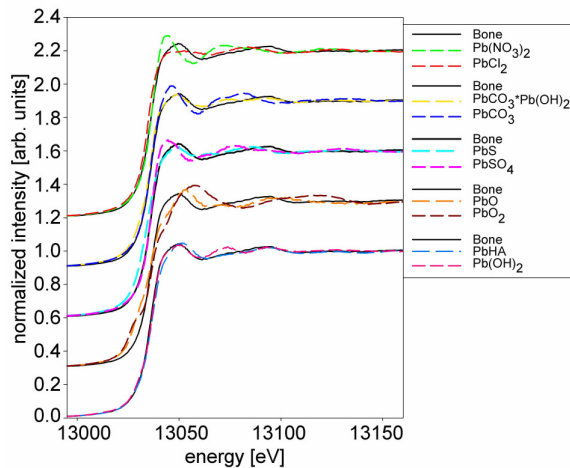


**Figure 8.1.8: Pb L<sub>3</sub>-edge XANES spectra for all reference substances of this study compared to the merged XANES spectrum of all three bone samples (Bone) [161]**

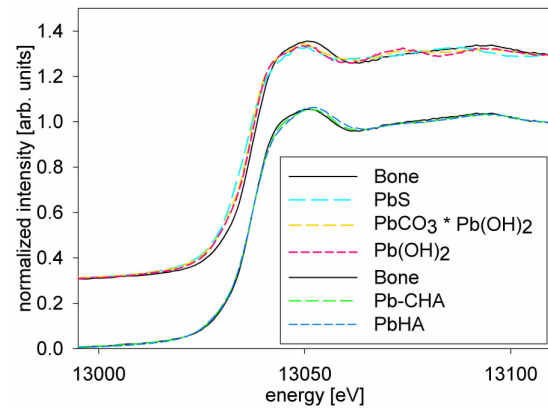


**Figure 8.1.9: Comparison of best fitting reference XANES spectra with a merge of all XANES spectra recorded for the different bone samples (Bone). The synthetic hydroxiapatite reference Pb-CHA has higher carbon content than the synthetic hydroxiapatite reference PbHA) [161].**

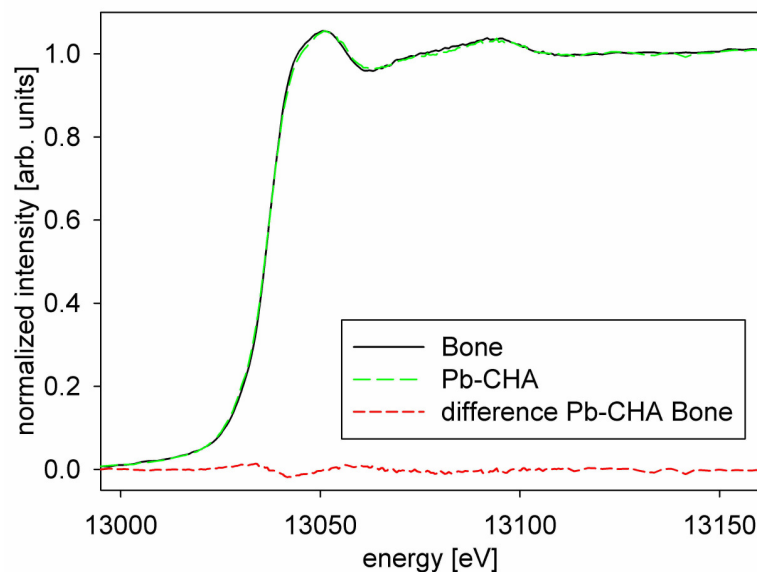


**Figure 8.1.10: Pb-L<sub>3</sub>-edge XANES spectra of merged tidemark/bone (Bone) spectra and synthetic carbonated Pb hydroxyapatite (Pb-CHA). The bottom (dotted red) line shows the difference between the two XANES spectra [161].**

### 8.1.7) Discussion

This study demonstrates that the spatial resolved  $\mu$ -XANES technique on the SUL-X beam line is well suited to allocate the chemical form of Pb, present in only low concentrations in human bone and calcified articular cartilage tissue.

The feasibility of  $\mu$ -XANES measurements at the Pb-L<sub>3</sub> edge of samples showing low Pb concentrations using the SUL-X beamline could be affirmed by comparing spectra from synthetic Pb reference compounds recorded at the SUL-X and the ANKA XAS beamlines, respectively. This is worth mentioning, because the Pb concentrations in these reference compounds were rather low (approx. 300  $\mu$ g/g to 1200  $\mu$ g/g Pb; see Table 8.1.3). Although the number of photons hitting the sample area is slightly higher at the SUL-X beamline than at the ANKA XAS beamline it was not expected that the quality of the spectra of the SUL-X beamline is equal or even slightly better. The higher flux of the SUL-X beamline seems to compensate for better averaging on the sample and being less sensitive to fluctuation of intensity and beam positions of the non-focusing optics at the ANKA-XAS beamline. The experimental results proved the competitive capability of the SUL-X  $\mu$ -XANES setup in comparison to a beamline dedicated to bulk XAS and assured the quality of the data from bone samples. The variations found in the XANES of reference compounds with Pb in different chemical environment demonstrated its sensitivity to allocate the chemical state of Pb in the samples. Thus it can be assumed that the results obtained for the bone sample are reliable although Pb concentrations in bone are generally low (in the range of about 5 [12] to 10  $\mu$ g/g, [170]).

XANES spectra recorded at different positions of the tidemark of both samples showed no differences, supporting the assumption that Pb is in the same chemical state in the complete tidemark. Further more the XANES spectra from the tidemark turned out to be identical with the ones obtained from the "normal" bone, indicating that Pb in the tidemark and in bone is bound the same way. This is astonishing as the chemical composition of the articular cartilage region is known to be completely different to the composition of the subchondral / trabecular bone [174]. Even a mix of different binding states of Pb in the tidemark could be excluded.

The comparison of the XANES spectra obtained from the three different bone samples with reference materials allowed concluding that most of the Pb in the tidemark and the subchondral / trabecular bone is bound to calcium hydroxyapatite crystals with high carbon

content. Very small differences could be observed right above the absorption edge, suggesting either that a tiny fraction of Pb could be present in an unknown state or that the carbon concentration in the hydroxyapatite reference material is not perfectly matching the carbon content in human bone material.

This is in agreement with the fact that carbonate substitution occurs at both hydroxyl and phosphate sites, and, along with Ca-deficient hydroxyapatite, plays an important role in the nanocrystalline structure of bone tissue [163]. Bone is a composite material containing mineral nano crystallites and a protein matrix that is predominantly cross-linked type I collagen. Previous studies have shown that the mineral is a carbonated calcium phosphate within the apatite crystalline structure group. Moreover, bone is unique in comparison to the geological apatite hydroxyapatite in that carbonate substitutes for about 6–8% of the phosphate and relatively little hydroxide is present (20% or less) [175-177].

The substitution of Pb in calcium hydroxyapatite is a well known mechanism in the fields of biochemistry and environmental science, where synthetic HA is successfully applied in remediation of heavy metal contaminated soil, water or waste [178]. Besides Pb, metal substitution on the Ca site involves, for example, the biological important Fe, Cu, Zn and Cd. The  $\text{Pb}^{2+}$  in solution exchanges with Ca, causing morphological changes in the surface region. In case of high Pb concentrations the formation of Pb substituted CaHA is followed by the formation of the pyromorphite phase, where all Ca is replaced with Pb [165, 168]. Currently, four possible immobilization routines, including ion exchange process, surface complexation, dissolution and precipitation and co-precipitation were generally suggested for Pb immobilization mechanism of hydroxyapatite [163].

The mechanism of Pb substitution in the apatite structure has been studied at high Pb concentrations. According to [179, 180] it can be assumed that the same is true for very low Pb concentrations (e.g. in the Pb doped synthetic HAs and in the bones samples). In addition the Pb present in bone is can be accumulated during the mineralization phase. Pb present as  $\text{Pb}^{2+}$  ions in the serum are chemically similar to  $\text{Ca}^{2+}$  ions. It has been demonstrated that  $\text{Pb}^{2+}$  is directly competing with  $\text{Ca}^{2+}$  at the voltage activated  $\text{Ca}^{2+}$  channels [181, 182]. Thus it can be assumed that  $\text{Pb}^{2+}$  is transported into the bone as  $\text{Ca}^{2+}$  and is build into the CCaHA crystal lattice instead of  $\text{Ca}^{2+}$  during the mineralization. It has been shown that  $\text{Pb}^{2+}$  is able to occupy both  $\text{Ca}^{2+}$  sites in the CaHA crystal [4, 183-185]. Therefore it can be excluded with almost certainty that separate, Pb containing phases are present; leading to the

conclusion that Pb in bone is in fact incorporated into the structure of carbonated calcium hydroxyapatite.

Many of the adverse effects of Pb on human health [3] and bone metabolism are known [4, 115, 182]. However the impact on the metabolism in articular cartilage has not been studied to that extent. It is however suggested the Pb is negatively influencing the chondrocytes [114]. There are reports that Pb can induce osteoarthritic changes in joints [110, 186, 187] and has adverse effects on bone healing mechanisms [111].

The consequences of the Pb accumulation in the tidemark of articular cartilage are still a point of investigation and discussion.

### 8.1.8) Conclusion

The  $\mu$ -XANES setup at SUL-X beamline is well suited to analyse the chemical binding of Pb in very low concentrations, as they are present in human bone and competes with the dedicated bulk XAS beamline at ANKA. The setup at HASYLAB beamline L turned out to be not the perfect choice for this type of investigations.

Pb is incorporated into the carbonated calcium hydroxyapatite crystal in both, the subchondral bone and the tidemark of human bone and cartilage samples.

## **8.2 Differential Accumulation of Zinc, Strontium and Lead in Human Bone [132]**

### 8.2.1) Introduction

As bone is the main sink of Pb and other (heavy) metals with divalent states [182] great efforts have been undertaken to determine the incorporated amounts [11, 12] of these elements. However, almost all previous studies to shed light on the distribution merely differentiated between cortical and trabecular bone and lacked any further spatial resolution [14, 17, 18]. Several groups were performing SR  $\mu$ -XRF measurements on bone samples [13, 15, 16], but due to a lack of resolution the elemental levels in different structural units of bone (e.g.: bone packets, osteons, cement lines) could not be resolved.

In recent studies on the elemental distribution in the osteochondral region of human bone samples synchrotron radiation induced confocal micro X-Ray fluorescence analysis (SR  $\mu$ -XRF) was used to detect Zn and Pb at a sufficient resolution to link the bone morphology with the element distributions. A significant accumulation of Zn and Pb at the transition zone between mineralized and non-mineralized articular cartilage was found compared to subchondral bone [24].

The purpose of the present study was to shed more light on the mechanisms of incorporation of the trace elements Zn, Pb and Sr into mineralized bone matrix through the determination of the levels of these trace elements in the different basic structural units BSUs (e. g.: osteons, bone packets) and cement lines of bone matrix. The hypothesis was that the kind of trace element and its amount of incorporation is depending on the one hand on the age (the degree of mineralization) of the mineralized bone matrix and on the other hand on the biochemical composition, which is varying between the different BSU types. It was suspected that the trace element incorporation into bone matrix<sup>6</sup> has a positive linear correlation with the Ca content of the bone matrix, as the trace elements are assumed to be incorporated during the primary and secondary mineralization process.

---

<sup>6</sup> In the following the term mineralized bone matrix will describe both, the osteons and the interstitial bone in the osteonal bone region and bone packets in cancellous bone region.



Further interest was to find out if the different composition of the cement lines compared to mineralized bone matrix in cortical and trabecular bone has a profound influence on the trace element incorporation.

To achieve the proposed aims, tissue from human femoral necks and heads including trabecular as well as cortical bone was analyzed applying quantitative backscattered electron imaging (qBEI) and SR  $\mu$ -XRF.

### 8.2.2) Bone Samples

For this study 14 human bone samples were analyzed. An aged matched set of 10 femoral necks consisting of 5 samples from patients suffering an osteoporotic femoral neck fracture and 5 samples from forensic autopsies of individuals without a history of metabolic bone diseases from a previous study [188] was used. The average age of the individuals was 81.5 years ranging from 74 to 92 years. Additionally 4 femoral heads from 60 to 80 years individuals suffering an osteoporotic femoral neck fracture were obtained during hip replacement surgery at the AUVA trauma Centre Meidling (Vienna). More details on the samples can be found in Tab. 8.2.1.

To the best of our knowledge, none of the patients has been exposed to higher Pb concentrations than the natural levels in their living areas.

The study was in accordance and approved by the local ethics committee (Institutional Ethical Review Board of the Medical University of Vienna).

Measurements were performed in both, trabecular and cortical bone regions for the femoral neck samples and only in the trabecular region for the femoral head samples resulting in a total of 35 areas.

**Table 8.2.1: Details of the samples analyzed for this study. Bone tissue: F. N. . . . femoral neck; F. H.: . . . femoral head; n. a. . . . not assigned (not part of a matched pair)**

Sample ID	No. of maps	Tissue	Group (Pair No.)	Sex	Age
FNX1	3	F. N.	fractured (1)	f	89
FNX2	3	F. N.	control (1)	f	84
FNX3	2	F. N.	fractured (2)	f	77
FNX4	3	F. N.	control (2)	f	77
FNX5	3	F. N.	fractured (3)	f	80
FNX6B	3	F. N.	fractured (4)	f	92
FNX7	2	F. N.	fractured (5)	f	74
FNX8	2	F. N.	control (5)	f	75
FNX9	2	F. N.	control (3)	f	79
FNX10	3	F. N.	control (4)	f	88
CYX6	2	F. H.	fractured (n.a.)	f	76
CYX10	2	F. H.	fractured (n.a.)	f	70
CYX14	2	F. H.	fractured (n.a.)	f	85
CYX18	2	F. H.	fractured (n.a.)	f	79

The femoral neck samples were cut in the transversal plane and the femoral head samples were cut perpendicular to the articular surface from the superior, weight-bearing region of the femoral head (frontal plane). A more details description of the sample preparation is given in Chap. 6.4.

### 8.2.3) qBEI Analysis

qBEI was performed in a digital SEM as describe in detail in (Chap. 6.3). Images at different magnifications 12-fold for overviews and 200-fold (pixel resolution of about  $0,88 \times 0,88 \mu\text{m}^2$ ) were obtained to select and define the regions of interest in bone for SR- $\mu$ -XRF analysis. Especially areas (bone packets, osteons) containing mineralized bone matrix with different degrees of mineralization have been selected.

### 8.2.4) SR $\mu$ -XRF Analysis

The measurements have been carried out at the synchrotron facility ANKA at the Karlsruhe Institute of Technology Campus North (Karlsruhe, Germany). A confocal SR  $\mu$ -XRF setup with the polycapillary half lenses and the  $50\text{mm}^2$  Vortex SDD at the micro focus end-station at the FLUO beamline was used (see Chap. 6.1.3).

The lateral beamsizes was  $17 \mu\text{m} \times 12 \mu\text{m}$  (horizontal x vertical) and a depth resolution  $19 \mu\text{m}$  at 9.71 keV (Au-La). The excitation energy was set to 17 keV.

Area scans in the sample surface were performed in the range of 500  $\mu\text{m}$  x 500  $\mu\text{m}$  up to 500  $\mu\text{m}$  x 650  $\mu\text{m}$  with a step width of 15  $\mu\text{m}$  horizontal and 10  $\mu\text{m}$  vertical. Due to the low Pb content, acquisition time per spectrum (pixel) in the range 7 of to 20 seconds were tested. Acquisition times longer than 12 seconds per pixel did not show any significant improvements in the signal to noise ratio of the obtained elemental maps.

For each area of interest, several depth scans were performed to determine the correct measurement plane – the surface layer of the sample. The optimal depth is where the Ca-K $\alpha$  intensity of the depth scans reaches a maximum. Furthermore, this procedure ensures that the sample surface and the measurement plane are parallel and all measured voxels are within the same depth of the sample.

The treatment of the acquired spectra and the generation of the  $\mu$ -XRF maps are described in Chap. 5.1.

### 8.2.5) Data Evaluation

The information about bone tissue structure and mineral content as obtained by qBEI was combined and correlated with the X-Ray intensities of the corresponding elemental maps as described in Chap. 5.2. The 2D data evaluation software ImageJ and custom made routines were applied to pre-process the obtained data prior to statistical evaluation with GraphPad Prism (v4.0c, GraphPad Software Inc., La Jolla, USA).

#### 8.2.5.1) Statistical Evaluation

For each sample the medians of the normalized count rates of Ca, Zn, Pb and Sr for the mineralized bone matrix and the cement line ROIs were calculated. The levels of significance of the differences between mineralized bone matrix and cement lines were tested with the non-parametric Mann-Whitney test for each sample separately. For this purpose all evaluated mineralized bone matrix and cement line ROIs of the respective sample were used. The number of mineralized bone matrix and cement line ROIs was different for all samples. The number of cement line ROIs was larger for all samples. The count rate ratios between cement lines and mineralized bone matrix were calculated for each sample using the median of the values for the mineralized bone matrix and the cement line. To evaluate the changes in count rate ratios between cement lines and mineralized bone

matrix the Wilcoxon signed rank test with the hypothetical median value 1 ( $\triangle$  equal elemental distribution) was used.

The significance of the correlation between Ca content and trace element levels of all evaluated mineralized bone matrix ROIs of all samples (n=402) was tested with the non-parametric Spearman test.

To evaluate the changes in mineralized bone matrix count rate ratios between osteoporotic fractured and non-fractured controls the non-parametric Mann-Whitney test was used. Only the data from the femoral neck sample set (five age matched pairs of fractured and controls) was used (details on the samples see Tab. 8.2.1)

Differences or correlations with  $p < 0.05$  were considered significant for all performed tests.

### 8.2.6) Results

#### 8.2.6.1) $\mu$ -XRF Maps of Bone Tissue

In Fig. 8.2.1 examples of spatial distribution/maps of the elements Ca, Zn, Pb and Sr in bone tissue are shown.

- i) The corresponding qBEI images of osteonal (a) and trabecular (b) bone display regions with different mineral content (dark gray, low and bright grey, high mineral content).
- ii) None of the elemental XRF maps show a homogeneous distribution within the bone tissue.
- iii) Zn exhibits a remarkable increase in the cement lines and at the borders to the haversian channels. Zn intensities appear to be rather constant in the bone matrix. This accumulation of Zn in the cement lines is shown in Fig. 8.2.1b. The numerous parallel cement lines seen in the qBEI image correspond with bands of high Zn-K $\alpha$  intensities in  $\mu$ -XRF map.
- iv) Pb also accumulates in the cement lines and in the borders of the haversian channels. Moreover Pb shows a strong correlation to the Ca-content in the bone matrix. Thus, the central young osteon with low mineralization and therefore low Ca content has such a low Pb content that the detection limit of the SR- $\mu$ -XRF method is reached. In Fig. 8.2.1b the Pb levels of the bone samples are so low, that the Pb maps exhibit only a noise signal.

v) The behaviour of Sr distribution is different to Zn and Pb. There is no accumulation at cement lines and haversian channel borders. However there are distinctly visible differences between the mineralized bone matrix areas of the various osteons.

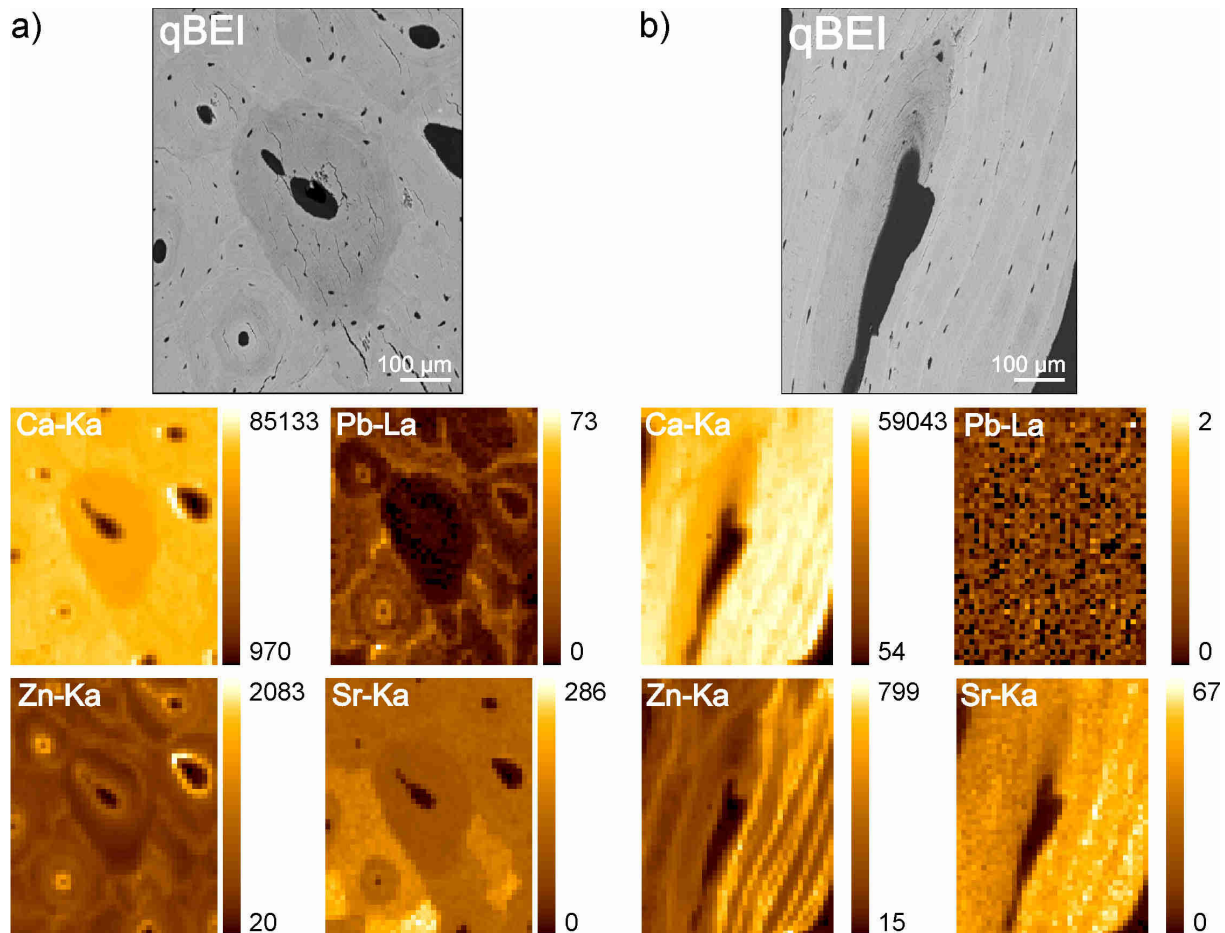


**Figure 8.2.1: Examples of qBEI images with corresponding SR  $\mu$ -XRF element maps of Ca, Zn, Pb, Sr: (a) osteonal bone region of the human femoral neck (b) cancellous bone region of the human femoral neck. The colour-coded X-Ray intensities are normalized to counts per second (cps), 100 mA Ring current and are scaled from minimum to maximum within each individual map. qBEI images show younger bone packets (less mineralized) as darker, and older bone packets (higher mineralized) as brighter grey levels. Sample (b) exhibiting multiple parallel cement lines (a: FNX3-A1 OTH69 scan 106; b: FNX6B-A1 OTH73 scan 114) [132].**

#### 8.2.6.2) Comparison of Trace Element Levels Between Cement Lines and Mineralized Bone Matrix

In all investigated samples significantly higher Zn and Pb intensities were found in the cement lines compared to the mineralized bone matrix (Fig. 8.2.2), with the level of significance  $p < 0.05$  for each sample. Even in the sample which had the lowest Pb level ( $\mu$ -XRF maps shown in Fig. 8.2.1b), a significantly higher Pb content in the cement lines could

be observed. There was a large interindividual variation in Zn and Pb XRF intensities of mineralized bone matrix and cement lines, which however was smaller for the Zn values (Fig. 8.2.2).

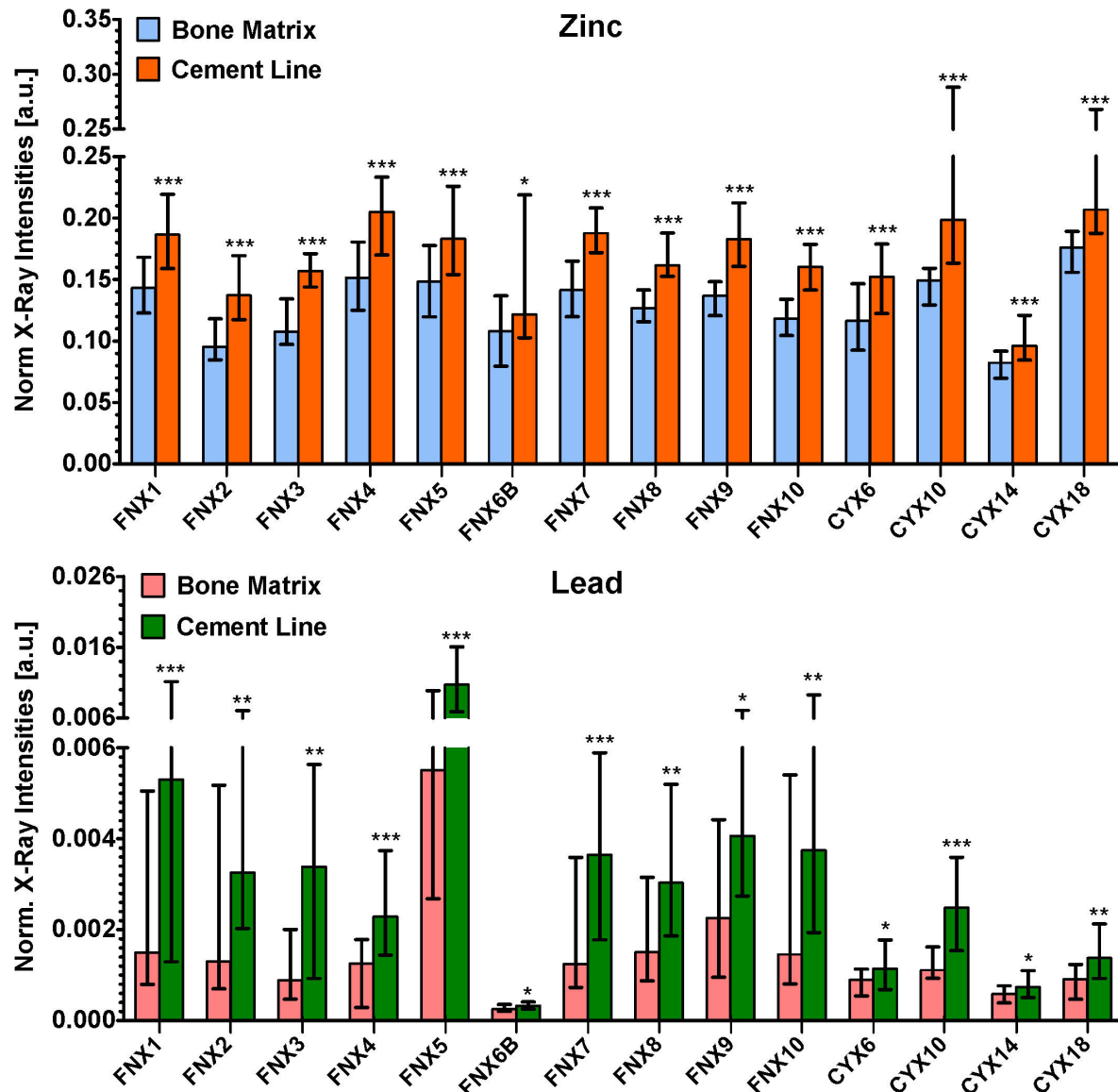


**Figure 8.2.2: Differential accumulation of Zn and Pb in mineralized bone matrix and cement lines in femoral head and neck sample in the osteonal as well as in the cancellous bone region. For each sample medians (box) and interquartil range (error bars) resulting from all evaluated mineralized bone matrix and cement lines ROIs of all recorded maps are shown. The Difference of each pair was tested using Mann-Whitney test and  $p < 0,05$  was considered as significant: \*  $p < 0.05$ ; \*\*  $p < 0.01$ ; \*\*\*  $p < 0.001$ ;**

When analyzing the cement line to mineralized bone matrix ratios for Zn and Pb (Fig. 8.2.3) of all samples, greater inter individual differences for Pb than for Zn (The ratios are shown as: *median [lower quartile; upper quartile]*) were found:

- i) The Zn content was in median 1.3 [1.2; 1.4] times higher in cement line than in mineralized bone matrix ( $p < 0,05$ ).
- ii) The Pb levels were in median 2.0 [1.5; 2.5] times higher in the cement line than in bone matrix ( $p < 0,05$ ). In one sample the Pb level was 3.8 times increased compared to the mineralized bone matrix (Fig. 8.2.3).
- iii) In contrast, Sr intensities were not significantly increased between mineralized bone matrix and cement lines.

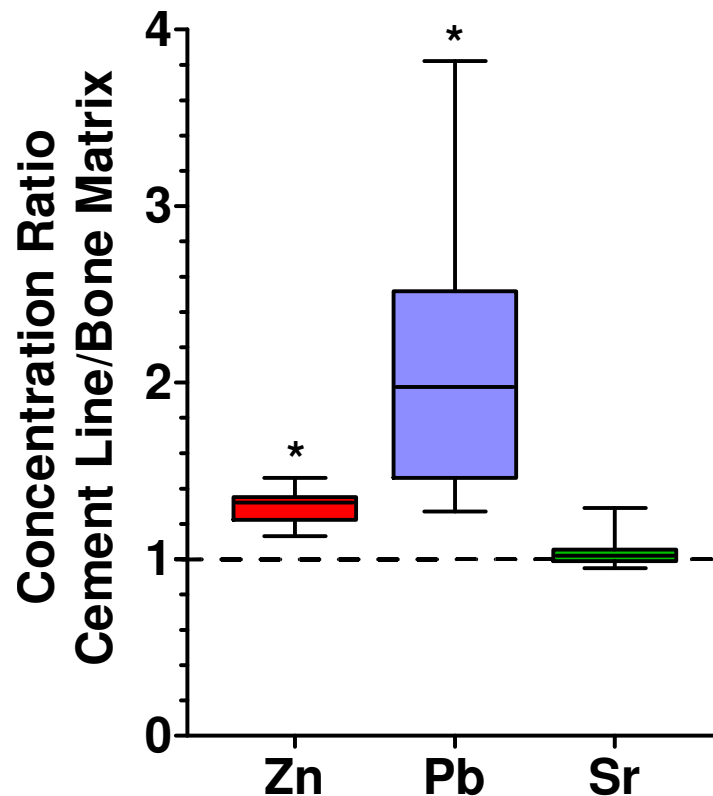


Figure 8.2.3: Ratios of trace elements Zn, Pb and Sr between cement lines and bone matrix. Whisker plots displaying median, interquartil range (box) and range (error bars). A “\*” indicates significant difference ( $p < 0,05$ ) for a hypothetical equal distribution (dashed line) tested with Wilcoxon signed rank test. [132]

**Table 8.2.2: Levels (normalized X-Ray intensities according to formulas 5.2.1 & 5.2.2) of the trace elements Zn, Pb and Sr obtained for mineralized bone matrix (BM) and cement lines (CL) of the analyzed bone samples. Data shown are the median and interquartil range [25th percentile; 75th percentile] calculated for all respective ROI of each bone sample. The p-values were obtained between the mineralized bone matrix and the cement lines for each element for all samples. Tested with Mann-Whitney test and  $p < 0,05$  was considered as significant: ns: none significant;**

	Zinc		Lead		Strontium		p-Values between bone and cement lines		
Sample	BP	CL	BP	CL	BP	CL	Zn	Pb	Sr
FNX1	0,143 [0,123; 0,168]	0,187 [0,159; 0,219]	0,0015 [0,0008; 0,0051]	0,0053 [0,0013; 0,0111]	0,042 [0,039; 0,055]	0,043 [0,038; 0,058]	< 0,0001	0,0003	ns
FNX2	0,095 [0,085; 0,118]	0,137 [0,117; 0,169]	0,0013 [0,0007; 0,0052]	0,0033 [0,002; 0,007]	0,04 [0,034; 0,049]	0,045 [0,036; 0,061]	< 0,0001	0,0066	ns
FNX3	0,108 [0,097; 0,134]	0,157 [0,144; 0,171]	0,0009 [0,0005; 0,002]	0,0034 [0,0009; 0,0056]	0,042 [0,037; 0,047]	0,043 [0,039; 0,048]	< 0,0001	0,0019	ns
FNX4	0,152 [0,125; 0,18]	0,205 [0,17; 0,233]	0,0013 [0,0003; 0,0018]	0,0023 [0,0014; 0,0037]	0,052 [0,048; 0,063]	0,053 [0,048; 0,06]	< 0,0001	< 0,0001	ns
FNX5	0,148 [0,12; 0,178]	0,183 [0,154; 0,226]	0,0055 [0,0027; 0,0099]	0,0107 [0,0069; 0,0161]	0,05 [0,041; 0,114]	0,065 [0,048; 0,105]	0,0003	0,0001	ns
FNX6B	0,108 [0,08; 0,137]	0,122 [0,103; 0,219]	0,00026 [0,0002; 0,00036]	0,00033 [0,00025; 0,00041]	0,024 [0,021; 0,026]	0,024 [0,023; 0,026]	0,0323	0,0423	ns
FNX7	0,141 [0,12; 0,165]	0,188 [0,172; 0,208]	0,0012 [0,0007; 0,0036]	0,0037 [0,0018; 0,0059]	0,048 [0,041; 0,055]	0,048 [0,043; 0,052]	< 0,0001	0,0004	ns
FNX8	0,127 [0,116; 0,141]	0,162 [0,153; 0,188]	0,0015 [0,0009; 0,0032]	0,003 [0,0019; 0,0052]	0,049 [0,046; 0,052]	0,048 [0,044; 0,051]	< 0,0001	0,0032	ns
FNX9	0,137 [0,121; 0,148]	0,183 [0,161; 0,212]	0,0023 [0,001; 0,0044]	0,0041 [0,0027; 0,0071]	0,063 [0,055; 0,07]	0,064 [0,057; 0,067]	< 0,0001	0,0191	ns
FNX10	0,118 [0,105; 0,134]	0,16 [0,141; 0,179]	0,0015 [0,0008; 0,0054]	0,0037 [0,0019; 0,0093]	0,033 [0,029; 0,062]	0,032 [0,026; 0,054]	< 0,0001	0,0016	ns
CYX6	0,12 [0,09; 0,15]	0,15 [0,12; 0,18]	0,0009 [0,0005; 0,0011]	0,0011 [0,0007; 0,0018]	0,034 [0,027; 0,039]	0,033 [0,027; 0,039]	0,0001	0,019	ns
CYX10	0,15 [0,13; 0,16]	0,2 [0,16; 0,29]	0,0011 [0,0009; 0,0016]	0,0025 [0,0015; 0,0036]	0,026 [0,021; 0,028]	0,027 [0,023; 0,032]	0,0001	< 0,0001	ns
CYX14	0,08 [0,07; 0,09]	0,1 [0,08; 0,12]	0,0006 [0,0004; 0,0008]	0,0007 [0,0005; 0,0011]	0,012 [0,01; 0,014]	0,012 [0,01; 0,013]	0,0004	0,0356	ns
CYX18	0,18 [0,16; 0,19]	0,21 [0,19; 0,27]	0,0009 [0,0005; 0,0012]	0,0014 [0,0009; 0,0021]	0,022 [0,019; 0,027]	0,025 [0,021; 0,03]	< 0,0001	0,0048	ns



### 8.2.6.3 Dependency of Zn, Pb and Sr Levels on the Mineralization in Mineralized Bone Matrix

The correlation of Ca content (qBEI obtained Ca wt%) and trace element levels was evaluated using data obtained from all mineralized bone matrix ROIs of all samples. Diagrams showing the relationships of Zn, Pb and Sr to the Ca content are presented in Fig. 8.2.4. No correlations between Zn and Ca levels were found, while Pb and Sr showed a non-linear increase with the degree of mineralization, which was significant ( $p < 0,001$ ; Spearman rank correlation test).

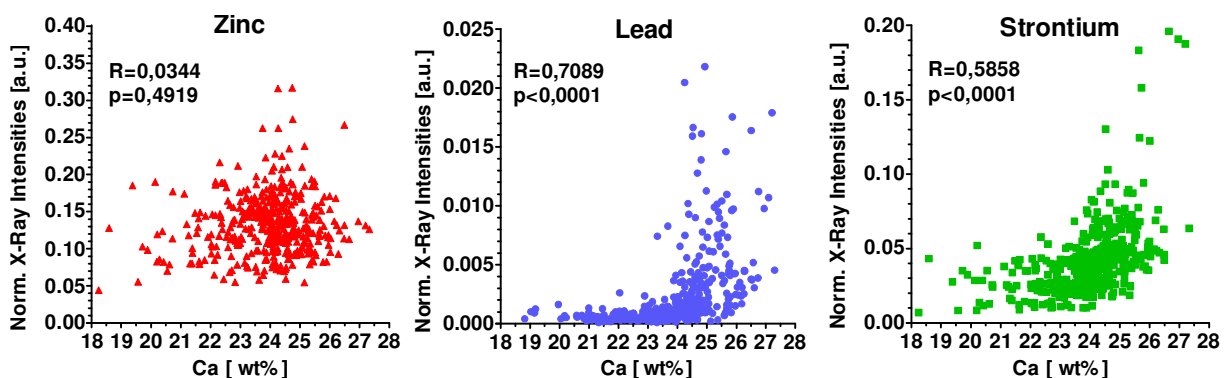


**Figure 8.2.4: Correlations between Ca-content and levels of the trace elements Zn, Pb and Sr in the bulk bone of the femoral neck and the femoral head samples. x-axis: qBEI obtained Ca wt% y-axis: Normalized X-Ray intensities using formulas 5.2.1 & 5.2.2. The displayed data points correspond to all mineralized bone matrix ROIs obtained from all analyzed maps. One data point represents one mineralized bone matrix ROI. Spearman's rank correlation test: R . . . correlation coefficient, p-value significant for  $p < 0.05$ , number of pairs:  $n=402$  [132].**

### 8.2.6.4) Influence of Osteoporotic Fractures on the Trace Element Levels and Distribution

To see if the distribution and levels of the trace elements Zn, Pb and Sr is altered in case of osteoporotic fractures, the data from the two subgroups, osteoporotic fractured femoral neck samples and age matched non fractured controls (details see Chap. 8.2.2) was evaluated. No distinct differences for Zn, Pb and Sr levels in the mineralized bone matrix were observed (see Fig. 8.2.5). The correlation of the trace element levels with the Ca content (qBEI obtained Ca wt%) revealed no significant differences between osteoporotic fractured and control samples (see Fig. 8.2.6).

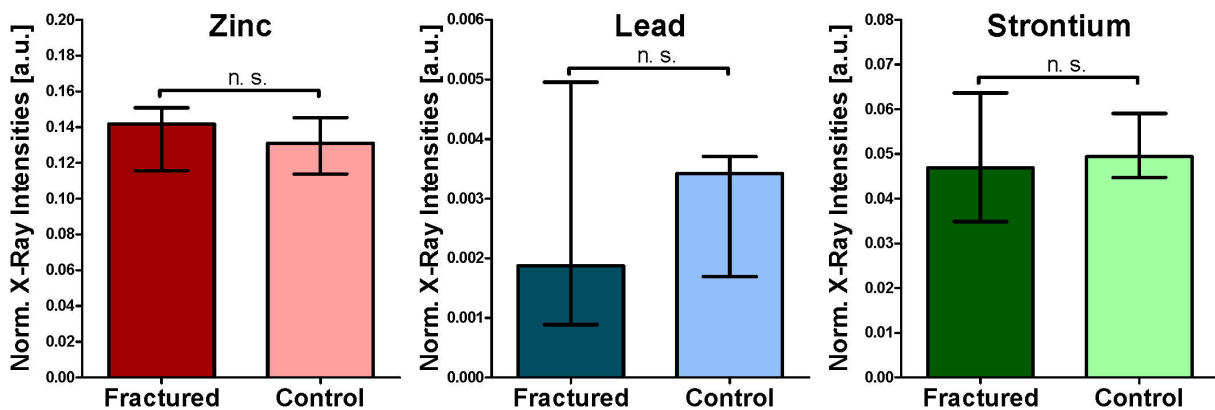


**Figure 8.2.5:** Comparison of trace element levels of the osteoporotic fractured and non-fractured aged matched controls. The data from different maps of one sample were averaged. For each element the medians of the normalized intensities (using formulas 5.2.1 & 5.2.2) including the interquartil range of the respective sample group (fractured, control) are shown. The results were tested using Mann-Witney test with a significance level of  $p < 0,05$ .

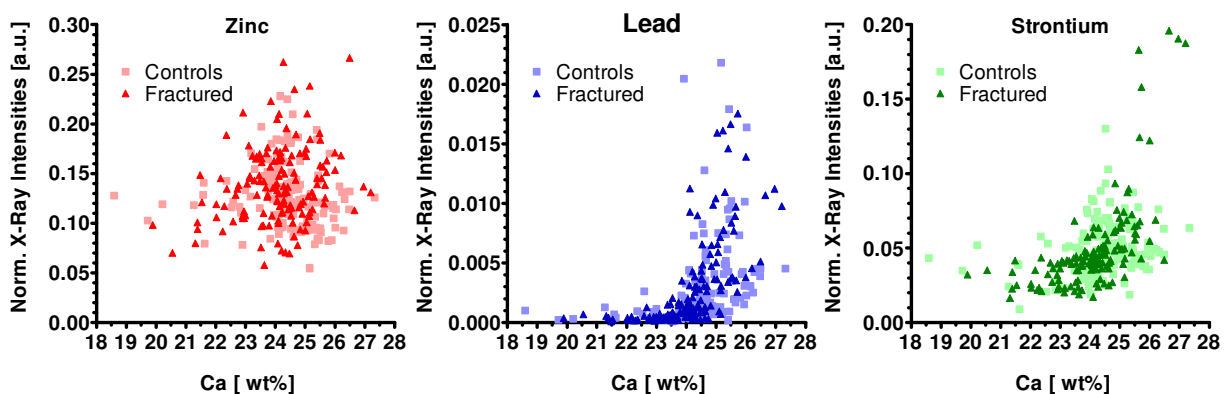


**Figure 8.2.6:** Correlation of Zn, Pb and Sr levels and Ca content in mineralized bone matrix of the femoral neck samples – osteoporotic fractured vs. non-fractured controls. x-axis: qBEI obtained Ca wt%. y-axis: normalized XRF intensities using formulas 5.2.1 & 5.2.2. The shown data points correspond to all mineralized bone matrix ROIs – one point per ROI.

#### 8.2.7) Discussion

SR  $\mu$ -XRF together with qBEI have been applied in this study to evaluate the differential accumulation of the trace elements Zn, Pb and Sr into mineralized bone matrix and cement lines of human bone. Therefore the influence of the different biochemical composition and the degree of mineralization on the incorporation of these trace elements was elucidated. Analysis of the elemental levels revealed an increase of Zn and Pb in the cement lines compared to the adjacent bone matrix. Levels of Pb and Sr were strongly dependent on the Ca content of the bone packets / osteons, contrary to Zn.

This is the first time that the qBEI images were superimposed with the corresponding SR  $\mu$ -XRF elemental maps to get a link between bone morphology and X-Ray intensities.

### 8.2.7.1) Mineralized Bone Matrix vs. Cement Lines

Compared to the bone matrix, the cement lines present throughout higher Zn and Pb values indicating a different process of Zn and Pb accumulation / incorporation in these two types of bone tissue. Unlike the bone matrix, which is made up of collagen type I fibrils reinforced with mineral platelets (carbonated calcium hydroxiapatite) [19], the cement lines (more precise cement surfaces) consist of a matrix rich in non-collagenous proteins like osteocalcin and osteopontin [20]. During bone remodelling the newly formed cement line is exposed to the interstitial fluid until the osteoid matrix (produced by the osteoblasts) starts to mineralize. In this period Pb ions present in the interstitial fluid can accumulate in the surface of the old mineralized bone matrix and may deposited cement line material. The increased Pb concentrations in the cement line may be due to the osteocalcin, which has a higher affinity to Pb than to Ca even at low Pb levels [115]. Additional time might be of importance, as Pb can be accumulated from the interstitial fluid into the cement line until the contact to the interstitial fluid is cut off. Therefore variations in the Pb and Zn content between the cement lines are assumed to reflect either varying trace element concentrations in the serum and / or difference in duration of the reversal phase.

In previous studys a coincident increase of Pb and Zn was also observed in the transition zone between mineralized and non-mineralized cartilage [23, 24, 29].

Hence, Zn is essential for bone metabolism, as it is part of several enzymes (e.g. matrix metalloproteinases MMPs) that are playing an important role in the remodelling mechanisms of bone [189] and it is a cofactor of bone alkaline phospatase [b-ALP] [190-194] responsible for osteoblastic activity and mineralization. This increased Zn levels in the cement line suggest that these enzymes are deposited there during the remodelling process. This is supported by the fact that Zn set free during bone remodelling is not increasing the serums levels, as it is almost immediately incorporated back into the newly formed bone [195-197].

The far smaller interindividual variations of Zn levels compared to Pb (Fig. 4a) are an indication that Zn is an inherent component of the cement line.

Contrary to Pb and Zn, Sr seems not to be accumulated in the cement lines at significant levels, though  $\text{Sr}^{2+}$  ions are able to substitute  $\text{Ca}^{2+}$  ions. The outcome of animal studies suggest, that Ca can be replaced by Sr in nearly any physiological process and is almost exclusively incorporated into bone [126]. Ca and Sr have a similar protein binding affinity [128]. As said before (Chap.4.4.) the dietary amount of Sr can vary widely without occurrence of symptoms of intoxication and it is not under homeostatic control so the blood and serum levels are not kept constant [126].

Sr might be increased in the cement lines, however the increase of Sr is presumably too small to be distinguished in the measurement voxel with a lateral size of about  $17\text{ }\mu\text{m} \times 12\text{ }\mu\text{m}$  (horizontal x vertical) and a cement line thickness of only 1 to  $2\text{ }\mu\text{m}$  (elaborated in Chap. 8.2.7.4 "Limitations").

### 8.2.7.2) Trace Element Content vs. Mineralization

Within a BSU the trace elements are uniformly distributed similar to element Ca. Our hypothesized mechanism of trace element incorporation is therefore, that Zn, Sr and Pb are incorporated into the bone mineral (carbonated calcium hydroxyapatite) during bone formation, when the osteoid gets mineralized by progression of the mineralization front (primary mineralization phase) [85]. The amount of the incorporated trace elements is thereby dependent on serum levels present. This assumption is strongly supported by the studies we made on Sr incorporation in bone during Sr-ranelate treatments (human and animals [146, 198, 199]). It could be shown that Sr was incorporated mainly in bulk bone, which was formed during Sr ranelate treatment. Further, the Sr content was proportional to the Sr serum levels [198]. Moreover, the analysis of the mineral crystal lattice characteristics proved that the Sr ion was incorporated in the apatite crystal lattice [199].

The Pb present in bulk bone is most likely accumulated during the mineralization phase. Pb present as  $\text{Pb}^{2+}$  ions in the serum are chemically similar to  $\text{Ca}^{2+}$  ions. It has been demonstrated that  $\text{Pb}^{2+}$  is directly competing with  $\text{Ca}^{2+}$  at the voltage activated  $\text{Ca}^{2+}$  channels [181, 182]. Thus it can be assumed that  $\text{Pb}^{2+}$  is transported into the bone as  $\text{Ca}^{2+}$  and is built into the CcHA crystal lattice instead of  $\text{Ca}^{2+}$  during the mineralization. It has been shown that  $\text{Pb}^{2+}$  is able to occupy both  $\text{Ca}^{2+}$  sites in the CaHA crystal [4, 183-185]. Similar was suggested for  $\text{Sr}^{2+}$  ions [126, 199]. We assume that as for Sr [22, 198-202] the

amount of Pb incorporated during the mineralization is depending of the Pb serum levels. More  $\text{Pb}^{2+}$  ions present in the serum result in an increased Pb incorporation into bone. In addition it is well founded from various studies that calcium hydroxiapatite (CaHA) has the ability to accumulate (immobilize)  $\text{Pb}^{2+}$ ,  $\text{Zn}^{2+}$ ,  $\text{Sr}^{2+}$  and other divalent metal ions [163, 165, 168, 203-206]. At the moment four different pathways are suggested for the immobilization mechanisms of CaHA: i) ion exchange process, ii) surface complexation, ii) dissolution and precipitation and co- precipitation [163]. These mechanisms can be expected to be very similar for the other divalent ions. It has to be noted that all these mechanisms have been studied in-vitro using synthetic CaHA as well as bovine bone meal, to test the usability of CaHA in remediation processes of heavy-metal-contaminated soil and water [178]. In these studies rather high concentrations of the heavy metals have been used. However according to Bigi et al. (1989) [179] and Bückner et al. (1995) [180] it is almost certain that the accumulation mechanisms of CaHA for  $\text{Pb}^{2+}$  are also valid at low concentrations, as they are present in humans.

For Pb we have shown that it is almost exclusively bond to carbonated calcium hydroxyapatite [161], which is backing up the above assumptions how Pb is incorporated into bulk bone.

Interestingly, despite high intra and inter-individual variations of Pb (Fig. 8.2.2) and Sr levels, a non-linear increase with Ca-content of the bulk bone was found (Fig. 8.2.4). The over-proportional increase of Pb and Sr at the high mineralization range, may be explained by the fact that BSUs reach a plateau of mineralization (about 26 wt%Ca) [85] with prolonged time of mineralization (secondary mineralization phase). However, accumulation processes, as already stated above, of  $\text{Pb}^{2+}$  and  $\text{Sr}^{2+}$  ions in the apatite crystals may be still ongoing with time, after the crystals had stopped growing. The  $\text{Sr}^{2+}$ ,  $\text{Pb}^{2+}$  and presumably all other divalent metal ions reach the inner parts of the bone through the vascular and haversian channels. An animal study using radiostrontium ( $^{85}\text{Sr}$ ) showed that the  $\text{Sr}^{2+}$  ions pass through the wall of the haversian capillaries by diffusion to reach the extracellular fluids [207]. The same way can be assumed for  $\text{Pb}^{2+}$  ions. From there and the bone marrow the osteocyte lacunae canaliculi network might be used as pathway for the  $\text{Pb}^{2+}$  and  $\text{Sr}^{2+}$  into the mineralized bone matrix. Resulting in the observed overproportional increase of these elements compared to Ca.

Though it has been reported that Zn is concomitantly incorporated with Ca during the mineralization [124], no correlation between Zn and the degree of mineralization like for Sr and Pb was detected by our measurements (Fig. 8.2.4). This is in agreement with prior investigations of Lappalainen et al. (1982), who showed that Ca is not a significant factor for explaining the Zn concentrations in bone [208].

Zn bond to CaHA is very likely incorporated during the fast crystallization process as experiments of Tang et al. have shown 2009. However the preference coordination site of Zn, the Ca<sub>2</sub> site of the CaHA crystal, would allow the uptake and release of Zn as at the Ca<sub>2</sub> site the framework of the structure is not disrupted [209]. Matsunaga et. al described in a study 2010 a mechanism for Zn<sup>2+</sup> incorporation into CaHA: Zn<sup>2+</sup> is not simply incorporated by ion exchange processes, but Ca<sup>2+</sup> vacancy-defects can act as plausible sites for Zn<sup>2+</sup> substitution [210].

As said above, Zn is essential for bone metabolism, as it is part of enzymes important for the remodelling mechanisms of bone and the Zn released during bone remodelling is incorporated back into bone [189, 193, 195].

This may be one explanation of our findings, that Zn is not correlated with the degree of mineralization. Therefore Zn is suggested to be under homeostatic control.

### 8.2.7.3) General and Medical Implications

The main sources of Pb exposure in industrialized countries derived in the past from leaded water pips and leaded gasoline. Much effort has been taken to eliminate almost all of these sources [3]. Keeping in mind that the biological half life in human bone is about 20 years [117, 118], individuals in the range of 60 to 80 years have already accumulated a significant amount of Pb in their skeleton [119, 120], which still present in measurable concentrations. Bone seems to act as filter for Pb to reduce the concentration in circulation protecting this way the brain and other organs from the toxic effects of the heavy metal.

As for our findings we can speculate that in case of an undisturbed bone remodelling cycle the Pb<sup>2+</sup> released during resorption of the cement lines and bulk bone is influencing the bone metabolism locally due to increased Pb levels at the resorption site. The effects of Pb on bone cells and bone metabolism and thus bone remodelling is described in detail in literature for whole body exposure to high levels of Pb [4, 112, 115, 182, 211]. Pb has been shown to alter the Ca homeostasis and perturb the cellular metabolism or activity of

osteoclasts [212] and osteoblasts [213-218]. As already stated  $\text{Pb}^{2+}$  has a much higher affinity to osteocalcin than  $\text{Ca}^{2+}$  [211] and as a consequence the  $\text{Pb}^{2+}$  is influencing the binding properties of osteocalcin to the bone minerals is negatively [115]. We can speculate the same mechanisms may take effect locally, though to a much lower extent, as the concentration of  $\text{Pb}^{2+}$  ions will be diluted with not Pb contaminated blood or extracellular fluids.

Medical conditions or diseases, such as osteoporosis, hyperthyroidism, hyperparathyroidism and pregnancy cause an increased bone turnover and are accordingly linked with elevated release of Pb immobilized and stored in the skeleton [108, 219, 220]. The remobilization of bone Pb back into the circulation is a potentially relevant source of soft-tissue Pb exposure and toxicity long after the external Pb exposure ceased [113]. The Pb in serum may increase to levels, which are possibly toxic for inner organs more sensitive to Pb and other heavy metals like the nervous and the hematopoietic system. Even metabolic processes in bone are adversely affected by Pb [4, 112, 115, 182, 211]. Further, Pb has been stated as potential risk factor for osteoporosis [109] and has negative influences on bone healing mechanisms [111] and might affect the articular cartilage tissue [104].

The Sr incorporation is most likely depending on the dietary habits of the individuals. It has been reported that sea food contains increased amounts of Sr [221]. The extensive consumption of sea food may therefore lead to increased Sr accumulations in the BSUs build at this time. Exposure may also result from contaminated phosphate binders and the use of parenteral and dialysis fluids containing Sr [222-224].

The incorporated Pb, Zn and Sr ions in CaHA will most likely distort the crystal lattice of the mineral due to the different atomic sizes compared with Ca. A distortion of the crystal lattice could be shown in the case of SrR treatment compared to the placebo group. However changes in bone mineral quality and strength due to incorporation of higher amounts of Sr could not be detected [198]

### 8.2.7.4) Limitations

Directly matching qBEI images with  $\mu$ -XRF obtained elemental maps has one drawback, the different lateral resolution ( $\sim 10 - 20 \mu\text{m}$  for SR  $\mu$ -XRF and  $1 \mu\text{m}$  for qBEI) makes an exact overlap impossible. Sharp features in the qBEI are blurred in the  $\mu$ -XRF maps. Furthermore, the larger information depth of SR  $\mu$ -XRF ( $\sim 20 \mu\text{m}$  for Ca-K $\alpha$ ) compared to

qBEI ( $\sim 1 \mu\text{m}$ ) contributes to the blurring. Features just below the surface (e.g. cement lines, or cavities) cannot be detected with qBEI but are visible in the corresponding  $\mu\text{-XRF}$  maps. However, superimposing the  $\mu\text{-XRF}$  elemental maps and the corresponding BE images turned out to be a suitable method to link bone morphology with X-Ray intensities.

As the cement lines are much thinner (up to about  $5 \mu\text{m}$ ) than the focused X-Ray beam width, the obtained fluorescence intensities of Zn and Pb in the cement lines are the result of averaging the XRF signal over a larger matrix volume than the true cement line feature occupies. Accordingly the actual increase of the elemental levels in the cement lines compared to the bone packets is always underestimated by our SR  $\mu\text{-XRF}$  analysis. So the obtained data shows a lower limit for the real relative elemental concentration.

Assuming a SR  $\mu\text{-XRF}$  voxel size of  $12 \times 13 \times 17 \mu\text{m}^3$  and a cement line of thickness of  $1 \mu\text{m}$ , which fills only  $\sim 6\%$  of the measurement voxel at the best, a 2-fold increased Pb level in the cement line as measured by  $\mu\text{XRF}$ , might be the result of an actual 34-fold increase. Additionally the exact localisation of Zn and Pb, whether the trace elements are present right in the cement line or in the adjacent remaining old or new formed bone was not possible, due to the limitations in the spatial resolution. To assess this information measurements at a nanofocus beamline with sufficient photon flux such as the P06 at Petra III (Hasylab Hamburg, Germany) would be required.

### 8.2.8) Conclusion

Using a combination of qBEI and SR  $\mu\text{-XRF}$  it was shown for the first time that the local distribution of Zn, Sr, and Pb in bone tissue is not uniform. The results of the investigations imply that the incorporation of Zn, Pb and Sr is strongly depending on the bone tissue type. Compared to adjacent bone matrix, cement lines accumulate higher amounts of Zn and Pb. Further the amount of Pb and Sr incorporated in BSUs was found to be dependent on the degree of mineralization. Interestingly this was not the case for Zn.

Though bone turnover is altered in osteoporosis no evidence was found in the investigations, that the trace element levels or distributions are influenced by this disease.



### **8.3 Sr Incorporation into Bone During Osteoporosis Treatment with Strontium Drugs**

Finding new ways of treating osteoporosis and reducing the negative impacts (e.g. vertebral and non-vertebral fractures) of this disease is one of the urgent topics in medicine. Attempts to use strontium as drug for skeletal diseases are already studied for about 50 years [225-229].

In a number of countries strontium ranelate (SrR) is allowed to be used as therapeutic agent for postmenopausal osteoporosis (pmpOP), after it could be shown that this drug reduces vertebral and non-vertebral fractures [10]. Several studies dealt with the effects that are supposed to cause the reducing of the fracture risk by SrR. These studies include the investigation of bone remodelling balance, the micro architecture and the influence of Sr on the Ca receptors in bone cells [22, 230-232]. Further investigations were made on the impact on the material properties and how long the Sr is stored in bone [198, 199, 233]. As Sr has double the atomic weight of Ca, the incorporation of Sr is drastically influencing an important parameter in clinical diagnostics of the fracture risk, the bone mineral density (BMD). Higher BMD in Sr treated patients is not only a result of less bone resorption or increased formation, it is also caused by the incorporated heavier Sr atoms. Thus the results become more delicate to interpret [234-236]. In numerous studies, mainly animal experiments have shown that a higher Sr serum level leads to more incorporation of Sr into bone [22, 198-202]. The Sr atoms are incorporated into the crystal lattice of the carbonated calcium hydroxyapatite crystals by replacing the Ca ions with Sr ions. This takes mainly place in the BSUs formed during the Sr therapy [22, 198, 199] and it has to be mentioned that about 99% of the body Ca and Sr are present in the skeleton [201]. The Sr atoms are incorporated into the crystal lattice of the bone hydroxyapatite by ionic substitution of calcium [199].

Little is known whether calcium deficiency can affect the incorporation of Sr into bone. Bone samples of an experimental animal model [22] have been measured to shed more light on the topic of Sr uptake into bone during osteoporosis treatment with different Sr drugs and altered nutritional Ca intake.

Furthermore there was the opportunity to analyze two human bone biopsy samples from patients receiving SrR therapy.

### 8.3.1) Increased Strontium Uptake in Trabecular Bone of Ovariectomized Calcium Deficient Rats Treated with Strontium Ranelate or Strontium Chloride [146]

A recent study in ovariectomized (OVX) rats [22] determined the effects of high (150mg/kg/day) and low (25 mg/kg/day) dose SrR on bone histomorphometric indices, mechanical properties and Sr uptake. Furthermore, the role of dietary calcium in modulating the effect of SrR on the skeleton was examined by feeding rats either a normal (1.19% Ca) or a low calcium diet (0.1% Ca). The concentration and distribution of Ca and Sr in cortical bone tissue of the tibial midshaft region was determined using SR  $\mu$ -XRF. Animals treated with high dose SrR had significantly higher Sr incorporation, regardless of Ca intake. However, compared to the normal Ca diet, the low Ca diet increased the incorporation of Sr into the bone for low and high dose SrR groups. All animals treated with SrR had a higher Sr fraction at the periosteal bone surface (newly formed bone regions) compared to intracortical bone regions (older bone).

Within this study the investigation on the effects of low and normal calcium diets on the Sr incorporation have been extended to the uses of  $\text{SrCl}_2$  as therapeutic agent in addition to SrR. Further the far more complex structure of trabecular bone in vertebrae was studied using SR  $\mu$ -XRF and qBEI analysis with respect to the incorporation of Sr during the treatment with the two different Sr drugs depending on the Ca intake.

#### 8.3.1.1) Samples

We analyzed bone samples from the previously reported study [22] on Sr treatment in three-month old OVX Sprague-Dawley rats. The animal study was approved by Indiana University's Institutional Animal Care and Use Committee. OVX rats were randomized by body mass 3 weeks post surgery and divided into eight different treatment regimens: low (25 mg/kg/d) and high (150 mg/kg/d) dose SrR with low (0.1% Ca) and normal (1.19% Ca) dietary Ca; low (25 mg/kg/d) and high (150 mg/kg/d)  $\text{SrCl}_2$  with low (0.1% Ca) and normal (1.19% Ca) dietary Ca. The  $\text{Sr}^{2+}$  ion equivalents for SrR with the chemical formula of  $\text{C}_{12}\text{H}_6\text{N}_2\text{O}_8\text{SSr}_2$  (513.49 g/mol) were 8.5 mg/kg/d and 51 mg/kg/d, and for  $\text{SrCl}_2$  with the chemical formula  $\text{SrCl}_2 \cdot 6(\text{H}_2\text{O})$  (266.62g/mol) were 9.4 mg/kg/d and 56 mg/kg/d, for the low and high Sr doses, respectively. SHAM operated and untreated OVX rats fed a normal Ca diet served as controls. Animals were treated daily for 90 days. According to previously published Sr serum level data [22] the different treatments regimes led to following mean Sr

serum levels: 22,7 and 23,3 ng/mL for untreated SHAM and OVX, 2226,7 and 293,5 ng/mL for 25 mg/kg/d SrR treatment at 0,1% and 1,19% Ca diet, respectively, 12611,1 and 1746,0 ng/mL for 150 mg/kg/d SrR treatment at 0,1% and 0,19% Ca diet, respectively. One L3 vertebra from each group was used for analysis, while all the measurements of the bone samples were performed blinded to the treatment (Tab. 8.3.1).

The vertebrae cut in sagittal plane were prepared as described in Chap. 6.4.

### 8.3.1.2) qBEI Analysis

qBEI was performed in a digital SEM as describe in detail in (Chap. 6.3). The entire cancellous bone area was imaged by qBEI using a pixel resolution of 4 $\mu$ m. From the obtained grey-scale images ROIs containing both, old and newly formed BSUs, were selected for the element mapping with confocal SR  $\mu$ -XRF.

### 8.3.1.3) SR $\mu$ -XRF Analysis

A confocal SR  $\mu$ -XRF setup using the polycapillary half lenses and the 50mm<sup>2</sup> Vortex SDD at the FLUO beamline at ANKA at the Karlsruhe Institute of Technology Campus North (Karlsruhe, Germany) (see Chap. 6.1.3) was used. The lateral beamsize was about 10 x 10  $\mu$ m<sup>2</sup> and a depth resolution of 12  $\mu$ m at 14,2 keV (at Sr-Ka). To achieve optimal excitation conditions for Sr K-Lines, the excitation energy was adjusted to 17.7 keV and the measuring time was set to 1 second/pixel. Area scans, ranging from 300 x 300  $\mu$ m<sup>2</sup> up to 850 x 850  $\mu$ m<sup>2</sup> depending on the qBEI determined areas of interest, were performed in 10  $\mu$ m steps. The sensitivity of the method was sufficient to easily detect the natural Sr content of bone (about 0,1 wt %).

The treatment of the acquired spectra and the generation of the  $\mu$ -XRF maps are described in Chap. 5.1.

### 8.3.1.4) Data Evaluation

Due to the large number of maps (up to 8 scans per sample and 10 samples resulting to a total of 42 scans), an automated image data analysis technique - K-Means Clustering (KMC) in combination with Principal Component Analysis (PCA) pre treatment - was used to extract the typical Sr to Ca Ka-line count fractions of the measured bone areas (see Chap. 5.3).

The median and range [min; max] (Tab. 8.3.1) of the Sr to Ca count fraction values ( $\text{Sr}/(\text{Ca}+\text{Sr})$ ) of cluster C4 from the individual elemental maps per bone tissue sample was determined. Cluster C4 was the region of highest Sr count fractions representing the newly formed mineralized bone matrix (compare Fig 8.3.1).

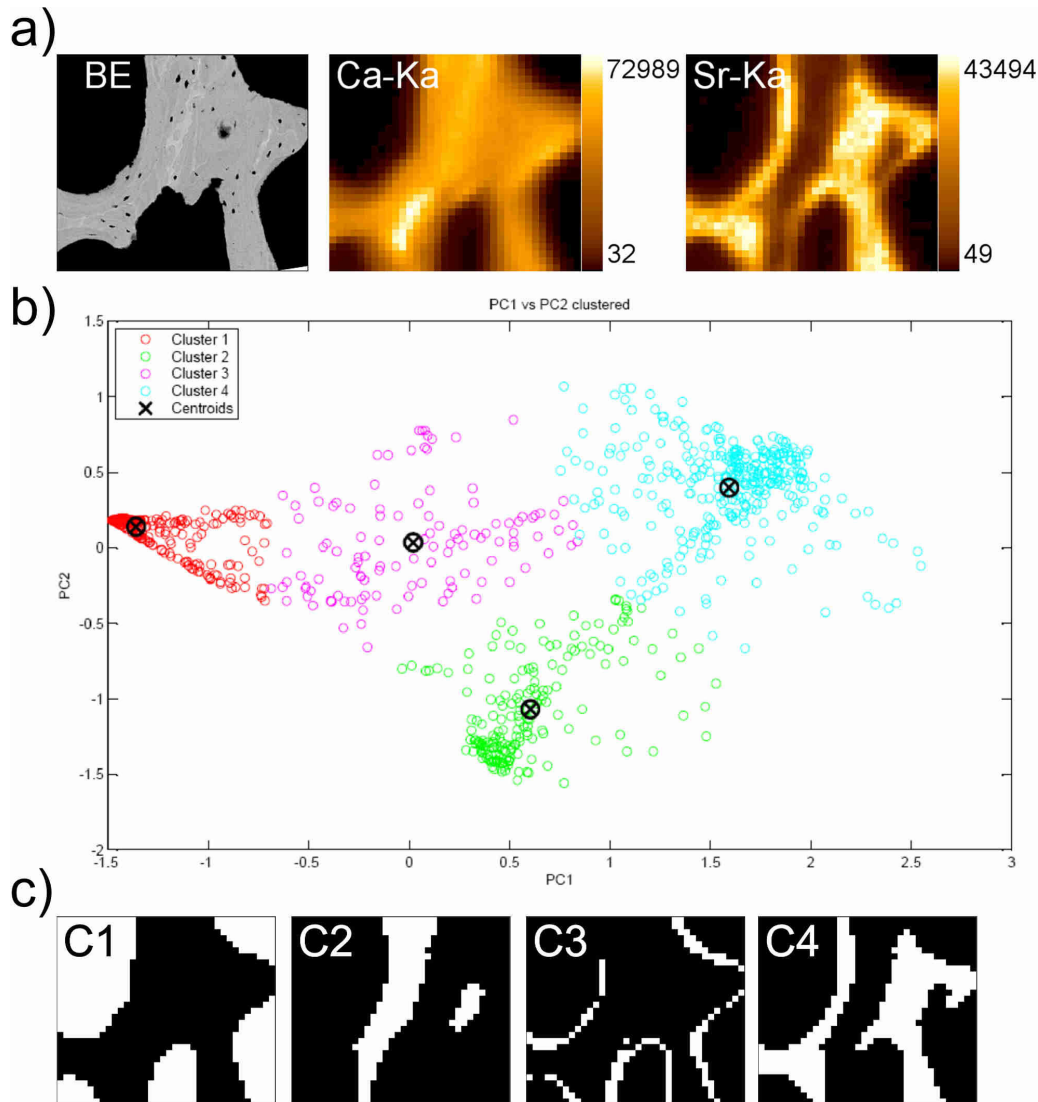


**Figure 8.3.1: Example of a PCA+KMC analysis: The scan was done on a sample (P02 of Table 8.3.1) with high dose SrR treatment at deficient Ca diet. [146]**

**a) qBEI and corresponding  $\mu$ -XRF maps (Ca & Sr) of the sample.**

**b) Score plot of principle components PC1 vs PC2 derived from a plot of Ca versus Sr intensities by linear transformation exhibiting a new set mutually orthogonal axis. PC1 axis represents the direction, where Ca and Sr intensities are related like, more Ca more Sr. PC2 axis represents the direction, where Ca and Sr intensities are related like, more Ca less Sr and vice versa. The KMC analysis of the PCA score plot used four clusters ( $k=4$ ): color-coded red (C1), green (C2), pink (C3) and blue (C4);**

**c) The meaning of the clusters can be explained by generating binary images, where all pixels corresponding to a certain cluster are displayed in white.**

**Table 8.3.1: Analyzed samples and information about the treatment including the Sr/(St+Ca) values obtained for cluster C4 (region of highest Sr levels). The median and range [min; max] for each bone sample are given; N is the number of maps per sample; p-values in brackets (...) means, the data of SrR and SrCl<sub>2</sub> samples were pooled. Significance was obtained using the Mann-Whitney test; p<0,05 was considered significant.**

experimental data					p-values between groups of maps			
sample (N)	Fed drug doses [mg/kg/d]	Sr <sup>2+</sup> doses [mg/kg/d]	Ca- diet [weight %]	Sr/(Ca+Sr) (count rates)	vs. control	low vs. high Sr	deficient vs. normal Ca	SrR vs SrCl <sub>2</sub>
P06 (3)	SHAM non	non	1.19	0,0012 [0,0010;0,0013]				
P05 (4)	OVX non	non	1.19	0,0011 [0,0011;0,0012]	<0.01			
P07 (5)	SrR 25	SrR 8,5	1.19	0,024 [0,020;0,024]	<0.01			ns
P09 (4)	SrCl <sub>2</sub> 25	SrCl <sub>2</sub> 9,4	1.19	0,02148 [0,018;0,023]	<0.05		<0.05 (<0.001)	
P04 (3)	SrR 25	SrR 8,5	0.1	0,1015 [0,094;0,109]	<0.01		<0.05 (<0.001)	ns
P08 (4)	SrCl <sub>2</sub> 25	SrCl <sub>2</sub> 9,4	0.1	0,085 [0,081;0,095]	<0.01	<0.05 (<0.001)		
P01 (4)	SrR 150	SrR 51	1.19	0,140 [0,136;0,153]	<0.001	<0.01 (<0.001)		<0.05
P10 (8)	SrCl <sub>2</sub> 150	SrCl <sub>2</sub> 56	1.19	0,130 [0,105;0,138]	<0.05	0.1 (<0.001)	0.05 (<0.001)	
P02 (3)	SrR 150	SrR 51	0.1	0,4252 [0,418;0,435]	<0.01	<0.05 (<0.001)	<0.01 (<0.001)	0,057
P03 (4)	SrCl <sub>2</sub> 150	SrCl <sub>2</sub> 56	0.1	0,3528 [0,322;0,378]				

Mann-Whitney tests between the groups of single Sr/(Ca+Sr) outcomes from each bone sample were performed to determine the significance levels (p-values) of the differences. A p<0.05 was considered as significant. Additionally, the significance of differences between low and high Sr doses or deficient and normal Ca nutrition was also evaluated independently for type of administration (SrR and SrCl<sub>2</sub>). In these cases the outcomes of SrR and SrCl<sub>2</sub> samples were correspondingly pooled (Tab. 8.3.1).

#### 8.3.1.5) Results

The incorporation of Sr into the BSUs of rat vertebrae during a differential treatment with two Sr drugs (SrR and SrCl<sub>2</sub>) at normal and deficient Ca diet was analysed using SR  $\mu$ -XRF. The ROIs for measurement were selected from the qBEIs with respect to the presence of young (low mineralized - darker grey-levels in qBEI) and old (well mineralized lighter grey-levels in qBEI) bone. In Fig. 8.3.1 an example maps set (Ca-K $\alpha$ , Sr-K $\alpha$  including the corresponding qBEI) is shown. For these images it can be easily seen, that Sr was

predominantly incorporated into the new, less mineralized bone packets, indicated by the highest Sr-K $\alpha$  intensity values. The areas of incorporation were mainly found at the outer boarder of the trabeculae.

In the controls the Sr levels presented a totally homogeneous distribution, caused by the natural Sr intake (Fig. 8.3.2a), suggesting that the base level of natural Sr was equally incorporated in all bone build during the lifetime.

The results were sorted with respect to the maximum obtained Sr count rates (Fig. 8.3.2).

The Sr count rates increased for the various treatment groups as follows:

1. control groups
2. low does Sr with normal Ca diet
3. high does Sr with normal Ca diet
4. low does Sr with deficient Ca diet
5. high does Sr with deficient Ca diet

The different types of Sr drugs were not distinguished. Low dose SrR and SrCl<sub>2</sub> were pooled as well as the high dose groups.

Further all measured samples (P01 to P10) could be assigned consistently to the different treatment groups through the evaluation with PCA and KMC. The cluster with the largest Sr/(Sr+Ca) values (C4) could be linked to the new formed BSUs - which could be assured by comparison with the respective qBEI data (Fig. 8.3.2). The data obtained for cluster C4 are tabulated in Tab. 8.3.1.

In case of normal Ca diet the incorporated Sr values increased for low SrR dose 20,8-fold and for high SrR dose 121,7-fold in relation to the untreated controls.

The maximum Sr incorporation as increased due to Ca deficiency 89-fold for low dose and 365-fold for high dose of SrR. This is shown clearly in Fig. 8.3.2.

In case of low dose Sr the incorporation in the new bone was lower for the SrCl<sub>2</sub> treatment for both of Ca diets (deficient: -9.1%, normal: -7.1%). However this was not significant. In case of high Sr dose treatment the values for SrCl<sub>2</sub> were distinct lower (deficient: -19,8%, normal: -20,4%), but only partly significant.

The uptake of Sr in the SrR treatment was always slightly higher the for the SrCl<sub>2</sub> though the Sr<sup>2+</sup> dose of SrR is 10% smaller than for the SrCl<sub>2</sub> (see Tab. 8.3.1 or Fig 8.3.2)

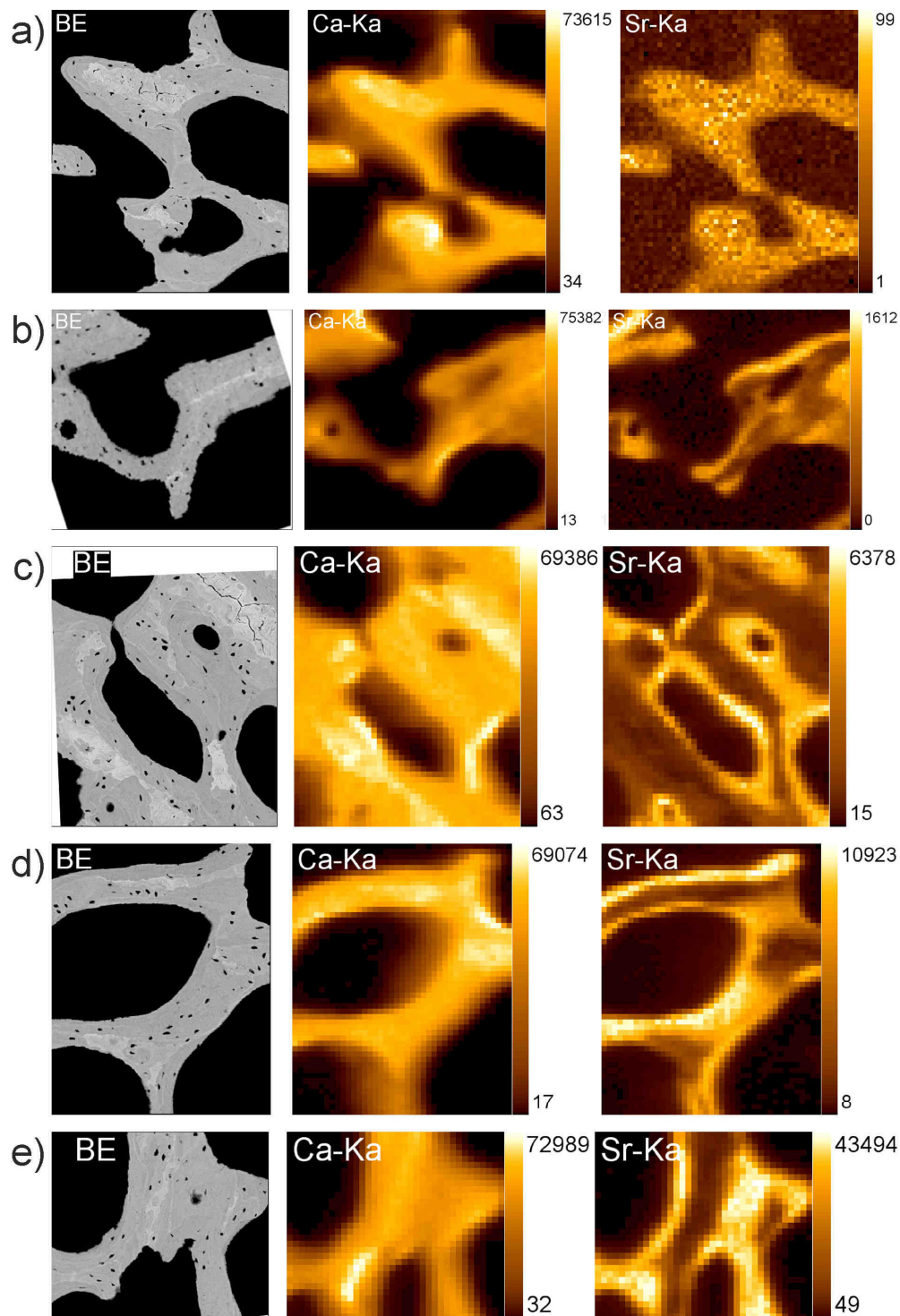


**Figure 8.3.2: Examples of qBEI images and the corresponding SR  $\mu$ -XRF elemental maps Ca and Sr: (a) untreated, low Sr dose with (b) normal and (c) deficient Ca diet, high Sr dose with (d) normal and (e) deficient Ca diet. SrR and SrCl<sub>2</sub> treatment were not distinguished [146].**

**Pixel size: 10  $\mu$ m x 10  $\mu$ m, normalization to 100 mA R-C and cps;**

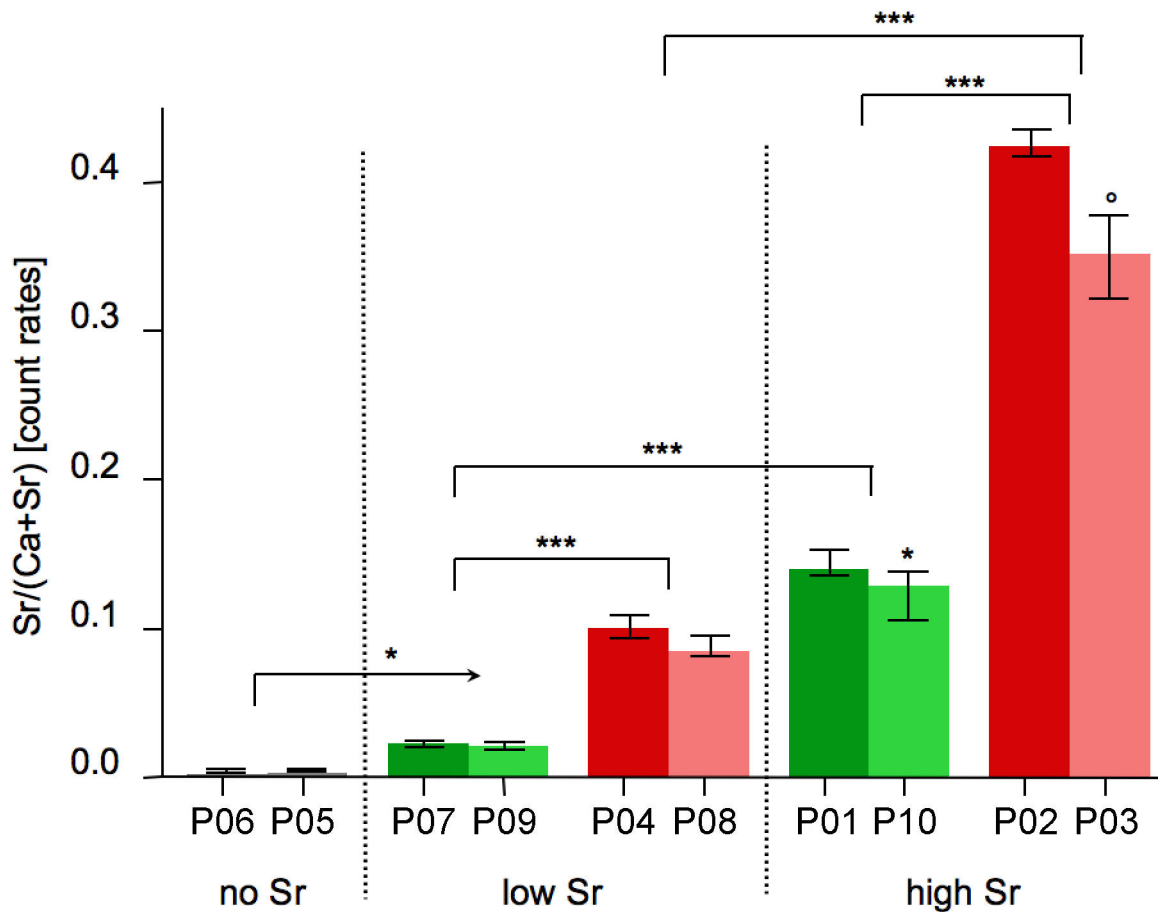


**Figure 8.3.3: Effect on the Sr incorporation due to the Ca diet within the new formed bone. The bars show the median for each sample and the error bars the range; deficient (red) Ca diet, SrR dark colours and SrCl<sub>2</sub> light colour. For each sample median and range (error bars) resulting from all maps recorded are indicated. Significance test: Mann Whitney test; \*  $p < 0.05$ , \*\*\*  $P < 0.001$ , °  $p = 0.057$ . (Adopted from [146])**

#### 8.3.1.6) Discussion

The combination of qBEI, SR  $\mu$ -XRF and the automated evaluation of the XRF maps of Sr and Ca with PCA and KMC enabled the right assignment of the measurement data to the different treatment groups (not distinguishing SrR and SrCl<sub>2</sub>)

The PCA-KMC combination was previously applied to rock and glass samples [145]. However it was to the best knowledge the first time it was used in combination with bone samples to cluster the regions of similar characteristics e.g. more Ca less Sr or more Sr less Ca. The idea of using a mathematical method was to avoid a possible bias through the interaction with the observer (data evaluating scientist). One more advantage of the PCA



KMC treatment is, that it is very fast and a large number of maps (42 scans) can be treated easily in batch mode. This method can be also used for more than two elements (see [145]). The present analysis of the bone tissue regions with a maximum in Sr to Ca counts fraction consistently and correctly identified tissue from none treated and from all animals treated differently with the 8 combinations of Sr treatment and dietary Ca.

Low Ca significantly increased (3-4 times, Table 1) the Sr to Ca counts fraction in the C4 cluster identified by qBEI imaging as newly formed bone, i.e., regions with low Ca content predominantly at the bone surface. In this context, it is interesting, how the serum levels were influenced by dietary Ca, because the serum level of Sr determines how much Sr is incorporated in the HA lattice during bone formation [198, 199]. As previously reported [22] these rats treated with 25 or 150 mg/kg/day of SrR and fed the low calcium diet (0,1% Ca) showed >7x increases in serum Sr levels compared to rats fed the normal calcium diet (1,19% Ca). Such an effect of nutritional Ca deficiency might be of importance concerning safety issues of Sr-treatment in patients with osteoporosis. Normal serum Ca levels, and adequate Ca and vitamin D intake must be a prerequisite of any osteoporosis treatment. Low serum Ca levels would result in higher uptake of Sr, which can induce osteomalacia and mineralization defects [229, 237, 238].

We also compared Sr uptake in bone with administration of 2 different forms of Sr, (SrR and SrCl<sub>2</sub>). At both Sr<sup>2+</sup> doses, low and high, the Sr uptake in the new mineralized bone matrix was higher with SrR compared to SrCl<sub>2</sub>, even though the Sr<sup>2+</sup> equivalent with SrCl<sub>2</sub> was 10% higher than with SrR. For the normal Ca diet, it was about 8% higher, while for the low Ca diet it was +20% higher. The results suggest that when Sr treatment occurs at normal dietary Ca levels, SrR promotes greater uptake to bone compared to SrCl<sub>2</sub>. However, care has to be taken for adequate Ca serum levels, because SrR might deliver too much Sr into the serum in case of Ca deficiency.

### 8.3.1.7) Limitations

The study was designed as a pilot study for testing the sensitivity to detect spatially resolved Sr in bone after different Sr treatment regimes using a special confocal SR  $\mu$ -XRF set up. For this purpose we analyzed just one vertebral bone sample per group from 10 groups; two from untreated animals (SHAM and OVX) and eight from animals of different treatment regimens (low and high Sr as SrR or SrCl<sub>2</sub> combined with normal or low dietary Ca).

However, the consistency in relationship between sample outcome and treatment regime as well as agreement with the previous analysis of the tibial/periosteal bone (n=10/group) [22], suggests that the one tissue/group analyzed in this study was representative of its treatment group. Although several numerical differences were large, many were not statistically significant. This is likely due to the limited number of scans per bone tissue (in majority 3 to 4 scans).

Another limitation is that the reported Sr and Ca concentrations are not given in absolute values (weight %), but always in fractions of Sr to Ca X-Ray peak count rates. Unfortunately, there are no suitable reference standards for this novel experimental set up that would have allowed calculation of absolute Sr and Ca concentrations from the X-Ray count rates. Differences in sensitivity of the system to detect Ca and Sr, and differences in matrix effects between Ca K $\alpha$  and Sr K $\alpha$  X-Rays make it difficult to generate suitable reference standards.

Sr serum concentrations in this study were lower or encompassed levels (12,611 ng/mL, or 185  $\mu$ mol/L) comparable to those produced by SrR treatment of postmenopausal osteoporosis (10,560 ng/mL or 120.4  $\mu$ mol/L)[198, 239]. In this human study an atomic fraction for Sr to Ca of 5% was found (Roschger *et al.*, 2010, Li *et al.*, 2010), but extrapolation from animals to humans and vice versa should be done with caution.

### 8.3.1.8) Conclusions

In conclusion, dietary and serum levels of Ca are important determinants of serum Sr levels and Sr uptake into bone with SrR treatment for osteoporosis. To avoid higher uptake rates of Sr and improve safety in patients being treated with SrR, adequate Ca and Vitamin D intake is essential.

### 8.3.2) Human Biopsy Samples of Strontium Ranelate Treated Patients

Samples from human patients treated with strontium ranelate are quite rare, as treated patients tend to suffer less vertebral and non-vertebral fractures [10] and permissions for taking bone biopsies of healthy patients are subject to rigorous regulations.

Despite these facts there was the possibility to analyse two samples from human patients treated with SrR with the confocal  $\mu$ -XRF setup at ANKA FLUO beamline. One sample (4653a) was collected during the treatment and the second sample (4567x) 6 months after the treatment with SrR was stopped.

The concept of measuring these samples was to see if the effects of Sr incorporation into human bone is comparable the observations from the rat model. Further more it was possible to elucidate the influence of a break in the SrR treatment on the Sr incorporation.

#### 8.3.2.1) Samples

The two analyzed samples are of human origin. The samples were initially taken for clinical purposes, to check the impact of the treatment and to obtain data basis for the further treatment strategies. The patients agreed that the samples can be further used for scientific analysis beyond the clinical necessary ones.

The first sample (4653) was harvested from a 90 year women during surgery in AUVA Trauma Center Meidling, Vienna, after suffering a hip fracture. The patient received Protelos® SrR treatment starting 3 years before the sample collection.

The second sample (4567) was collected from a 48 year old women suffering from idiopathic osteoporosis with vertebral fractures. The treatment was 15 month of bisphosphonates followed by 12 month of Protelos® SrR. The sample was obtained by means of an iliac crest biopsy in II. Med. KH Barmherzige Schwestern, Vienna, 6 month after the SrR treatment was finished.

**Table 8.3.2: List of measured human SrR treated bone samples**

Sample No.	Age	Sex	SrR treatment	sample collection
4567x	48 yr	F	1 year	6 month after treatment
4653a	90 yr	F	3 years	during treatment

Both samples were prepared in the same way as the rat vertebrae, as PMMA embedded blocks, polished and carbon coated for qBEI analysis prior to SR  $\mu$ -XRF measurements. For further details on the sample preparation see Chap. 6.4.

### 8.3.2.2) qBEI Analysis

qBEI was performed in a digital SEM as describe in detail in (Chap. 6.3). The entire cancellous bone area was imaged by qBEI using a pixel resolution of 1 $\mu$ m. From these qBEI grey-scale images areas of interest (ROI) have been selected for elemental mapping by confocal SR  $\mu$ -XRF. The selection criteria were such that the ROI contained bone features with BSUs (packets, osteons) of low and light grey levels representing the coexistence of young and older bone matrix.

### 8.3.2.3) SR $\mu$ -XRF Analysis

The confocal SR  $\mu$ -XRF setup at the FLUO beamline at ANKA (Karlsruhe, Germany) (see Chap. 6.1.3) was used.

Sample 4653a was analyzed with a beam size of 12 x 15  $\mu$ m<sup>2</sup> and the depth resolution was 20  $\mu$ m at 9.71 keV (Au-La). The excitation energy was set to 17.0 keV. The measuring time was set 1 sec./pixel for each map and the step width was 10 $\mu$ m in both directions. At the six positions, selected from the qBEI data, area scans on the sample surface in the size of 600 x 500  $\mu$ m were performed.

Sample 4567x was measured with a beam size of 13 x 12  $\mu$ m<sup>2</sup> and the depth resolution was 19  $\mu$ m at 9.71 keV (Au-La). The excitation energy was set to 16.7 keV. The measuring time was set 1 sec./pixel for each map and the step width was 10 $\mu$ m in both directions. At the five positions selected from the qBEI data area scans on the sample surface in the range of 1000 x 500  $\mu$ m up to 1050 x 1000  $\mu$ m were performed. As written in Chap 8.2.4 depth scans were performed to determine the correct measurement plane – the surface layer of the sample

The treatment of the acquired spectra and the generation of the  $\mu$ -XRF maps are described in Chap. 5.1.

### 8.3.2.4) Data Evaluation

The data from the human samples were treated the same way as the data from the rat samples. PCA and k-means clustering were used to identify areas of similar properties. Details can be found above (Chap. 5.3). As before 4 clusters turned out to be sufficient. The used PCA-KMC software was developed and written by Martin Fölser (Atominstitut TU Wien 2008) [144].

Mann-Whitney tests between the Sr/(Ca+Sr) outcomes of the bone areas build without and during the SrR treatment were performed to determine the significance levels (p-values) of the differences. A  $p < 0.05$  was considered as significant.

ImageJ (v1.44, Wayne Rasband, National Institutes of Health, USA, <http://rsb.info.nih.gov/ij>) [130] was used to roughly estimate Sr-Ka and Ca-Ka count rates in the mineralized bone matrix build before and after the SrR treatment of sample 4567x - these features could not be separated satisfying using the PCA-KMC approach. Regions of interest (ROIs) have been selected with respect to the Sr and Ca maps.

### 8.3.2.5) Results

In Fig. 8.3.4 and Fig. 8.3.5 example maps of both sample obtained from two SrR treated humans are shown. As with the rat samples, comparing the  $\mu$ XRF maps of Sr with the corresponding qBEI revealed that Sr was predominantly incorporated into the newly formed mineralized bone matrix mainly adjacent to the bone surface (darker grey-levels in qBEI; indicated as 2), while Sr was marginally incorporated into the old, higher mineralized bone packets (brighter grey-levels in the qBEI images; indicated as 1). Further more it has to be noted that in the maps of the sample treated 12 month with SrR and a 6 month break before collection (No. 4567x) low mineralized bone matrix with hardly any Sr incorporation can be found adjacent to the bone surface (in Fig. 8.3.4 indicated as 3). Even so the automated image segmentation using PCA and KMC did not identify these areas in a separate cluster (see Fig. 8.3.4 bottom left). They have been included in the cluster C1 (black in KMC map in Fig. 8.3.4 & 8.3.5 bottom left) representing the areas with low Sr levels and higher mineralized bone matrix. In the sample collected during the SrR treatment no such features were observed.

The areas with high Sr levels have been properly grouped in one cluster C4 (white), likewise the PMMA, which is represented by cluster C2 (brown). Pixels of the boarder between mineralized bone matrix and PMMA, often partial filled detection volumes, were grouped in cluster C3 (organge).

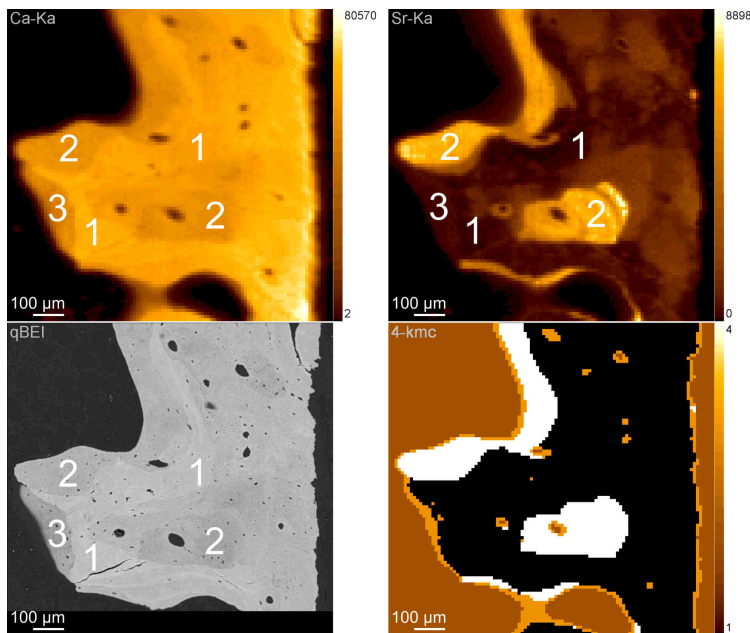


**Figure 8.3.4:** Example of the human bone sample 4567x treated 12 months with SrR and treatment stop 6month before sample collection. SR  $\mu$ -XRF elemental maps of calcium (Ca) and strontium (Sr) based on Ca  $K\alpha$  and Sr  $K\alpha$  fluorescence lines, qBEI image and the corresponding cluster map (black: bone formed without Sr treatment, brown: PMMA orange: boarder bone - PMMA, white: bone formed during Sr treatment) are shown. Bone packets build (1) before, (2) during and (3) after treatment with SrR is indicated with the respective numbers.

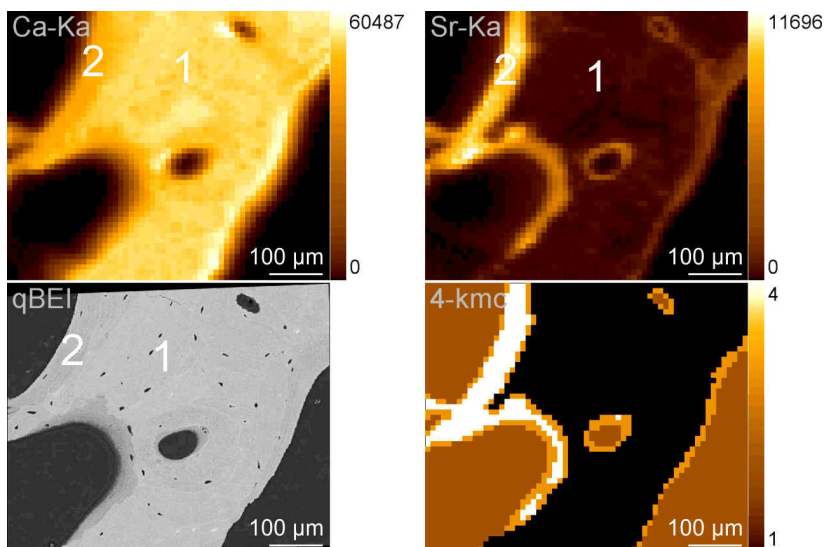


**Figure 8.3.5** Example of human bone sample 4653a treated 3 years with SrR before sample collection. SR  $\mu$ -XRF elemental maps of calcium (Ca) and strontium (Sr) based on Ca  $K\alpha$  and Sr  $K\alpha$  fluorescence lines, qBEI image and the corresponding cluster map (black: bone formed before and after Sr treatment, brown: PMMA orange: boarder bone - PMMA, white: bone formed during Sr treatment) are shown. Bone packets build (1) before and (2) during the SrR are indicated with the respective numbers (adopted from [144]).

The results obtained from the cluster analysis were similar to the rat experiment. The areas build during the SrR treatment presented higher Sr values than the areas build without additional Sr ingestion (Fig 8.3.6). This increase was obtained for all maps of both samples. The increased Sr/(Sr+Ca) values compared to the mineralized bone matrix build without SrR treatment turned out to be significant. The Sr values in the bone areas build without SrR treatment were similar in both samples, no significant difference could be observed. The mineralized bone matrix build during the SrR treatment in sample 4653a (3 years SrR treatment) however had significantly higher Sr values than sample 4567x (1 year SrR treatment) (see Tab. 8.3.3).

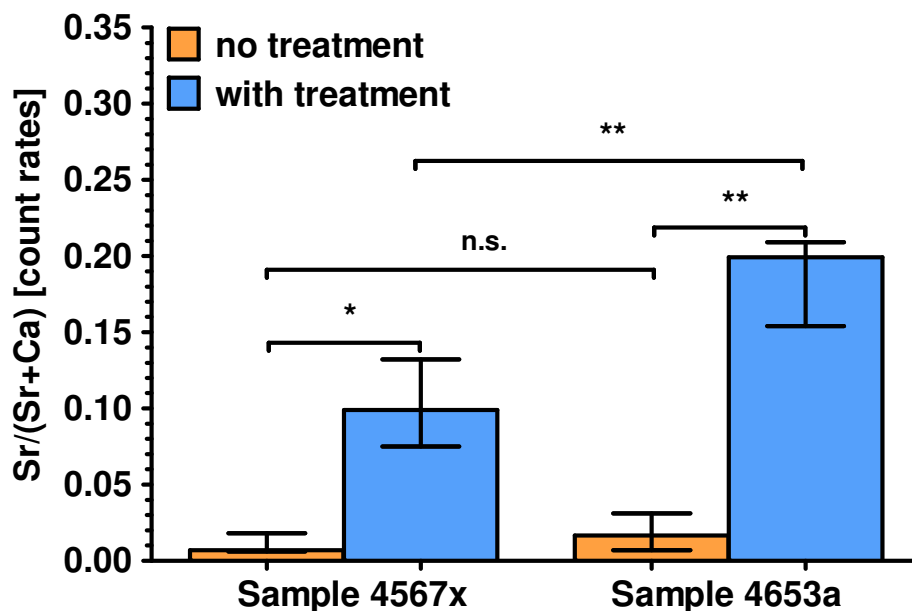


**Figure 8.3.6: Influence of SrR treatment on the Sr uptake in human mineralized bone matrix as quantified by cluster analysis (compare Cap. 8.3.1)). Values of mineralized bone matrix formed before and during the SrR treatment are indicated by orange and blue bars, respectively. For both samples median and range (error bars) resulting from all maps recorded are indicated. Significance levels as obtained by Mann Whitney tests: \*  $p < 0.05$ , \*\*  $P < 0.01$ , n.s: not significant.**

**Table 8.3.3:  $\text{Sr}^{2+}$  uptake of bone tissues analysed. Data shown are median and range [min; max] obtained from the elemental maps performed for each bone tissue sample; N= number of maps per sample; p-values between the  $\text{Sr}/(\text{Ca}+\text{Sr})$  outcomes of the treated and non treated bone areas and between the samples.**

experimental data		$\text{Sr}/(\text{Ca}+\text{Sr})$ (count rates)		p-values		
sample (N)	treatment duration	no treatment	SrR treatment	SrR treated vs. not treated	vs. 4567x (treated)	vs. 4567x (not treated)
4567x (5)	1 yr (6 m break)	0,007 [0,006; 0,018]	0,099 [0,0750; 0,132]	0,012		
4653a (6)	3 yr	0,0165 [0,0007; 0,0310]	0,199 [0,154; 0,209]	0,005	0,008	0,1396

#### 8.3.2.6) Discussion & Conclusions

The human samples yield similar results as the rat model. Differences in the  $\text{Sr}/(\text{Sr}+\text{Ca})$  ratios may be due to different serum levels of  $\text{Sr}^{2+}$ , which however have not been available. The serum level of Sr determines the amount of Sr build into the hydroxyapatite crystal, when the bone mineral is formed [198, 199].

Nevertheless it seems to be possible to extrapolate conclusions drawn from the rat model to humans.

The differences between the two human samples in the areas build during the treatment may be due to the different treatment duration and different  $\text{Sr}^{2+}$  serum levels (which were not known). The sample of the longer treated patient (3 yr vs. 1 yr) presented the higher Sr values.

The used image segmentation approach (PCA and KMC) had limitations. For sample 4567x it was not possible to distinguish between the mineralized bone matrix build before and after the SrR treatment (Fig 8.3.4 bottom right). In both areas, build before and after the SrR treatment, the Sr count rates were similar (~500 and ~200 cps/100mA respectively) compared to the areas build during the SrR treatment (~6500 cps/100mA). This might be the reason why these two areas could not be separated by the cluster analysis. Also choosing a number of allowed cluster greater then 4 did no work out, though the Ca count rates of the mineralized bone matrix build before the SrR treatment were higher (~62000 cps/100mA)



then the count rates of the mineralized bone matrix build after the treatment (~50000 cps/100mA) (Fig. 8.3.4 top left) and the differences in the degree of mineralization could also be clearly observed in the qBEI images (Fig 8.3.4 bottom left).

In the case of the patient whose SrR treatment was stopped 6 month before the sample collection it could be shown that Sr is predominantly incorporated in the mineralized bone matrix build during the treatment. The mineralized bone matrix formed before and after the SrR treatment showed no increase in Sr levels. This indicates that the Sr incorporation is strongly depending on the serum levels of  $\text{Sr}^{2+}$  which in turn is depending on the ingestion of Sr.



## Chapter 9

# Comparison of SR $\mu$ -XRF with ATI Lab Setup Measurements [74]

### 9.1 Introduction

SR  $\mu$ -XRF has many advantages compared to tube excited  $\mu$ -XRF - high intensity and collimation of the primary beam lead to good counting statistics, short measurement times and good detection limits. Linear polarization in orbital plane and selectable monoenergetic excitation energy lead to a very low background. However, beamtime at synchrotron radiation facilities is very limited and not easily available. A lab based system has the advantage that it can be used at almost any time.

The aim was to see if the laboratory system at the Atominstitut can be used as pre screening tool for SR  $\mu$ -XRF studies. So the most interesting samples or areas on samples can be selected in advance to gain optimal use of the allocated beamtime at the synchrotron.

To assess the capabilities and limitations of the laboratory system three rat bone samples that were measured using SR  $\mu$ -XRF were analyzed. The rats were fed with different amounts of dietary Ca, normal (1.19 wt% Ca) and deficient (0.1 wt% Ca), to assess the influence of Ca levels on the Sr incorporation into the bone matrix. Further different Sr drugs,  $\text{SrCl}_2$  and strontium ranelate (SrR) were applied. More detailed information can be found in Chap 8.3 or Pemmer et al. 2011[146].

### 9.2 Samples

From the Sr treated rat vertebrae [239] that were measured prior at the synchrotron (details see Chap. 8.3) 3 samples (details see Tab. 9.1) were selected for comparative measurements with the laboratory  $\mu$ -XRF setup at the Atominstitut. Only samples from rats treated with the higher Sr dose were chosen. More details about the samples and the background of the animal study can be found in Chap. 8.3.1.1

**Table 9.1: List of Sr treated rat bone samples used for comparing SR  $\mu$ -XRF and lab  $\mu$ -XRF.**

Sample	Fed drug doses [mg/kg/d]	Sr <sup>2+</sup> doses [mg/kg/d]	Ca- diet [weight %]	No. of maps ANKA	No. of maps ATI
P10	SrCl <sub>2</sub> 150	SrCl <sub>2</sub> 56	1.19	8	2
P03	SrCl <sub>2</sub> 150	SrCl <sub>2</sub> 56	0.1	4	2
P02	SrR 150	SrR 51	0.1	3	2

### 9.3 SR $\mu$ -XRF Analysis

The confocal  $\mu$ -XRF setup at ANKA FLUO with a beam size of about  $10 \times 10 \mu\text{m}^2$  and a depth resolution of  $12 \mu\text{m}$  at  $14,2 \text{ keV}$  (Sr-Ka) was used. The excitation energy was set to  $17,7 \text{ keV}$  and the measuring time was set to 1 second/pixel. The scans on the sample surface were performed as area scans, ranging from  $300 \times 300 \mu\text{m}^2$  up to  $850 \times 850 \mu\text{m}^2$ , in  $10 \mu\text{m}$  steps. The maps of net intensities were normalized to counts per second (cps) and 100 mA storage ring current.

More about this analysis can be found in Chap. 8.3.1.3 and the setup of the FLUO beamline is described in Chap. 6.1.3.

### 9.4 Lab $\mu$ -XRF Analysis

As measurement conditions with the confocal  $\mu$ -XRF setup in the laboratory at Atominstitut (details see Chap. 6.2) a tube voltage of  $50 \text{ kV}$ , a current of  $1 \text{ mA}$  and the  $100 \mu\text{m}$  Al filter to suppress the low energie X-Rays were selected. The measuring time was set to 50 second/pixel real time and the measurement chamber was evacuated. The lateral beam size was about  $50 \times 50 \mu\text{m}^2$  and the depth resolution  $50 \mu\text{m}$ . The scans on the sample surface were performed as area scans in the size of  $1000 \times 1000 \mu\text{m}^2$  with  $25 \mu\text{m}$  steps. The maps of net intensities were dead time corrected.

### 9.5 Data Evaluation

The  $\mu$ -XRF data recorded with the laboratory setup was evaluated with the same strategy and software as the synchrotron obtained data to ensure the comparability of the results. As already elaborated in Chap. 8.3.1.4 PCA and KMC were applied to the Ca and Sr maps [145] to obtain the  $\text{Sr}/(\text{Ca}+\text{Sr})$  values.

## 9.6 Results & Discussion

As an example two spectra - one acquired at the SR  $\mu$ -XRF data and one from the lab system - are shown for comparison in Fig. 9.3.1. The measurement time at the synchrotron was set to  $t=1$  s (life time) and in the lab to  $t=50$  s (real time). The low spectral background of the SR data can be clearly seen. Further the Sr peak is distinct and the Zn peak a little higher than in the laboratory spectrum due to the optimization of the excitation energy for Sr. The Ca peak however is higher in the lab spectrum, as the data were collected under vacuum condition.

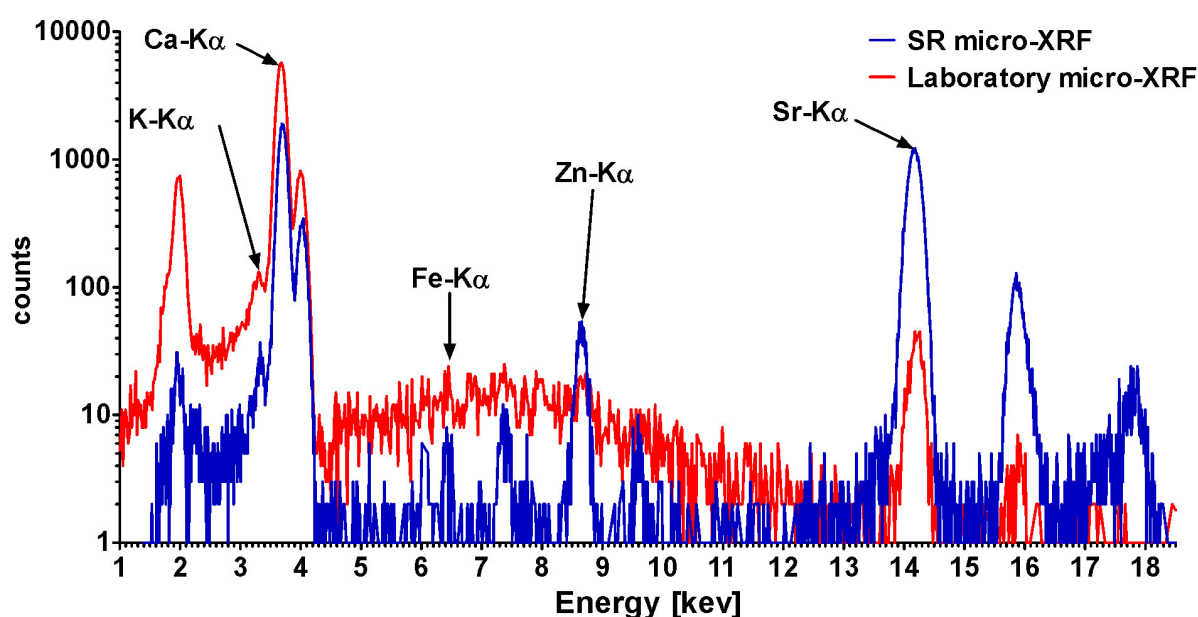


**Figure 9.3.1:** Spectra recorded at the FLUO beamline at ANKA (blue;  $t=1$ s) and with the laboratory  $\mu$ -XRF setup at Atominstut (red;  $t=50$ s). X-Ray  $K\beta$ -lines, the scatter peaks (incoherent and coherent) and artificial peaks (sum and escape peaks) are not labelled.

A comparison of acquired Ca and Sr maps of the same area on sample P02 (Ca deficient, higher SrR dose) together with a qBEI picture on the right is displayed in Fig 9.3.2. It can be seen that both measurements (SR and lab  $\mu$ -XRF) are comparable.

Admittedly, several differences can be observed:

- i. The Ca- $K\alpha$  intensity is higher with the lab system - compared to Sr- $K\alpha$  intensity. This is a result of the fact that the lab system was developed for low Z analysis, featuring a vacuum chamber (details see Chap. 6.2)

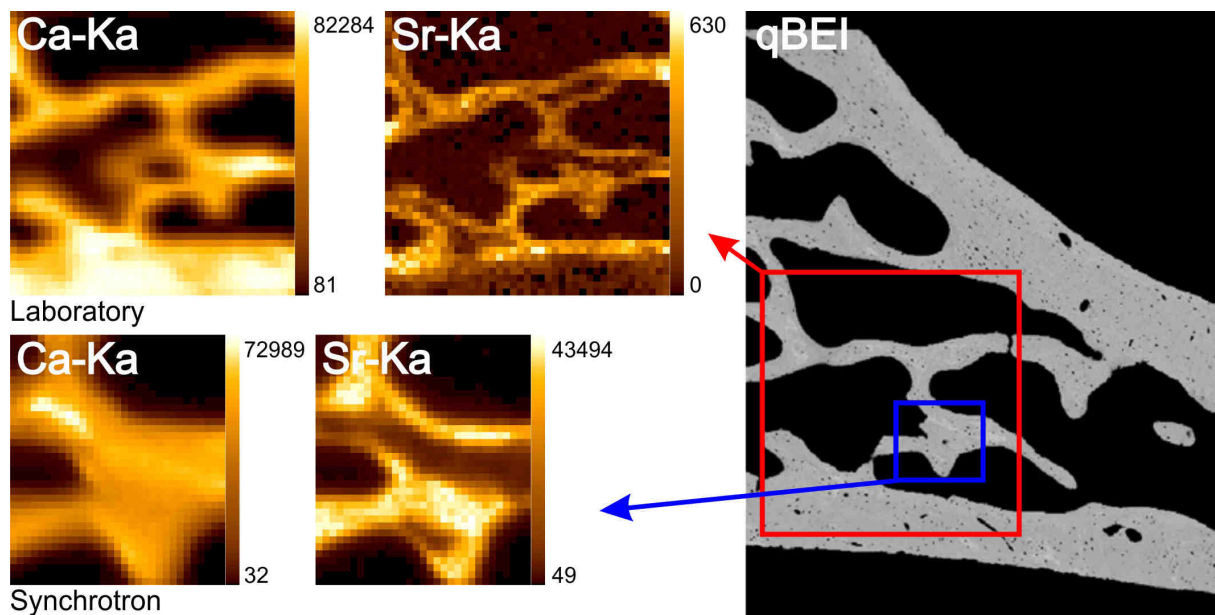


**Figure 9.3.2:** Comparison of element maps of Ca (left) and Sr (right) recorded at the FLUO beamline at ANKA (bottom; lateral resolution:  $10 \times 10 \mu\text{m}^2$ ) and with the laboratory  $\mu$ -XRF setup at Atominstitut (top; lateral resolution:  $\sim 50 \times 50 \mu\text{m}^2$ ) of a SrR treated rat vertebrae (sample P02): deficient Ca diet 0,1wt%,  $\text{Sr}^{2+}$  dose:  $51 \text{ mg kg}^{-1} \text{ d}^{-1}$ ) (adopted from [74]).

- ii. Sr can be measured, but only with a quite low intensity. Lower concentrations, as present in the sample, would be hard to measure with the lab system.
- iii. The significantly different spatial resolution (about  $50 \times 50 \times 50 \mu\text{m}^3$  for the lab-setup and  $10 \times 10 \times 12 \mu\text{m}^3$  for the setup at FLUO beamline). For fine structured materials, like bone, the lateral resolution of the laboratory system is not good enough. The structures are almost too small. As a consequence artefacts like partial filled volumes are more likely and lead to problem in post measurement data treatment.

Though the  $\text{Sr}/(\text{Sr}+\text{Ca})$  values obtained with the lab system were about 88-fold smaller compared to the synchrotron data the findings for the experimental animal model using rats were the same. The influence of Ca diet on Sr uptake during  $\text{SrCl}_2$  treatment ( $\text{Sr}^{2+}$  dose:  $56 \text{ mg kg}^{-1} \text{ d}^{-1}$ ) and the better efficacy of the strontium ranelate ( $\text{Sr}^{2+}$  dose:  $51 \text{ mg kg}^{-1} \text{ d}^{-1}$ ) at Ca deficient diet can be clearly seen with both setups (Fig 9.3.3):

- i) An about 2,7-fold increase of  $\text{Sr}/(\text{Sr}+\text{Ca})$  values for the Ca deficient sample treated with  $\text{SrCl}_2$ .
- ii) Significantly increased  $\text{Sr}/(\text{Sr}+\text{Ca})$  values for the Ca deficient sample with Strontium Ranelate (SrR) treatment, despite the lower dose of Sr ions compared to  $\text{SrCl}_2$  treatment.

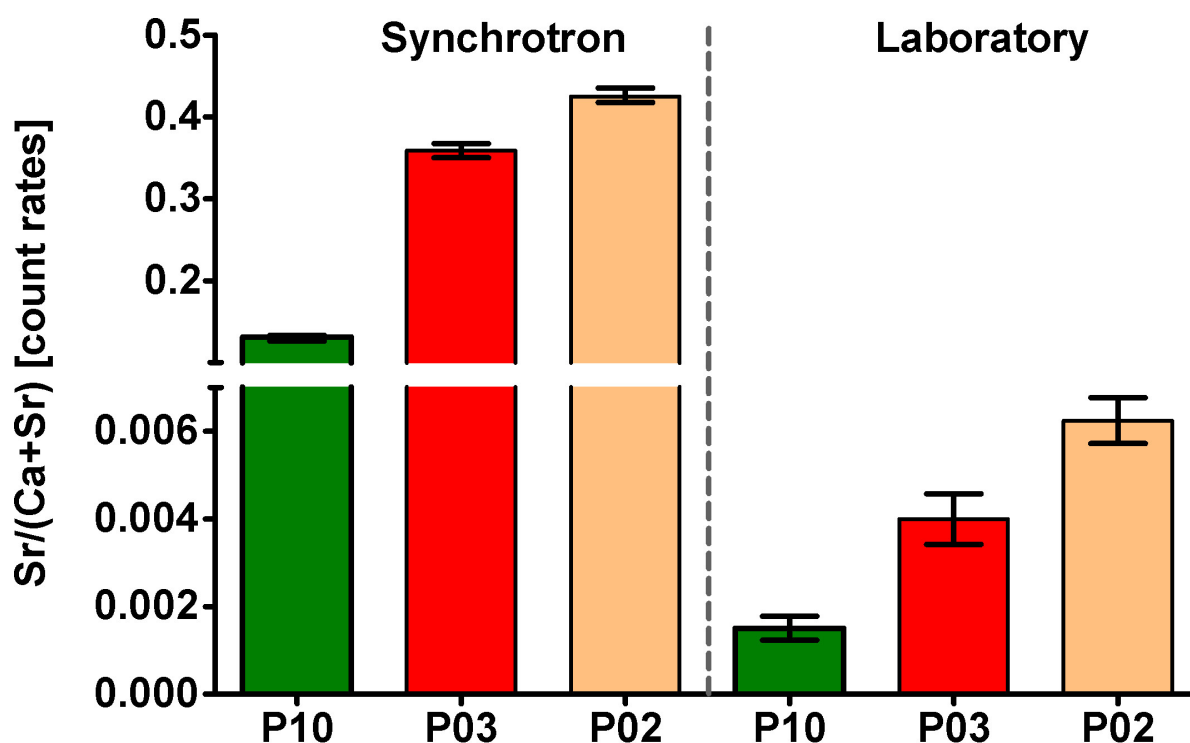


Figure 9.3.3: Comparison of SR  $\mu$ -XRF and laboratory  $\mu$ -XRF measurements of Sr treated rat vertebrae. The mean (box) Sr/(Sr+Ca) values including the standard deviation (error bars) obtained for the maps of each sample is shown.

P10: normal ca diet,  $\text{SrCl}_2$  treatment ( $\text{Sr}^{2+}$  dose:  $56 \text{ mg kg}^{-1} \text{ d}^{-1}$ )

P03: deficient ca diet,  $\text{SrCl}_2$  treatment ( $\text{Sr}^{2+}$  dose:  $56 \text{ mg kg}^{-1} \text{ d}^{-1}$ )

P02: deficient ca diet, SrR treatment ( $\text{Sr}^{2+}$  dose:  $51 \text{ mg kg}^{-1} \text{ d}^{-1}$ )

## 9.7 Conclusion

From the obtained results it can be concluded that a reliable comparison of measurements performed with the lab spectrometer and at the synchrotron is feasible. It can therefore be used as easy accessible pre-screening tool for synchrotron studies. However it has to be kept in mind that the lateral resolution is quite different - only sample with large structures should be used. Further only elements present in sufficient amounts (like in Sr treated bone samples) can be compared, due to the much high lower limit of detection of the lab setup.





## Chapter 10

### Concluding Remarks

In the presented work three analytical methods were combined to analyze and characterise human and animal bone sample with respect to the distribution and levels of the major, minor and trace elements within the basic structural units (BSUs; e.g. bone packets, osteons) and cement lines. Beyond that the influence of postmenopausal osteoporosis (pmpOP) and nutritional Ca amounts during Strontium Ranelate (SrR) treatment were evaluated within that context.

The histological and morphological properties, including the absolute Ca wt% values of the bone sample were acquired with qBEI. SR  $\mu$ -XRF in confocal geometry was applied to obtain the lateral distributions and levels of Ca, Zn, Sr and Pb in the areas of interest that were selected from the qBEI measurements. In addition XAS was used to elucidate the chemical binding of Pb in subchondral / trabecular bone and in the tide mark of the articular cartilage, where in previous studies [24] a significant accumulation of Pb and Zn was found.

In the past years the trace element distribution in bone was studied basically differentiating between cortical and trabecular bone [14, 17, 18]. The resolution of the applied setups did not allow distinguishing between the different BSUs and cement lines. Using the confocal setup at ANKA FLUO beamline, offering a nominal lateral resolution of 12  $\mu\text{m}$  x 12  $\mu\text{m}$ , it was possible to determine the localization of the trace elements Zn, Sr and Pb amongst the different BSUs and the cement lines. Correlating the  $\mu$ -XRF maps with the histological information from the qBEI data it was shown for the first time that Zn and Pb levels in the cement lines are significantly higher compared to the neighbouring normal mineralized bone matrix. This suggests that the incorporation of Pb and Zn is strongly depending on the bone tissue type. Admittedly it has to be emphasized, that the spot size of the confocal SR  $\mu$ -XRF setup is about 5 times wider than the width of the cement lines. Thus the relative levels of trace elements in the cement lines presented in this study are actually a distinct underestimate of the real levels of trace elements.

## Concluding Remarks

Further an overproportional increase of the Pb and Sr values with the degree of mineralization was found for the mineralized bone matrix. Interestingly Zn did not show this behaviour and therefore was uncorrelated with the Ca content. Thus, it could be hypothesised that Sr and Pb are incorporated over a longer period of time after the mineralization stopped, and that Zn is under homeostatic control, as it is an essential trace element.

The samples used for the trace element analysis consisted partly of a paired age matched set of osteoporotic fractured and non-fractured healthy controls (n=5). Hence it was additionally checked if the drastically altered bone metabolism in pmpOP does influence the trace element localization or levels. However, within the analyzed paired sample set no influence of pmpOP on the trace elements could be ascertained.

Osteoporosis is one of the urgent topics in human medicine as it affects more than 75 million people in the western countries. Since a few years Strontium Ranelate (SrR) is an approved drug in the therapy of pmpOP. However little was known whether calcium deficiency and the type of Sr drug have an influence on the Sr incorporation into bone. Vertebrae from an animal model in rats, treated with different Ca diets (deficient and normal) and two Sr drugs (SrR and  $\text{SrCl}_2$ ) at high and low dose, were considered sufficient to address this issue.

It was determined that the nutritional Ca intake has a tremendous impact on the Sr incorporations. A Ca deficient diet leads to a significantly increased Sr incorporation into bone formed during the treatment, for both Sr drugs and doses. In normal Ca diet cases the Sr content in bone was also elevated, but to a much lower extent. Concerning the form of Sr administration, SrR was the far more efficient drug in all studied cases, though the amount of  $\text{Sr}^{2+}$  ions was about 10% smaller for SrR compared to  $\text{SrCl}_2$ .

In case of SrR therapy of pmpOP it has to be taken care that the nutritional Ca intake is sufficient, which can be achieved by accompanying Ca and vitamin D supplementation. Thus higher Sr incorporation into bone can be limited and patient safety during the SrR treatment is improved.

In previous investigations [24] a specific accumulation of Pb on the osteochondral region of human bone was found. The Pb levels in the so-called tidemark, the boarder between

mineralized and non-mineralized articular cartilage were significantly increased compared to the subchondral bone region.

Microscopic XANES at the SUL-X beamline at ANKA in Karlsruhe offered sufficient spatial resolution, within the range of the width of the tidemark ( $\sim 20 \mu\text{m}$ ). Comparing XANES analysis of reference materials to the data obtained with dedicated XAS beamline, it could be proven, that the beamline is well suited for this analysis. It could be shown, that the Pb present in the tidemark and mineralized bone matrix is bond the same way. The different chemical composition of the tidemark region, e.g. high sulphur content, has no influence on the chemical composition of the present Pb. The comparison of the XANES data from the mineralized bone matrix and tidemark with various Pb reference compounds revealed that Pb in bone and tidemark is almost exclusively bond to carbonated calcium hydroxyapatite (CCaHA). This is in agreement with the literature [19] stating that the bone mineral is mainly CCaHA.

In addition to the measurements at the ANKA FLUO beamline selected samples from the rat animal model were also measured at a confocal setup, equipped with a low power X-Ray tube, in the laboratory at the Atominstitut (Vienna University of Technology, Austria). Compared to measurements at the synchrotron, in the laboratory setup the excitation conditions (less intensity and polychromatic primary spectrum) and the lateral resolution of  $50 \mu\text{m} \times 50 \mu\text{m}$  (about 4 to 5 times larger) are inferior. Nevertheless, the results obtained at the laboratory system showed that a reliable comparison of measurements performed with the laboratory spectrometer and at the synchrotron is feasible. The same significant differences that were found for the different treatment groups at the synchrotron could be obtained in the laboratory. The idea of using the laboratory system as easy accessible pre-screening tool for synchrotron studies is therefore reasonable.

The analysis carried out at ANKA FLUO using the confocal setup yielded new insights into the lateral distribution and Zn, Sr, and Pb, identifying an accumulation of Zn and Pb in the cement lines. However, the width of the cement lines is at maximum  $5 \mu\text{m}$  and thus the resolution offered at the FLUO beamline is not sufficient for a more detailed analysis of the cement line region.

## Concluding Remarks

To assess the detailed structure of the Pb and Zn distribution in the cement line region and at the boarder of the haversion channels further analysis with lateral resolutions in the sub  $\mu\text{m}$  range are obligatory. These are for instance possible at the P06 beamline at Petra III at HASYLAB in Hamburg.

## Bibliography

- [1] SKY-PECK, H. H. JOSEPH, B. J.: Determination of trace elements in human serum by energy dispersive X-ray fluorescence. *Clin Biochem*, 1981. **14**(3): p. 126-131 DOI: [http://dx.doi.org/10.1016/S0009-9120\(81\)90253-8](http://dx.doi.org/10.1016/S0009-9120(81)90253-8).
- [2] AASETH, J., BOIVIN, G. ANDERSEN, O.: Osteoporosis and trace elements--an overview. *J Trace Elem Med Biol*, 2012. **26**(2-3): p. 149-152 DOI: <http://dx.doi.org/10.1016/j.jtemb.2012.03.017>.
- [3] JARUP, L.: Hazards of heavy metal contamination. *Br Med Bull*, 2003. **68**(1): p. 167-182 DOI: <http://dx.doi.org/10.1093/bmb/ldg032>.
- [4] POUNDS, J. G., LONG, G. J. ROSEN, J. F.: Cellular and molecular toxicity of lead in bone. *Environ Health Perspect*, 1991. **91**: p. 17-32.
- [5] BARRY, P. S.: A comparison of concentrations of lead in human tissues. *Br J Ind Med*, 1975. **32**(2): p. 119-139.
- [6] ITO, A., KAWAMURA, H., OTSUKA, M., IKEUCHI, M., OHGUSHI, H., ISHIKAWA, K., ONUMA, K., KANZAKI, N., SOGO, Y. ICHINOSE, N.: Zinc-releasing calcium phosphate for stimulating bone formation. *Materials Science and Engineering: C*, 2002. **22**(1): p. 21-25 DOI: [http://dx.doi.org/10.1016/s0928-4931\(02\)00108-x](http://dx.doi.org/10.1016/s0928-4931(02)00108-x).
- [7] KAJI, M. NISHI, Y.: Growth And Minerals: Zinc. *Growth, Genetics and Hormones*, 2006. **22**(1): p. 1-7.
- [8] MASER, R. E., STABLEY, J. N., LENHARD, M. J., OWUSU-GRIFFIN, P., PROVOST-CRAIG, M. A. FARQUHAR, W. B.: Zinc intake and biochemical markers of bone turnover in type 1 diabetes. *Diabetes Care*, 2008. **31**(12): p. 2279-2280 DOI: <http://dx.doi.org/10.2337/dc08-1068>.
- [9] NISHI, Y.: Zinc and growth. *J Am Coll Nutr*, 1996. **15**(4): p. 340-344.
- [10] REGINSTER, J.-Y., FELSENBURG, D., BOONEN, S., DIEZ-PEREZ, A., RIZZOLI, R., BRANDI, M.-L., SPECTOR, T. D., BRIXEN, K., GOEMAERE, S., CORMIER, C., BALOGH, A., DELMAS, P. D. MEUNIER, P. J.: Effects of long-term strontium ranelate treatment on the risk of nonvertebral and vertebral fractures in postmenopausal osteoporosis: Results of a five-year, randomized, placebo-controlled trial. *Arthritis & Rheumatism*, 2008. **58**(6): p. 1687-1695.
- [11] CHETTLE, D. R., SCOTT, M. C. SOMERVILLE, L. J.: Lead in bone: sampling and quantitation using K X-rays excited by 109Cd. *Environ Health Perspect*, 1991. **91**: p. 49-55.
- [12] ROSEN, J. F., CROCKETT, A. F., BALBI, K., BALBI, J., BAILEY, C., CLEMENTE, I., REDKEY, N. GRAINGER, S.: Bone lead content assessed by L-line x-ray fluorescence in lead-exposed and non-lead-exposed suburban populations in the United States. *Proc Natl Acad Sci U S A*, 1993. **90**(7): p. 2789-2792.
- [13] BELLIS, D. J., LI, D., CHEN, Z., GIBSON, W. M. PARSONS, P. J.: Measurement of the microdistribution of strontium and lead in bone via benchtop monochromatic microbeam X-ray fluorescence with a low power source. *J Anal At Spectrom*, 2009. **24**(5): p. 622-626 DOI: <http://dx.doi.org/10.1039/B820067J>.
- [14] CARVALHO, M. L., MARQUES, A. F., LIMA, M. T. REUS, U.: Trace elements distribution and post-mortem intake in human bones from Middle Age by total

- reflection X-ray fluorescence. *Spectrochimica Acta Part B: Atomic Spectroscopy*, 2004. **59**(8): p. 1251-1257 DOI: <http://dx.doi.org/10.1016/j.sab.2004.01.019>.
- [15] LIMA, I., ANJOS, M. J., FLEIUSS, M. L. F., ROSENTHAL, D. LOPES, R. T.: Characterization of osteoporotic bone structures by bidimensional images through x-ray microfluorescence with synchrotron radiation. *X-Ray Spectrometry*, 2008. **37**(3): p. 249-254 DOI: <http://dx.doi.org/10.1002/xrs.986>.
- [16] ZHANG, Y., CHENG, F., LI, D., WANG, Y., ZHANG, G., LIAO, W., TANG, T., HUANG, Y. HE, W.: Investigation of elemental content distribution in femoral head slice with osteoporosis by SRXRF microprobe. *Biol Trace Elem Res*, 2005. **103**(2): p. 177-185 DOI: <http://dx.doi.org/10.1385/BTER:103:2:177>.
- [17] SAMUDRALWAR, D. ROBERTSON, J.: Determination of major and trace elements in bones by simultaneous PIXE/PIGE analysis. *Journal of Radioanalytical and Nuclear Chemistry*, 1993. **169**(1): p. 259-267 DOI: <http://dx.doi.org/10.1007/bf02046801>.
- [18] TAKATA, M. K., SAIKI, M., SUMITA, N. M., SALDIVA, P. H. N. PASQUALUCCI, C. A.: Activation analysis methods and applications Trace element determinations in human cortical and trabecular bones. *Journal of Radioanalytical and Nuclear Chemistry*, 2005. **264**(1): p. 5-8 DOI: <http://dx.doi.org/10.1007/s10967-005-0666-0>.
- [19] FRATZL, P., GUPTA, H. S., PASCHALIS, E. P. ROSCHGER, P.: Structure and mechanical quality of the collagen-mineral nano-composite in bone. *Journal of Materials Chemistry*, 2004. **14**(14): p. 2115-2123.
- [20] SKEDROS, J. G., HOLMES, J. L., VAJDA, E. G. BLOEBAUM, R. D.: Cement lines of secondary osteons in human bone are not mineral-deficient: New data in a historical perspective. *The Anatomical Record Part A: Discoveries in Molecular, Cellular, and Evolutionary Biology*, 2005. **286A**(1): p. 781-803 DOI: <http://dx.doi.org/10.1002/ar.a.20214>.
- [21] ROSCHGER, P., PLENK, H., JR., KLAUSHOFER, K. ESCHBERGER, J.: A new scanning electron microscopy approach to the quantification of bone mineral distribution: backscattered electron image grey-levels correlated to calcium K alpha-line intensities. *Scanning Microsc*, 1995. **9**(1): p. 75-86; discussion 86-88.
- [22] FUCHS, R. K., ALLEN, M. R., CONDON, K. W., REINWALD, S., MILLER, L. M., MCCLENATHAN, D., KECK, B., PHIPPS, R. J. BURR, D. B.: Strontium ranelate does not stimulate bone formation in ovariectomized rats. *Osteoporos Int*, 2008. **19**(9): p. 1331-1341 DOI: <http://dx.doi.org/10.1007/s00198-008-0602-6>.
- [23] ROSCHGER, A., HOFSTAETTER, J. G., PEMMER, B., ZOEGER, N., WOBRAUSCHEK, P., FALKENBERG, G., SIMON, R., BERZLANOVICH, A., THALER, H. W., ROSCHGER, P., KLAUSHOFER, K. STRELI, C.: Differential accumulation of lead and zinc in double-tidemarks of articular cartilage. *Osteoarthritis and Cartilage*, 2013 DOI: <http://dx.doi.org/10.1016/j.joca.2013.06.029>.
- [24] ZOEGER, N., ROSCHGER, P., HOFSTAETTER, J. G., JOKUBONIS, C., PEPPONI, G., FALKENBERG, G., FRATZL, P., BERZLANOVICH, A., OSTERODE, W., STRELI, C. WOBRAUSCHEK, P.: Lead accumulation in tidemark of articular cartilage. *Osteoarthritis and Cartilage*, 2006. **14**(9): p. 906-913.
- [25] ZOEGER, N., WOBRAUSCHEK, P., STRELI, C., PEPPONI, G., ROSCHGER, P., FALKENBERG, G. OSTERODE, W.: Distribution of Pb and Zn in slices of human bone by synchrotron  $\mu$ -XRF. *X-ray spectrom*, 2005(34): p. 140-143.

- [26] MADRY, H., VAN DIJK, C. N.MUELLER-GERBL, M.: The basic science of the subchondral bone. *Knee Surg Sports Traumatol Arthrosc*, 2010. **18**(4): p. 419-433 DOI: <http://dx.doi.org/10.1007/s00167-010-1054-z>.
- [27] REINERT, T., REIBETANZ, U., SCHWERTNER, M., VOGT, J., BUTZ, T.SAKELLARIOU, A.: The architecture of cartilage: Elemental maps and scanning transmission ion microscopy/tomography. *Nuclear Instruments and Methods in Physics Research Section B: Beam Interactions with Materials and Atoms*, 2002. **188**(1-4): p. 1-8.
- [28] SIMON, R., BUTH, G.HAGELSTEIN, M.: The X-ray-fluorescence facility at ANKA, Karlsruhe: Minimum detection limits and micro probe capabilities. *Nuclear Instruments & Methods in Physics Research Section B-Beam Interactions with Materials and Atoms*, 2003. **199**: p. 554-558 DOI: [http://dx.doi.org/10.1016/S0168-583X\(02\)01418-0](http://dx.doi.org/10.1016/S0168-583X(02)01418-0)
- [29] ZOEGER, N., STRELI, C., WOBRAUSCHEK, P., JOKUBONIS, C., PEPPONI, G., HOFSTAETTER, J. G., BERZIANOVICH, A., WEGRZYNEK, D., CHINEA-CANO, E., MARKOWICZ, A., SIMON, R.FALKENBERG, G.: Determination of the elemental distribution in human joint bones by SR micro XRF. *X-Ray Spectrometry*, 2008. **37**(1): p. 3-11 DOI: <http://dx.doi.org/10.1002/xrs.998>.
- [30] ELDER, F. R., GUREWITSCH, A. M., LANGMUIR, R. V.POLLOCK, H. C.: Radiation from Electrons in a Synchrotron. *Physical Review*, 1947. **71**(11): p. 829-830.
- [31] SCHWINGER, J.: On the Classical Radiation of Accelerated Electrons. *Physical Review*, 1949. **75**(12): p. 1912-1925.
- [32] DUKE, P.:Synchrotron Radiation: Production and Properties. 2008: *OUP Oxford* DOI.
- [33] WINICK, H.:Synchrotron Radiation Sources: A Primer. 1995: *World Scientific* DOI.
- [34] WILLE, K.: Synchrotron radiation sources. *Reports on Progress in Physics*, 1991. **54**(8): p. 1005.
- [35] WIEDEMANN, H.:Synchrotron Radiation. *Advanced Texts in Physics*. 2003, Berlin: *Springer*. 288 DOI.
- [36] WILLE, K.:Physik der Teilchenbeschleuniger und Synchrotronstrahlungsquellen.: Eine Einführung. 1996: *Teubner B.G. GmbH* DOI.
- [37] KOCH, E. E.:Handbook on synchrotron radiation. 1983: *North Holland Pub. Co.* DOI.
- [38] BUZANICH, G.: Characterization of Compound Refractive Lenses for synchrotron  $\mu$ -XRF and  $\mu$ -XAS and applications with high spatial resolution, *PhD Thesis*, Atominstitut, Strahlenphysik, Technische Universität Wien; Wien 2012.
- [39] BARTOLINI, R.: Synchrotron radiation energy flux, [Online], 2010, Accessed: 2013-08-14; Available from: [https://en.wikipedia.org/wiki/File:Synchrotron\\_radiation\\_energy\\_flux.png](https://en.wikipedia.org/wiki/File:Synchrotron_radiation_energy_flux.png).
- [40] HORNTRICH, C.: Characterization of the influence of the sample shape on accuracy, statistics and reproducibility in TXRF analysis of semiconductor surfaces *PhD Thesis*, Atominstitut, Strahlenphysik, Technische Universität Wien; Wien 2011.
- [41] EPSIM 3D/JF SANTARELLI SYNCHROTRON SOLEIL: General diagram of Synchrotron Soleil, [Online], 2011,2011-11-17 Accessed: 2013-08-14; Available from: [http://commons.wikimedia.org/wiki/File:Sch%C3%A9ma\\_de\\_principe\\_du\\_synchrotron.png](http://commons.wikimedia.org/wiki/File:Sch%C3%A9ma_de_principe_du_synchrotron.png).
- [42] HOLST, B.: Wiggler / Undulator Schematic, [Online], 2005,2006-01-27 Accessed: 2013-08-14; Available from: <http://en.wikipedia.org/wiki/File:Undulator.png>.

## Bibliography

- [43] ZOEGER, N.: Micro X-ray Fluorescence Analysis and Micro-Tomography of Human Bone and Tissue, *PhD Thesis*, Atominstitut, Strahlenphysik, Technische Universität Wien; Wien 2005.
- [44] ADVANCED PHOTON SOURCE: Spectral brilliance of X-Ray Sources, *U.S. Department of Energy Office of Science*, [Online], 2013, Accessed: 2013-08-14; Available from: [http://www.aps.anl.gov/About/APS\\_Overview/Images/billcurvesREV.jpg](http://www.aps.anl.gov/About/APS_Overview/Images/billcurvesREV.jpg).
- [45] Average brilliance of XFELs and undulators, *Deutsches Elektronen-Synchrotron - A Research Centre of the Helmholtz Association*, [Online], 2013, Accessed: 2013-08-27; Available from: [http://photon-science.desy.de/research/studentsteaching/sr\\_and\\_fel\\_basics/fel\\_basics/tdr\\_spectral\\_characteristics/index\\_eng.html](http://photon-science.desy.de/research/studentsteaching/sr_and_fel_basics/fel_basics/tdr_spectral_characteristics/index_eng.html).
- [46] COOLIDGE, W. D.: A Powerful Röntgen Ray Tube with a Pure Electron Discharge. *Physical Review*, 1913. **2**(6): p. 409--430.
- [47] BLACKWOOD, D., HATHAWAY, J., PASKEVICH, V., POPPE, L.: A Laboratory Manual for X-Ray Powder Diffraction, *U. S. Geological Survey*, [Online], 2001, Accessed: 2013-08-14; Available from: <http://pubs.usgs.gov/of/2001/of01-041/html/docs/xrpd.htm>.
- [48] KIERANMAHER: Tube Spectrum, [Online], 2001, Accessed: 2013-08-14; Available from: <http://en.wikibooks.org/wiki/File:XrtSpectrum.jpg>.
- [49] KRIEGER, H., PEZOLD, W.: Strahlenphysik, Dosimetrie und Strahlenschutz. 2nd ed. 1988, Stuttgart: *B. G. Teubner* DOI.
- [50] DYSON, N. A.: X-rays in Atomic and Nuclear Physics. 1990: *Cambridge University Press* DOI.
- [51] JENKINS, R.: X-Ray Fluorescence Spectrometry. 2 ed. *Chemical Analysis: A Series of Monographs on Analytical Chemistry and Its Applications*, ed. JENKINS, R. Vol. 152. 1999, New York: *John Wiley & Sons* DOI.
- [52] PEMMER, B.: Studien zur Quantifizierung: In vivo energiedispersive Röntgenfluoreszenzanalyse von Blei im menschlichen Knochen, *Master Thesis*, Atominstitut, Strahlenphysik, Technische Universität Wien; Wien 2007.
- [53] JENKINS, R., GOULD, R. W., GEDCKE, D.: Quantitative X-ray Spectrometry. 4th ed. 1981, New York: *M. Dekker Inc.* DOI.
- [54] LAMBERT, J. H.: Photometria, sive De mensura et gradibus luminis, colorum et umbrae. 1760: *W. Engelmann* DOI.
- [55] BEER: Bestimmung der Absorption des rothen Lichts in farbigen Flüssigkeiten. *Annalen der Physik*, 1852. **162**(5): p. 78-88 DOI: <http://dx.doi.org/10.1002/andp.18521620505>.
- [56] GOLDSTEIN, J. I., NEWBURY, D. E., ECHLIN, P., JOY, D. C., ROMINF, A. D., LYMAN, C. E., FIORI, C., LIFSHIN, E.: Scanning Electron Microscopy and X-Ray Microanalysis. 2nd ed. 1992, New York: *Plenum Press* DOI.
- [57] MOSELEY, H. G. J.: The High Frequency Spectra of the Elements Part II. *Philosophical Magazine*, 1914. **27**: p. 703-713.
- [58] MOSELEY, H. G. J.: The High Frequency Spectra of the Elements. *Philosophical Magazine*, 1913. **26**: p. 1024-1034.
- [59] EMILIO, G., PAVEL, R.: Semiconductor Drift Chamber - An Application of a Novel Charge Transport Scheme. *Nuclear Instruments and Methods in Physics Research Section B: Beam Interactions with Materials and Atoms*, 1984. **225**: p. 608-614.



- [60] EGGERT, T.: Der Ketek Silizium Driftdetektor: Grundlagen Anwendungen Funktionsprinzipien. 2004, *KETEK GmbH*: München
- [61] SNIGIREV, A.SNIGIREVA, I.: Hard X-Ray Microoptics, in Modern Developments in X-Ray and Neutron Optics, ERKO, A., IDIR, M., KRIST, T.MICHETTE, A., Editors. 2008, *Springer Berlin Heidelberg*. p. 255-285 DOI: [http://dx.doi.org/10.1007/978-3-540-74561-7\\_17](http://dx.doi.org/10.1007/978-3-540-74561-7_17).
- [62] LAST, A.: X-Ray Optics, [Online], 2013, Accessed: 2013-08-13; Available from: <http://www.x-ray-optics.de>.
- [63] MATTHIAS, M.: Bragg diffraction, [Online], 2008, Accessed: 2013-08-14; Available from: <http://commons.wikimedia.org/wiki/File:Bragg.svg>.
- [64] UNDERWOOD, J. H.: X-Ray Data Booklet - Multilayers and Crystals, [Online], 2009, Accessed: 2013-08-14; Available from: [http://xdb.lbl.gov/Section4/Sec\\_4-1.html](http://xdb.lbl.gov/Section4/Sec_4-1.html).
- [65] KLOCKENKÄMPER, R.: Total reflection X-ray fluorescence analysis. 1997: *Wiley* DOI.
- [66] KIRKPATRICK, P.BAEZ, A. V.: Formation of Optical Images by X-Rays. *J. Opt. Soc. Am.*, 1948. **38**(9): p. 766-773.
- [67] SCHIELDS, P. J., GIBSON, D. M., GIBSON, W. M., GAO, N., HUANG, H.PONOMAREV, I. Y.: Overview of polycapillary X-ray optics. *Powder Diffraction*, 2002. **17**(02): p. 70-80 DOI: <http://dx.doi.org/10.1154/1.1482080>.
- [68] JANSSENS, K., PROOST, K.FALKENBERG, G.: Confocal microscopic X-ray fluorescence at the HASYLAB microfocuss beamline: characteristics and possibilities. *Spectrochimica Acta Part B: Atomic Spectroscopy*, 2004. **59**(10-11): p. 1637-1645.
- [69] KANNGIEßER, B., MALZER, W., RODRIGUEZ, A. F.REICHE, I.: Three-dimensional micro-XRF investigations of paint layers with a tabletop setup. *Spectrochimica Acta Part B: Atomic Spectroscopy*, 2005. **60**(1): p. 41-47.
- [70] SMIT, Z., JANSSENS, K., PROOST, K.LANGUS, I.: Confocal [mu]-XRF depth analysis of paint layers. *Nuclear Instruments and Methods in Physics Research Section B: Beam Interactions with Materials and Atoms*, 2004. **219-220**: p. 35-40.
- [71] KANNGIEßER, B., MALZER, W.REICHE, I.: A new 3D micro X-ray fluorescence analysis set-up - First archaeometric applications. *Nuclear Instruments and Methods in Physics Research Section B: Beam Interactions with Materials and Atoms*, 2003. **211**(2): p. 259-264 DOI: [http://dx.doi.org/10.1016/s0168-583x\(03\)01321-1](http://dx.doi.org/10.1016/s0168-583x(03)01321-1).
- [72] PROOST, K., JANSSENS, K., VINCZE, L., FALKENBERG, G., GAO, N.BLY, P.: Feasibility and characteristics of Confocal micro-XRF at Hasylab BL L, in *HASYLAB rep*. 2002.
- [73] VINCZE, L., VEKEMANS, B., BRENNER, F. E., FALKENBERG, G., RICKERS, K., SOMOGYI, A., KERSTEN, M.ADAMS, F.: Three-Dimensional Trace Element Analysis by Confocal X-ray Microfluorescence Imaging. *Anal. Chem.*, 2004. **76**(22): p. 6786-6791.
- [74] SMOLEK, S., PEMMER, B., FOLSER, M., STRELI, C.WOBRAUSCHEK, P.: Confocal micro-x-ray fluorescence spectrometer for light element analysis. *Rev Sci Instrum*, 2012. **83**(8): p. 083703-083701 - 083703-083706 DOI: <http://dx.doi.org/10.1063/1.4744934>.
- [75] BAUMGARTEL, H.: EXAFS, SEXAFS, XANES: X-Ray Absorption - Principles, Applications, Techniques of EXAFS, SEXAFS and XANES. Von D. Koningsberger und R. Prins. John Wiley & Sons Ltd., Chichester 1988. 673 S., Abb., Tab., Formeln. ISBN 0-471-87547-3. *Nachrichten aus Chemie, Technik und*

## Bibliography

- Laboratorium*, 1988. **36**(6): p. 650-650 DOI: <http://dx.doi.org/10.1002/nadc.19880360617>.
- [76] REHR, J. J. ALBERS, R. C.: Theoretical approaches to x-ray absorption fine structure. *Reviews of Modern Physics*, 2000. **72**(3): p. 621-654.
  - [77] NEWVILLE, M.: The Fundamentals of XAFS. 2004. **Revision 1.7**.
  - [78] YANO, J. YACHANDRA, V. K.: X-ray absorption spectroscopy. *Photosynth Res*, 2009. **102**(2-3): p. 241-254 DOI: <http://dx.doi.org/10.1007/s11120-009-9473-8>.
  - [79] KOENIGSBERGER, D. C. PRINS, R.: eds. X-ray Absorption Principles, Applications, Techniques of EXAFS, SEXAFS, and XANES. *Chemical Analysis: A Series of Monographs on Analytical Chemistry and Its Applications*. 1988, Wiley: New York.
  - [80] ROSCHGER, A.: Localization of Trace Elements in Bone Tissue using Synchrotron Radiation Induced Micro-XRF in Combination with Quantitative Backscattered Electron Imaging, *Master Thesis*, Atominstytut, Technischen Universität Wien; Wien 2011.
  - [81] Scanning Electron Microscope. Art., *Encyclopædia Britannica Online*, [Online], 2008, Accessed: 2013-08-11; Available from: <http://www.britannica.com/EBchecked/media/110970/Scanning-electron-microscope>.
  - [82] KRUMEICH, F.: SEM imaging: edge effect, [Online], 2012, 2012-04-14 Accessed: 2013-07-12; Available from: <http://www.microscopy.ethz.ch/se.htm>.
  - [83] KRUMEICH, F.: Inelastic Interactions of Electrons with Matter [Online], 2012, 2012-05-14 Accessed: 2013-07-12; Available from: <http://www.microscopy.ethz.ch/inelast.htm>.
  - [84] CHAMBOST, E.: Everhart-Thornley detector, [Online], 2007, Accessed: 2013-07-08; Available from: [https://commons.wikimedia.org/wiki/File:Everhart-Thornley\\_detector.JPG](https://commons.wikimedia.org/wiki/File:Everhart-Thornley_detector.JPG).
  - [85] ROSCHGER, P., PASCHALIS, E. P., FRATZL, P. KLAUSHOFER, K.: Bone mineralization density distribution in health and disease. *Bone*, 2008. **42**(3): p. 456-466 DOI: <http://dx.doi.org/10.1016/j.bone.2007.10.021>.
  - [86] NAKAYAMA, H., TAKAKUDA, K., MATSUMOTO, H., MIYATA, A., BABA, O., TABATA, M., USHIKI, T., ODA, T., MCKEE, M. TAKANO, Y.: Effects of Altered Bone Remodeling and Retention of Cement Lines on Bone Quality in Osteopetrotic Aged &lt;i>c- Src</i>-Deficient Mice. *Calcified Tissue International*, 2010. **86**(2): p. 172-183 DOI: <http://dx.doi.org/10.1007/s00223-009-9331-x>.
  - [87] EGERER, A. K., SAHA, S., MCMILLAN, P. J. RIVERA, J.: Morphology of the cement line in human bone and its relationship to bone strength. *Proceedings of the 17th Southern Biomedical Engineering Conference*, 1996: p. 7-18.
  - [88] YENI, Y. N. NORMAN, T. L.: Calculation of porosity and osteonal cement line effects on the effective fracture toughness of cortical bone in longitudinal crack growth. *Journal of Biomedical Materials Research*, 2000. **51**(3): p. 504-509 DOI: [http://dx.doi.org/10.1002/1097-4636\(20000905\)51:3<504::aid-jbm27>3.0.co;2-i](http://dx.doi.org/10.1002/1097-4636(20000905)51:3<504::aid-jbm27>3.0.co;2-i).
  - [89] BURR, D. B., SCHAFFLER, M. B. FREDERICKSON, R. G.: Composition of the cement line and its possible mechanical role as a local interface in human compact bone. *Journal of Biomechanics*, 1988. **21**(11): p. 939-945 DOI: [http://dx.doi.org/10.1016/0021-9290\(88\)90132-7](http://dx.doi.org/10.1016/0021-9290(88)90132-7).
  - [90] FRATZL, P., SCHREIBER, S., ROSCHGER, P., LAFAGE, M. H., RODAN, G. KLAUSHOFER, K.: Effects of sodium fluoride and alendronate on the bone mineral in minipigs: a

- small-angle X-ray scattering and backscattered electron imaging study. *J Bone Miner Res*, 1996. **11**(2): p. 248-253 DOI: <http://dx.doi.org/10.1002/jbmr.5650110214>.
- [91] ROSCHGER, P., ESCHBERGER, J. PLENK, H. J.: Formation of ultracracks in methacrylate-embedded undecalcified bone samples by exposure to aqueous solutions. *Cells and Materials*, 1993. **3**(4): p. 361–365.
- [92] SCHAFFLER, M. B., BURR, D. B. FREDERICKSON, R. G.: Morphology of the osteonal cement line in human bone. *The Anatomical Record*, 1987. **217**(3): p. 223-228 DOI: <http://dx.doi.org/10.1002/ar.1092170302>.
- [93] FROST, H. M.: Skeletal structural adaptations to mechanical usage (SATMU): 2. Redefining Wolff's law: the remodeling problem. *Anat Rec*, 1990. **226**(4): p. 414-422 DOI: <http://dx.doi.org/10.1002/ar.1092260403>.
- [94] PARFITT, A. M.: Osteonal and hemi-osteonal remodeling: the spatial and temporal framework for signal traffic in adult human bone. *J Cell Biochem*, 1994. **55**(3): p. 273-286 DOI: <http://dx.doi.org/10.1002/jcb.240550303>.
- [95] DEMPSTER, D., FELSENBURG, D. VAN DER GEEST, S.: The Bone Quality Book: A Guide to Factors Influencing Bone Strength. 2006: *Excerpta Medica Elsevier* DOI.
- [96] STEPIEN, E.: Acceleration of New Biomarkers Development and Discovery in Synergistic Diagnostics of Coronary Artery Disease, in Coronary Angiography - Advances in Noninvasive Imaging Approach for Evaluation of Coronary Artery Disease, BASKOT, B., Editor. 2011, *InTech Europe*: Rijeka, Croatia. p. 353-374 DOI: <http://dx.doi.org/10.5772/18940>.
- [97] MISOF, B. M., ROSCHGER, P., COSMAN, F., KURLAND, E. S., TESCH, W., MESSMER, P., DEMPSTER, D. W., NIEVES, J., SHANE, E., FRATZL, P., KLAUSHOFER, K., BILEZIKIAN, J. LINDSAY, R.: Effects of intermittent parathyroid hormone administration on bone mineralization density in iliac crest biopsies from patients with osteoporosis: a paired study before and after treatment. *J Clin Endocrinol Metab*, 2003. **88**(3): p. 1150-1156.
- [98] PARFITT, A. M.: Bone remodeling. *Henry Ford Hosp Med J*, 1988. **36**(3): p. 143-144.
- [99] KANIS, J. A., JOHNELL, O., ODEN, A., JONSSON, B., DE LAET, C. DAWSON, A.: Risk of hip fracture according to the World Health Organization criteria for osteopenia and osteoporosis. *Bone*, 2000. **27**(5): p. 585-590 DOI: [http://dx.doi.org/10.1016/S8756-3282\(00\)00381-1](http://dx.doi.org/10.1016/S8756-3282(00)00381-1).
- [100] COOPER, C., CAMPION, G. MELTON, L. J., 3RD: Hip fractures in the elderly: a world-wide projection. *Osteoporos Int*, 1992. **2**(6): p. 285-289.
- [101] LANE, N. E.: Epidemiology, etiology, and diagnosis of osteoporosis. *Am J Obstet Gynecol*, 2006. **194**(2 Suppl): p. S3-11 DOI: <http://dx.doi.org/10.1016/j.ajog.2005.08.047>.
- [102] KHALIL, N., CAULEY, J. A., WILSON, J. W., TALBOTT, E. O., MORROW, L., HOCHBERG, M. C., HILLIER, T. A., MULDOON, S. B. CUMMINGS, S. R.: Relationship of blood lead levels to incident nonspine fractures and falls in older women: the study of osteoporotic fractures. *J Bone Miner Res*, 2008. **23**(9): p. 1417-1425.
- [103] GRUBER, H. E., GONICK, H. C., KHALIL-MANESH, F., SANCHEZ, T. V., MOTSINGER, S., MEYER, M. SHARP, C. F.: Osteopenia induced by long-term, low- and high-level exposure of the adult rat to lead. *Miner Electrolyte Metab*, 1997. **23**: p. 65-73.

## Bibliography

- [104] NELSON, A. E., SHI, X. A., SCHWARTZ, T. A., CHEN, J. C., RENNER, J. B., CALDWELL, K. L., HELMICK, C. G., JORDAN, J. M.: Whole blood lead levels are associated with radiographic and symptomatic knee osteoarthritis: a cross-sectional analysis in the Johnston County Osteoarthritis Project. *Arthritis Res Ther*, 2011. **13**(2): p. R37 DOI: <http://dx.doi.org/10.1186/ar3270>.
- [105] NELSON, A. E., CHAUDHARY, S., KRAUS, V. B., FANG, F., CHEN, J.-C., SCHWARTZ, T. A., SHI, X. A., RENNER, J. B., STABLER, T. V., HELMICK, C. G., CALDWELL, K., ROBIN POOLE, A., JORDAN, J. M.: Whole blood lead levels are associated with biomarkers of joint tissue metabolism in African American and white men and women: The Johnston County Osteoarthritis Project. *Environmental Research*, 2011. **111**(8): p. 1208-1214 DOI: <http://dx.doi.org/10.1016/j.envres.2011.08.002>.
- [106] WONG, M., CARTER, D. R.: Articular cartilage functional histomorphology and mechanobiology: a research perspective. *Bone*, 2003. **33**(1): p. 1-13.
- [107] MAROUDAS, A.: in *Adult Articular Cartilage*, FREEMAN, M. A. R., Editor. 1979, Pitman: Tunbridge Wells, United Kingdom.
- [108] TSAIH, S. W., KORRICK, S., SCHWARTZ, J., LEE, M. L., AMARASIRIWARDENA, C., ARO, A., SPARROW, D., HU, H.: Influence of bone resorption on the mobilization of lead from bone among middle-aged and elderly men: the Normative Aging Study. *Environ Health Perspect*, 2001. **109**(10): p. 995-999.
- [109] SUN, Y., SUN, D., ZHOU, Z., ZHU, G., ZHANG, H., CHANG, X., LEI, L., JIN, T.: Osteoporosis in a Chinese population due to occupational exposure to lead. *Am J Ind Med*, 2008. **51**(6): p. 436-442 DOI: <http://dx.doi.org/10.1002/ajim.20567>.
- [110] SLAVIN, R. E., SWEDO, J., CARTWRIGHT, J., JR., VIEGAS, S., CUSTER, E. M.: Lead arthritis and lead poisoning following bullet wounds: a clinicopathologic, ultrastructural, and microanalytic study of two cases. *Hum Pathol*, 1988. **19**(2): p. 223-235.
- [111] CARMOUCHE, J. J., PUZAS, J. E., ZHANG, X., TIYAPATANAPUTI, P., CORY-SLECHTA, D. A., GELEIN, R., ZUSCIK, M., ROSIER, R. N., BOYCE, B. F., O'KEEFE, R. J., SCHWARZ, E. M.: Lead exposure inhibits fracture healing and is associated with increased chondrogenesis, delay in cartilage mineralization, and a decrease in osteoprogenitor frequency. *Environ Health Perspect*, 2005. **113**(6): p. 749-755.
- [112] ESCRIBANO, A., REVILLA, M., HERNANDEZ, E. R., SECO, C., GONZALEZ-RIOLA, J., VILLA, L. F., RICO, H.: Effect of lead on bone development and bone mass: a morphometric, densitometric, and histomorphometric study in growing rats. *Calcif Tissue Int*, 1997. **60**(2): p. 200-203.
- [113] SILBERGELD, E. K., SCHWARTZ, J., MAHAFFEY, K.: Lead and osteoporosis: mobilization of lead from bone in postmenopausal women. *Environ Res*, 1988. **47**(1): p. 79-94.
- [114] PUZAS, J. E., SICKEL, M. J., FELTER, M. E.: Osteoblasts and chondrocytes are important target cells for the toxic effects of lead. *Neurotoxicology*, 1992. **13**(4): p. 783-788.
- [115] DOWD, T. L., ROSEN, J. F., MINTS, L., GUNDBERG, C. M.: The effect of Pb(2+) on the structure and hydroxyapatite binding properties of osteocalcin. *Biochim Biophys Acta*, 2001. **1535**(2): p. 153-163.
- [116] MAVROPOULOS, E., ROSSI, A. M., COSTA, A. M., PEREZ, C. A. C., MOREIRA, J. C., SALDANHA, M.: Studies on the Mechanisms of Lead Immobilization by

- Hydroxyapatite. *Environmental Science & Technology*, 2002. **36**(7): p. 1625-1629  
DOI: <http://dx.doi.org/10.1021/es0155938>.
- [117] MAÑAY, N., COUSILLAS, A., HELLER, T.: Blood Lead Level (BLL, B-Pb) in Human and Animal Populations: B-Pb as a Biological Marker to Environmental Lead Exposure Cellular Effects of Heavy Metals, in Cellular Effects of Heavy Metals, BANFALVI, G., Editor. 2011, *Springer Netherlands*. p. 315-330 DOI: [http://dx.doi.org/10.1007/978-94-007-0428-2\\_15](http://dx.doi.org/10.1007/978-94-007-0428-2_15).
- [118] RABINOWITZ, M. B.: Toxicokinetics of bone lead. *Environ Health Perspect*, 1991. **91**: p. 33-37.
- [119] PIRKLE, J. L., BRODY, D. J., GUNTER, E. W., KRAMER, R. A., PASCHAL, D. C., FLEGAL, K. M., MATTE, T. D.: The decline in blood lead levels in the United States. The National Health and Nutrition Examination Surveys (NHANES). *JAMA*, 1994. **272**(4): p. 284-291.
- [120] VIG, E. K., HU, H.: Lead toxicity in older adults. *J Am Geriatr Soc*, 2000. **48**(11): p. 1501-1506.
- [121] EUROPEAN PARLIAMENT COUNCIL: Directive 98/70/EC of the European Parliament and of the Council of 13 October 1998 relating to the quality of petrol and diesel fuels and amending Council Directive 93/12/EEC. COMMUNITY, E., Editor. 1998.
- [122] AITKEN, J.: Factors affecting the distribution of zinc in the human skeleton. *Calcified Tissue International*, 1976. **20**(1): p. 23-30 DOI: <http://dx.doi.org/10.1007/bf02546394>.
- [123] BRÄTTER, P., GAWLIK, D., LAUSCH, J., RÖSICK, U.: On the distribution of trace elements in human skeletons. *Journal of Radioanalytical and Nuclear Chemistry*, 1977. **37**(1): p. 393-403 DOI: <http://dx.doi.org/10.1007/bf02520545>.
- [124] CALHOUN, N. R., SMITH, J. C., JR., BECKER, K. L.: The role of zinc in bone metabolism. *Clin Orthop Relat Res*, 1974(103): p. 212-234.
- [125] KENNEY, M. A., MCCOY, H.: Adding zinc reduces bone strength of rats fed a low-calcium diet. *Biol Trace Elem Res*, 1997. **58**(1-2): p. 35-41.
- [126] PORS NIELSEN, S.: The biological role of strontium. *Bone*, 2004. **35**(3): p. 583-588 DOI: <http://dx.doi.org/10.1016/j.bone.2004.04.026>.
- [127] JONES, J. H.: The Metabolism Of Calcium And Phosphorus As Influenced By The Addition To The Diet Of Salts Of Metals Which Form Insoluble Phosphates. *American Journal of Physiology*, 1938. **124**(1): p. 230-237.
- [128] WALSER, M.: Renal excretion of alkaline earths, in Mineral metabolism. An advanced treatise, COMAR, C. L., BRONNER, F., Editors. 1969, *Academic Press*: New York. p. 235-320.
- [129] VAN ESPEN, P., JANSSENS, K., NOBELS, J.: AXIL-PC: software for the analysis of complex X-ray spectra. *Chemometrics Intell. Lab. Syst.*, 1986. **1**(1): p. 109-114 DOI: [http://dx.doi.org/10.1016/0169-7439\(86\)80031-4](http://dx.doi.org/10.1016/0169-7439(86)80031-4).
- [130] RASBAND, W.: ImageJ - Image processing and analysis in Java (v1.44c), *National Institutes of Health*, [Online], 2011; Available from: <http://rsb.info.nih.gov/ij/>.
- [131] SCHNEIDER, C. A., RASBAND, W. S., ELICEIRI, K. W.: NIH Image to ImageJ: 25 years of image analysis. *Nat Methods*, 2012. **9**(7): p. 671-675.
- [132] PEMMER, B., ROSCHGER, A., WASTL, A., HOFSTAETTER, J. G., WOBRAUSCHEK, P., SIMON, R., THALER, H. W., ROSCHGER, P., KLAUSHOFER, K., STRELI, C.: Spatial



## Bibliography

- distribution of the trace elements zinc, strontium and lead in human bone tissue. *Bone*, 2013. **57**(1): p. 184-193 DOI: <http://dx.doi.org/10.1016/j.bone.2013.07.038>.
- [133] SMITH, L. I.: A tutorial on Principal Components Analysis. 2002.
- [134] JOLLIFFE, I. T.: Principal component analysis. 2nd ed. *Springer series in statistics*. 2002, New York: *Springer*. xxix, 487 s. DOI.
- [135] DING, C. HE, X.: K-means clustering via principal component analysis, in *ICML 2004: Proceedings of the twenty-first international conference on Machine learning*. 2004, ACM: Banff, Alberta, Canada. p. 29.
- [136] ZHA, H. Y., HE, X. F., DING, C., SIMON, H. GU, M.: Spectral relaxation for K-means clustering. *Advances in Neural Information Processing Systems 14, Vols 1 and 2*, 2002. **14**: p. 1057-1064.
- [137] DUDA, R. O., HART, P. E. STORK, D. G.: Pattern classification. 2. ed. A *Wiley-Interscience publication*. 2001, New York: *Wiley*. xx, 654 s. DOI.
- [138] HASTIE, T., TIBSHIRANI, R. FRIEDMAN, J. H.: The elements of statistical learning : data mining, inference, and prediction : with 200 full-color illustrations. *Springer series in statistics*. 2001, New York: *Springer*. xvi, 533 p. DOI.
- [139] JAIN, A. K. DUBES, R. C.: Algorithms for clustering data. *Prentice-Hall advanced reference series*,. 1988, Englewood Cliffs: *Prentice Hall*. xiv, 320 s. DOI.
- [140] HARTIGAN, J. A.: Clustering algorithms. *Wiley series in probability and mathematical statistics*,. 1975, New York: *Wiley*. xiii, 351 s. DOI.
- [141] LLOYD, S. P.: Least Squares Quantization in PCM's. *Bell Telephone Laboratories Papers*, 1957.
- [142] MACQUEEN, J.: Some methods for classification and analysis of multivariate observations Source. *Proc. Fifth Berkeley Symp. on Math. Statist. and Prob.*, 1967. **1**: p. 281-297.
- [143] SHAPIRO, L. G. STOCKMAN, G. C.: Computer Vision. 2001, Upper Saddle River, New Jersey: *Prentice Hall* DOI.
- [144] FÖLSER, M.: Automated Evaluation of SR- $\mu$ XRF-Samples with PCA and Clustering, *Projektarbeit*, Atominstitut, TU-Wien; Wien 2012.
- [145] VEKEMANS, B., JANSSENS, K., VINCZE, L., AERTS, A., ADAMS, F. HERTOGEN, J.: Automated Segmentation of  $\mu$ -XRF Image Sets. *X-Ray Spectrometry*, 1997. **26**: p. 333-346.
- [146] PEMMER, B., HOFSTAETTER, J. G., MEIRER, F., SMOLEK, S., WOBRAUSCHEK, P., SIMON, R., FUCHS, R. K., ALLEN, M. R., CONDON, K. W., REINWALD, S., PHIPPS, R. J., BURR, D. B., PASCHALIS, E. P., KLAUSHOFER, K., STRELI, C. ROSCHGER, P.: Increased strontium uptake in trabecular bone of ovariectomized calcium-deficient rats treated with strontium ranelate or strontium chloride. *J Synchrotron Radiat*, 2011. **18**(6): p. 835-841 DOI: <http://dx.doi.org/10.1107/S090904951103038X>.
- [147] GraphPad Statistics Guide, *GraphPad Software, Inc.*, [Online], 2013, Accessed: 2013-07-14; Available from: <http://www.graphpad.com/guides/prism/6/statistics/>.
- [148] EASTON, V. J. MCCOLL, J. H.: Statistics Glossary, *Statistical Education through Problem Solving, University of Glasgow*, [Online], 1997, 1997-09 Accessed: 2013-07-14; Available from: <http://www.stats.gla.ac.uk/steps/glossary/>.
- [149] MCCLUSKEY, A. LALKHEN, A. G.: Statistics III: Probability and statistical tests. *Continuing Education in Anaesthesia, Critical Care & Pain*, 2007. **7**(5): p. 167-170 DOI: <http://dx.doi.org/10.1093/bjaceaccp/mkm028>.
- [150] ROWE, P. HEINISCH, C.: Statistik für Mediziner und Pharmazeuten. 2012: *Wiley* DOI.

- [151] STEPHENSON, D. B.: Data analysis methods in weather and climate research, *University of Reading, Department of Meteorology*, [Online], 2004,2005-09-30 Accessed: 2013-07-14; Available from: <http://empslocal.ex.ac.uk/people/staff/dbs202/cag/courses/MT37C/course/course.html>.
- [152] TOUTENBURG, H., HEUMANN, C., SCHOMAKER, M. WISSMANN, M.: Induktive Statistik: eine Einführung mit R und SPSS. 2008: Springer DOI.
- [153] WEISBERG, H. F.: Central Tendency and Variability. *Sage University Paper Series on Quantitative Applications in the Social Sciences*. 1992: SAGE PUBN Inc. DOI.
- [154] LIAO, C.-P.: Boxplot and a probability density function of a Normal Population., [Online], 2011,2011-03-09 Accessed: 2013-07-14; Available from: [http://en.wikipedia.org/wiki/File:Boxplot\\_vs\\_PDF.svg](http://en.wikipedia.org/wiki/File:Boxplot_vs_PDF.svg).
- [155] ANKA - Die Synchrotronstrahlungsquelle am KIT, *KIT - ANKA Synchrotron*, [Online], 2013,2013-01-17 Accessed: 2013-07-16; Available from: <http://www.anka.kit.edu/28.php>.
- [156] GOETTLICHER, J. STEININGER, R.: SUL-X Beamline Description, *KIT - ANKA Synchrotron*, [Online], 2013,2013-01-16 Accessed: 2013-07-16; Available from: <http://www.anka.kit.edu/1629.php>.
- [157] MANGOLD, S.: XAS Beamline Description, *KIT - ANKA Synchrotron*, [Online], 2013,2013-07-16 Accessed: 2013-07-16; Available from: <http://www.anka.kit.edu/979.php>.
- [158] SIMON, R.: FLUO Beamline Description, *KIT - ANKA Synchrotron*, [Online], 2012,2012-10-05 Accessed: 2013-07-16; Available from: <http://www.anka.kit.edu/979.php>.
- [159] SIMON, R.: Schematic of FLUO beamline. 2012: Karlsruhe - Note: private communication
- [160] ROSCHGER, P., FRATZL, P., ESCHBERGER, J. KLAUSHOFER, K.: Validation of quantitative backscattered electron imaging for the measurement of mineral density distribution in human bone biopsies. *Bone*, 1998. **23**(4): p. 319-326 DOI: [http://dx.doi.org/10.1016/S8756-3282\(98\)00112-4](http://dx.doi.org/10.1016/S8756-3282(98)00112-4).
- [161] MEIRER, F., PEMMER, B., PEPPONI, G., ZOEGER, N., WOBRAUSCHEK, P., SPRIO, S., TAMPIERI, A., GOETTLICHER, J., STEININGER, R., MANGOLD, S., ROSCHGER, P., BERZLANOVICH, A., HOFSTAETTER, J. G. STRELI, C.: Assessment of chemical species of lead accumulated in tidemarks of human articular cartilage by X-ray absorption near-edge structure analysis. *J Synchrotron Radiat*, 2011. **18**(2): p. 238-244 DOI: <http://dx.doi.org/10.1107/S0909049510052040>.
- [162] LEMPERG, R.: The subchondral bone plate of the femoral head in adult rabbits. *Virchows Archiv*, 1971. **352**(1): p. 1-13.
- [163] ELLIS, D. E., TERRA, J., WARSCHKOW, O., JIANG, M., GONZÁLEZ, G. B., OKASINSKI, J. S., BEDZYK, M. J., ROSSI, A. M. EON, J. G.: A theoretical and experimental study of lead substitution in calcium hydroxyapatite. *Phys Chem Chem Phys.*, 2006. **8**(8): p. 967-976.
- [164] CHARTIER, A., MEIS, C. GALE, J. D.: Computational study of Cs immobilization in the apatites  $\text{Ca}_{10}(\text{PO}_4)_6\text{F}_2$ ,  $\text{Ca}_4\text{La}_6(\text{SiO}_4)_6\text{F}_2$  and  $\text{Ca}_2\text{La}_8(\text{SiO}_4)_6\text{O}_2$ . *Physical Review B*, 2001. **64**(8): p. 085110.

## Bibliography

- [165] MA, Q. Y., TRAINA, S. J., LOGAN, T. J. RYAN, J. A.: In situ lead immobilization by apatite. *Environmental Science & Technology*, 1993. **27**(9): p. 1803-1810 DOI: <http://dx.doi.org/10.1021/es00046a007>.
- [166] MEIS, C., GALE, J. D., BOYER, L., CARPENA, J. GOSSET, D.: Theoretical Study of Pu and Cs Incorporation in a Mono-silicate Neodymium Fluoroapatite  $\text{Ca}_9\text{Nd}(\text{SiO}_4)(\text{PO}_4)_5\text{F}_2$ . *The Journal of Physical Chemistry A*, 2000. **104**(22): p. 5380-5387 DOI: <http://dx.doi.org/10.1021/jp000096j>.
- [167] PARK, H. S., KIM, I. T., KIM, H. Y., LEE, K. S., RYU, S. K. KIM, J. H.: Application of Apatite Waste Form for the Treatment of Water-Soluble Wastes Containing Radioactive Elements. Part I: Investigation on the Possibility. *Journal of Industrial and Engineering Chemistry*, 2002. **8**(4): p. 318-327.
- [168] XU, Y. SCHWARTZ, F. W.: Lead immobilization by hydroxyapatite in aqueous solutions. *Journal of Contaminant Hydrology*, 1994. **15**(3): p. 187-206 DOI: [http://dx.doi.org/10.1016/0169-7722\(94\)90024-8](http://dx.doi.org/10.1016/0169-7722(94)90024-8).
- [169] PROOST, K., VINCZE, L., JANSSENS, K., GAO, N., BULSKA, E., SCHREINER, M. ET AL.: Characterization of a polycapillary lens for use in micro-XANES experiments. 2003. **32**(3): p. 215-222.
- [170] SOMERVILLE, L. J. ET AL.: In vivo measurement of lead in bone using X-ray fluorescence. *Physics in Medicine and Biology*, 1985. **30**(9): p. 929.
- [171] NEWVILLE, M.: IFEFFIT: interactive XAFS analysis and FEFF fitting. *Journal of Synchrotron Radiation*, 2001. **8**(2): p. 322-324 DOI: <http://dx.doi.org/10.1107/S0909049500016964>.
- [172] RAVEL, B. NEWVILLE, M.: ATHENA, ARTEMIS, HEPHAESTUS: data analysis for X-ray absorption spectroscopy using IFEFFIT. *Journal of Synchrotron Radiation*, 2005. **12**(4): p. 537-541 DOI: <http://dx.doi.org/10.1107/S0909049505012719>.
- [173] NEWVILLE, M.: IFEFFIT: Interactive program suite for XAFS Analysis, *The IFEFFIT homepage, The Consortium For Advanced Radiation Sources (CARS)*, [Online], 2009, 2009-10-13 Accessed: 2010-07-07; Available from: <http://cars9.uchicago.edu/ifeffit/>.
- [174] KUHLMAN, R. E.: in Fundamental and clinical bone physiology, URIST, M. R., Editor. 1980, *J. B. Lippincott Company*: Philadelphia, Penns.
- [175] AWONUSI, A., MORRIS, M. D. TECKLENBURG, M. M.: Carbonate assignment and calibration in the Raman spectrum of apatite. *Calcif Tissue Int.*, 2007. **81**(1): p. 46-52.
- [176] CHO, G. Y., WU, Y. T. ACKERMAN, J. L.: Detection of hydroxyl ions in bone mineral by solid-state NMR spectroscopy. *Science*, 2003. **300**: p. 1123-1127 DOI: <http://dx.doi.org/10.1126/science.1078470>.
- [177] PASTERIS, J. D., WOPENKA, B., FREEMAN, J. J., ROGERS, K., VALSAMI-JONES, E., VAN DER HOUWEN, J. A. M. SILVA, M. J.: Lack of OH in nanocrystalline apatite as a function of degree of atomic order: implications for bone and biomaterials. *Biomaterials*, 2004. **25**: p. 229-238.
- [178] CHATURVEDI, P. K., SETH, C. S. MISR, V.: Sorption kinetics and leachability of heavy metal from the contaminated soil amended with immobilizing agent (humus soil and hydroxyapatite). *Chemosphere*, 2006. **64**(7): p. 1109-1114.
- [179] BIGI, A., RIPAMONTI, A., BRUCKNER, S., GAZZANO, M., ROVERI, N. THOMAS, S. A.: Structure refinements of lead-substituted calcium hydroxyapatite by X-ray powder



- fitting. *Acta Crystallographica Section B*, 1989. **45**(3): p. 247-251 DOI: <http://dx.doi.org/10.1107/S0108768189001928>.
- [180] BRÜCKNER, S., LUSVARDI, G., MENABUE, L.SALADINI, M.: Crystal structure of lead hydroxyapatite from powder X-ray diffraction data. *Inorganica Chimica Acta*, 1995. **236**(1-2): p. 209-212.
- [181] BUSSELBERG, D., EVANS, M. L., RAHMANN, H.CARPENTER, D. O.: Lead and zinc block a voltage-activated calcium channel of Aplysia neurons. *J Neurophysiol*, 1991. **65**(4): p. 786-795.
- [182] SCHIRRMACHER, K., WIEMANN, M., BINGMANN, D.BUSSELBERG, D.: Effects of lead, mercury, and methyl mercury on gap junctions and  $[Ca^{2+}]_i$  in bone cells. *Calcif Tissue Int*, 1998. **63**(2): p. 134-139.
- [183] BRES, E. F., VOEGEL, J. C., BARRY, J. C., WADDINGTON, W. G.FRANK, R. M.: Feasibility study for the detection of lead substitution sites in the hydroxyapatite crystal structure using high-resolution electron microscopy (HREM) at optimum focus. *Journal of Applied Crystallography*, 1986. **19**(3): p. 168-173 DOI: <http://dx.doi.org/10.1107/S0021889886089719>.
- [184] MIYAKE, M., ISHIGAKI, K.SUZUKI, T.: Structure refinements of  $Pb^{2+}$  ion-exchanged apatites by x-ray powder pattern-fitting. *Journal of Solid State Chemistry*, 1986. **61**(2): p. 230-235 DOI: [http://dx.doi.org/10.1016/0022-4596\(86\)90026-5](http://dx.doi.org/10.1016/0022-4596(86)90026-5).
- [185] VERBEECK, R. M., LASSUYT, C. J., HEIJLIGERS, H. J., DRIESSENS, F. C.VROLIJK, J. W.: Lattice parameters and cation distribution of solid solutions of calcium and lead hydroxyapatite. *Calcif Tissue Int*, 1981. **33**(3): p. 243-247.
- [186] HARDING, N. R., LIPTON, J. F., VIGORITA, V. J.BRYK, E.: Experimental lead arthropathy: an animal model. *J. Trauma*, 1999. **47**(5): p. 951-955.
- [187] BOLANOS, A. A., VIGORITA, V. J., MEYERSON, R. I., D'AMBROSIO, F. G.BRYK, E.: Intra-articular histopathologic changes secondary to local lead intoxication in rabbit knee joints. *J. Trauma*, 1995. **38**(4): p. 668-671.
- [188] LOVERIDGE, N., POWER, J., REEVE, J.BOYDE, A.: Bone mineralization density and femoral neck fragility. *Bone*, 2004. **35**(4): p. 929-941 DOI: <http://dx.doi.org/10.1016/j.bone.2004.05.025>.
- [189] KRANE, S. M.INADA, M.: Matrix metalloproteinases and bone. *Bone*, 2008. **43**(1): p. 7-18 DOI: <http://dx.doi.org/10.1016/j.bone.2008.03.020>.
- [190] BONNER, F. W., KING, L. J.PARKE, D. V.: Cadmium-induced reduction of bone alkaline phosphatase and its prevention by zinc. *Chemico-Biological Interactions*, 1980. **29**(3): p. 369-372.
- [191] BRZOSKA, M. M., ROGALSKA, J., GALAZYN-SIDORCZUK, M., JURCZUK, M., ROSZCZENKO, A., KULIKOWSKA-KARPINSKA, E.MONIUSZKO-JAKONIUK, J.: Effect of zinc supplementation on bone metabolism in male rats chronically exposed to cadmium. *Toxicology*, 2007. **237**(1-3): p. 89-103 DOI: <http://dx.doi.org/10.1016/j.tox.2007.05.001>.
- [192] IWAMI, K.MORIYAMA, T.: Comparative effect of cadmium on osteoblastic cells and osteoclastic cells. *Archives of Toxicology*, 1993. **67**(5): p. 352-357.
- [193] MEUNIER, N., O'CONNOR, J. M., MAIANI, G., CASHMAN, K. D., SECKER, D. L., FERRY, M., ROUSSEL, A. M.COUDRAY, C.: Importance of zinc in the elderly: the ZENITH study. *Eur J Clin Nutr*, 2005. **59 Suppl 2**: p. S1-4 DOI: <http://dx.doi.org/10.1038/sj.ejcn.1602286>.

## Bibliography

- [194] YAMAGUCHI, M.: Role of zinc in bone formation and bone resorption. *The Journal of Trace Elements in Experimental Medicine*, 1998. **11**(2-3): p. 119-135 DOI: [http://dx.doi.org/10.1002/\(sici\)1520-670x\(1998\)11:2/3<119::aid-jtra5>3.0.co;2-3](http://dx.doi.org/10.1002/(sici)1520-670x(1998)11:2/3<119::aid-jtra5>3.0.co;2-3).
- [195] BEATTIE, J. H.AVENELL, A.: Trace element nutrition and bone metabolism. *Nutr Res Rev*, 1992. **5**(1): p. 167-188 DOI: <http://dx.doi.org/10.1079/NRR19920013>.
- [196] MURRAY, E. J.MESSER, H. H.: Turnover of Bone Zinc during Normal and Accelerated Bone Loss in Rats. *The Journal of Nutrition*, 1981. **111**(9): p. 1641-1647.
- [197] SHERMAN, S. S., SMITH, J. C., JR., TOBIN, J. D.SOARES, J. H., JR.: Ovariectomy, dietary zinc, and bone metabolism in retired breeder rats. *Am J Clin Nutr*, 1989. **49**(6): p. 1184-1191.
- [198] ROSCHGER, P., MANJUBALA, I., ZOEGER, N., MEIRER, F., SIMON, R., LI, C., FRATZL-ZELMAN, N., MISOF, B. M., PASCHALIS, E. P., STRELI, C., FRATZL, P.KLAUSHOFER, K.: Bone material quality in transiliac bone biopsies of postmenopausal osteoporotic women after 3 years of strontium ranelate treatment. *J Bone Miner Res*, 2010. **25**(4): p. 891-900 DOI: <http://dx.doi.org/10.1359/jbmr.091028>.
- [199] LI, C., PARIS, O., SIEGEL, S., ROSCHGER, P., PASCHALIS, E. P., KLAUSHOFER, K.FRATZL, P.: Strontium is Incorporated Into Mineral Crystals Only in Newly Formed Bone During Strontium Ranelate Treatment. *Journal of Bone and Mineral Research*, 2010. **25**(5): p. 968-975 DOI: <http://dx.doi.org/10.1359/jbmr.091038>.
- [200] BOIVIN, G., DELOFFRE, P., PERRAT, B., PANCZER, G., BOUDEULLE, M., MAURAS, Y., ALLAIN, P., TSOUDEROS, Y.MEUNIER, P. J.: Strontium distribution and interactions with bone mineral in monkey iliac bone after strontium salt (S 12911) administration. *Journal of Bone and Mineral Research*, 1996. **11**(9): p. 1302-1311 DOI: <http://dx.doi.org/10.1002/jbmr.5650110915>.
- [201] DAHL, S. G., ALLAIN, P., MARIE, P. J., MAURAS, Y., BOIVIN, G., AMMANN, P., TSOUDEROS, Y., DELMAS, P. D.CHRISTIANSEN, C.: Incorporation and distribution of strontium in bone. *Bone*, 2001. **28**(4): p. 446-453.
- [202] FARLAY, D., BOIVIN, G., PANCZER, G., LALANDE, A.MEUNIER, P. J.: Long-Term Strontium Ranelate Administration in Monkeys Preserves Characteristics of Bone Mineral Crystals and Degree of Mineralization of Bone. *Journal of Bone and Mineral Research*, 2005. **20**(9): p. 1569-1578 DOI: <http://dx.doi.org/10.1359/JBMR.050405>.
- [203] MA, Q. Y., TRAINA, S. J., LOGAN, T. J.RYAN, J. A.: Effects of Aqueous Al, Cd, Cu, Fe(II), Ni, and Zn on Pb Immobilization by Hydroxyapatite. *Environmental Science & Technology*, 1994. **28**(7): p. 1219-1228 DOI: <http://dx.doi.org/10.1021/es00056a007>.
- [204] MESKI, S., KHIREDINE, H., ZIANI, S., RENGARAJ, S.SILLANPÄÄ, M.: Comparative study on the removal of zinc(II) by bovine bone, billy goat bone and synthetic hydroxyapatite. *Desalination and Water Treatment*, 2010. **16**(1-3): p. 271-281 DOI: <http://dx.doi.org/10.5004/dwt.2010.1058>.
- [205] FENG, Y., GONG, J.-L., ZENG, G.-M., NIU, Q.-Y., ZHANG, H.-Y., NIU, C.-G., DENG, J.-H.YAN, M.: Adsorption of Cd (II) and Zn (II) from aqueous solutions using magnetic hydroxyapatite nanoparticles as adsorbents. *Chemical Engineering Journal*, 2010. **162**(2): p. 487-494 DOI: <http://dx.doi.org/10.1016/j.cej.2010.05.049>.
- [206] IGNAT, M., ALEXANDROAEI, M.LUNGU, N. C.: The removal of Zn<sup>2+</sup> Ions from groundwater using hydroxyapatite nanoparticles. *Revista de Chimie*, 2011. **62**.

- [207] DAVIES, D. R., BASSINGTHWAIGHTE, J. B. KELLY, P. J.: Transcapillary exchange of strontium and sucrose in canine tibia. *J Appl Physiol*, 1976. **40**(1): p. 17-22.
- [208] LAPPALAINEN, R., KNUUTTILA, M., LAMMI, S., ALHAVA, E. M. OLKKONEN, H.: Zn and Cu content in human cancellous bone. *Acta Orthop Scand*, 1982. **53**(1): p. 51-55.
- [209] TANG, Y., CHAPPELL, H. F., DOVE, M. T., REEDER, R. J. LEE, Y. J.: Zinc incorporation into hydroxylapatite. *Biomaterials*, 2009. **30**(15): p. 2864-2872 DOI: <http://dx.doi.org/10.1016/j.biomaterials.2009.01.043>.
- [210] MATSUNAGA, K., MURATA, H., MIZOGUCHI, T. NAKAHIRA, A.: Mechanism of incorporation of zinc into hydroxyapatite. *Acta Biomater*, 2010. **6**(6): p. 2289-2293 DOI: <http://dx.doi.org/10.1016/j.actbio.2009.11.029>.
- [211] DOWD, T. L., ROSEN, J. F., GUNDBERG, C. M. GUPTA, R. K.: The displacement of calcium from osteocalcin at submicromolar concentrations of free lead. *Biochim Biophys Acta*, 1994. **1226**(2): p. 131-137 DOI: [http://dx.doi.org/10.1016/0925-4439\(94\)90020-5](http://dx.doi.org/10.1016/0925-4439(94)90020-5).
- [212] MIYAHARA, T., KOMIYAMA, H., MIYANISHI, A., TAKATA, M., NAGAI, M., KOZUKA, H., HAYASHI, T., YAMAMOTO, M., ITO, Y., ODAKE, H. KOIZUMI, F.: Stimulative effects of lead on bone resorption in organ culture. *Toxicology*, 1995. **97**(1-3): p. 191-197.
- [213] DOWD, T. L., ROSEN, J. F. GUPTA, R. K.: <sup>31</sup>P NMR and saturation transfer studies of the effect of Pb<sup>2+</sup> on cultured osteoblastic bone cells. *J Biol Chem*, 1990. **265**(34): p. 20833-20838.
- [214] KLEIN, R. F. WIREN, K. M.: Regulation of osteoblastic gene expression by lead. *Endocrinology*, 1993. **132**(6): p. 2531-2537.
- [215] LONG, G. J. ROSEN, J. F.: Lead perturbs epidermal growth factor (EGF) modulation of intracellular calcium metabolism and collagen synthesis in clonal rat osteoblastic (ROS 17/2.8) cells. *Toxicology and Applied Pharmacology*, 1992. **114**(1): p. 63-70 DOI: [http://dx.doi.org/10.1016/0041-008X\(92\)90097-C](http://dx.doi.org/10.1016/0041-008X(92)90097-C).
- [216] LONG, G. J., ROSEN, J. F. POUNDS, J. G.: Lead impairs the production of osteocalcin by rat osteosarcoma (ROS 17/2.8) cells. *Toxicology and Applied Pharmacology*, 1990. **106**(2): p. 270-277.
- [217] SCHANNE, F. A. X., DOWD, T. L., GUPTA, R. K. ROSEN, J. F.: Lead increases free Ca<sup>2+</sup> concentration in cultured osteoblastic bone cells: Simultaneous detection of intracellular free Pb<sup>2+</sup> by <sup>19</sup>F NMR. *Proceedings of the National Academy of Sciences of the United States of America*, 1989. **86**(13): p. 5133-5135.
- [218] SCHANNE, F. A. X., DOWD, T. L., GUPTA, R. K. ROSEN, J. F.: Effect of lead on parathyroid hormone-induced responses in rat osteoblastic osteosarcoma cells (ROS 17 2.8) using <sup>19</sup>F-NMR. *BBA - Molecular Cell Research*, 1990. **1054**(2): p. 250-255.
- [219] OSTERODE, W., REINING, G., MANNER, G., JAGER, J. VIERHAPPER, H.: Increased lead excretion correlates with desoxypyridinoline crosslinks in hyperthyroid patients. *Thyroid*, 2000. **10**(2): p. 161-164.
- [220] OSTERODE, W., WINKER, R., BIEGLMAYER, C. VIERHAPPER, H.: Effects of parathyroidectomy on lead mobilization from bone in patients with primary hyperparathyroidism. *Bone*, 2004. **35**(4): p. 942-947.

## Bibliography

- [221] CABRERA, W. E., SCHROOTEN, I., DE BROE, M. E.D'HAESE, P. C.: Strontium and bone. *J Bone Miner Res*, 1999. **14**(5): p. 661-668 DOI: <http://dx.doi.org/10.1359/jbmr.1999.14.5.661><http://dx.doi.org/>.
- [222] COHEN-SOLAL, M.: Strontium overload and toxicity: impact on renal osteodystrophy. *Nephrology Dialysis Transplantation*, 2002. **17**(suppl 2): p. 30-34 DOI: [http://dx.doi.org/10.1093/ndt/17.suppl\\_2.30](http://dx.doi.org/10.1093/ndt/17.suppl_2.30).
- [223] MAURAS, Y., ANG, K. S., SIMON, P., TESSIER, B., CARTIER, F., ALLAIN, P.: Increase in blood plasma levels of boron and strontium in hemodialyzed patients. *Clin Chim Acta*, 1986. **156**(3): p. 315-320.
- [224] SCHROOTEN, I., ELSEVIERS, M. M., LAMBERTS, L. V., DE BROE, M. E.D'HAESE, P. C.: Increased serum strontium levels in dialysis patients: an epidemiological survey. *Kidney Int*, 1999. **56**(5): p. 1886-1892 DOI: <http://dx.doi.org/10.1046/j.1523-1755.1999.00740.x>.
- [225] MARIE, P. J., GARBA, M. T., HOTT, M., MIRAVET, L.: Effect of low doses of stable strontium on bone metabolism in rats. *Miner Electrolyte Metab*, 1985. **11**: p. 5-13.
- [226] MCCASLIN, F., JANES, J.: The effect of strontium lactate in the treatment of osteoporosis. *Proc Mayo Clin*, 1959. **34**: p. 329-334.
- [227] SHORR, E., CARTER, A. C.: The usefulness of strontium as an adjuvant to calcium in the remineralization of the skeleton in man. *Bull Hosp Joint Dis*, 1952. **13**: p. 59-66.
- [228] SKORYNA, S. C.: Effects of oral supplementation with stable strontium. *Can Med Assoc J*, 1981. **125**(7): p. 703-712.
- [229] STOREY, E.: Intermittent bone changes and multiple cartilage defects in chronic strontium rickets in rats. *J Bone Joint Surg Br*, 1962. **44-B**: p. 194-208.
- [230] AMMANN, P., SHEN, V., ROBIN, B., MAURAS, Y., BONJOUR, J.-P., RIZZOLI, R.: Strontium Ranelate Improves Bone Resistance by Increasing Bone Mass and Improving Architecture in Intact Female Rats. *Journal of Bone and Mineral Research*, 2004. **19**(12): p. 2012-2020 DOI: <http://dx.doi.org/10.1359/jbmr.040906>.
- [231] BRENNAN, T. C., RYBCHYN, M. S., GREEN, W., ATWA, S., CONIGRAVE, A. D., MASON, R. S.: Osteoblasts play key roles in the mechanisms of action of strontium ranelate. *British Journal of Pharmacology*, 2009. **157**(7): p. 1291-1300 DOI: <http://dx.doi.org/10.1111/j.1476-5381.2009.00305.x>.
- [232] HURTEL-LEMAIRE, A. S., MENTAVERRI, R., CAUDRILLIER, A., COURNARIE, F., WATTEL, A., KAMEL, S., TERWILLIGER, E. F., BROWN, E. M., BRAZIER, M.: The Calcium-sensing Receptor Is Involved in Strontium Ranelate-induced Osteoclast Apoptosis. *Journal of Biological Chemistry*, 2009. **284**(1): p. 575-584 DOI: <http://dx.doi.org/10.1074/jbc.M801668200>.
- [233] AMMANN, P., BADOUD, I., BARRAUD, S., DAYER, R., RIZZOLI, R.: Strontium Ranelate Treatment Improves Trabecular and Cortical Intrinsic Bone Tissue Quality, a Determinant of Bone Strength. *Journal of Bone and Mineral Research*, 2007. **22**(9): p. 1419-1425 DOI: <http://dx.doi.org/10.1359/jbmr.070607>.
- [234] BÄRENHOLDT, O., KOLTHOFF, N., NIELSEN, S. P.: Effect of long-term treatment with strontium ranelate on bone strontium content. *Bone*, 2009. **45**(2): p. 200-206 DOI: <http://dx.doi.org/10.1016/j.bone.2009.04.196>.
- [235] BLAKE, G. M., FOGELMAN, I.: The correction of BMD measurements for bone strontium content. *J Clin Densitom*, 2007. **10**(3): p. 259-265 DOI: <http://dx.doi.org/10.1016/j.jocd.2007.03.102>.

- [236] KENDLER, D. L., ADACHI, J. D., JOSSE, R. G.SLOSMAN, D. O.: Monitoring strontium ranelate therapy in patients with osteoporosis. *Osteoporos Int*, 2009. **20**(7): p. 1101-1106 DOI: <http://dx.doi.org/10.1007/s00198-009-0886-1>.
- [237] OMDAHL, J. L.DELOUCA, H. F.: Strontium induced rickets: metabolic basis. *Science*, 1971. **174**(12): p. 949-951.
- [238] SOBEL, A. E., COHEN, J.KRAMER, B.: The nature of the injury to the calcifying mechanism in rickets due to strontium. *Biochem J*, 1935. **29**(12): p. 2640-2645.
- [239] FUCHS, R., ALLEN, M., CONDON, K., REINWALD, S., MILLER, L., MCCLENATHAN, D., KECK, B., PHIPPS, R.BURR, D.: Calculating clinically relevant drug doses to use in animal studies. *Osteoporosis International*, 2008. **19**(12): p. 1815-1817 DOI: <http://dx.doi.org/10.1007/s00198-008-0741-9>.

## Bibliography

# Appendix





# Curriculum Vitae

## Personal data:

**Name:** Bernhard Pemmer  
**Academic degree:** Dipl.-Ing.  
**Date of birth:** 17.09.1980  
**Place of birth:** St. Pölten, Austria  
**Personal status:** unmarried  
**Nationality:** Austria  
**Private address:** Ferdinand Grasser Straße 352  
3511 Furth bei Göttweig  
Austria  
**E-mail:** bernhard.pemmer@aon.at

## Education:

**since 10/2009:** **Vienna University of Technology, Austria**  
PhD study in Technical Physics at Atominstitut  
Thesis title: *"Synchrotron Micro X-Ray Fluorescence  
Imaging of Trace Elements in Articular Cartilage and Bone  
in Health and Disease"*  
Accomplished under supervision of Prof. Dr. Christina  
Streli

**since 02/2005:** **Vienna University of Technology**  
Teacher training in Physics and Mathematics

**08/2003 - 06/2004:** **Uppsala Universitet, Sweden**  
Study of Physics

**09/2000 - 01/2008:** **Vienna University of Technology, Austria**  
Study of Technical Physics  
Diploma thesis at Atominstitut  
Thesis title: *"Studien zur Quantifizierung: In vivo  
energiedispersive Röntgenfluoreszenzanalyse von Blei im  
menschlichen Knochen"*  
Accomplished under supervision of Prof. Dr. Peter  
Wobrauschek

**09/1991 - 06/1999:** **Bundesgymnasium und Bundesrealgymnasium  
Krems**  
  
Piaristengasse 2,  
Krems, Austria

## Work Experience:

- 10/2009-09/2013:** **Vienna University of Technology, Atominstitut:**  
*Scientific assistant*
- 08/2006:** **Möller Gebäudeautomation KG** (now Eaton Industries GmbH) - Laboratory Vienna:  
*Frequency dependency of ground fault circuit interrupters: Development and implementation of measurement setup; documentation*
- 08/2005:** **Möller Gebäudeautomation KG** (now Eaton Industries GmbH) - Laboratory Vienna:  
*FEM simulations of magnetic forces in trigger systems of automatic circuit breakers; documentation*
- 08/2004:** **Möller Gebäudeautomation GmbH** (now Eaton Industries GmbH) - Laboratory Vienna:  
*Heat transport and conductivity: literature research, calculations and documentation*
- 08/2001:** **Österreichische Post AG, Krems:**  
*vacation replacement delivery service*
- 09/1999 - 05/2000:** **Federal armed forces:** military service - fully served
- 08/1997:** **Rudolf Leiner Ges.m.b.H., Krems:**  
*vacation replacement in warehouse*

## Languages:

- German:** native language
- English:** fluent in speech and writing (publications and oral presentations in English)
- Swedish:** basic knowledge

## Additional Skills:

- Software:** Windows, Linux, MacOS  
Office, LaTeX, Corel (Draw, PhotoPaint)  
Data evaluation software: GraphPad Prism, Origin, Sigmaplot, AXIL, Athena  
Programming languages: Visual Basic for Applications (VBA) (basic knowledge), LabView (basic knowledge)
- Driving License:** Category B (vehicles up to 3500kg)

## Refereed Scientific Articles and Publications:

1. MEIRER, F., PEMMER, B., PEPPONI, G., ZOEGER, N., WOBRAUSCHEK, P., SPRIO, S., TAMPIERI, A., GÖTTLICHER, J., STEININGER, R., MANGOLD, S., ROSCHGER, P., BERZLANOVICH, A., HOFSTÄTTER, J., STRELI, C.: Assessment of chemical species of lead accumulated in tidemarks of human articular cartilage by X-ray absorption near-edge structure analysis. In: *Journal of Synchrotron Radiation* 18 (2011), No. 2, P. 238–244. DOI: <http://dx.doi.org/10.1107/S0909049510052040>
2. PEMMER, B., HOFSTÄTTER, J., MEIRER, F., SMOLEK, S., WOBRAUSCHEK, P., SIMON, R., FUCHS, R. K., ALLEN, M. R., CONDON, K. W., REINWALD, S., PHIPPS, R. J., BURR, D. B., PASCHALIS, E., KLAUSHOFER, K., STRELI, C., ROSCHGER, P.: Increased strontium uptake in trabecular bone of ovariectomized calcium-deficient rats treated with strontium ranelate or strontium chloride. In: *Journal of Synchrotron Radiation* 18 (2011), No. 6, P. 835–841. DOI: <http://dx.doi.org/10.1107/S090904951103038X>
3. SMOLEK, S., PEMMER, B., FÖLSER, M., STRELI, C., WOBRAUSCHEK, P.: Confocal micro-x-ray fluorescence spectrometer for light element analysis. In: *Review of Scientific Instruments* 83 (2012), No. 8, P. 083703–1 – 083703–6. DOI: <http://dx.doi.org/10.1063/1.4744934>
4. STEINHAUSER, G., ADLASSNIG, W., BAINS, W., BAUMGARTNER, T., BICHLER, M., CALNE, R., CELEC, P., CSOKA, A. B., DREWA, T., EDER, F., FOSTER, M., GITTLER, G., GÖSSELSBERGER, C., HAJEK, M., IVANOVSKI, P., NIKOLIC, D., KOLLERPEROUTKA, M., LENDL, B., NEUNTEUFL, B., MÖSSMER, G., PEARCE, N. J. G., PEMMER, B., SALLETMAIER, M., SAUERZOPF, C., SEPPI, D., SKOYLES, J. R., SOMMER, W., STERBA, J. H., STRATFORD, J., STRELI, C., SUMMHAMMER, J., TREVISANATO, S. I., TRIMMEL, M., WAGNER, C., WEINBERGER, P., WOODLEY, M. A. et al.: Peer review versus editorial review and their role in innovative science. In: *Theoretical Medicine and Bioethics* 33 (2012), No. 5, P. 359–376. DOI: <http://dx.doi.org/10.1007/s11017-012-9233-1>
5. PEMMER, B., ROSCHGER, A., WASTL, A., HOFSTÄTTER, J. G., WOBRAUSCHEK, P., SIMON, R., THALER, H. W., ROSCHGER, P., KLAUSHOFER, K., STRELI, C.: Spatial distribution of the trace elements zinc, strontium and lead in human bone tissue. In: *Bone* 52 (2013), No. 1, 184–193. DOI: <http://dx.doi.org/10.1016/j.bone.2013.07.038>. – ISBN 8756–3282
6. ROSCHGER, A., HOFSTÄTTER, J. G., PEMMER, B., ZOEGER, N., WOBRAUSCHEK, P., FALKENBERG, G., SIMON, R., BERZLANOVICH, A., THALER, H. W., ROSCHGER, P., KLAUSHOFER, K., STRELI, C.: Differential accumulation of lead and zinc in double-tidemarks of articular cartilage. In: *Osteoarthritis and Cartilage* (2013). DOI: <http://dx.doi.org/10.1016/j.joca.2013.06.029>. – ISBN 1063–4584. – in Press

## Not Refereed Scientific Articles and Publications:

1. PEMMER, B., MEIRER, F., STRELI, C., WOBRAUSCHEK, P., ROSCHGER, P., HOFSTÄTTER, J., GÖTTLICHER, J.: Micro XANES spectroscopy in human bone and cartilage / ANKA. 2009. – Annual Report
2. PEMMER, B., HOFSTÄTTER, J., STADLBAUER, F., WOBRAUSCHEK, P., SIMON, R., ROSCHGER, P., KLAUSHOFER, K., STRELI, C.: Synchrotron Micro X-Ray Fluorescence Imaging of Trace Elements in Articular Cartilage and Bone in osteonecrosis / ANKA. 2010. – Annual Report
3. PEMMER, B., PEPPONI, G., MEIRER, F., STRELI, C., WOBRAUSCHEK, P., HOFSTÄTTER, J., ROSCHGER, P., GÖTTLICHER, J., STEININGER, R.: Speciation of Lead in Articular Cartilage and Subchondral Bone in case of Osteoarthritis / ANKA. 2010. – Annual Report
4. PEMMER, B., ROSCHGER, A., HOFSTÄTTER, J., SIMON, R., ROSCHGER, P., KLAUSHOFER, K., WOBRAUSCHEK, P., STRELI, C.: Spatial Distribution of Trace Elements in Human Osteoporotic Bone using Synchrotron Micro X-Ray Fluorescence Imaging / ANKA. 2010. – Annual Report
5. PEMMER, B., ROSCHGER, A., HOFSTÄTTER, J., SIMON, R., ROSCHGER, P., KLAUSHOFER, K., WOBRAUSCHEK, P., STRELI, C.: Trace Element Distribution in Human Osteoporotic Fractured Femoral Necks using Synchrotron Micro X-Ray Fluorescence Imaging / ANKA. 2011. – Annual Report
6. STRELI, C., INGERLE, D., PEMMER, B., WOBRAUSCHEK, P., MEIRER, F., PEPPONI, G.: Synchrotron radiation induced x-ray spectrometry / IAEA. 2011. – Final report on the second research co-ordination meeting (RCM) of the co-ordinated research project (CRP) on micro-analytical techniques based on nuclear spectroscopy for environmental monitoring and material studies

## Scientific Conference Contributions:

1. PEMMER, B., WOBRAUSCHEK, P., STRELI, C.: *Studies on Quantification of Pb in Bone in vivo using L-Shell Excitation*. 2007. – Posterpräsentation: Denver X-Ray Conference, Colorado Springs (USA); 2007-08-00
2. MEIRER, F., HOFSTÄTTER, J., SMOLEK, S., PEMMER, B., WOBRAUSCHEK, P., SIMON, R., FUCHS, R. K., ALLEN, M. R., CONDON, K. W., REINWALD, S., MCCLENATHAN, D., KECK, B., PHIPPS, R. J., BURR, D. B., ROSCHGER, P., PASCHALIS, E., KLAUSHOFER, K., STRELI, C.: *Level and spatial distribution of trace elements in bone following strontium treatment in calcium deficient rats*. 2009. – Vortrag: ICXOM 2009, Karlsruhe; 2009-09-17 – 2009-09-20
3. MEIRER, F., PEMMER, B., ZÖGER, N., STRELI, C., GÖTTLICHER, J., STEININGER, R., MANGOLD, S., TAMPIERI, A., SPRIO, S., PEPPONI, G., HOFSTÄTTER, J., ROSCHGER, P., KLAUSHOFER, K.: *Speciation of Pb in the tidemark of human articular Cartilage using XANES at the SUL-X beamline of ANKA*. 2009. – Vortrag: ICXOM 2009, Karlsruhe; 2009-09-17 – 2009-09-20

4. MEIRER, F., ZÖGER, N., PEMMER, B., STRELI, C., GÖTTLICHER, J., STEININGER, R., MANGOLD, S., TAMPIERI, A., SPRIO, S., PEPPONI, G., HOFSTÄTTER, J., ROSCHGER, P., KLAUSHOFER, K.: *Speciation of Pb in the tidemark of human articular Cartilage using micro-XRF-XANES*. 2009. – Vortrag: öpg Jahrestagung 2009 Innsbruck, Innsbruck; 2009-09-02 – 2009-09-04
5. ZÖGER, N., MEIRER, F., PEMMER, B., STRELI, C., GÖTTLICHER, J., STEININGER, R., MANGOLD, S., TAMPIERI, A., SPRIO, S., PEPPONI, G., HOFSTÄTTER, J., ROSCHGER, P., KLAUSHOFER, K.: *Speciation of Pb in the tidemark of human articular Cartilage*. 2009. – Vortrag: 36th ECTS conference, Wien; 2009-05-23 – 2009-05-27
6. MEIRER, F., HOFSTÄTTER, J., SMOLEK, S., PEMMER, B., WOBRAUSCHEK, P., SIMON, R., FUCHS, R. K., ALLEN, M. R., CONDON, K. W., REINWALD, S., MCCLENNATHAN, D., KECK, B., PHIPPS, R. J., BURR, D. B., ROSCHGER, P., PASCHALIS, E., KLAUSHOFER, K.: *Levels and Spatial Distribution of Trace Elements in Bone Following Strontium Treatment in Calcium Deficient Rats*. 2010. – Posterpräsentation: EXRS 2010, Figueira da Foz, Portugal; 2010-06-20 – 2010-06-25
7. MEIRER, F., HOFSTÄTTER, J., SMOLEK, S., PEMMER, B., WOBRAUSCHEK, P., SIMON, R., FUCHS, R. K., ALLEN, M. R., CONDON, K. W., REINWALD, S., MCCLENNATHAN, D., KECK, B., PHIPPS, R. J., BURR, D. B., ROSCHGER, P., PASCHALIS, E., KLAUSHOFER, K., STRELI, C.: *Levels and Spatial Distribution of Trace Elements in Bone Following Strontium Treatment in Calcium Deficient Rats*. 2010. – Vortrag: 59th Annual Denver X-ray Conference, Denver; 2010-08-02 – 2010-08-06
8. MEIRER, F., PEMMER, B., ZÖGER, N., STRELI, C., GÖTTLICHER, J., STEININGER, R., MANGOLD, S., TAMPIERI, A., SPRIO, S., PEPPONI, G., HOFSTÄTTER, J., ROSCHGER, P., KLAUSHOFER, K.: *Speciation of Pb at the Tidemark of Articular Cartilage and in Trabecular Bone*. 2010. – Posterpräsentation: EXRS 2010, Figueira da Foz, Portugal; 2010-06-20 – 2010-06-25
9. GÖTTLICHER, J., MEIRER, F., PEMMER, B., ZÖGER, N., STRELI, C., STEININGER, R., MANGOLD, S., TAMPIERI, A., SPIRO, S., PEPPONI, G., HOFSTÄTTER, J., KLAUSHOFER, K.: *Speciation of Pb in Human Trabecular Bone and the Tidemark of Articular Cartilage*. 2010. – Vortrag: 88. Jahrestagung der Deutschen Mineralogischen Gesellschaft, Münster, Deutschland; 2010-09-19 – 2010-09-22
10. STRELI, C., MEIRER, F., WOBRAUSCHEK, P., ZÖGER, N., SMOLEK, S., PEMMER, B., ROSCHGER, P., HOFSTÄTTER, J., KLAUSHOFER, K., PEPPONI, G., FALKENBERG, G., SIMON, R., GÖTTLICHER, J.: *Ortsaufgelöste Elementverteilung in Knochenproben mit Mikro-Röntgenfluoreszenzspektrometrie*. 2010. – Vortrag: Institutsseminar 2010, Institut für Leichtbau, TU Wien; 2010-01-08
11. MEIRER, F., HOFSTÄTTER, J., SMOLEK, S., PEMMER, B., WOBRAUSCHEK, P., SIMON, R., FUCHS, R. K., ALLEN, M. R., CONDON, K. W., REINWALD, S., MCCLENNATHAN, D., KECK, B., PHIPPS, R. J., BURR, D. B., ROSCHGER, P., PASCHALIS, E., KLAUSHOFER, K., STRELI, C.: *Levels and Spatial Distribution of Trace Elements in Bone Following Strontium Treatment in Calcium Deficient Rats*. 2011. – Posterpräsentation: 7th European Winter School on Neutrons and Synchrotron Radiation, Planneralp, Austria; 2011-03-06 – 2011-03-12

12. MEIRER, F., PEMMER, B., ZOEGER, N., STRELI, C., PEPPONI, G., GÖTTLICHER, J., STEININGER, R., MANGOLD, S., TAMPIERI, A., SPRIO, S., ROSCHGER, P., KLAUSHOFER, K., HOFSTÄTTER, J.: *Speciation of Pb at the Tidemark of Articular Cartilage and in Trabecular Bone*. 2011. – Posterpräsentation: 7th European Winter School on Neutrons and Synchrotron Radiation, Planneralp, Austria; 2011-03-06 – 2011-03-12
13. MEIRER, F., ZOEGER, N., PEMMER, B. and, STRELI, C., GÖTTLICHER, J., STEININGER, R., MANGOLD, S., TAMPIERI, A., SPRIO, S., PEPPONI, G., HOFSTÄTTER, J., ROSCHGER, P., KLAUSHOFER, K.: *Speciation of Pb at the Tidemark of Articular Cartilage and in Trabecular Bone*. 2011. – Posterpräsentation: ANKA Seminar, Karlsruhe, Germany; 2011-10-13 – 2011-10-14
14. PEMMER, B., ROSCHGER, A., WOBRAUSCHEK, P., STRELI, C., HOFSTÄTTER, J., ROSCHGER, P., KLAUSHOFER, K., SIMON, R.: *Trace element distribution in trabecular and cortical bone of fractured femoral necks of postmenopausal osteoporotic women: a synchrotron micro x-ray fluorescence imaging study*. 2011. – Posterpräsentation: Denver X-Ray Conference, Colorado Springs, USA; 2011-08-01 – 2011-08-05
15. PEMMER, B., ZOEGER, N., STRELI, C., PEPPONI, G., MEIRER, F., GÖTTLICHER, J., STEININGER, R., MANGOLD, S., TAMPIERI, A., SPIRO, S., ROSCHGER, P., KLAUSHOFER, K., HOFSTÄTTER, J.: *Speciation of Pb at the Tidemark of Articular Cartilage and in Trabecular Bone*. 2011. – Posterpräsentation: Denver X-Ray Conference, Colorado Springs, USA; 2011-08-01 – 2011-08-05
16. ROSCHGER, A., PEMMER, B., WOBRAUSCHEK, P., STRELI, C., HOFSTÄTTER, J., ROSCHGER, P., KLAUSHOFER, K., SIMON, R.: *Differential accumulation of lead in double-tidemarks in articular cartilage of osteoarthritic human joints*. 2011. – Posterpräsentation: Denver X-Ray Conference, Colorado Springs, USA; 2011-08-01 – 2011-08-05
17. ROSCHGER, A., HOFSTÄTTER, J., PEMMER, B. and, ZOEGER, N., WOBRAUSCHEK, P., SIMON, R., FALKENBERG, G., ROSCHGER, P., KLAUSHOFER, K., STRELI, C.: *Differential accumulation of lead in double-tidemarks in articular cartilage of osteoarthritic human joints*. 2011. – Posterpräsentation: ANKA Seminar, Karlsruhe, Germany; 2011-10-13 – 2011-10-14
18. GÖTTLICHER, J., STEININGER, R., GAMALETOS, P., GODELITSAS, A., KERSTEN, M., MAJZLAN, J., MEIRER, F., MERTZIMEKIS, T. J., PEMMER, B., PEPPONI, G., ROSCHGER, P., SCHMIDT, G., STRELI, C., WOBRAUSCHEK, P., ZOEGER, N.: *Environmental Research at the SUL-X Beamline of the Synchrotron Radiation Source ANKA*. 2011. – Vortrag: Frontiers in Environmental Geosciences, Wales, GB; 2011-06-21 – 2011-06-24
19. PEMMER, B., ROSCHGER, A., HOFSTÄTTER, J., WOBRAUSCHEK, P., SIMON, R., ROSCHGER, P., KLAUSHOFER, K., STRELI, C.: *SR  $\mu$ -XRF Imaging of Osteoporotic Bone*. 2011. – eingeladen; Vortrag: ANKA User Meeting 2011, Karlsruhe, Germany; 2011-10-13 – 2011-10-14

20. PEMMER, B., ROSCHGER, A., HOFSTÄTTER, J., WOBRAUSCHEK, P., SIMON, R., ROSCHGER, P., KLAUSHOFER, K., STRELI, C.: *Trace element distribution in trabecular and cortical bone of fractured femoral necks of postmenopausal osteoporotic women: a synchrotron micro x-ray fluorescence imaging study.* 2011. – Posterpräsentation: öGKM Herbsttagung 2011, Vienna, Austria; 2011-10-25
21. PEMMER, B., WOBRAUSCHEK, P., STRELI, C., ROSCHGER, A., ROSCHGER, P., KLAUSHOFER, K., HOFSTÄTTER, J.: *2D and 3D Imaging of Human Tissue.* 2011. – Vortrag: Imaging in Life Sciences 2, Vienna, Austria; 2011-12-07
22. ROSCHGER, A., PEMMER, B., HOFSTÄTTER, J., ZOEGER, N., WOBRAUSCHEK, P., SIMON, R., FALKENBERG, G., ROSCHGER, P., KLAUSHOFER, K., STRELI, C.: *Differential accumulation of lead in double-tidemarks in articular cartilage of osteoarthritic human joints.* 2011. – Vortrag: öGKM Herbsttagung 2011, Vienna, Austria; 2011-10-25
23. ROSCHGER, A., PEMMER, B., ROSCHGER, P., HOFSTÄTTER, J., SIMON, R., KLAUSHOFER, K., STRELI, C.: *Lokale Verteilung der Spurenelemente Blei, Zink und Strontium im menschlichen Knochen.* 2011. – Vortrag: 3 Ländertagung der öGMP, DGMP und SGSMP - medizinische Physik 2011, Vienna, Austria; 2011-10-01
24. ROSCHGER, P., PEMMER, B., FRATZL, P., KLAUSHOFER, K.: *Strontium-ranelate treatment leads to uptake of strontium in bone.* 2011. – Vortrag: ÖGKM Herbsttagung 2011, Vienna, Austria; 2011-10-25
25. STRELI, C., INGERLE, D., PEMMER, B., WOBRAUSCHEK, P., MEIRER, F., PEPPONI, G.: *Synchrotron radiation induced x-ray spectrometry.* 2011. – Vortrag: Micro-analytical techniques based on nuclear spectrometry for environmental monitoring and material studies, Vienna, Austria; 2011-10-10 – 2011-10-14
26. STRELI, C., PEMMER, B., MEIRER, F., PEPPONI, G., WOBRAUSCHEK, P.: *Synchrotron radiation induced TXRF and micro XRF.* 2011. – Vortrag: Seminar, Mumbai, India; 2011-12-05
27. STRELI, C., PEMMER, B., WOBRAUSCHEK, P., INGERLE, D., MEIRER, F., PEPPONI, G.: *Synchrotron radiation induced TXRF.* 2011. – Vortrag: Seminar, Indore, India; 2011-12-07
28. STRELI, C., WOBRAUSCHEK, P., KREGSAMER, P., PEMMER, B., MEIRER, F., PEPPONI, G., ZOEGER, N., FALKENBERG, G., SIMON, R., GÖTTLICHER, J.: *Synchrotron X-Ray Fluorescence Spectrometry.* 2011. – Vortrag: 7th European Winter School on Neutrons and Synchrotron Radiation, Planneralp, Austria; 2011-03-06 – 2011-03-12
29. WOBRAUSCHEK, P., MEIRER, F., PEMMER, B., STRELI, C.: *Synchrotron radiation based micro and trace XRF analysis.* 2011. – eingeladen; Vortrag: Seminar on Nondestructive Instrumental Analysis for Forensic investigation, Osaka, Japan; 2011-11-10
30. WOBRAUSCHEK, P., STRELI, C., PEMMER, B.: *Synchrotron radiation based micro and trace XRF analysis.* 2011. – Vortrag: Seminar, Indore, India; 2011-12-07

31. PEMMER, B., WEIXELBAUMER, C., FÖLSER, M., ROSCHGER, A., HOFSTÄTTER, J., WOBRAUSCHEK, P., WINDHAGER, R., LANG, S., SIMON, R., ROSCHGER, P., KLAUSHOFER, K. , STRELI, C.: *Distribution of trace elements in human osteosarcoma - a malignant bone tumour*. 2012. – Vortrag: Denver X-Ray Conference, Denver, USA; 2012-08-06 – 2012-08-10
32. PEMMER, B., ROSCHGER, A., HOFSTÄTTER, J., WOBRAUSCHEK, P., SIMON, R., ROSCHGER, P., KLAUSHOFER, K. , STRELI, C.: *Distribution of Trace Elements Zn, Pb and Sr in Bone Packets and Cement Lines of Cortical and Trabecular Human Bone*. 2012. – Posterpräsentation: European Calcified Tissue Society 2012, Stockholm, Sweden; 2012-05-19 – 2012-05-23
33. PEMMER, B., ROSCHGER, A., HOFSTÄTTER, J., WOBRAUSCHEK, P., THALER, H., SIMON, R., ROSCHGER, P., KLAUSHOFER, K. , STRELI, C.: *SR  $\mu$ -XRF Imaging of Osteoporotic Bone*. 2012. – Vortrag: EXRS Conference, Vienna, Austria; 2012-06-18 – 2012-06-22
34. PEMMER, B., SMOLEK, S., WEIXELBAUMER, C., FÖLSER, M., ROSCHGER, A., HOFSTÄTTER, C., WOBRAUSCHEK, P., WINDHAGER, R., LANG, S., SIMON, R., ROSCHGER, P., KLAUSHOFER, K. , STRELI, C.: *Synchrotron and laboratory  $\mu$ -XRF analysis of trace element distribution of mineralized human osteosarcoma tissue*. 2012. – Posterpräsentation: International Conference on Progress in Bone and Mineral Research 2012, Vienna, Austria; 2012-11-29 – 2012-12-01
35. PEMMER, B., WEIXELBAUMER, C., FÖLSER, M., ROSCHGER, A., HOFSTÄTTER, J., WOBRAUSCHEK, P., SIMON, R., ROSCHGER, P., KLAUSHOFER, K. , STRELI, C.: *Distribution of trace elements in the mineralized matrix of human osteosarcoma tissue*. 2012. – Posterpräsentation: EXRS Conference, Vienna, Austria; 2012-06-18 – 2012-06-22
36. PEMMER, B., WOBRAUSCHEK, P., SMOLEK, S. , STRELI, C.: *2D and 3D elemental imaging using X-ray sepcrometry*. 2012. – Vortrag: Imaging in Life Sciences Workshop IV, Vienna, Austria; 2012-11-12
37. ROSCHGER, A., PEMMER, B., HOFSTÄTTER, J., ZOEGER, N., WOBRAUSCHEK, P., SIMON, R., FALKENBERG, G., ROSCHGER, P., KLAUSHOFER, K. , STRELI, C.: *Differential accumulation of Pb and Zn in mineralization-fronts of articular cartilage*. 2012. – Posterpräsentation: European Calcified Tissue Society 2012, Stockholm, Sweden; 2012-05-19 – 2012-05-23
38. STRELI, C., PEMMER, B. , WOBRAUSCHEK, P.: *2D and 3D elemental imaging of human tissue*. 2012. – Vortrag: Imaging in Life Sciences Workshop III, Vienna, Austria; 2012-06-28
39. WEIXELBAUMER, C., PEMMER, B., ROSCHGER, A., THALER, H., WOBRAUSCHEK, P. , STRELI, C.: *Quantitative analysis of the trace elements zinc, strontium and lead in human bone by energy dispersive x-ray fluorescence analysis*. 2012. – Posterpräsentation: EXRS Conference, Vienna, Austria; 2012-06-18 – 2012-06-22



40. WEIXELBAUMER, C., PEMMER, B., WOBRAUSCHEK, P., STRELI, C. , ROSCHGER, A.: *Quantitative analysis of the trace elements zinc, strontium and lead in human bone by EDXRS*. 2012. – Posterpräsentation: Denver X-Ray Conference, Denver, USA; 2012-08-06 – 2012-08-10
41. PEMMER, B., SMOLEK, S., WEIXELBAUMER, C., FOELSER, M., RAUWOLF, M., MADERITSCH, A., WOBRAUSCHEK, P., STRELI, C. , ROSCHGER, A., ROSCHGER, P., KLAUSHOFER, K., SIMON, R., WINDHAGER, R., LANG, S. , HOFSTAETTER, J.: *Distribution of S, Ca, Fe And Zn in Human Osteosarcoma Tissue Determined with Synchrotron and Laboratory  $\mu$ -XRF Analysis*. 2013. – Posterpräsentation: 62th Denver X-Ray conference, Westminster, USA; 2013-08-05 – 2013-08-09
42. PEMMER, B., SMOLEK, S., WEIXELBAUMER, C., FOELSER, M., RAUWOLF, M., MADERITSCH, A., WOBRAUSCHEK, P., STRELI, C., ROSCHGER, A., ROSCHGER, P., KLAUSHOFER, K., SIMON, R., WINDHAGER, R., LANG, S. , HOFSTAETTER, J.: *Distribution of S, Ca, Fe And Zn in Human Osteosarcoma Tissue Determined with Synchrotron and Laboratory  $\mu$ -XRF Analysis*. 2013. – Vortrag: 8th European NESY Winter-School, Donnersbach, Austria; 2013-03-10 – 2013-03-16

Vienna, on 1st September 2013

Place, Date

---

Dipl.-Ing. Bernhard Pemmer

